Millennial-scale ice-ocean-climate variability during the last glacial: High-resolution records from the NE Atlantic

Victoria Louise Peck

School of Earth, Ocean and Planetary Sciences,

Cardiff University

May 2006

UMI Number: U585548

All rights reserved

INFORMATION TO ALL USERS
The quality of this reproduction is dependent upon the quality of the copy submitted.

In the unlikely event that the author did not send a complete manuscript
and there are missing pages, these will be noted. Also, if material had to be removed,
a note will indicate the deletion.

UMI®
Dissertation Publishing

UMI U585548
Published by ProQuest LLC 2013. Copyright in the Dissertation held by the Author.
Microform Edition © ProQuest LLC.
All rights reserved. This work is protected against
unauthorized copying under Title 17, United States Code.

ProQuest®

ProQuest LLC
789 East Eisenhower Parkway
P.O. Box 1346
Ann Arbor, MI 48106-1346

DECLARATION

This work has not previously been accepted for any degree and is not currently submitted in candidature for any degree.

Signed.....J. Peck..... **(candidate)**

Date.....20/9/06.....

STATEMENT 1

This thesis is the result of my own investigations, except where otherwise stated. Other sources are acknowledged by footnotes giving explicit references. A bibliography is appended.

Signed.....J. Peck..... **(candidate)**

Date.....20/9/06.....

STATEMENT 2

I hereby give consent for my thesis, if accepted, to be available for photocopying and for inter-library loan, and for the title and summary to be made available to outside organisations.

Signed.....J. Peck..... **(candidate)**

Date.....20/9/06.....

SUMMARY

Marine sediment core MD01-2461 recovered from the European Margin, SW of Ireland (51° 45' N, 12° 55' W) at a water depth of 1153m provides material for multi-decadal to centennial scale investigation into ice-ocean-climate variability during the period 60 to 8 kyrs BP. Particular focus is placed on the oceanic and climatic conditions under which periodic collapse of the North American Laurentide ice sheet (LIS) occurred, so called Heinrich (H) events, and the involvement of the NW European ice sheets (NWEIS) within episodes of abrupt climate change.

Presented here are records of circum-North Atlantic ice sheet growth, dynamics and decline from lithological and geochemical analysis of ice-rafted debris. Paired Mg/Ca and $\delta^{18}O$ data from the surface dwelling *Globigerina bulloides* and subsurface dwelling *Neogloboquadrina pachyderma* sinistral are used to determine late-glacial variability of temperature, salinity and stratification of the upper water column, and benthic $\delta^{13}C$ records from *C. wuellerstorfi* documents the interchange of glacial northern and southern-sourced intermediate water signatures along the European Margin when compared to similar records from the Portuguese Margin and high-latitude North Atlantic basin.

A picture emerges that the BIS was in a continuing state of readjustment and never fully reached steady state. Persistent 2 kyr instability of the BIS fluxes throughout the late glacial (26.5-10 kyr BP) suggests that 'precursor events' were not directly implicated in the collapse of the LIS. However, negative salinity excursions of up to 2.6 indicate significant incursions of meltwater associated with peaks in NWEIS instability, stratifying the upper water column. Such events are associated with reduced ventilation of intermediate waters, recorded in depleted epibenthic $\delta^{13}C$ suggesting that instability and meltwater forcing of the NWEIS temporarily weakened Glacial North Atlantic Intermediate Water formation, allowing transient advance of southern-sourced waters to the site of MD01-2461. NWEIS-instability and associated perturbation to the North Atlantic thermohaline circulation may have set the stage for H event initiation; regional cooling associated with a preliminary reduction in MOC may have promoted the growth of a LIS-fringing ice-shelf and subsequent subsurface warming and sea level rise may have destabilised the ice margin. Additionally, high-resolution summer sea surface temperature records based on the $Mg/Ca_{G.\ bulloides}$ suggest that mild, even warm summer months may be a have been a feature of H events.

AUTHOR'S NOTE

Chapters Four, Five, Six and **Seven** of this thesis have been presented as papers to four different international publications. The present status of these publications is summarised as follows:

Chapter Four has been submitted to *Quaternary Science Reviews* as: Peck, V.L., Hall, I.R., Zahn, R., Grousset, F.E., Hemming, S.R., Scourse, J.D. The relationship of Heinrich events and their European precursors over the past 60 kyr BP: A multi-proxy ice rafted debris provenance study in the NE Atlantic.

Chapter Five has been published in *Earth and Planetary Science Letters* as: Peck, V.L., Hall, I.R., Zahn, R., Elderfield, H., Grousset, F.E., Hemming, S.R., Scourse, J.D. (2006) High Resolution Evidence for Linkages between European Ice Sheet Instability and Atlantic Meridional Overturning Circulation (Vol. 243, p 476-488).

Chapter Six has been submitted to *Paleoceanography* as: Peck, V.L., Hall, I.R., Zahn, R., Elderfield, H., Scourse, J.D. Millennial-scale surface and subsurface palaeothermometry from the NE Atlantic, 55-8 kyr BP: a multi-proxy approach.

Chapter Seven has been submitted to *Geochemistry, Geophysics, Geosystems* as: Peck, V.L., Hall, I.R., Zahn, R., Scourse, J.D. High resolution records of progressive Atlantic Meridional Overturning Circulation reduction from the NE Atlantic prior to Heinrich events; response to NW European ice sheet instabilities?

As a consequence of chapters of this thesis being published as individual papers in scientific journals, some repetition of statement could not be avoided.

Declaration of co-author contributions

Chapter Four **The relationship of Heinrich events and their European precursors over the past 60 kyr BP: A multi-proxy ice rafted debris provenance study in the NE Atlantic.**

Hall, I.R., Zahn, R.	Reviewed several versions of manuscript.
Grousset, F.E.	Sr-Nd isotopic composition measurements on 27 samples of non-carbonate IRD.
Hemming, S.R.	Analysed and determined 40Ar/39Ar ages for 214 ice rafted hornblende grains, reviewed final version of manuscript.
Scourse, J.D.	Reviewed final version of manuscript.

Chapter Five **High Resolution Evidence for Linkages between European Ice Sheet Instability and Atlantic Meridional Overturning Circulation**

Hall, I.R.	Reviewed several versions of manuscript.
Zahn, R.	Calculated water density. Reviewed several versions of manuscript.
Elderfield, H.	Provided laboratory use for Mg/Ca analysis and reviewed final version of manuscript.
Grousset, F.E., Hemming, S.R., Scourse, J.D.	As Chapter Four

Chapter Six **Millennial-scale surface and subsurface palaeothermometry from the NE Atlantic, 55-8 kyr BP: a multi-proxy approach.**

Hall, I.R., Zahn, R.	As Chapter Four
Elderfield, H.	As Chapter Five

Chapter Seven **High resolution records of progressive Atlantic Meridional Overturning Circulation reduction from the NE Atlantic prior to Heinrich events; response to NW European ice sheet instabilities?**

Hall, I.R., Zahn, R. As Chapter Four

ACKNOWLEDGEMENTS

Thank you to my immediate supervisor Ian Hall who has demonstrated endless inspiration, support and patience throughout this PhD. Co-supervisors Rainer Zahn and James Scourse are thanked for guidance throughout. Co-authors on submitted manuscripts are also acknowledged; Harry Elderfield specifically for allowing laboratory use for Mg/Ca analysis and invaluable advice on Mg/Ca-temperature calibration; Francis Grousset for facilitating Sr-Nd measurements and Sidney Hemming $^{40}Ar/^{39}Ar$ dating of hornblende grains.

An especially big thank you goes to Mervyn Greaves for enthusiastically sharing his expertise in Mg/Ca analysis; Giancarlo Bianchi for stable isotope analysis; Brian Long and Helen Medley for sample preparartion; Rehannah Chaudri for picking foraminifera for ^{14}C-AMS dating; Jeremy Young and Craig Koch for identifying coccoliths in chalk grains, and Ghaleb Bassam (Montreal) U-series dating of deep-sea corals.

John T. Andrews and Harunar Rashid are thanked for their constructive reviews of Peck et al. (2006)/Chapter Five, and Stephen Barker for commenting on an early draft of Chapter Six.

On personal level particular thanks has to go to Mairi, Dave and Rich, Julia and Ronja, Helen and the rest of Ian's girls for having kept me sane or at least humouring me when I wasn't over the last 3+ years. Everyone else I met along the way, you know who you are, thank you!

Finally, a big thank you to Mum and Dad for their endless support throughout (and proof-reading!).

List of abbreviations

AAIW	Antarctic intermediate water
AMOC	Atlantic meridional oceanic circulation
AMS	Accelerator Mass spectrometry
BIS	British ice sheet
EG/IIS	East Greenland/Icelandic ice sheet
GIS	Greenland ice sheet
GISP	Greenland Ice Sheet Project
GNAIW	Glacial North Atlantic Intermediate Water
H	Heinrich
HCG	Haematite-coated grains
IIS	Icelandic ice sheet
IRD	Ice rafted debris
kyr BP	thousand years before present (calendar)
LGM	Last glacial maximum
LIS	Laurentide ice sheet
MIS	Marine isotope stage
MOW	Mediterranean outflow water
NAAZII	North Atlantic ash zone II
NAD	North Atlantic Drift
NADW	North Atlantic Deep Water
NEAW	North East Atlantic Water
NWEIS	North West European ice sheets
SCW	Southern component water
SSS	sea surface salinity
SST	sea surface temperature
SubSS	subsurface salinity
SubST	subsurface temperature

LIST OF CONTENTS

Declaration ii
Summary iii
Author's note iv
Declaration of co-author contributions v
Acknowledgements vii
List of Abbreviations viii
List of Contents ix

CHAPTER ONE

Introduction

1.1 Rationale 1-1
1.2 Aims of study 1-6
1.3 Thesis layout 1-7

CHAPTER TWO

Material and methods

2.1 Core and location 2-1
2.1.1 Present day hydrography 2-3
2.1.2 Glacial conditions 2-6
2.2 Methods 2-8
2.2.1 Core handling, shipboard analyses and physical properties 2-8
2.2.2 Sample preparation 2-9
2.2.3 IRD accumulation 2-9
2.2.4 Last glacial North Atlantic ice sheet and IRD provenance fingerprinting 2-11
2.2.4.1 Lithological provenance 2-12
2.2.4.2 $^{40}Ar/^{39}Ar$ ages of individual hornblende grains 2-13
2.2.4.3 Sr-Nd isotopic composition 2-13
2.2.5 Hydrographical reconstructions 2-15
2.2.5.1 Upper water column conditions 2-15
2.2.5.2 Stable isotope analysis 2-16
2.2.5.3 Foraminiferal ecology 2-17
2.2.5.4 Mg/Ca analysis 2-18
2.2.5.4.1 Calcite dissolution and Mg/Ca-temperatures 2.19
2.2.5.4.2 Mg/Ca-temperature calibration 2-20
2.2.5.5 Relative abundance of *N. pachyderma* sin. as a SST proxy 2-23
2.2.5.6 Considerations for surface and subsurface salinity reconstructions 2-24
2.2.5.7 Bottom water conditions 2-24

CHAPTER THREE

Age model construction

3.1 Radiocarbon dating 3-1
3.2 Limitations of radiocarbon dating and additional age constraints 3-6
3.2.1 Tephrachronology 3-7
3.2.1.1 Vedde Ash 3-7
3.2.1.2 North Atlantic Ash Zone II 3-8
3.2.2 U-Th dating of deep-sea corals 3-12
3.2.3 Tuning of palaeoclimate records 3-13
3.3 Finalised age model 3-14
3.3.1 Core stretching? 3-17
3.4 Age model comparison and implications for ^{14}C-marine reservoir age.... 3-20
3.4.1 ^{14}C-marine reservoir age variability and AMOC 3-21

CHAPTER FOUR

Multi-proxy ice rafted debris provenance studies in the NE Atlantic –decadal to centennial scale record of last glacial ice sheet growth, variability and decline. The relationship of Heinrich events and their 'European precursors'

4.1 Introduction 4-2
4.2 Material and methods 4-3
4.2.1 Physical properties 4-4
4.2.2 IRD concentration and composition 4-5
4.2.3 Benthic oxygen isotopes 4-7
4.2.4 Chronology 4-7
4.3 Results 4-11
4.3.1 Physical properties and IRD concentration and composition 4-11
4.3.2 Hornblende grain ages 4-15
4.3.3 Sr-Nd isotopic composition 4-17
4.4 Discussion 4-19
4.4.1 Provenance allocation 4-19
4.4.2 IRD flux: Ice sheet growth, variability and decline 4-22
4.4.2.1 Approaching the LGM 4-23
4.4.2.2 Ice sheet variability 4-25
4.4.2.3 Deglaciation 4-26
4.5 Summary and interpretation of 'European precursor' events 4-27

CHAPTER FIVE

High Resolution Evidence for Linkages between European Ice Sheet Instability and Atlantic Meridional Overturning Circulation

5.1 Introduction 5-2
5.2 Materials and methods 5-3
5.3 Results and discussion 5-9
5.3.1 Ice sheet instabilities 5-9
5.3.2 Surface, subsurface and intermediate water conditions associated with ice rafting events 5-14
5.3.3 Ice sheet processes in response to ocean-climate forcing 5-22
5.3.4 NW European ice sheet instability and AMOC variability 5-25
5.4 Summary 5-26

CHAPTER SIX

High resolution records of last glacial surface and subsurface temperatures and Meridional Overturn Circulation variability from the NE Atlantic – a multi-proxy approach

6.1 Introduction 6-2
6.2 Materials and methods 6-3
6.2.1 Trace element and stable isotope analysis 6-4
6.2.2 Faunal counts 6-7
6.3 Results and discussion 6-8
6.3.1 Coupling surface and subsurface Mg/Ca and oxygen isotope records 6-9
6.3.2 Mg/Ca-temperature calibration and shortfalls 6-11
6.3.3 Mg/Ca and faunal density records 6-16
6.3.4 Upper ocean conditions 55-26.5 kyr BP 6-17
6.3.5 LGM-deglacial conditions and the British ice sheet 6-18
6.3.6 Millennial scale events; maybe Heinrich events were not so cold 6-20
6.3.7 Robustness of Mg/Ca_{Gb} signal 6-20
6.3.8 Artificial seasonality and anomalous years 6-21
6.3.9 Implications of mild summers associated with Heinrich events 6-23
6.4 Summary and conclusion 6-25

CHAPTER SEVEN

High resolution records of progressive AMOC reduction from the NE Atlantic prior to Heinrich events; response to NW European ice sheet instabilities?

7.1 Introduction 7-2
7.2 Materials and methods 7-4
7.3 Results and discussion 7-8
7.3.1 Benthic ^{13}C records from MD01-2461 7-9
7.3.2 Intermediate water ventilation changes from NE Atlantic records 7-12
7.3.3 Precursory meltwater forcing from the NWEIS 7-15
7.3.4 Ice sheet instability in response to North Atlantic THC changes 7-19
7.4 Conclusions 7-20

CHAPTER EIGHT

Summary and discussion

8.1 Introduction 8-1
8.2 Growth, instabilities and decline of the last glacial circum-North Atlantic ice sheets (chapter 4) 8-1
8.3 Involvement of the NWEIS in episodes of abrupt climatic change; NWEIS meltwater stratification and AMOC variability (Chapter 5) 8-3
8.4 Upper ocean climate reconstructions (Chapter 6) 8-4
8.5 Mapping wide-scale THC variability along the European margin (Chapter 7) 8-4
8.6 Millennial scale climate variability 8-5
8.7 Thoughts on further work 8-8
8.7.1 Age models 8-8
8.7.2 IRD provenance 8-8
8.7.3 Variability of the last glacial BIS 8-9
8.7.4 Palaeotemperature reconstructions 8-10
8.7.4.1 Species and region specific Mg/Ca-temperature calibrations for North Atlantic records 8-10
8.7.4.2 Further North Atlantic Mg/Ca records 8-10
8.7.4.3 Additional proxy records applied to MD01-2461 8-11
8.7.4.4 Individual specimen Mg/Ca analysis 8-11
8.7.5 AMOC 8-11
8.7.6 Interdisciplinary studies; data-model comparisons 8-12

APPENDICES

Appendix A **Age model**

Appendix B **IRD counts**

Appendix C **Sr and Nd isotopic composition of IRD**

Appendix D **Hornblende grain $^{40}Ar/^{39}Ar$ ages**

Appendix E **Faunal counts, stable isotopes and Mg/Ca**

References

ENCLOSURE

Peck *et al.* (2006) reprint

Chapter One

Introduction

1.1 Rationale

A key issue in the assessment of present day climate change and the extent of human influence on the Earth's environment is determining how the magnitude and rate of changes observed over the last 100 years differs from natural variability (IPCC Assessment of Global Warming 2001). However, distinguishing between anthropogenically-driven climate change and natural variation is seriously limited by our 'incomplete understanding of natural climate variability' (Hegerl, 1998), driving extensive investigation of past climatic conditions from annual to million year timescales.

Ice core records from the Greenland ice sheet provide annual to centennial resolution records of Northern Hemisphere climate variability for the past 110 kyr (e.g. Dansgaard *et al.*, 1993; Mayewski *et al.*, 1994; Andersen *et al.*, 2004). Unlike the relative stability of the Holocene Epoch, these ice core records reveal that the last glacial period was punctuated on a millennial time scale by extreme climatic swings, comprising Greenland air-temperature increases of 5-10 °C over just a few decades (Dansgaard *et al.*, 1993; Grootes *et al.*, 1993). Evidence from deep-sea sediments and ocean-climate modelling suggest that these so-called Dansgaard-Oeschger

oscillations within the Greeland ice core records likely resulted from switches in the mode of Atlantic Meridional Overturning Circulation (AMOC; Sarnthein *et al.*, 1994; Ganopolski and Rahmstorf, 2001; Clark *et al.*, 2002). Appreciation of this ocean-climate system and the mechanisms and thresholds involved may help to evaluate the potential threat of rapid variability within the climate system in response to increasing greenhouse gas concentrations.

At present, the AMOC is driven by the formation of deep waters in the northern North Atlantic and Labrador Sea (e.g. Broecker *et al.*, 1990), with liberation of heat transported to the north by the warm North Atlantic Drift (NAD) to the atmosphere, particularly in winter, maintaining the mild climate currently experienced in NW Europe (Bjerknes, 1964). Glacial advance approaching the Last Glacial Maximum (LGM, ~21 kyr BP) and migration of the polar front caused these convection centres to shift into the open North Atlantic, south of Iceland (e.g. Oppo and Lehman 1993; Sarnthein *et al.*, 1994), plausibly producing a metastable state prone to dramatic shifts in mode with small perturbations in the freshwater budget (Ganopolski and Rahmstorf, 2001). Reduced interhemispheric heat piracy to high northern latitudes through weakened or even shut-down AMOC likely accounted for the cold, stadial conditions recorded in Greenland ice cores and coincident southern Atlantic warming as part of the so called bipolar seesaw (Stocker, 1998; Seidov and Maslin, 2001).

Marine records reveal episodes of enhanced iceberg calving from the circum-North Atlantic ice sheets and reduced sea surface temperature (SST) corresponding to stadials within the Greenland air temperature record from 10 to 60 kyr BP (Bond *et al.*, 1992; 1993). Sediment-laden icebergs calved from circum-North Atlantic ice

sheets became entrained within a cyclonic surface gyre south of Iceland, depositing multi-sourced ice rafted debris (IRD) within the Ruddiman Belt, between 40° and 55° N (Heinrich, 1988; Bond *et al.*, 1992; Grousset *et al.*, 1993; Revel *et al.*, 1996). Detrital carbonate and distinctive geochemical signatures (e.g. Andrews and Tedesco, 1992; Bond *et al.*, 1992; Gwiazda *et al.*, 1996; Hemming *et al.*, 1998; Snoeckx *et al.*, 1999) suggest that large iceberg armadas originating from the Palaeozoic carbonate-floored Hudson Strait region of the Laurentide ice sheet (LIS) deposited these IRD-rich horizons (or layers) across the Ruddiman Belt every ~7 kyrs (Bond *et al.*, 1992; Hemming, 2004). These events, known as Heinrich (H) events (Broecker, 1994 after Heinrich, 1988), involved substantial collapse of the LIS; the volume of IRD deposited (100-400 km^3) derives iceberg volumes indicative of a loss of up to ~14 % of the LIS during each of these events (Hemming, 2004). The quantities of buoyant freshwater released during H events, evidenced through negative $\delta^{18}O$ excursions of planktonic foraminifera of increasingly polar-dominated assemblages (e.g. Bond *et al.*, 1992; Hillaire-Marcel *et al.*, 1994; Maslin *et al.*, 1995; Cortijo *et al.*, 1997) are likely to have greatly exceeded that required to affect the strength of the AMOC (e.g. Manabe and Stouffer, 1995; Seidov and Maslin, 1999; Ganopolski and Rahmstorf, 2002). Decreased benthic $\delta^{13}C$ values within the North Atlantic, associated with the deposition of the H layers suggest the periodic advance of poorly-ventilated southern-sourced waters (e.g. Vidal *et al.*, 1997; Zahn *et al.* 1997; Elliot *et al.*, 2002) inferring marked reductions in the strength of Glacial North Atlantic Intermediate Water (GNAIW) formation during these events. Furthermore, $^{231}Pa/^{230}Th$ ratios at two North Atlantic core sites approach production values during

the last H event, H1 at ~16.8 kyr BP, suggesting near-collapse of AMOC (McManus *et al.*, 2004; Hall *et al.*, submitted).

However, this scenario of LIS collapse, freshwater forcing and AMOC reduction is complicated by records appearing to reflect reduced GNAIW production prior to LIS collapse (Zahn *et al.*, 1997; Hall *et al.*, submitted), therefore demanding reassessment of the sequence of ice-ocean-climate interactions associated with H events, likely incorporating the smaller NW European ice sheets (NWEIS; Knutz *et al.*, 2001; Hall *et al.*, submitted). It is undoubtedly the small ice volume of the NWEIS compared to the LIS that has caused this potential meltwater source to be largely overlooked as a significant player in episodes of abrupt climatic change. However, positioning of these ice sheets, allowing meltwater to be targeted directly to the site of last glacial North Atlantic convection, likely made the NWEIS a principal component of ice-ocean-climate interaction. Occupying a maritime position within the path of the NAD/Gulf Stream and exhibiting a wet-based regime, the British ice sheet (BIS) was a sensitive recorder of climatic change, with NW European margin IRD records documenting frequent ice sheet instability (Knutz *et al.*, 2000; Wilson *et al.*, 2002; this study), possibly corresponding to instabilities of the East Greenland and Icelandic ice sheets (e.g. Fronval *et al.*, 1995; Elliot *et al.*, 1988; Dowdeswell *et al.*, 1999) and perhaps the SW extent of the LIS (Bond and Lotti, 1995).

Despite extensive research into H events and numerous ice-rafting events originating from other circum-North Atlantic ice sheets, there is no clear consensus on the ultimate driving force behind episodes of LIS instability, or more frequent instabilities of the ice sheets that covered Greenland, Iceland and NW Europe (see

review by Hemming, 2004). Modelling of ice sheet dynamics suggesting that a build up of geothermal heat at the base of the LIS over several thousand years could destabilise the ice sheet and cause periods of intense iceberg discharge on a ~7 kyr cycle, lead MacAyeal (1993) to propose a 'binge-purge' theory of H event initiation. However, doubt was soon cast upon theories involving internal ice sheet dynamics when further investigation revealed the quasi-synchronous instability of a number of circum-North Atlantic ice sheets during H events (Bond and Lotti, 1995; Revel *et al.*, 1996; Snoeckx *et al.*, 1999), prompting H event initiation proposals involving a common (climatic) forcing (e.g. Bond and Lotti, 1995; Grousset *et al.*, 2000; Scourse *et al.*, 2000). Extensive studies of IRD provenance and fluxes in the NE Atlantic however, suggest that the marine margins of the NW European and Greenland ice sheets fluctuated with a 1.5-3 kyr periodicity (Bond *et al.*, 1997, 2001; Knutz *et al.*, 2001), apparently independent of LIS instabilities, prompting the idea of a pervasive, background climatic driver, e.g. solar forcing (Bond *et al.*, 2001) affecting the smaller, more climatically sensitive ice sheets. More recent proposals of ice sheet destabilisation make analogies to ice sheet processes observed today on the Western Antarctic and Greenland ice sheets, principally involving surface and subsurface warming of ice shelves/marine margins (Hulbe, 1997; Moros *et al.*, 2002; MacAyeal *et al.*, 2003; Hulbe *et al.*, 2004; Flückiger *et al.*, in press). Despite the growing number of theories concerning the origin of H events, one which satisfies all criteria 1) positioning within the climate record, 2) provenance and scale of LIS-sourced debris and ice, 3) rapid and extensive distribution of icebergs, 4) involvement of other ice sheets, is yet to be found, possibly reflecting gaps in the database of evidence (Hemming, 2004).

Given the inability of the current dataset from North Atlantic sediment cores to prove or disprove the above scenarios, ideas concerning H event initiation remain speculative, demanding high-resolution, multi-proxy core analysis to offer further constraints. This thesis attempts to address this issue, presenting high-resolution records of ocean-ice sheet interaction as recorded in a marine sediment core in the NE Atlantic.

1.2 Aims of this study

The primary aim of this thesis is to enhance our present understanding of the mechanisms involved in episodes of abrupt climatic during the last glacial period. To tackle this issue I will reconstruct records of ice sheet-ocean-climate variability at a multi-decadal to centennial-scale resolution and assess the involvement of the NWEIS within episodes of abrupt climatic change, and develop our understanding of the oceanic and climatic states under which H events occurred. Proxy records spanning the last ~58 kyr will be obtained from a marine sediment core, MD01-2461, collected from the continental slope SW of Ireland. In achieving these aims the key objectives were as follows:

1. To develop a robust age model using radiocarbon and graphical tuning of SST reconstructions with existing palaeorecords, principally Greenland ice core records, in order to correlate observations from core MD01-2461 with marine, terrestrial and ice-core records from across the globe.

2. To infer ice sheet growth, variability and decline through the analysis of IRD deposited at the core site. An array of provenance tools will determine likely

source areas while the flux of IRD will document the extent and stability of marine margins.

3. To construct high-resolution upper ocean hydrographic records from the NE Atlantic using stable oxygen isotopes and Mg/Ca palaeothermometry on surface and subsurface-dwelling planktonic foraminifera.

4. To document variability of the AMOC using stable carbon isotopes of benthic foraminifera.

1.3 Thesis layout

The principal scientific findings of this study are structured into four research papers (Chapters 4, 5, 6 and 7) addressing the main objectives outlined above. Chapters 2 and 3 summarise the techniques used in this study and detail the development of a robust age model for MD01-2461, while chapters 8 and 9 discuss and conclude respectively, the main scientific results of this investigation. The thesis is thus divided as follows:

Chapter 2 describes the material used in this study, the core location and present and past hydrography and the background and detail of the various proxies used.

Chapter 3 focuses on the development of the MD01-2461 age model.

Chapter 4 presents records of flux, lithological characteristics and geochemical composition of IRD deposited at MD01-2461 over the period 55-8 kyr BP, allowing spatial and temporal determination of ice sheet growth, variability and decline around the North Atlantic basin.

Chapter 5 presents upper ocean conditions; surface and subsurface temperature, salinity and density reconstructions from MD01-2461, which are investigated in relation to ice sheet instability and intermediate water mass ventilation over the period 27-14 kyr BP.

Chapter 6 presents SST records from MD01-2461 derived from different proxy approaches and discusses how a more comprehensive picture of surface ocean conditions (e.g. seasonality, stratification, mean annual v. anomalous years) may be inferred from multi-proxy approaches.

Chapter 7 presents benthic $\delta^{13}C$ records from MD01-2461 over the period 55-8 kyr BP and provides insights into effect of NWEIS instability and basin wide THC variability through comparison with benthic $\delta^{13}C$ records from the Portuguese Margin and Björn Drift.

Chapter 8 draws together the key scientific results of the research which are detailed in the discussion points of **chapters 4, 5, 6** and **7**, and provides insights into their significance for our understanding of past, present and future climatic change. Proposals for future work concludes the chapter.

Chapter 9 lists the main conclusions of this thesis.

Chapter Two

Material and Methods

Investigation into the interaction of the last glacial ice-ocean-climate system within this study is based on data collected from a giant piston (CALYPSO) core collected from the NE Atlantic. Here I describe the core location, the present hydrography and last glacial conditions and the proxies used to construct records of individual ice sheet variability, upper ocean condition and intermediate water ventilation which may reflect more regional variability of AMOC.

2.1 Core and location

Sediment core MD01-2461 was recovered from the NW flank of the Porcupine Seabight (51° 45' N, 12° 55' W; Fig. 2.1) during *RV Marion Dufresne* cruise MD123, 7-11 September 2001 (van Rooij *et al.*, 2001). The site of MD01-2461 at present is at a water depth of 1153 m with clear seismic laminations dipping to the SW parallel to the seafloor recognised through sub-bottom 3.5 kHz profiles (Fig. 2.2).

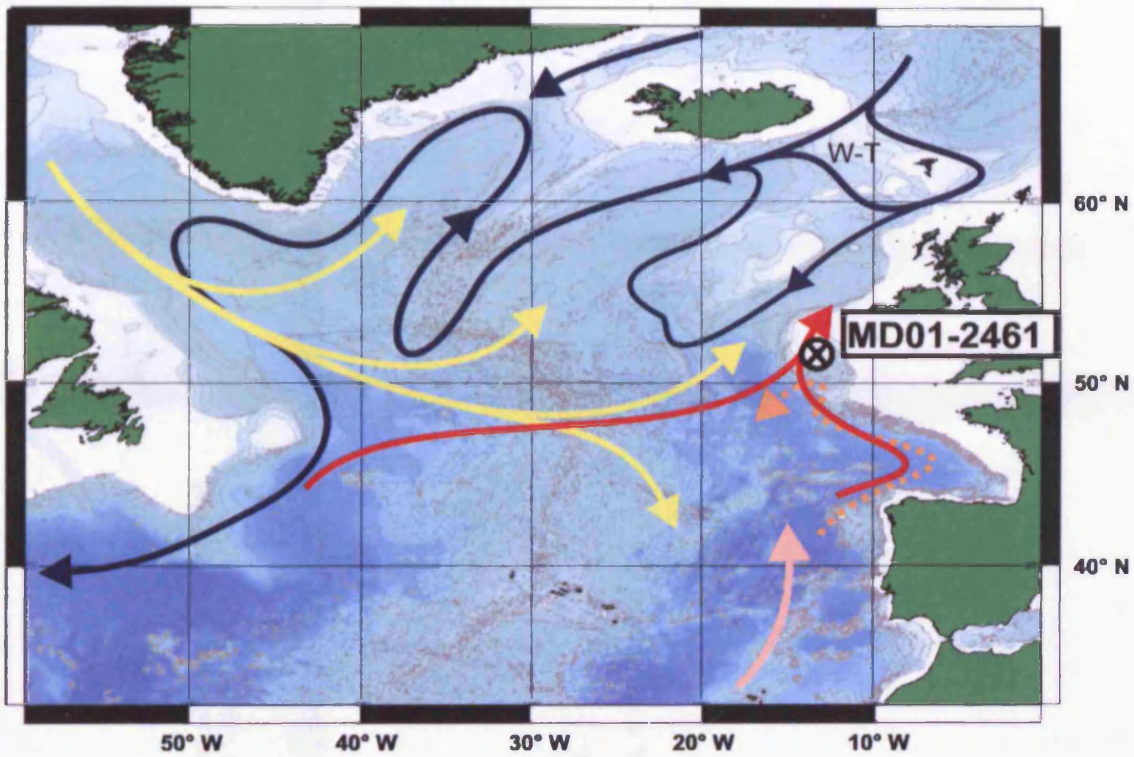

Figure 2.1. Location of core MD01-2461 and modern circulation patterns. Purple arrows illustrate the pathways of the NADW across the Wyville-Thomson Ridge (W-T) and recirculation in the eastern North Atlantic basin at ~ 2000-3000 m water depth. Yellow arrows represent LSW at 1500-2000 m. The dashed orange shows the path of MOW at ~ 1000 m depth, and red arrows show surface North Atlantic Current and ENAW (to depths of ~750 m). The pink arrow depicts Southern Component Water (SCW).

The 20.2 m gravity core recovered olive-grey silty-clay sediments with frequent drop stones (Fig. 2.3). Visual and x-ray evidence (Fig. 2.4, 2.5) suggest a largely homogenous sediment with minimal core disturbance and no obvious turbidite sequences, which may have been a major sedimentary mechanism in such a slope environment.

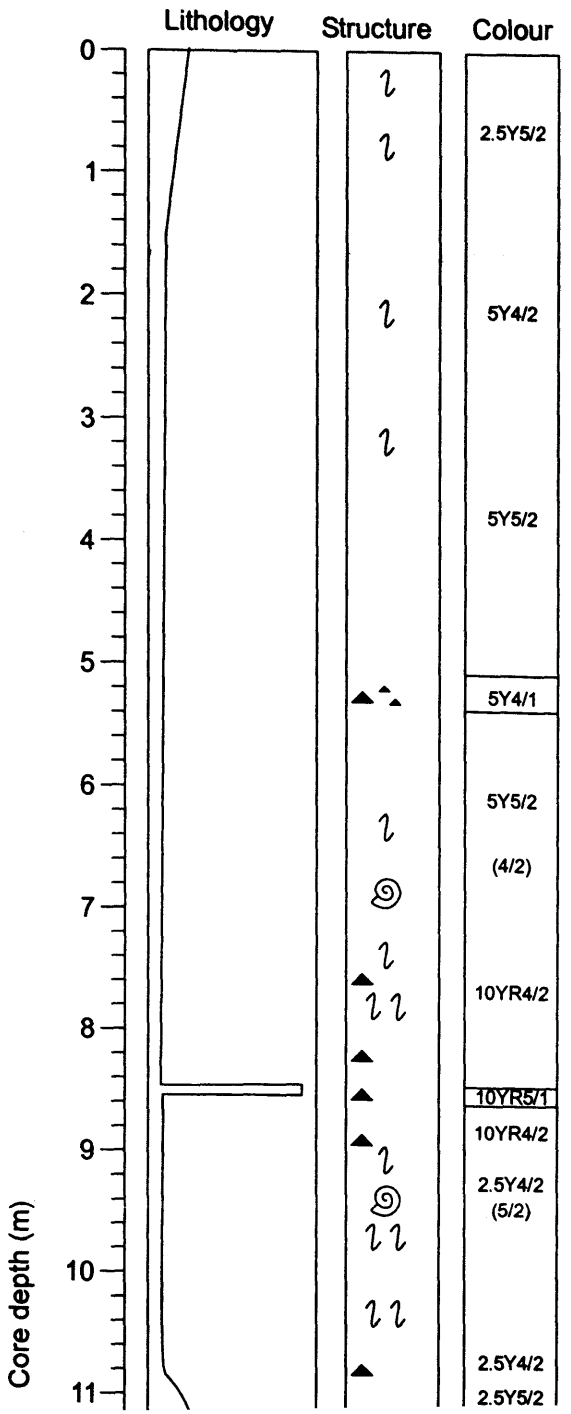

Greyish-brown **silty clay**. Very soft, some silt-sand pockets. Faint bioturbation. Soupy sediment at top and 139-150 cm.

Bioturbated **silty clay** with numerous FeS specks. Nannofossils present.

cm-scale burrows and numerous fluid sediment pockets. Core disturbance or slurry in empty in empty burrows.

Homogeneous, structureless **silty clay** with small FeS specks. Nannos present, some forams, some fine sand

Dark grey **silty clay** with significant fine sand and dropstones

Homogeneous, bioturbated **silty clay** with FeS specks. Horizontal burrows.

Coral

Bioturbated **silty clay** with FeS specks. Several cm-scale dropstones.

Sandy layer, rare nannos

Coral
Homogeneous, structureless bioturbated **silty clay** with FeS specks. Abundant nannos, forams present.
Small lense of medium sand and gravel

Lamination of darker toned sediment throughout section

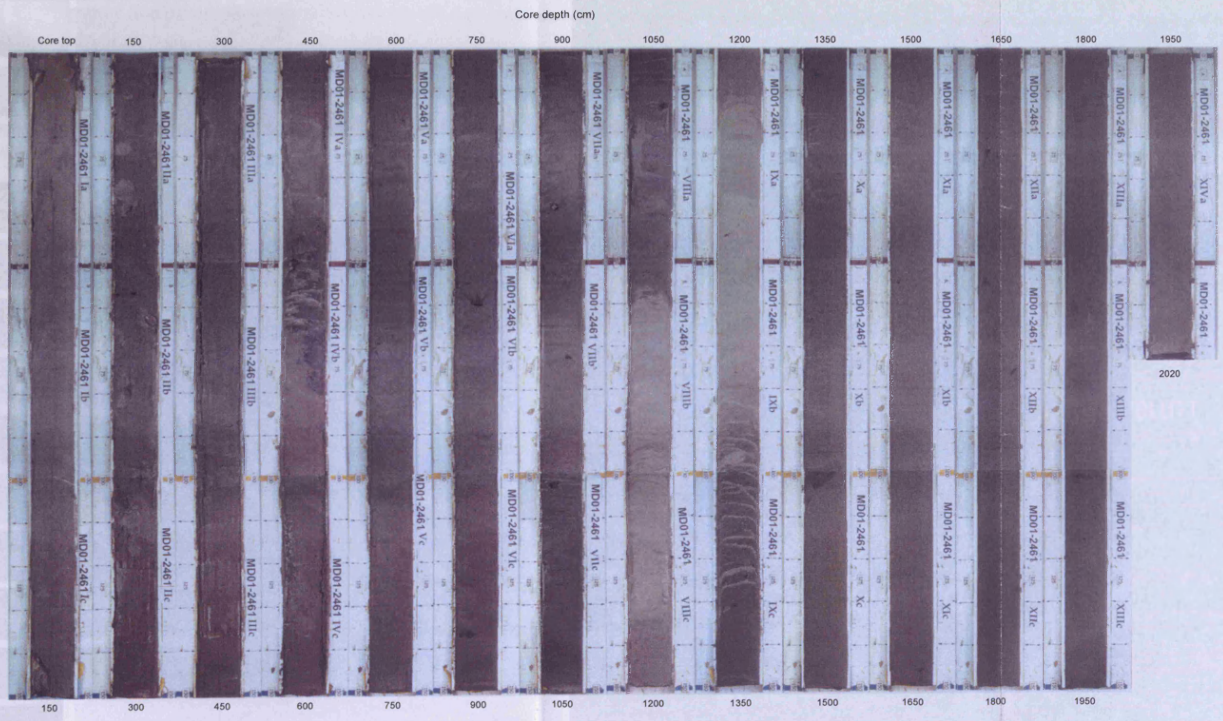

Fig. 2.4 Photograph of core MD01-2461. 150 cm length sections of the working half

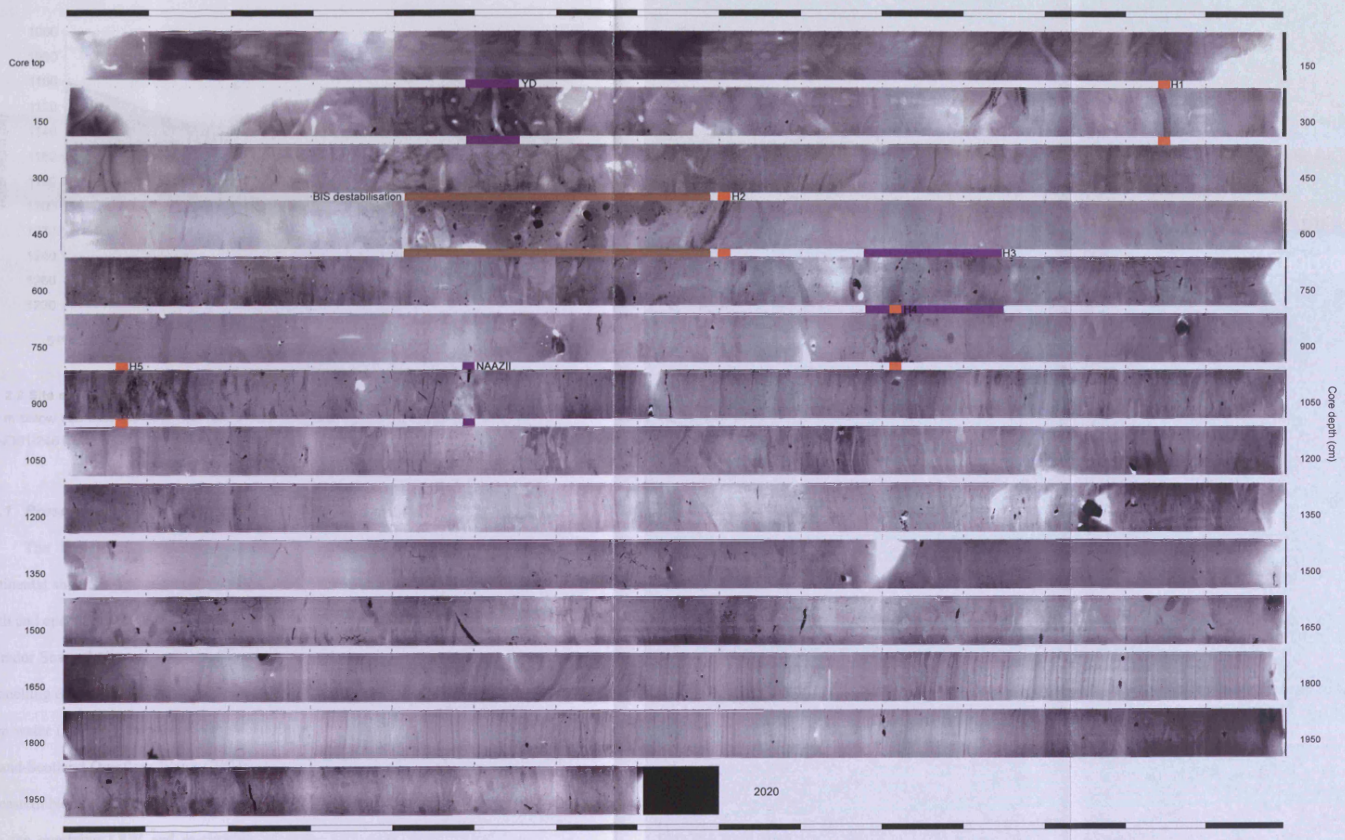

Figure 2.5 X-radiograph of MD01-2461. 150 cm core sections from base (2020 cm), bottom right, to core top (0 cm), top left. Black and white bars represent 10 cm intervals. The upper 1000 cm were investigated within this study. Coloured bars locate key stratigraphical horizons determined from geochemical and lithological study of the IRD assemblages (see sections 2.2.1 - 2.2.2 and Chapter 4). YD, Younger Dryas; H, Heinrich event; BIS, British ice sheet; NAAZII, North Atlantic ash zone II.

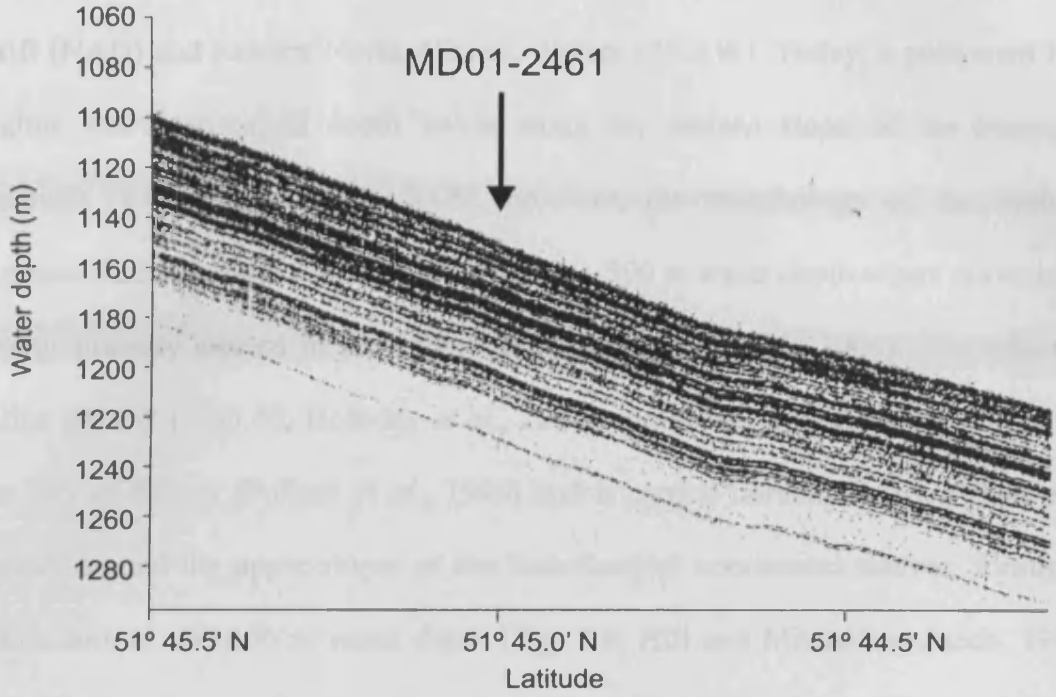

Fig. 2.2 Site survey/ 3.5kHz sub-bottom profile. Parallel sub-bottom reflectors to at least ~60 m below sea floor are clearly observed. Cruise track, 209°. Arrow indicates coring site for MD01-2461.

2.1.1 Present day hydrography

The Porcupine Seabight represents a N-S trending embayment in the continental shelf SW of Ireland, gradually deepening to the south, to ~3000 m water depth and opening onto the Porcupine Abyssal Plain. Thermohaline convection in the Labrador Sea and Norwegian-Greenland Sea drives the present mode of circulation, channelling dense deepwater masses, Labrador Sea Water (LSW) and North Atlantic Deep water (NADW), into the North Atlantic basin (McCartney and Talley, 1984). Iceland-Scotland Overflow Water (ISOW; the eastern component of NADW) enters the eastern North Atlantic basin by flowing over the Wyville-Thomson Ridge, to mix with the overlying LSW and re-circulate over the Porcupine Abyssal Plain (van Aken, 2000). This southward penetration of deepwater masses is compensated by the

return of warm, saline surface waters to the Norwegian Sea via the North Atlantic Drift (NAD) and Eastern North Atlantic Waters (ENAW). Today, a pole-ward flow regime characterises all depth levels along the eastern slope of the Porcupine Seabight (Rüggerberg *et al.*, 2005), however, the morphology of the Seabight prevents direct through flow of waters below ~ 500 m water depth where currents are topographically steered in a cyclonic direction (Frank *et al.*, 2004). The relatively saline ENAW (> 35.40; Holliday *et al.*, 2000) originates from winter mixing within the Bay of Biscay (Pollard *et al.*, 1996) and is carried northwards by a shelf edge current around the upper slopes of the Irish-Scottish continental shelves, forming a saline core at 100-400 m water depth (Fig. 2.6; Hill and Mitchelson-Jacob, 1993). ENAW overlies and mixes with Mediterranean Outflow Water (MOW), characterised by a salinity maximum and oxygen minimum at a depth of 1000-1200 m (Frank *et al.*, 2004) and bathing the site of MD01-2461. In deeper parts of the basin (>1600 m water depth) colder, low salinity LSW is recognised (Fig. 2.6, 2.7; De Mol *et al.*, 2002).

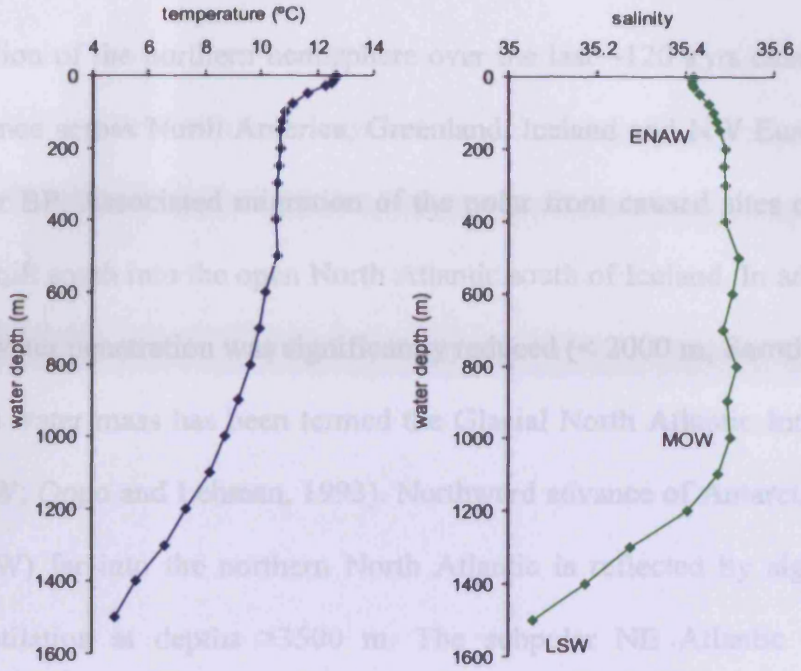

Figure 2.6. Modern annual average temperature and salinity in the Porcupine Seabight. ENAW; Eastern North Atlantic Water, MOW; Mediterranean Outflow Water, LSW; Labrador Sea Water. Data from the Levitus World Ocean Atlas.

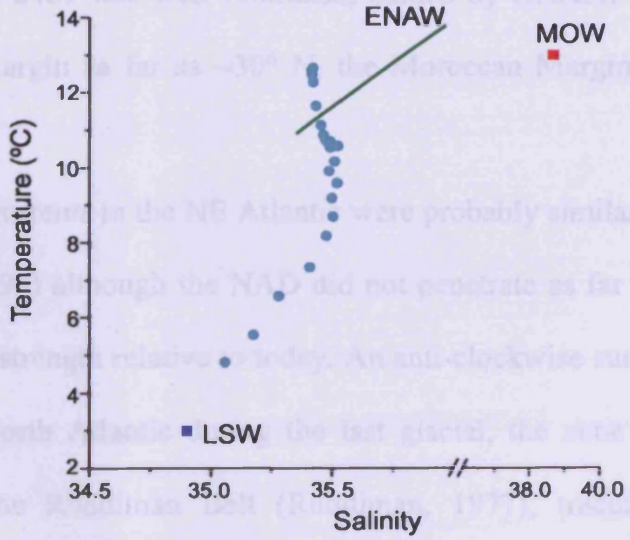

Figure 2.7. T-S diagram showing water mass end-members that contribute today to the site of core MD01-2461. ENAW; Eastern North Atlantic Water (Pérez *et al.*, 1995), MOW; Mediterranean Outflow Water (Zenk, 1975), LSW; Labrador Sea Water (Talley and McCartney, 1982). Temperature and salinity from the site of MD01-2461; blue circles (Levitus World Ocean Atlas). Note break in salinity axis.

2.1.2 Glacial conditions

Glaciation of the northern hemisphere over the last ~120 kyrs culminated in ice sheet advance across North America, Greenland, Iceland and NW Europe at the LGM, ~21 kyr BP. Associated migration of the polar front caused sites of NADW formation to shift south into the open North Atlantic south of Iceland. In addition the depth of deepwater penetration was significantly reduced (< 2000 m; Sarnthein *et al.*, 1994) and this water mass has been termed the Glacial North Atlantic Intermediate Water (GNAIW; Oppo and Lehman, 1993). Northward advance of Antarctic Bottom Waters (AABW) far into the northern North Atlantic is reflected by significantly decreased ventilation at depths >3500 m. The subpolar NE Atlantic was then effectively stratified with ^{13}C-enriched GNAIW to depths of ~2000 m overlying $\delta^{13}C$-depleted Southern Component Water (SCW) (Boyle and Keigwin, 1987; Duplessy *et al*, 1988; Oppo and Lehman, 1993; Sarnthein *et al.*, 1994). During this time, site MD01-2461 was well ventilated, bathed by GNAIW flowing south along the European Margin as far as ~30° N, the Moroccan Margin (Williamowski and Zahn, 2000).

Surface currents in the NE Atlantic were probably similar to today (e.g. Oppo and Lehman, 1995) although the NAD did not penetrate as far north and may have been reduced in strength relative to today. An anti-clockwise surface gyre was active in the central North Atlantic during the last glacial, the zone of preferential IRD accumulation, the Ruddiman Belt (Ruddiman, 1977), tracing principal iceberg pathways (Grousset *et al.*, 1993).

A warm-based glaciological regime and extreme maritime position made the BIS a sensitive recorder of climatic change (McCabe and Clark, 1998; Knutz *et al.*,

2001). Proximal to the BIS, IRD deposited at the site of MD01-2461 documents growth and instabilities of the southernmost extent of the last glacial NWEIS. Additionally, icebergs sourced from each of the circum-North Atlantic ice sheets would have become entrained in the surface gyre and have drifted towards the European margin depositing multi-provenance IRD at MD01-2461 (Fig. 2.8; Grousset *et al.*, 1993).

2.2 Methods

To achieve the objectives defined in section 1.2, a comprehensive array of sedimentological and geochemical approaches was applied to MD01-2461 to reconstruct last glacial conditions in the NE Atlantic and allow interpretation of ice-ocean-climate interaction. Below is an overview to the methods used within this thesis.

2.2.1 Core handling, shipboard analysis and physical properties

Once extracted from the core barrel, sediment core MD01-2461 (within PVC core liner) was cut to standard 150 cm length sections and split onboard the *RV Marion Dufresne* using a rotary saw into working and archive halves. The working half was subsequently lithologically described (Fig. 2.3), photographed (Fig. 2.4) and passed through a GEOTEK multi-sensor core logging system (MST). Bulk physical and acoustic properties were measured at 2 cm resolution and include gamma-ray density, P-wave velocity and magnetic susceptibility. In addition, spectral light reflectance made at a 2 cm resolution with a MINOLTA spectrophotometer (model CM-2002; Shipboard party, 2001). These data are summarised with CIE (Commission International de l'Eclairage) 'L*' (lightness) and 'a' (red-to-yellow colour balance). Selected multi-elemental analyses (K, Ca, Ti, Mn, Fe, Cu and Sr) measured in counts s^{-1} at 1 cm resolution, were carried out on the ITRAX™ core-scanning X-Ray Fluorescence (XRF) at the National Oceanography Centre, Southampton. X-radiography imaging of MD01-2461 was performed using the Scopix system at the University of Bordeaux 1 and is shown in Fig. 2.5.

The working half of MD01-2461 was subsequently sampled and processed at the University of Wales, Bangor (see section 2.2.2). The archive half is currently stored at Bordeaux Université I.

Whole-core low-frequency magnetic susceptibility measurements were also subsequently performed on U-channel sub-samples of MD01-2461 using a Bartington MS2B Dual Frequency Susceptibility Meter (Wadsworth, 2005) at a 2 cm resolution, improving the accuracy of initial shipboard measurements.

2.2.2 Sample preparation

The top 10 m of MD01-2461 were sampled at 1-2 cm resolution. Each sample was initially weighed, dried at 45 °C and weighed again to obtain the wet and dry total mass. The coarse fraction was separated by wet-sieving samples through a 63 μm sieve using distilled water. The >63 μm fraction was then dried at 45 °C, sieved with a 1 mm mesh and the separate fractions weighed and stored separately awaiting analysis.

2.2.3 IRD accumulation

Lithic grains >150 μm embedded in pelagic sediment are assumed to be IRD and therefore a proxy of iceberg flux to the core site. Concentration and lithological composition of IRD grains were determined by use of a light microscope. In the >150 μm fraction a minimum of 300 grains per sample were counted, with larger samples being split. Concentration of IRD within MD01-2461 (grains cm^{-3}) is converted into flux (number of grains cm^{-2} kyr^{-1}) as described below.

The finalised age model (see section 3.5) is used to extrapolate the bulk mass accumulation rate as follows:

$$\text{BMAR (g cm}^{-2}\text{ kyr}^{-1}) = \text{LSR} \times \rho\text{DB}$$

where LSR is linear sedimentation rate (cm kyr^{-1}) and ρDB is dry bulk density (g cm^{-3}).

Dry bulk density is determined from wet and dry sample weights as follows.

Wet weight (+ salt water) = x g

Dry weight (+ salt) = y g

x-y = weight of water = weight of (seawater – salt) = (1-S)sw

Assuming

Sediment particle density	ρ_m	= 2.65 g cm^{-3}	
Salinity	S	= 35 g kg^{-1}	=0.035

Water density	ρ_w	= 1.025 g cm^{-3}	
Sediment – salt	Y	= (y-Sx)/(1-S)	= (y-0.035x)/0.965
Salt content		= S(x-y)/(y-Sx)	
Dry mud volume	V_m	= Y/ρ_m	= Y/2.65 cm^3
Fluid volume	V_w	= $(x-Y)/\rho_w$	=(x-y)/1.025 cm^3

Therefore, wet sample volume V_x = [(Y/2.65) + (x-Y)/1.025)]

= (2.65x-1.625Y)/2.7162 cm^3

Dry bulk density ρDB = Y/V_x

IRD concentration ([IRD], grains g^{-1} dry sed.) was converted to IRD-flux (grains cm^{-2} kyr^{-1}).

$$\text{IRD-flux} = \text{BMAR} \times [\text{IRD}]$$

2.2.4 Last glacial North Atlantic ice sheets and IRD provenance fingerprinting

With the surface cyclonic gyre south of Iceland transporting icebergs derived from each of the circum-North Atlantic ice sheets to the core site, successful determination of IRD provenance has the potential to document instabilities of different marine margins (Hemming, 2004 and references therein), even individual ice streams (Scourse *et al.*, 2000). The Hudson Strait origin of H layer IRD is the ultimate example of successful provenance allocation, with a wide array of proxies tracing the same geologically distinctive source region (e.g. Andrews and Tedesco, 1992; Gwiazda *et al.*, 1996; Hemming *et al.*, 1998). Allocation of inter-H layer/non-LIS-derived IRD however, is prone to ambiguities, particularly relating to the similar bedrock histories of the Gulf of St. Lawrence, the British Isles and Scandinavia (Fig. 2.8) and specific allocation of an IRD source through geochemical approaches alone is unrealistic (Farmer *et al.*, 2003). To improve our understanding of spatial and temporal ice sheet variability in the NE Atlantic a comprehensive geochemical *and* lithological analysis of all IRD (H and inter-H layer) is used in an attempt to eliminate some of the ambiguities of single-proxy analysis highlighted by Farmer *et al.* (2003).

Lithological provenance, $^{40}Ar/^{39}Ar$ ages of individual hornblende grains and Sr-Nd isotopic composition help to constrain potential source regions, or at least eliminate unlikely source areas (Hemming, 2004). In the following I describe the methods used to determine IRD provenance and North Atlantic ice sheet variability while results derived from this multi-proxy approach are presented and discussed in **Chapter 4**.

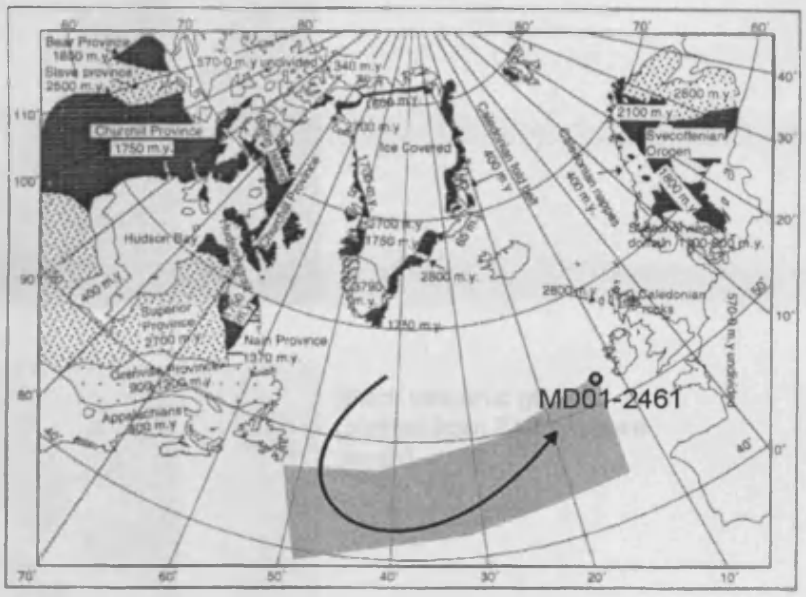

Fig. 2.8. Geological map of the continental areas surrounding the North Atlantic and potential IRD source areas (from Gwiazda *et al.*, 1996a). Main geological units of different ages are drawn with different patterns. Corresponding ages shown on the map. Location of MD01-2461 and iceberg pathway. Shaded area represents the Ruddiman Belt of preferential IRD accumulation.

2.2.4.1 Lithological provenance

A minimum number of 300 grains in the >150 μm fraction were lithologically categorised through the use of a light microscope. Census counts involved the following classifications: quartz, haematite coated grains (HCG; grains with any visible red staining under light microscope), volcanic debris (black glass, basalt and pumice), sedimentary clasts (predominantly dark, fine grained carbonates reacting violently to 10 % HCl and shales), dolomitic carbonate (coarse grained buff, weak reaction to 10 % HCl) and tephra (see Fig. 2.9). Minor quantities of hornblende, chalk, mica and a schist-like lithic are also recorded.

a.

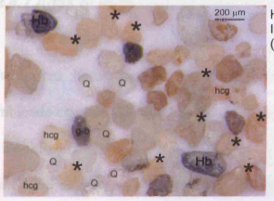

H layer 2
IRD assemblage
(528 cm core depth)

Dolomitic carbonate
(picked from 528 cm
core depth)

b.

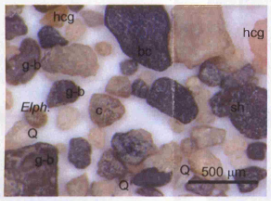

BIS dominated
IRD assemblage
(495 cm core depth)

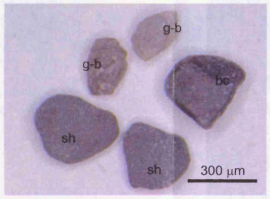

BIS debris
(picked from
495 cm core depth)

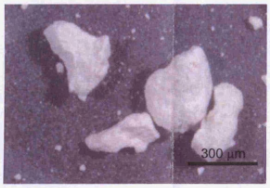

Chalk clasts dated as
Upper Campanian
(J. Young, pers. Comm;
picked from 325 cm
core depth)

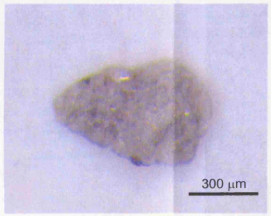

Schist (?) Grain
(picked from 750cm
core depth)

c.

HCG (picked from
670 cm core depth)

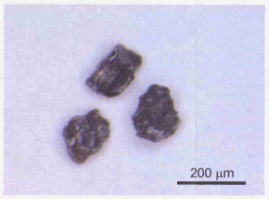

Black volcanic glass
(picked from 710 cm core
depth)

Tephra shards from NAAZII
(picked from 952 cm core
depth) and the Vedde Ash
(v; picked from 198 cm core
depth)

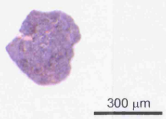

Pumice grain
(picked from 710 cm
core depth)

Fig. 2.9. Photographs illustrating the principal lithological classifications of IRD.
Column a presents a typical H layer assemblage,containing LIS-derived dolomitic carbonate and hornblende.
Column b presents typical debris derived from the BIS.
Column c presents additional IRD components, haematite coated grains and volcanic assemblages.
Abbreviations are as follows

*	dolomitic carbonate
Q	quartz
hcg	haematite coated grains
Hb	hornblende
c	carbonate
g-b	grey-brown carbonate
sh	shale
bc	black carbonate
v	Vedde Ash
Elph.	Benthic shelf foraminifera *Elphidium spp.*

2.2.4.2 Ages of individual hornblende grains

The Archean crust making up much of the continental mass around the North Atlantic has been subject to numerous thermal pulses that reset the ages of hornblende crystals (Hoffman, 1989; Hemming *et al.*, 1998) allowing age estimates for ice-rafted hornblende grains to determine potential continental sources (Hemming *et al.*, 1998; 2000a; 2000b; 2002; Hemming and Hajdas, 2003). Hornblende grains were picked from the >150 μm fraction wherever present. Grains were co-irradiated with hornblende monitor standard Mmhb (age = 525 Myr; Samon and Alexander, 1987) and $^{40}Ar/^{39}Ar$ ratios of individual hornblende grains were determined at the Ar geochronology laboratory at Lamont-Doherty Earth Observatory. Resulting ages have been corrected for mass discrimination, interfering nuclear reactions, procedural blanks and atmospheric Ar contamination (Hemming *et al.*, 1998; 2000a; 2000b) and are presented and discussed in detail in **Chapter 4**.

2.2.4.3 Sr-Nd isotopic composition

Similarly to hornblende grain ages, the Sr-Nd isotopic composition of carbonate-free IRD provides a geochemical fingerprint of potential source areas, with young, radiogenic (εNd(o) >0) volcanic/Icelandic debris and ancient, unradiogenic (εNd(o) <-20) Laurentide-sourced debris forming two distinct end members within the field of Sr-Nd isotopic compositions (Fig. 2.10; Snoeckx *et al.*, 1999; Grousset *et al.*, 2001). Although Farmer *et al.* (2003) highlight the inability of Sr and Nd isotopic data to clearly discriminate between European and southern Canadian Shield-derived IRD and call for re-assessment of assumed European-IRD events, specifically the

origin of H3, coupled lithological records effectively 'ground truth' the isotopic data at MD01-2461 and increase confidence in provenance allocation.

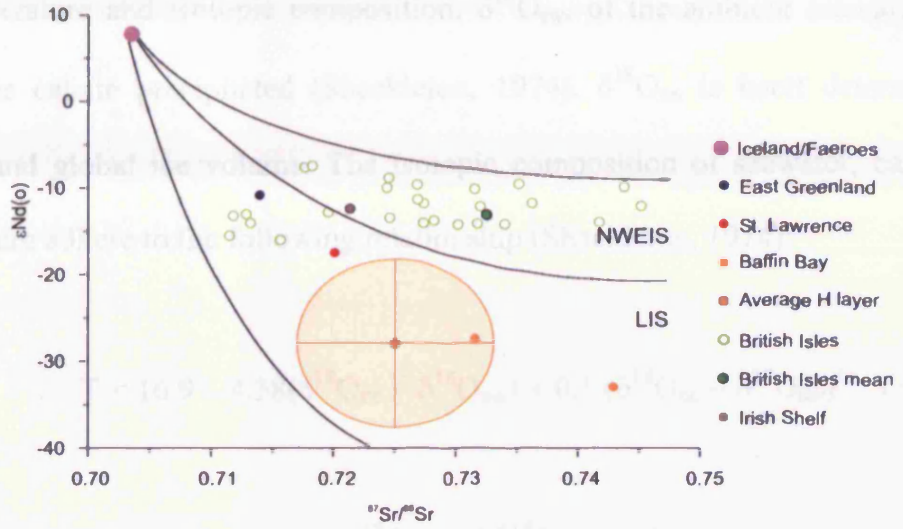

Fig. 2.10. $^{87}Sr/^{86}Sr$ ratios v. $^{143}Nd/^{144}Nd$, expressed as εNd(o) of potential source areas of IRD deposited at MD01-2461. Potential source areas (Grousset *et al.*, 2001) and British Isles samples (Davies, 1985). Mixing lines characterise Sr-Nd isotopic composition fields of the NWEIS and the LIS.

$^{87}Sr/^{86}Sr$ and $^{143}Nd/^{144}Nd$ measurements were performed on 150 mg of the carbonate-free, >150 μm fraction, following 1 M HCL-dissolution of calcium and dolomitic carbonate. Sr and Nd were chemically separated through ion-chromatographic columns and analysed on a Finnigan MAT 261 mass spectrometer at Toulouse University using the standard technique of Grousset *et al.* (1988). $^{143}Nd/^{144}Nd$ has been normalised and reported as εNd(o) following Grousset *et al.* (1998).

2.2.5 Hydrographical reconstructions

2.2.5.1 Upper water column conditions

The oxygen isotope composition of foraminiferal calcite is a function of both the temperature and isotopic composition, $\delta^{18}O_{sw}$, of the ambient seawater within which the calcite precipitated (Shackleton, 1974). $\delta^{18}O_{sw}$ is itself determined by salinity and global ice volume. The isotopic composition of seawater, calcite and temperature adhere to the following relationship (Shackleton, 1974):

$$T = 16.9 - 4.38(\delta^{18}O_{cc} - \delta^{18}O_{sw}) + 0.1\,(\delta^{18}O_{cc} - \delta^{18}O_{sw})^2 \quad (1)$$

where T is temperature in °C, and $\delta^{18}O_{cc}$ and $\delta^{18}O_{sw}$ are the isotopic compositions of the calcite test and ambient sea water respectively, both in ‰ relative to the VPDB standard. Solving equation (1) for $\delta^{18}O_{sw}$ gives

$$\delta^{18}O_{sw} = \delta^{18}O_{cc} + 0.27 - \frac{4.38 - \sqrt{[4.38^2 - 0.4(16.9-T)]}}{0.2} \quad (2)$$

allowing the isotopic composition of seawater to be computed from paired records of $\delta^{18}O_{cc}$ and calcification temperature (see section 2.2.5.4). Once corrected for global ice volume (e.g. Shackleton, 2000), $\delta^{18}O_{sw}$ may be used to estimate palaeo-salinities using a $\delta^{18}O_{sw}$-salinity (S) relationship, for example that of Craig and Gordon (1965) for the modern day North Atlantic, which takes the form

$$\delta^{18}O_{sw} = S \times 0.61 - 21.3 \quad (3)$$

Upper water column temperature and salinity structure were determined through paired oxygen isotope (see section 2.2.5.2) and Mg/Ca (see section 2.2.5.4) analysis of surface-dwelling *Globigerina bulloides* and subsurface dwelling *Neogloboquadrina pachyderma* sinistral.

2.2.5.2 Stable isotope analysis

For paired stable isotope and Mg/Ca (see section 2.2.5.4) analysis of the planktonic species, 50 individuals were selected wherever possible, with the minimum number of individuals used in a paired sample being 20. *G. bulloides* were selected from the 250-315 μm fraction and *N. pachyderma* sin. from the 150-250 μm fraction. Specimens were crushed just enough to break open the chambers, mixed and then split, thus minimising errors arising from sample heterogeneity. For benthic foraminiferal isotopes between 1 and 4 specimens of *C. wuellerstorfi* were selected from the >250 μm size fraction wherever present.

Prior to stable isotope analysis crushed tests were immersed in 3 % hydrogen peroxide for 30 minutes and ultrasonicated in methanol for 15 seconds before excess liquid and residue was removed and tests dried out at 45 °C. All stable isotope measurements were made at Cardiff University using a ThermoFinnigan MAT 252 coupled to a Kiel III Carbonate Device for automated sample preparation. The long-term external reproducibility of this system is ≤0.08 ‰ for $\delta^{18}O$ and 0.03 ‰ for $\delta^{13}C$. All stable isotope values are reported on the VPDB scale, calibrated through the NBS carbonate standard.

2.2.5.3 Foraminiferal ecology

Accurate interpretation of temperature and salinity estimates derived from paired stable isotope and Mg/Ca analysis requires prior knowledge of the ecology of the signal carriers, i.e. water depth habitat, seasonality, temperature and salinity tolerance. Therefore, before further details of geochemical methodology and temperature and salinity reconstructions, ecological and environmental considerations of both planktonic species used in this study are summarised.

G. bulloides calcify in the upper 60 m of the water column (e.g. Schiebel *et al.*, 1997), and following Barker and Elderfield (2002) we assume an average depth of calcification of 30 m, with a preferred summer growth season centred on July (cf. Hillaire-Marcel and Bilodeau, 2000). *N. pachyderma* sin. inhabit a broader and deeper depth domain. Juveniles occupy relatively shallow waters (~50 to 80 m), migrating to depths of up to 500-600 m as they mature, spending much of their lives along the pycnocline (between surface and intermediate waters (e.g. Carstens *et al.*, 1997; Bauch *et al.*, 1997; Hillaire-Marcel and Bilodeau, 2000). An average calcification depth for *N. pachyderma* sin of ~150 m is assumed, reflecting the depth of peak *N. pachyderma* sin. concentrations in subpolar waters (Bauch *et al.*, 1997; Volkmann, 2000; Simstich *et al.*, 2003) and stable isotopes and Mg/Ca records derived from *N. pachyderma* sin. are interpreted to reflect mean annual subsurface conditions.

2.2.5.4 Mg/Ca analysis

Planktonic foraminiferal sample splits for Mg/Ca analysis (~50 %) were cleaned following Barker *et al.* (2003). This cleaning procedure involves;

1. ultrasonification in deionised, ultra-high purity water (Elga PURELAB UHQ II) water and then methanol to remove clays;
2. 2. oxidation of organic matter with alkali-buffered 1% H_2O_2 at 100 °C;
3. manual removal of silicates or oxides;
4. weak acid leach/polish (0.001 M HNO_3) removed any secondary coating;
5. dissolution in 0.075 M HNO_3.

Samples were transferred to new, pre-cleaned vials after steps 3 and 5.

Clean samples were then diluted to a fixed Ca concentration of 100 ppm where possible (following an initial concentration determination on a 50 µl sub-sample of the 300 µl sample prepared), with no samples containing less than 40 ppm Ca. Analyses were carried out on a Varian Vista ICP-AES at Cambridge University. Intensity ratios were calibrated against elemental ratios following de Villiers *et al.* (2002) to eliminate any Ca matrix effect. Precision and accuracy determined from replicate runs of a standard solution of Mg/Ca = 5.130 (60 ppm Ca) and Mg/Ca = 1.289 (100 ppm Ca) was found to be $\leq$0.4 % (2 σ). Blank analyses find that Mg-leaching from vials or laboratory-contamination was below detection. Aluminium concentrations were monitored to ensure the effective removal of clay, and any samples with detectable aluminium were discarded. Sample reproducibility is found to be ± 4 %, translating to an error on temperature estimates of ± 0.4 °C. However, further uncertainties derive from Mg/Ca-temperature calibration and a conservative

error of ± 1 °C is placed on all Mg/Ca-derived temperature estimates as discussed below (section 2.2.5.4.2) and in **Chapter 5**.

2.2.5.4.1 *Calcite dissolution and Mg/Ca analysis*

Calcification temperature underestimates may result from tests that have been subject to post-depositional calcite dissolution (Rosenthal *et al.*, 2000; de Villiers, 2003). Average test weights were measured using a high precision (±0.1 mg) top pan balance. An average of 20 specimens were weighed in each case. Test weights appear to remain stable throughout the record (Fig. 2.11), suggesting that calcite dissolution is unlikely to have influenced Mg/Ca values recorded at MD01-2461 (Rosenthal and Lohmann, 2002). The site of MD01-2461, at 1153 m water depth, is situated well above the lysocline which is currently found at a water depth of ~4 km in the North Atlantic (Van Kreveld *et al.*, 1995). Although the carbonate compensation depth did shoal during glacials (Sarnthein *et al.*, 1982), it is unlikely to have reached this shallow core site allowing excellent preservation of foraminiferal tests at MD01-2461. In fact, test weights, those of *N. pachyderma* sin. in particular, display an anti-phase relationship with Mg/Ca, perhaps reflecting thicker test precipitation during colder periods.

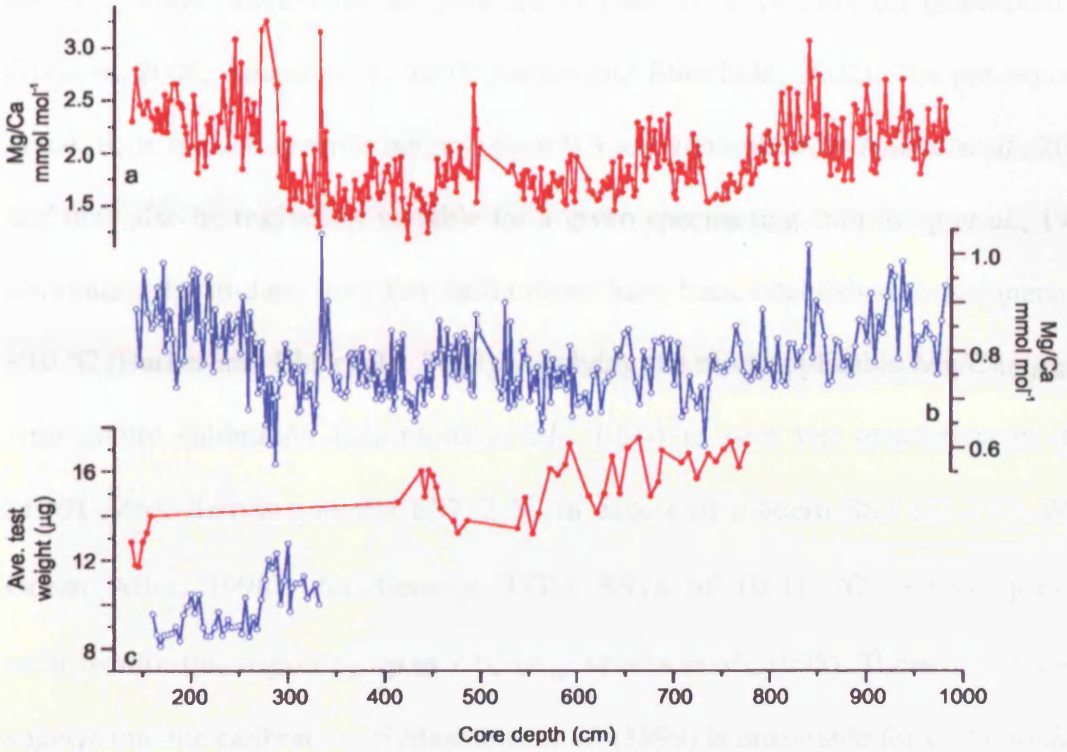

Fig. 2.11. Mg/Ca values and average test weights from MD01-2461. Down core Mg/Ca records from *G. bulloides* (a) *and N. pachyderma* sin. (b). Average test weights (c), *G. bulloides* weights red, *N. pachyderma* sin. weights blue.

2.2.5.4.2 Mg/Ca-temperature calibration

Mg/Ca analysis of foraminiferal calcite is becoming a well-established palaeotemperature proxy (Kucera *et al.*, 2005). With just a few exceptions, all planktonic species show a significant (r = 0.93) relationship with temperature of the form

$$Mg/Ca = Be^{(AT)}$$

where T is the calcification temperature (°C) and A is typically 0.1 (Elderfield and Ganssen, 2000; Anand *et al.*, 2003; Barker and Elderfield, 2002). The pre-exponent value, B, is species specific ranging from 0.3 to 1 (complied by Anand *et al.*, 2003), and may also be regionally variable for a given species (e.g. Nürnberg *et al.*, 1996). Unfortunately, to date, very few calibrations have been established for temperatures <10 °C (Barker and Elderfield, 2002). Applying the most applicable $Mg/Ca_{G.\ bulloides}$-temperature calibration (Mashiotta *et al.*, 1999) to core top measurements from MD01-2461, derives summer SST 2 °C in excess of modern SST (13.7°C; World Ocean Atlas, 1998). Additionally, LGM SSTs of 10-11 °C, exceed previous estimates for this region by up to 7 °C (e.g. Maslin *et al.*, 1995). These discrepancies suggest that the calibration of Mashiotta *et al.* (1999) is unsuitable for *G. bulloides* in the NE Atlantic, consistent with findings of Kandiano *et al.* (2003).

Establishment of Mg/Ca-temperature calibrations for both *G. bulloides* and *N. pachyderma* sin. is discussed in **Chapter 5** and summarised here.

Assuming MD01-2461 core top is intact, average $Mg/Ca_{G.\ bulloides}$ from 0 - 5 cm core depth, 2.58 mmol mol^{-1} (n = 3), is calibrated to modern June-July water temperatures at 30 m water depth (13.3 °C) assuming an exponent value, A, of 0.1 (Mashiotta *et al.*, 1999; Barker and Elderfield, 2002). Using this approach the following Mg/Ca-T calibration for *G. bulloides* was derived

$$Mg/Ca_{Gb} = 0.68\ e^{(0.1T)}$$

similar to that of Barker and Elderfield (2002) derived from North Atlantic core top *G. bulloides* at NEAP 8K (59° 48' N, 2360 m water depth; $Mg/Ca = 0.72 \times e^{0.1T}$).

N. pachyderma sin. is absent in the core top it was not possible to assess the calibration of Nürnberg *et al.* (1996) for this species. Mg/Ca-temperature calibration

for *N. pachyderma* sin. relies on the assumption that the period 20-19 kyr BP, when the $\delta^{18}O$ values of both *G. bulloides* and *N. pachyderma* sin. are broadly identical (Fig. 5.4a), represents an episode of persistent, year-round mixing of the upper water column (cf. Hillaire-Marcel and Bilodeau, 2000; Simstich *et al.*, 2003) in which both species were exposed to identical water mass and calcification temperatures. Assuming also that the $Mg/Ca_{G.\ bulloides}$-temperature calibration is valid over glacial-interglacial conditions and an exponent value of 0.1 for *N. pachyderma* sin. (Nürnberg *et al.* 1996), the ratio of pre-exponent values *G. bulloides*:*N. pachyderma* sin. within the 20-19 kyr BP time interval is determined as follows. An average of the Mg/Ca values of both species was taken over the 20-19 kyr BP period;

$$Mg/Ca_{Gb} = 1.560 \text{ mmol mol}^{-1}$$

$$Mg/Ca_{Nps} = 0.751 \text{ mmol mol}^{-1}$$

Using $T = \ln [(Mg/Ca)/A]/B$

where A = pre-exponent and B = exponent and calcification temperatures are similar it follows that

$$1.56/A_{Gb} = 0.751/A_{Nps}$$

such that $A_{Gb}:A_{Nps} = 2.1$

and $Mg/Ca_{Nps} = 0.32\ e^{(0.1T)}$

This *N. pachyderma* sin. Mg/Ca–temperature calibration effectively equates to the generic calibration of Anand *et al.* (2003; $Mg/Ca = 0.38 \times e^{0.09T}$), and overestimates calcification temperatures by 2-3°C compared to the Mg/Ca *N. pachyderma* sin.-temperature calibration of Nürnberg *et al.* (1996; $Mg/Ca = 0.47 \times e^{0.08T}$ after Barker *et al.*, 2005) derived using laboratory cultures and Norwegian Sea core top samples. However, early-Holocene (9.6-8.6 kyr BP) *N. pachyderma* sin.

calcification temperatures derived from our calibration average 10.3 °C (unpublished data) and compare well with modern temperatures at a water depth of 150 m (10.6 °C; World Ocean Atlas, 1998), substantiating our calibration and supporting regional differences in the Mg/Ca *N. pachyderma* sin. relationship (Nürnberg, 1995).

Chapter 6 presents further discussion of the calibrations derived here, comparison with published calibrations and other proxy approaches to reconstructing palaeo-ocean temperatures, including faunal assemblage records from MD01-2461 (see below).

2.2.5.5 Relative abundance of *N. pachyderma* sin. as a SST proxy.

The relative abundance of the polar species *N. pachyderma* sin. is commonly used as a palaeo-indicator of polar waters (Bé, 1977; Reynolds and Thunell, 1986; Johannessen *et al*; 1994; Pflaumann *et al.*, 1996; 2003). In waters of summer SST <8 °C, this species dominates the planktonic foraminiferal assemblage (Pflaumann *et al.*, 1996). *N. pachyderma* sin. dominated planktonic assemblages in the NE Atlantic during the last glacial (cf. Pflaumann *et al.*, 1996) such that transfer function technique SST estimates are significantly influenced by the relative abundance of *N. pachyderma* sin. within this region during glacial times (Kandiano and Bauch, 2003) and the relative abundance of *N. pachyderma* sin. serves as a quick, easy and (generally accepted) reliable proxy for palaeo-SST.

A minimum of 300 planktonic foraminiferal shells were counted from sample splits >150 μm (CLIMAP, 1976, 1984, standard size fraction) to determine *N. pachyderma* sin. %. Reproducibility error is found to be ± 5 %.

2.2.5.6 Considerations for surface and subsurface salinity reconstructions

Following correction for global ice volume (e.g. Shackleton, 2000) and any vital effect (e.g. Shackleton, 1974; Duplessy *et al.*, 1981; also see **Chapter 5**) Mg/Ca-temperatures may be used to extract the temperature component from $\delta^{18}O_{calcite}$, allowing $\delta^{18}O_{sw}$ to be determined. Carbonate ion concentration, relating to atmospheric CO_2 concentrations may also affect $\delta^{18}O$ values on a glacial-interglacial scale (Spero *et al.*, 1997), however, this factor is not considered within this study. Incorporating an error on temperature of ± 1 °C, on $\delta^{18}O_{calcite}$ of 0.08 ‰ and an uncertainty of 0.08 on the $\delta^{18}O_{sw}$–salinity relationship of Craig and Gordon (1965), error on salinity estimates is in the order of ± 0.2.

2.2.5.7 Bottom water ventilation

Carbon isotope values recorded in the calcite tests of benthic foraminifera are found to vary systematically with bottom water masses (e.g. Duplessy *et al.*, 1984). This nutrient proxy is proven to be a useful tool in the reconstruction of deep ocean paleocirculation through mapping of benthic foraminiferal stable carbon isotope ratios from sediment cores on the European margin, the open North Atlantic, and the Norwegian- Greenland Seas (e.g. Boyle and Keigwin, 1987; Oppo and Lehman, 1993; Sarnthein *et al.*, 1994; Zahn at al., 1997; Elliot *et al.*, 2002). Benthic, epifaunal species *Cidicidoides wuellerstorfi* accurately records the $\delta^{13}C$ of dissolved inorganic carbon in ambient bottom water at the core location as demonstrated by youngest benthic foraminiferal $\delta^{13}C$ values from MD01-2461 (1.1 ‰ VPDB) and recent (core top) values derived from nearby sites of a similar water depth (1.07 ‰ VPDB at

V29-198, 1139 m water depth; 1.17 ‰ VPDB at V28-73, 2063 m water depth; Oppo and Lehman, 1993) and comparing well with $\delta^{13}C$ of ambient seawater total CO_2 of 1-1.1 ‰ VPDB (between 1000-1500 m water depth, GEOSECS station 23).

In the eastern tropical Pacific, last glacial maximum (LGM) benthic $\delta^{13}C$ values are ~0.3 ‰ lower than Holocene, suggesting a mean change of $\delta^{13}C$ of the marine carbon reservoir of this magnitude (e.g. Duplessy *et al.*, 1984; Boyle, 1988). To correct for an influence of carbon reservoir changes on epibenthic $\delta^{13}C$ along the MD01-2461 record would demand robust constraints on mean ocean $\delta^{13}C$ variations across the last glacial and early deglacial period (8-43 kyr BP) at high temporal resolution, which is currently unavailable. However, mean-ocean $\delta^{13}C$ changes will have affected $\delta^{13}C$ records from different core sites equally and therefore is not considered an obstacle in the regional comparison of epibenthic $\delta^{13}C$ gradients presented in **Chapter 7**.

Chapter 3

Age model construction

In order to relate records of ice sheet activity and hydrological changes derived from sediment core MD01-2461 to other marine, terrestrial and ice core records it was essential to develop a robust, high-resolution age model. The age-depth relationship of MD01-2461 is based on radiocarbon dating, fine-tuned through the correlation of sea surface temperature (SST) to the GISPII $\delta^{18}O_{ice}$ record and supported by tephrachronology. All aspects of age model construction and validation are discussed in this chapter.

3.1 Radiocarbon dating

Shipboard magnetic susceptibility measurements and spectrophotometry (L*; Shipboard Party, 2001) coupled with scanning X-Ray Fluorescence Spectroscopy (XRF)-Ca provided a preliminary age model for MD01-2461. High L* values and XRF-Ca counts, identifying high $CaCO_3$ content, clearly locate MIS 5e, 130-116 kyr BP (Shackleton, 1969; Martinson *et al.*, 1987) between 1300-1200 cm (Fig. 3.1b, c). Peaks in magnetic susceptibility (Fig. 3.1a) were used to locate potential H event horizons. The two strongest peaks in magnetic susceptibility centred at ~850 cm and spanning 530-500 cm identify H4 and H2 respectively (cf. Grousset *et al.*, 1993;

Robinson *et al.*, 1995). Published ages for H4 fall within the range 33.45 – 35.73 ^{14}C kyr BP (Vidal *et al.*, 1997; Cortijo *et al.*, 1997), approaching the limit of accurate radiocarbon dating and defining the maximum depth selected for ^{14}C-accelerator mass spectrometry (AMS) analysis.

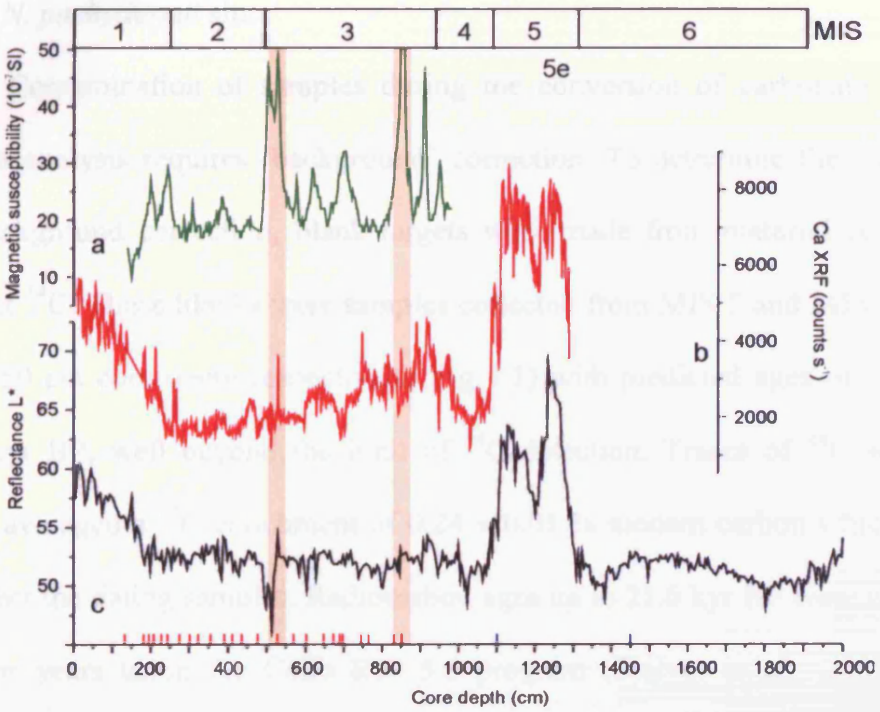

Fig. 3.1. Physical properties of MD01-2461 versus core depth.
(a). Shipboard magnetic susceptibility (10^{-7} SI), (b). Ca-XRF (counts s^{-1}), (c). L* values. Marine isotope stages stratigraphy (MIS 1-6) is suggested in the upper panel. Orange bars locate potential H2 and H4 layers. Red markers on (c) locate ^{14}C-AMS dates, blue markers locate beyond range 'blanks' used for background correction (see text).

Twenty-five ^{14}C-AMS measurements were performed on monospecific samples of planktonic foraminifers, either *G. bulloides* or *N. pachyderma* sin. Samples were selected from depths corresponding to SST maxima and minima (see

section 3.2.3), H layers (4, 2 and 1), and a coral used for U-series dating (see section 3.2.2). In addition, depths of high foraminiferal abundance were chosen to minimise error due to bioturbation. No radiocarbon measurements were taken from the core top due to low foraminifera density reflecting the poorly compacted surface sediments and perhaps core top disturbance or stretching during recovery (see section 3.3.1). Samples weighed a minimum of 9 mg, representing ~1000 *G. bulloides* or ~1500 *N. pachyderma* sin.

Contamination of samples during the conversion of carbonate to graphite prior to analysis requires 'background' correction. To determine the magnitude of this background correction, blank targets were made from material containing no inherent ^{14}C. These blanks were samples collected from MIS 5 and MIS 6 (1100 cm and 1450 cm core depth respectively; Fig 3.1) with predicted ages of ~75 kyr and >130 kyr BP, well beyond the limit of ^{14}C detection. Traces of ^{14}C within these blanks averaged a ^{14}C enrichment of 0.24 ± 0.01 % modern carbon which was used to correct the dating samples. Radiocarbon ages up to 21.6 kyr BP were calibrated to calendar years using the Calib Rev 5.0 program (Stuiver *et al.*, 2005) with the MARINE04 calibration data set, which incorporates a marine reservoir age of 400 years. The same 400 years reservoir correction was applied to ^{14}C dates of 22 kyr BP and older, which were then converted to calendar years using the calibration equation of Bard (1988; Cal yr BP = $-6.2724 \times 10^{-6} \times [^{14}C \text{ yr BP}]^2 + 1.3818 \times [^{14}C \text{ yr BP}] - 1388$). Calibrated ages use the mid-point across the analytical 2σ errors, which as quoted ($\pm 1\sigma$ years; Table 3.1) are less than 1 % of the age estimate, except for the four oldest dates where the error is less than 2 %.

Of the 25 radiocarbon dates that were measured, three samples displayed age reversals and were discarded (Table 3.1). The radiocarbon age model assumes linear sedimentation rates between AMS dates (Fig. 3.2).

Table 3.1 Radiocarbon dates for MD01-2461

Laboratory Code	Material	Depth Cm	^{14}C Age yr BP	Error Age ± 1σ yr	Calendar Age yr BP
SUERC-3299	*G. bulloides*	134.0	7,623	29	8,079
SUERC-3300	*N. pachyderma* sin.	182.5	5,929	24	6,338*
SUERC-3302	*N. pachyderma* sin.	196.5	11,032	39	12,709
SUERC-3303	*G. bulloides*	208.5	12,551	46	13,992
SUERC-3306	*N. pachyderma* sin.	228.5	11,950	43	13,337*
SUERC-3287	*N. pachyderma* sin.	244.5	14,530	58	16,819
SUERC-3307	*N. pachyderma* sin.	276.5	15,118	64	17,692
SUERC-3308	*N. pachyderma* sin.	302.5	15,518	63	18,564
SUERC-3309	*N. pachyderma* sin.	324.5	15,174	60	17,586*
SUERC-3288	*N. pachyderma* sin.	356.5	17,130	77	19,993
SUERC-3289	*G. bulloides*	392.5	18,233	87	21,053
SUERC-3290	*N. pachyderma* sin.	412.5	18,665	89	21,688
SUERC-3292	*N. pachyderma* sin.	436.5	19,128	94	22,287
SUERC-2278	*G. bulloides*	478.0	20,193	118	23,702
SUERC-2279	*N. pachyderma* sin.	528.5	20,931	129	24,577
SUERC-2275	*N. pachyderma* sin.	570.5	21,565	128	25,647
SUERC-2274	*N. pachyderma* sin.	602.5	22,234	147	25,792
SUERC-3293	*N. pachyderma* sin.	648.5	24,074	168	27,809
SUERC-3296	*N. pachyderma* sin.	674.0	25,312	195	29,142
SUERC-3311	*N. pachyderma* sin.	690.5	25,863	208	29,730
SUERC-3312	*N. pachyderma* sin.	698.5	25,928	209	29,799
SUERC-3313	*N. pachyderma* sin.	746.5	28,526	287	32,515
SUERC-3316	*G. bulloides*	766.5	29,592	326	33,604
SUERC-3317	*G. bulloides*	832.5	32,426	462	36,432
SUERC-3318	N. *pachyderma* sin.	852.5	35,613	684	39,491

*Discarded age reversals.

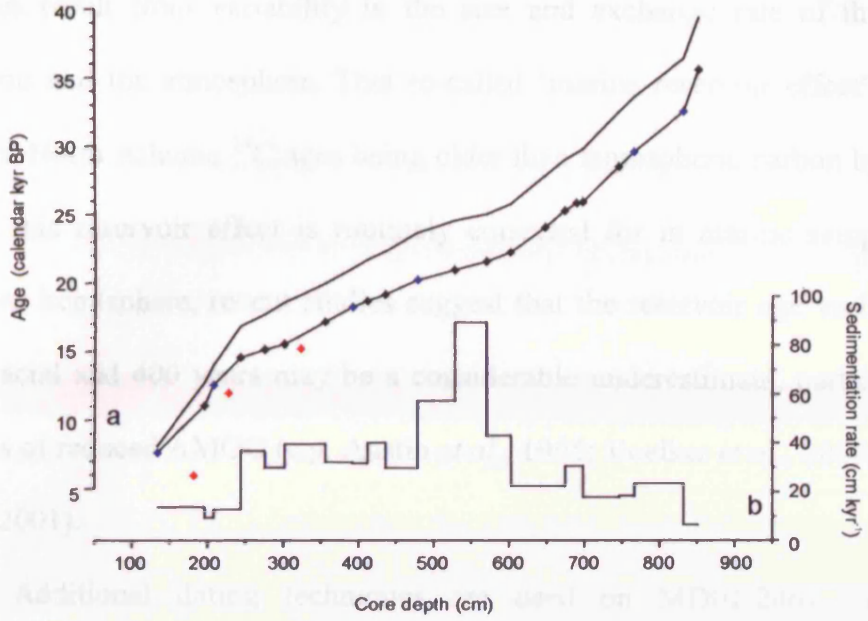

Fig. 3.2. Radiocarbon age-depth relationship
(a) Raw ^{14}C ages, based on *N. pachyderma* sin.; black diamonds, *G. bulloides*; blue diamonds. Discarded age reversals (all *N. pachyderma* sin.); red diamonds. Calibrated ^{14}C-age model; black line with no symbols. (b). Resultant sedimentation rate (cm kyr^{-1}).

3.2 Limitations of radiocarbon dating and additional age constraints

Although recent AMS radiocarbon techniques allow accurate dating of materials up to 40 kyr BP, uncertainties in this dating method arise due to changes in the rate of ^{14}C production and atmospheric concentration (Voelker *et al.*, 1998; Beck *et al.*, 2001), necessitating the conversion of radiocarbon years into calendar years through the use of a robust calibration curve (Stuiver *et al.*, 1991). Such calibration of ^{14}C ages has been achieved through the use of numerous independent age controls, including U-Th dated corals (Bard *et al.*, 1990; Bard *et al.*, 1998; Fairbanks *et al.*, 2005), dendrochronology (Becker, 1993) and the correlation of high-resolution planktonic foraminiferal $\delta^{18}O$ records with the GISPII $\delta^{18}O$ ice record (Voelker *et al.*, 2000; Shackleton *et al.*, 2004). Additional uncertainties in the dating of marine

samples result from variability in the size and exchange rate of the marine ^{14}C reservoir and the atmosphere. This so-called 'marine reservoir effect' accounts for modern North Atlantic ^{14}C ages being older than atmospheric carbon by ~400 years. While this reservoir effect is routinely corrected for in marine samples from the northern hemisphere, recent studies suggest that the reservoir age varied during the last glacial and 400 years may be a considerable underestimate, particularly during periods of reduced AMOC (e.g. Austin *et al.*, 1995; Voelker *et al.*, 2000; Waelbroeck *et al.*, 2001).

Additional dating techniques are used on MD01-2461 to assess the radiocarbon age model and the validity of a fixed 400 year ^{14}C-marine reservoir age correction over the last glacial period.

3.2.1 Tephrachronology

Tephrachronology provides time-parallel marker-horizons allowing precise correlation of Late Quaternary marine, terrestrial and ice-core records (e.g. Gronvold et al., 1995; Austin et al., 2004). Two ash layers were deposited at MD01-2461 during the last glacial period and are discussed below.

3.2.1.1 Vedde Ash

Shards of rhyolitic ash are found within sediment core MD01-2461 between 210-160 cm, peaking at 192 cm (74 shards >150 μm g^{-1} dry sed.), with a secondary peak at 182 cm (53 shards >150 μm g^{-1} dry sed.; Fig. 3.3). Coincident with the final delivery of IRD to the core site during the Younger Dryas cold interval, located through the increased relative abundance of *N. pachyderma* sin. (see section 3.3), and

displaying a similar two-point peak to that of Austin and Kroon (1996) this ash horizon is considered to be the Vedde Ash, most recently dated as 12.1 kyr BP within the GISPII ice core (Zielinski *et al.*, 1997).

3.2.1.2 North Atlantic Ash Zone II

The second ash layer is located between 948-950 cm core depth within MD01-2461, with exceptionally high ash concentrations of >4,000 shards g^{-1} dry sediment (Fig. 3.3). Deposited before the dolomitic carbonate of H5 this horizon is likely North Atlantic Ash Zone II (NAAZII) first documented by Ruddiman and Glover (1972).

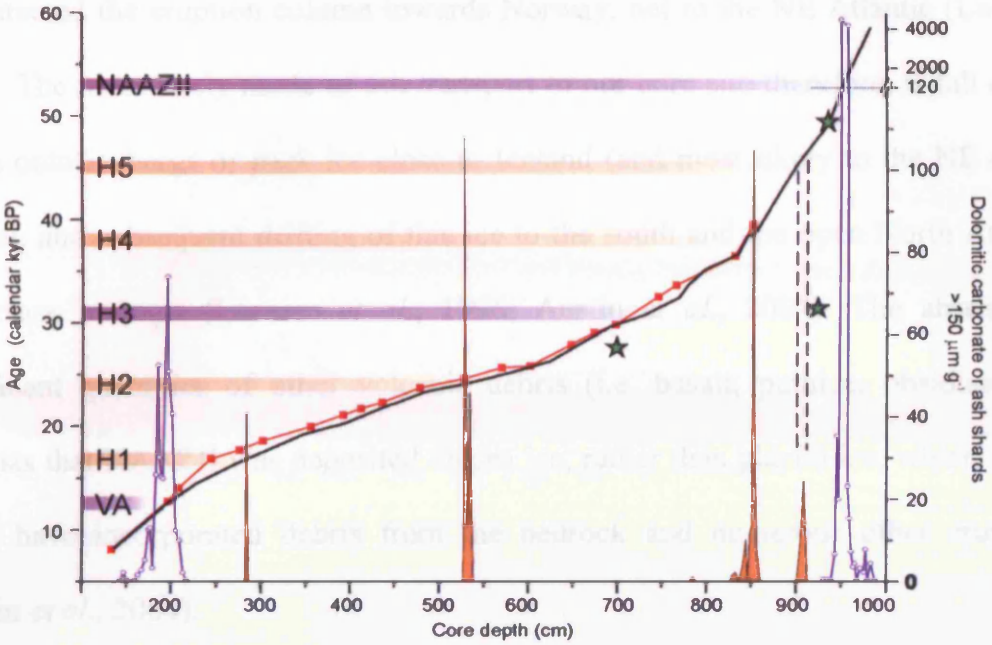

Fig. 3.3. Comparison of radiocarbon and finalised age-depth model.
Finalised age model based on GISPII correlation (see section 3.4) shown in black. Radiocarbon age model in red. Concentration of ash shards (purple, open circles; note break in axis for NAAZII) and dolomitic carbonate grains locate ash layers and H events respectively. Corresponding ages of H events as compiled by Hemming (2004), Vedde Ash (VA) age from Zielinski *et al.* (1997) and NAAZII from Meese *et al.* (1994). Note offsets between the two age models prior to H3 and around H1.

Maximum dimensions were measured on individual shards of tephra from the >63 µm size fraction using a light microscope with a calibrated eye-piece graticule (following Austin *et al.*, 2004). A minimum of 300 shards were measured per sample. The estimated size error, based on the calibration procedure and the magnification used, is ±10 µm. Ash-shard size frequency from the two samples of maximum abundance of NAAZII tephra (950 cm and 948 cm) is shown in Fig. 3.4. The well-sorted ash-size profile is typical of a wind sorted, primary air-fall deposit, however, with some shards exceeding 700 µm in diameter it is unlikely that they were delivered to this site, some 1500 km from Iceland, by atmospheric transport (Lacasse, 2001). Even if glacial winds had been stronger, prevailing westerlies would

have steered the eruption column towards Norway, not to the NE Atlantic (Lacasse, 2001). The most likely mode of ash transport to our core site therefore, is fall out of tephra onto icebergs or pack ice close to Iceland (and most likely to the NE of the source), and subsequent drifting of this ice to the south and the open North Atlantic in surface currents (Lacasse *et al.*, 1996; Austin *et al.*, 2004). The absence of significant quantities of other volcanic debris (i.e. basalt, pumice, obsidian etc.) suggests that NAAZII was deposited on sea ice, rather than glacial ice, which would likely have incorporated debris from the bedrock and numerous other eruptions (Austin *et al.*, 2004).

The shard-size profile of NAAZII tephra at MD01-2461 is indistinguishable to that from deposits in the Barra Fan (MD95-2006; Austin *et al.*, 2004; Fig. 3.4), suggesting that sea ice from the same region, beneath the same eruption column carried fall-out ash to both core sites. Correlation of high-resolution SST records from site MD95-2006 with the GISPII $\delta^{18}O_{ice}$ record implies ice rafted deposition of NAAZII in the NE Atlantic within just one or two decades of the NAAZII eruption (Austin *et al.*, 2004) dated as 53.269 ± 5 % kyr BP (Meese *et al.*, 1994).

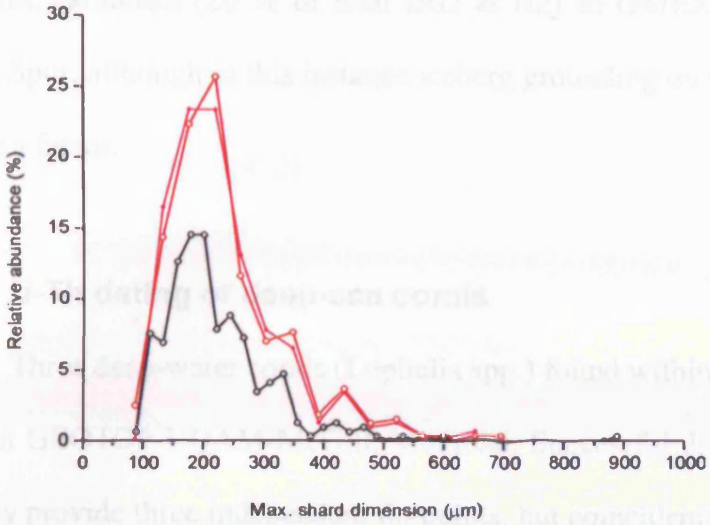

Fig. 3.4. Ash-shard size distribution of NAAZII tephra from MD01-2461 and MD95-2006. Tephra from two levels within NAAZII of MD01-2461 – 948 cm; pink, 950 cm; red. Tephra from MD95-2006; black (Austin *et al.*, 2004).

The concentration of ash shards at the more southerly site (MD01-2461) however, is substantially greater (by a factor of 50) than that found at MD95-2006 (74 shards g^{-1} dry sed.). This difference in concentration cannot be fully accounted for by sediment dilution due to enhanced accumulation rates in the Barra Fan (sedimentation rate at MD95-2006 is ~40 cm kyr^{-1} at the time of NAAZII deposition, compared to ~5 cm kyr^{-1} at MD01-2461). The flux of NAAZII tephra at MD01-2461 is calculated to be in the order of 15 shards >150 μm cm^{-2} yr^{-1}. Assuming a similar sediment density at the Barra Fan site to MD01-2461 (1.1 g cm^{-3}), a tephra flux of ~3 shards >63 μm cm^{-2} yr^{-1} is estimated. This pattern of ash flux likely reflects palaeo-surface currents of the NE Atlantic gyre (see Fig. 2.8), preferentially delivering NAAZII-laden ice to MD01-2461. Downstream, MD95-2006 received a diminished sea ice population. Congestion of icebergs/sea ice due to obstruction or reduced surface currents around the Porcupine Seabight is also a consideration. This idea of iceberg congestion may also account for unusually high concentrations of

dolomitic carbonate (20 % of total IRD at H2) in OMEX 2K recovered from the Goban Spur, although in this instance iceberg grounding on the continental shelf may also be a factor.

3.2.2 U-Th dating of deep-sea corals

Three deep-water corals (Lophelia spp.) found within MD01-2461 were U-Th dated at GEOTOP-UQAM-McGill, Montreal. Successful dating of the corals would not only provide three independent tie-points, but coincident with ^{14}C-AMS dating of foraminifera from the same sample, a U-series date derived from the shallowest (youngest) coral would potentially provide a ^{14}C-marine reservoir age at that time. U-series dates of the three corals are presented in Table 3.2.

Table 3.2 U-concentration, composition and ages of deep-sea corals recovered from MD01-2461.

Depth cm	[^{238}U] ppm (±2σ)	δ $^{234}U_{initial}$ ‰ (±2σ)	U-series derived age (calendar) kyr BP (±2σ)
698.5	3.836 ± 0.022	154.2 ± 0.7	27.6 ± 0.4
924.5	4.885 ± 0.029	132.5 ± 0.6	31.6 ± 0.4
935.5	4.224 ± 0.022	116.8 ± 1.4	49.4 ± 1.2

The ~18 kyr difference between the deepest two corals, recovered 11 cm apart within the core, raises concern over the accuracy of the U-series dates. ^{238}U concentration ([^{238}U]) and $^{234}U/^{238}U$ activity ratios were used to assess the possibility of diagenetic U- loss or gain that may account for this large offset. [^{238}U] in well preserved corals is typically ~3.2 ppm (B. Ghaleb, personal communication, 2005). The elevated values, >3.8 ppm, of the MD01-2461 corals suggest some degree of post-depositional U-gain. Additionally, the $\delta^{234}U$ composition of seawater over the last ~13 kyr has been 150 ± 2 ‰ (Edwards *et al.*, 1993). Significant deviation of

coral $\delta^{234}U_{initial}$ from this value in the corals recovered at 924.5 cm and 935.5 cm is again suggestive of some degree of post-deposition U-uptake. These factors are considered when finalising the age model (section 3.3).

3.2.3 Tuning of palaeoclimate records

Considering dating uncertainties that may derive from variability in the ^{14}C-marine reservoir age during the last glacial period and assuming that SST changes at MD01-2461 are effectively synchronous with atmospheric temperature changes over Greenland, the radiocarbon age model is assessed through tuning of the paleoclimate records. Fine-tuning of the radiocarbon age model, and extension beyond the limit of ^{14}C-AMS detection was achieved through the correlation of SST records (*N. pachyderma* sin. %; see section 2.2.5.5) and the GISPII $\delta^{18}O_{ice}$ atmospheric temperature record, *N. pachyderma* sin. % maxima corresponding to stadials in the climate record (Fig. 3.5; cf. Bond *et al.*, 1992; Knutz *et al.*, submitted.). The GISPII $\delta^{18}O_{ice}$ record is chosen on account of its robust age model based on annual layer counting back to 50 kyr BP, with an estimated error of ± 5 % (Meese *et al.* 1994).

The GISPII-tuned age model exhibits a reasonable correlation (r^2 = 0.70) between *N. pachyderma* sin. % and the Greenland air temperature record for the period 58-8 kyr BP. High accumulation rates around the LGM improve temporal resolution of the *N. pachyderma* sin. % record, increasing the correlation coefficient of the two records to r^2 = 0.84 between 25-8 kyr BP (Fig. 3.5).

3.3 Finalised age model

Construction of the finalised age model is shown in Fig. 3.5 and summarised below.

The two oldest tie-points correspond to NAAZII (950 cm; 53.3 kyr BP) and the 49.4 ± 1.24 kyr BP aged coral (935.5 cm), agreeing well with the *N. pachyderma* sin. %-SST v. GISPII age model (Fig. 3.4, 3.5). Between 40-35 kyr BP the oldest radiocarbon dates and tuned age model are in reasonable agreement (Fig. 3.3), positioning dolomitic carbonate of H4 at 38.6 kyr BP. Tuning of the paleoclimate records within this interval positions H5 at 45.6 kyr BP. The coral collected at 924 cm and dated as 31.6 kyr BP is significantly removed from this age-depth relationship (i.e. the U-series age is too young; Fig. 3.3) suggesting that the elevated [^{238}U] reflects diagenetic U-gain, as discussed in section 3.2.2. This potential tie-point is thus discarded.

No dolomitic-carbonate horizon is associated with 'atypical' H3, considered a predominantly European event (Grousset *et al.*, 1993; Gwiazda *et al.*, 1996). Correlation of *N. pachyderma* sin.%-SST with GISPII between H2 and H4 positions a peak of volcanic-rich IRD between 31.5 - 29.5 kyr BP, fitting an ~31 kyr BP age of H3 (Bond *et al.*, 1992, 1993).

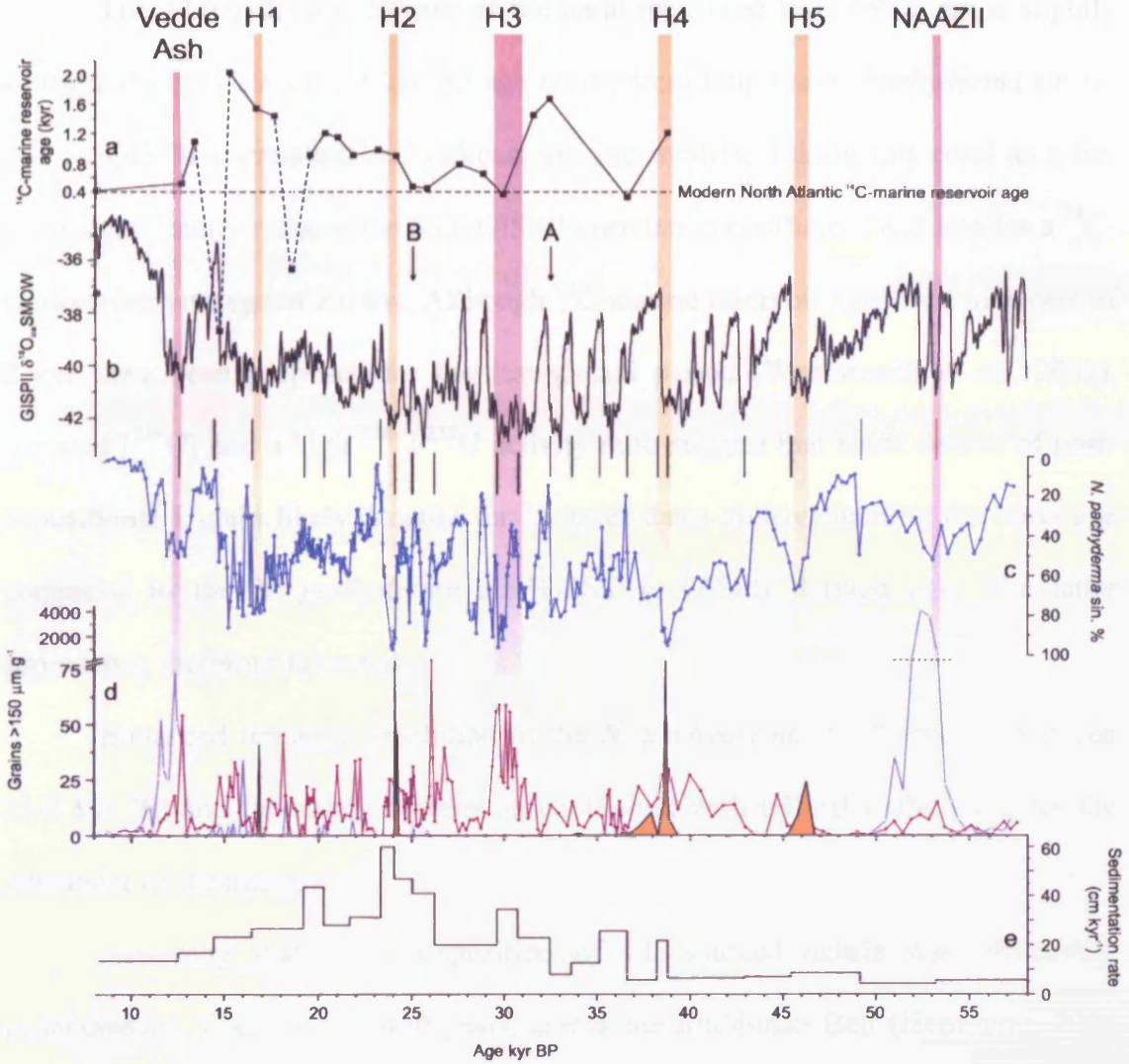

Fig. 3.5. Finalised age model for MD01-2461.

(a). Estimated ^{14}C-marine reservoir ages at MD01-2461 (blue symbols and dashed lines refer to discarded, age reversal radiocarbon dates), (b). high-resolution $\delta^{18}O_{ice}$ record (5-point smoothed) from the Greenland summit GISPII ice core (http://depts.washington .edu/qil/datasets/gisp2_main.html; Grootes and Stuiver, 1997), (c). relative abundance of *N. pachyderma* sin. (%; >150 µm planktonic population), (d). concentration of dolomitic carbonate (orange, solid), volcanic debris (purple, filled circles) rhyolitic ash shards (lilac, open circles) >150 µm g^{-1} dry sediment, (e). sedimentation rate, cm ky^{-1} at MD01-2461. Tie-points between (a) and (b), tuning of climate records, black; coral, green; NAAZII, purple. Correlation coefficient of *N. pachyderma* sin. % and GISPII $\delta^{18}O_{ice}$ for entire section r^2 = 0.70; from A to the core top r^2 = 0.82; from B to the core top r^2 = 0.84.

The 27.6 ± 0.4 kyr BP age of the coral recovered from 698.5 cm is slightly younger than the 29.8 ± 1.5 kyr BP age derive from both the *N. pachyderma* sin.%-SST v. GISPII correlation and radiocarbon age models. Taking this coral as a tie-point significantly reduces the SST-GISPII correlation coefficient and implies a ^{14}C-marine reservoir age of 2.6 kyr. Although ^{14}C-marine reservoir ages well in excess of 2 kyr have been proposed for the last glacial period (Waelbroeck *et al.*, 2001), elevated [^{238}U] and a high $^{238}U/^{238}U$ activity ratio suggest that some degree of post-depositional U-gain likely account for U-series dates underestimating the coral age compared to the *N. pachyderma* sin.%-SST v. GISPII derived age. The latter approach is therefore favoured.

Enhanced temporal resolution of the *N. pachyderma* sin. % record between 25-8 kyr BP and the strong correlation coefficient with GISPII is the basis for the remainder of the age model.

Assuming that initial deposition of LIS-sourced debris was effectively instantaneous, likely within 400 years, across the Ruddiman Belt (Hemming, 2004 (Table 3); Roche *et al.*, 2004), horizons containing the distinctive dolomitic carbonate of the Hudson Strait region (Andrews and Tedesco, 1992) are effective stratigraphical markers. Tuning of *N. pachyderma* sin. % with GISPII $\delta^{18}O_{ice}$ gives ages for dolomitic carbonate horizons in MD01-2461 that are consistent with previously published ages of these events (Table 3.3), heightening confidence in the correlation of MD01-2461 SST and temperatures over Greenland.

Table 3.3 Published ages for North Atlantic H events

H event	Age kyr BP	Basis	Source
H1	16.8	Radiocarbon (400 yr reservoir correction)	Bond *et al.*, 1997
H2	24.1	Radiocarbon (400 yr reservoir correction)	Bond *et al.*, 1997
H3	30.1	Radiocarbon (400 yr reservoir correction)	Bond *et al.*, 1997
H4	38	GISPII correlation	Meese *et al.*, 1997
H5	45	GISPII correlation	Meese *et al.*, 1997

3.3.1 Core stretching?

'Over-sampling' within giant piston cores such as MD01-2461 is a wide-spread problem and may result from cable rebound during the coring procedure. During core recovery acceleration of the piston up the barrel with respect to the sediment surface produces negative pressure within the core barrel, effectively syringing sediment upwards and stretching the upper portion of the core (Skinner and McCave, 2003). Such stretching would clearly distort the core depth-age relationship, biasing sedimentation rates and mass fluxes, potentially leading to misinterpretation of sedimentary processes. It is therefore essential to assess and correct for core deformation relating to the coring method.

The lack of an accompanying gravity core for MD01-2461 precludes attempts to use cross-correlation of the physical properties versus depth to determine the extent, if any, of 'over-sampling' in the upper portion of this giant piston core. However, a number of observations may be used to make a qualitative assessment of the degree of stretching in core MD01-2461. First, sedimentation rates suggested by the finalised age model display an increase towards the LGM typical of cores from the European Margin (Fig. 3.5e, 3.6). Prior to H4 sediment accumulation is <10 cm kyr^{-1}. Rates increase towards the LGM, peaking at 60 cm kyr^{-1} around H2, with

enhanced rates associated with both H4 and H3. Sedimentation rate decreases throughout the deglacial.. The youngest radiocarbon date and tuning of palaeoclimate record suggests an age of 8.08 kyr BP for sediments at 134 cm core depth. Assuming that the core top is intact and has an age of 0 yr BP linear interpolation derives sedimentation rates of 16-17 cm kyr^{-1} throughout the Holocene. No obvious distortion to the age model that may reflect core stretching (i.e. increased sedimentation rates towards the core top) is observed. Additionally, dry bulk densities within the section 130 to 490 cm (i.e. following H2) average 1.026 ± 0.077 g cm^{-3}, with no up-core trend of decreasing sediment density. Skinner and McCave (2003) suggest 'oversampling' due to imperfect (heavy) piston coring may occur down to a depth of ~10 m. If oversampling did occur during recovery of MD01-2461, the lack of distortion in sedimentation rates and dry bulk densities may reflect a uniform 'stretch' over the investigated section of core. However, for MD01-2461 the amplitude of cable recoil is likely to have been limited by the relatively shallow water depth at the coring location (water depth of 1153 m; Skinner and McCave, 2003) and near-perfect recovery is suggested.

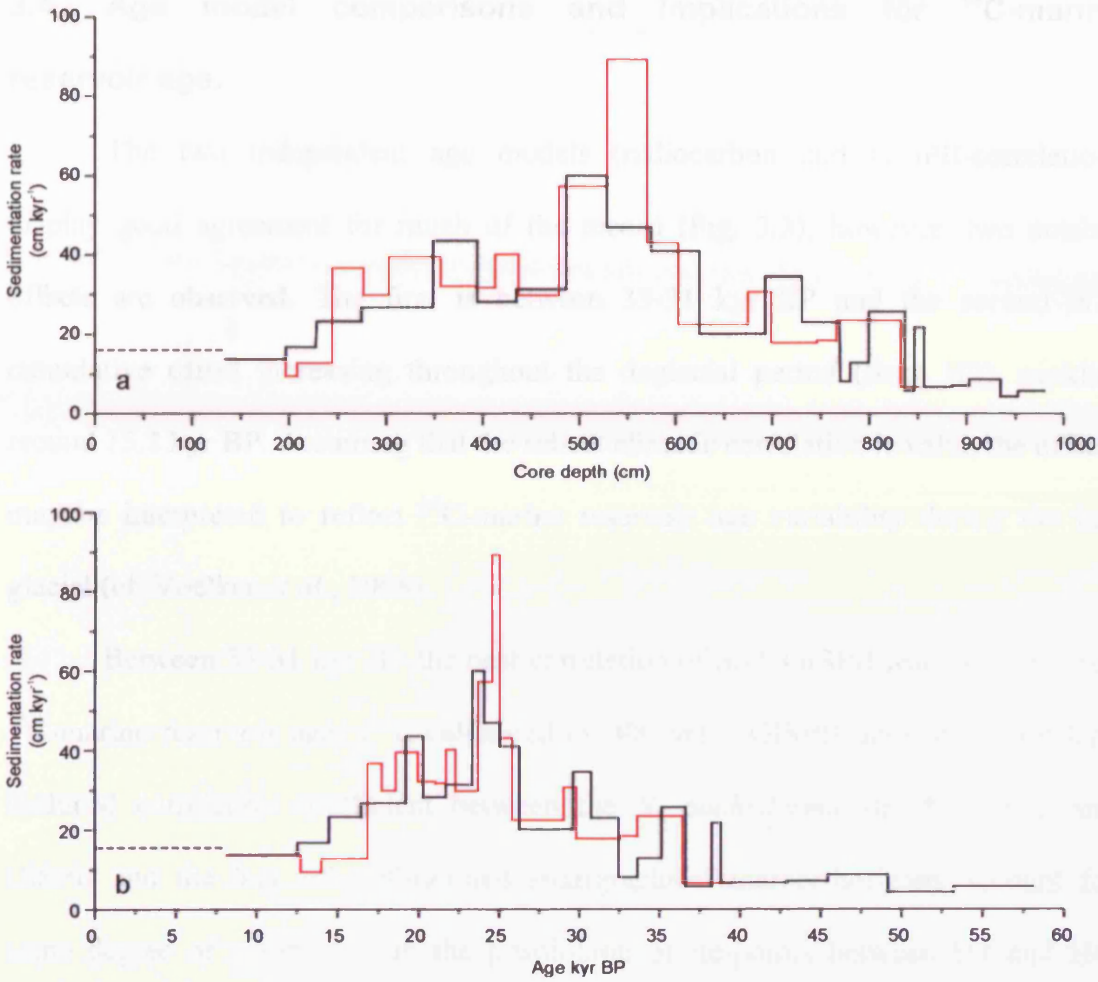

Fig. 3.6. Comparison of sedimentation rates determined from the radiocarbon and finalised age models for MD01-2461. Radiocarbon age model in red; finalised in black, versus core (a). depth, and (b) age. Suggested sedimentation rate for top 134 cm of core in dashed black line.

In addition to the apparent lack of, or at least uniform, distortion to the upper core, x-radiograph imagery show clear laminations with MD01-2461 at 1700-1950 cm core depth (Fig. 2.5), again suggesting 'perfect' coring undistorted by marginal strain or sediment flow.

3.4 Age model comparisons and implications for ^{14}C-marine reservoir age.

The two independent age models (radiocarbon and GISPII-correlation) display good agreement for much of the record (Fig. 3.3), however, two notable offsets are observed. The first is between 33-31 kyr BP and the second is a cumulative offset increasing throughout the deglacial period (from H2), peaking around 15.2 kyr BP. Assuming that the robust climatic correlation is valid, the offsets may be interpreted to reflect ^{14}C-marine reservoir age variability during the last glacial (cf. Voelker *et al.*, 1998).

Between 33-31 kyr BP the best correlation of SST-GISPII leads to predicted ^{14}C-marine reservoir ages (^{14}C-calibrated (+ 400 yr) – GISPII age) of 1.4-1.6 kyr. Reduced correlation coefficient between the *N. pachyderma* sin. % record and GISPII and the lack of well-defined stratigraphical marker-horizons account for some degree of uncertainty in the positioning of tie-points between H3 and H4, limiting confidence in estimates of ^{14}C-marine reservoir ages at this time.

Following 26.5 kyr BP however, sedimentation rates and temporal resolution of core records increase, improving confidence in the GISPII-tuned age model. At 25.6 kyr BP predicted ^{14}C-marine reservoir ages are 460 years, not dissimilar to the modern NE Atlantic (Bard *et al.*, 1987). Stepwise increases in ^{14}C-marine reservoir age of ~500 and almost 300 years are then associated with H2 (21.4 kyr BP) and following ice rafting at the LGM (~21.5 kyr BP) respectively, where ^{14}C-marine reservoir ages of ~1.2 kyr are implied. A temporary drop in reservoir ages to 960 years at 19.4 kyr BP follows before values reach 2050 years following H1 (15.2 kyr BP). ^{14}C-marine reservoir age then decreases through the Younger Dryas, reaching

modern North Atlantic values of 400 years at ~8 kyr BP where both age models are again in agreement.

3.4.1 ^{14}C-marine reservoir age variability and AMOC.

Variable ^{14}C-marine reservoir ages are increasingly documented in North Atlantic records, particularly at times of reduced AMOC and extensive sea-ice cover, reducing sea-atmosphere interaction (e.g. Bard *et al.*, 1994; Austin *et al.*, 1995; Voelker *et al.*, 1998; 2000; Waelbroeck *et al.*, 2001). Temporal variability of the ^{14}C-marine reservoir age implied at MD01-2461 is considered with surface ocean mixing and intermediate ventilation in **Chapter Five** and summarised below.

Each of the three stepwise increases of ^{14}C-marine reservoir age at MD01-2461 is associated with meltwater flux and stratification of the upper water column as indicated by divergent δ^{18}O values of the surface (*G. bulloides*) and subsurface (*N. pachyderma* sin.) dwelling planktonic foraminifera (Fig. 3.7b; Peck *et al.*, 2006). Associated reductions in $\delta^{13}C_{benthic}$ (Fig. 3.7c) suggest sluggish overturn of the AMOC, likely decreasing atmospheric-ocean interaction, increasing ^{14}C-marine reservoir age and accounting for increased ^{14}C-concentrations in the atmosphere (Beck *et al.*, 2001). An additional consideration may be the influx of 'fossil' CO_2 within meltwater potentially reducing the ^{14}C-concentration of surface ocean waters. A similar phenomenon occurs beneath the Antarctic ice shelves where carbon fixed by foraminifera is strongly influenced by aged, glacial-derived CO_2 (Domack *et al.*, 1989).

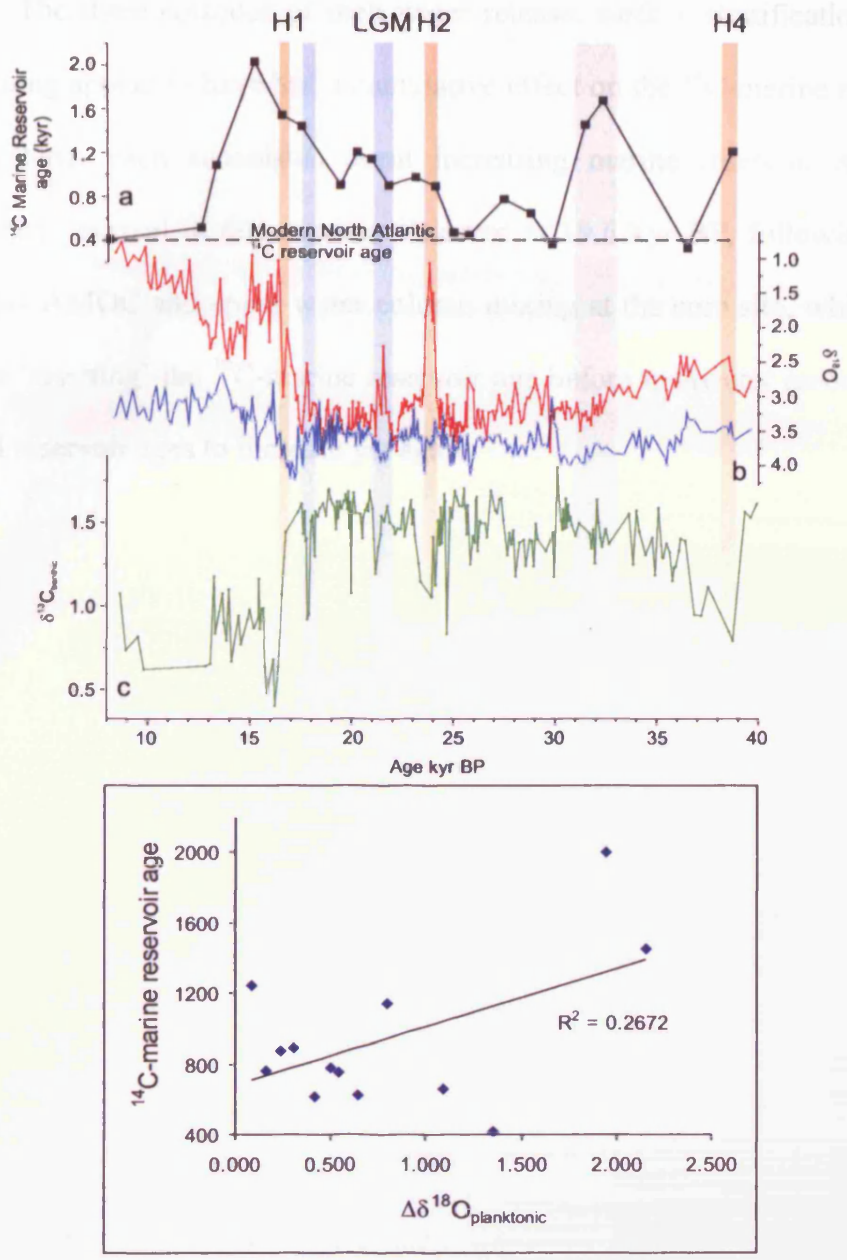

Fig. 3.7. Apparent relationship between upper water column structure, AMOC and ^{14}C-marine reservoir age variability at MD01-2461.

(a). Marine reservoir age implied by offset between the ^{14}C and GISPII age models, (b). $\delta^{18}O$ of surface dwelling *G. bulloides* (red) and subsurface *N.pachyderma* sin. (blue), (c) $\delta^{13}C_{benthic}$. Grey shaded area represents area of reduced confidence in age model. Episodes of meltwater release, stratification of the upper water column, highlighted through the anti-phase relationship of the $\delta^{18}O$ (surface and subsurface) and concurrent reduction in intermediate water ventilation coincide with step-wise increases in ^{14}C-marine reservoir age. Insert shows relationship between ^{14}C-marine reservoir age and surface ocean stratification ($\Delta\delta^{18}O_{planktonic}$ i.e. $\delta^{18}O_{N.\ pachyderma\ sin.} - \delta^{18}O_{G.\ bulloides}$).

The three episodes of melt water release, surface stratification and AMOC weakening appear to have had a cumulative effect on the ^{14}C-marine reservoir age at MD01-2461, each successive event increasing marine reservoir age further. A temporary reversal in this trend is observed at 19.6 kyr BP, following a period of vigorous AMOC and upper water column mixing at the core site, which went some way to 'resetting' the ^{14}C-marine reservoir age before meltwater associated with H1 caused reservoir ages to increase yet again.

Chapter 4

The relationship of Heinrich events and their European precursors over the past 60 kyr BP: A multi-proxy ice rafted debris provenance study in the North East Atlantic[1]

ABSTRACT

High resolution, multi-proxy records of ice rafted debris (IRD) flux and provenance in the NE Atlantic detail the development, variability and decline of marine margins of the last glacial circum-North Atlantic ice sheets. Coupled lithological identification, Sr and Nd isotopic composition and $^{40}Ar/^{39}Ar$ ages of individual hornblende grains reduce ambiguity as to IRD potential source region, allowing clear differentiation between Laurentide (LIS), Icelandic and British (BIS) ice sheet sources (the Icelandic and BIS are collectively referred to as the NW European ice sheet, NWEIS). A step-wise increase in the flux of IRD to the core site at ~26.5 kyr BP documents BIS advance and glaciation of Ireland. Millennial-scale variability of the BIS at a ~2 kyr periodicity is inferred through clusters of pulsed IRD fluxes throughout the late glacial (26.5-10 kyr BP). Combination of these European IRD events and the ~7 kyr periodicity of LIS instability is thought to account for quasi-synchronicity of the NWEIS and LIS IRD pulses at Heinrich event (H) 2 and H1, previously suggested to represent the possible involvement of the NWEIS in the initiation of H events. Furthermore, the lack of extensive NWEIS marine margin is inferred prior to H3 (31.5 kyr BP), such that no 'European precursor' event is associated with either H5 or H4. This suggests that 'precursor events' were not directly implicated in the collapse of the LIS, and the persistent instabilities of the BIS that are clustered at a 2 kyr periodicity are incompatible with the concept that both H events and their 'precursors' are independent responses to a common underlying trigger.

[1] Submitted to *Quaternary Science Reviews* as
Peck, V.L., Hall, I.R., Zahn, R., Grousset, F.E., Hemming, S.R., Scourse, J.D, The relationship of Heinrich events and their European precursors over the past 60 kyr BP: A multi-proxy ice rafted debris provenance study in the North East Atlantic

4.1 Introduction

Ice-rafted debris (IRD) horizons spanning the North Atlantic Ruddiman Belt, zone of preferential IRD accumulation 40-55° N (Ruddiman, 1977), attest to the involvement of last glacial northern hemisphere ice sheets in episodes of abrupt climatic change (Broecker, 1994). Massive destabilizations of the Laurentide ice sheet (LIS) evidenced by detrital carbonate-rich IRD-layers, Heinrich events (H), are inferred at the coldest stadials of the Greenland ice core record, hindering the formation of North Atlantic Deep Water and curtailing the Atlantic Meridional Overturning Circulation , accounting for exceptionally cold northern hemisphere climate (Heinrich, 1988; Bond *et al.*, 1992; 1993; Broecker, 1994; Ganopolski and Rahmstorf, 2001). While extensive petrological and geochemical analysis of Heinrich layers determine the Hudson Strait region of the LIS as the principal outlet of icebergs (e.g. Bond *et al.*, 1992; Andrews and Tedesco, 1992; Grousset *et al.*, 1993; Hemming *et al.*, 1998), quasi-synchronous instabilities of the NW European ice sheets (NWEIS) are also evidenced in NE Atlantic records (e.g. Revel *et al.*, 1996; Snoeckx *et al.*, 1999; Grousset *et al.*, 2000, 2001; Scourse *et al.*, 2000). Interpretation of such 'European precursor' events prior to H1 and H2 (16.8 kyr and 24 kyr BP respectively) play a key role in attempts to determine the ultimate forcing mechanism behind H event initiation, requiring a common external driving force, for example solar forcing to account for multiple ice sheet instabilities (e.g. Scourse *et al.*, 2000). However, ambiguity of provenance allocation, particularly through the use of Sr and Nd isotopic composition alone (Vance and Archer, 2002; Farmer *et al.*, 2003) and high frequency instability of the NWEIS throughout the latter stages of the last glacial (Bond and Lotti, 1995; Knutz *et al.* 2001) question the exact nature of 'European precursor' events.

Using lithological identification coupled with Sr and Nd isotopic analysis of bulk IRD and $^{40}Ar/^{39}Ar$ dating of individual hornblende grains we present a centennial scale record of IRD flux to the European margin during the last 58 kyr, interpreting individual ice sheet growth, variability and decline and the significance of 'European precursor' events.

4.2 Material and methods

Core MD01-2461 was recovered from the north-western flank of the Porcupine Seabight (51° 45'N, 12° 55'W) in a water depth of 1153 m (Fig. 4.1). The site is ideally located to monitor BIS variability as it is close to the last glacial Irish Sea ice stream, a principal outlet glacier draining the BIS (Scourse and Furze, 2001). As previous studies illustrate, a cyclonic surface gyre circulation in the subpolar North Atlantic routed iceberg drifts from the circum-North Atlantic ice sheets to this region (Grousset *et al.*, 1993; Peck *et al.*, 2006) so that the core records also monitor IRD derived from other North Atlantic margins.

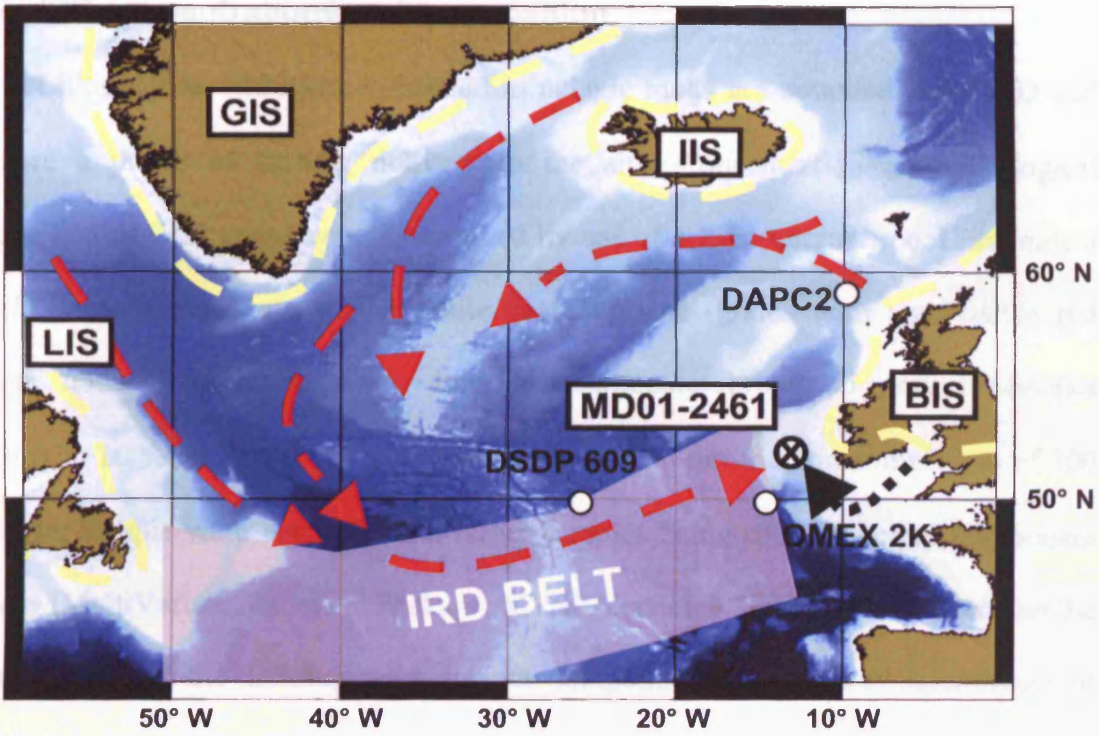

Fig. 4.1. Location of core MD01-2461 and additional core sites discussed in this study. Dashed lines indicate likely routes of icebergs derived from circum-North Atlantic ice sheets and the zone of preferential IRD accumulation is shaded (following Ruddiman, 1977; Grousset *et al.*, 1993). Dotted lines represent the limits of the last glacial ice sheets. BIS – British; IIS – Icelandic; GIS – Greenland; LIS – Laurentide. Dotted line indicates implied outflow from the Irish Sea ice stream.

4.2.1 Physical properties

Magnetic susceptibility of bulk samples was measured every 2 cm using a Bartington MS2 susceptibility meter with MS2B sensor (Wadsworth, 2005). Selected multi-elemental analyses (K, Ca, Ti, Mn, Fe, Cu and Sr), at 1cm resolution, were carried out on the ITRAX™ core-scanning X-Ray Fluorescence (XRF) at the National Oceanography Centre, Southampton.

4.2.2 IRD concentrations and composition

Lithic grains >150 μm embedded in pelagic muds are assumed to be IRD and therefore a proxy of iceberg delivery to the site. Concentration and lithological composition of IRD grains were determined by use of a light microscope. Lithological classification included quartz, haematite coated grains (grains with any visible red staining under light microscope), dolomitic carbonate, brown to grey limestones (reacting to 10 % HCl) and volcanic debris. In the >150 μm fraction a minimum of 300 grains per sample were counted, with larger samples being split. Principal component analysis (MultiVariate Statistical Package, MVSP Version 3.13m) was performed on the concentrations of the lithologically distinct components of the IRD assemblage to identify potential relationships, i.e. similar or dissimilar provenance.

IRD concentration ([IRD], grains g^{-1} dry sediment) was converted into IRD-flux (grains cm^{-2} kyr^{-1}).

$$\text{IRD-flux} = \text{BMAR} \times [\text{IRD}]$$

We used the age model to extrapolate the bulk mass accumulation rate (BMAR) as follows:

$$\text{BMAR (grains cm}^{-2}\text{ kyr}^{-1}) = \text{LSR} \times \rho\text{DB}$$

Where LSR is linear sedimentation rate (cm kyr^{-1}) and ρDB is dry bulk density (g cm^{-3}) determined from wet and dry sediment weights and correcting for salt content assuming sediment particle and waters densities of 2650 $kg.m^{-3}$ and 1025 $kg.m^{-3}$ respectively and pore water salinity of 35 $g.kg^{-1}$.

Power spectra of the total IRD flux was determined from the irregularly spaced data between 26.5-12 kyr BP using the Redfit 3.5 routine (Schulz and Mudelsee, 2002).

In addition to lithological provenance, we compare crustal histories, Sr-Nd isotopic composition of non-carbonate IRD and $^{40}Ar/^{39}Ar$ ages of individual hornblende grains to determine temporal variability in the sources of IRD to the core site (e.g. Snoeckx et al., 1999; Hemming *et al.*, 1998; Hemming and Hajdas, 2003). The Archean crust making up much of the continental mass of the North Atlantic region has been subject to numerous thermal pulses that reset the ages of hornblende crystals (Hoffman, 1989; Hemming *et al.*, 1998). Thermal overprinting of the Superior Province of North America and the Lewisian complex of NW Scotland give hornblendes $^{40}Ar/^{39}Ar$ ages in the order of ~2600 Myr and represent some of the oldest crustal material in the North Atlantic region. Metamorphism in the Paleoproterozoic reset the ages of hornblende crystals of the North American Churchill Province, bordering the Hudson Strait carbonate platform, to 1900-1650 Myr. Thermal overprinting of the Lewisian of NW Scotland persisted throughout this period such that hornblende grains from this region potentially display ages ranging from 2707 to 947 Myr (Friend *et al.*, 2003). Hornblende ages reset to ~1000 Myr during the Grenvillian orogeny are found in SE Canada and NE Scotland and ages of ~450 Myr resulting from the Caledonian-Appalachian orogeny are found in Canada, Eastern Greenland, the British Isles and Scandinavia). Hornblende grains were picked from the >150 μm wherever present. Grains were co-irradiated with hornblende monitor standard Mmhb (age = 525 Myr; Samon and Alexander, 1987) and $^{40}Ar/^{39}Ar$ ratios of individual hornblende grains were determined at the Ar geochronology laboratory at Lamont-Doherty Earth Observatory. Resulting ages were corrected for mass discrimination, interfering nuclear reactions, procedural blanks and atmospheric Ar contamination (Hemming *et al.*, 1998).

The $^{143}Nd/^{144}Nd$ of the carbonate-free, >150 μm fraction was determined for 27 samples. Chemically separated Sr and Nd were analysed on a Finnigan MAT 261 mass spectrometer at Toulouse University, with $^{143}Nd/^{144}Nd$ normalised and reported as εNd(o) following Grousset *et al.* (1998).

4.2.3 Benthic oxygen isotopes

Epibenthic foraminifera *Cibicidoides wuellerstorfi* were collected wherever present, generally 1-4 specimens per sample, picked from the >250 μm fraction. For stable isotope analysis crushed tests were immersed in 3 % hydrogen peroxide for 30 minutes and ultrasonicated in methanol for 15 seconds before excess liquid and residue was removed and tests dried out at 45 °C. All stable isotope analyses were made using a ThermoFinnigan MAT 252 and coupled carbonate preparation device with an external reproducibility of ≤0.08 ‰ for $\delta^{18}O$ and reported on the VPDB scale.

4.2.4 Chronology

Eleven AMS ^{14}C dates are added to the age model presented in Peck *et al.* (2006), corrected for a marine reservoir effect of 400 years and calibrated to calendar years before present (yr BP) using CALIB Rev 5.0/MARINE04 data set (Stuiver *et al.*, 2005) up to 20 ^{14}C kyr and Bard *et al.* (1998) thereafter (Table 4.1).

Table 4.1. Radiocarbon dates for MD01-2461

Laboratory Code	*Material*	*Depth Cm*	*^{14}C Age yr BP*	*Error Age ± 1σ yr*	*Calendar Age yr BP*
SUERC-3299	*G. bulloides*	134.0	7,623	29	8,079
SUERC-3300	*N. pachyderma* sin.	182.5	5,929	24	6,338*
SUERC-3302	*N. pachyderma* sin.	196.5	11,032	39	12,709
SUERC-3303	*G. bulloides*	208.5	12,551	46	13,992
SUERC-3306	*N. pachyderma* sin.	228.5	11,950	43	13,337*
SUERC-3293	*N. pachyderma* sin.	648.5	24,074	168	27,809
SUERC-3296	*N. pachyderma* sin.	674.0	25,312	195	29,142
SUERC-3311	*N. pachyderma* sin.	690.5	25,863	208	29,730
SUERC-3312	*N. pachyderma* sin.	698.5	25,928	209	29,799
SUERC-3313	*N. pachyderma* sin.	746.5	28,526	287	32,515
SUERC-3316	*G. bulloides*	766.5	29,592	326	33,604
SUERC-3317	*G. bulloides*	832.5	32,426	462	36,432
SUERC-3318	N. *pachyderma* sin.	852.5	35,613	684	39,491

*Age reversals removed.

Fine-tuning of the radiocarbon age model and extension beyond the limit of ^{14}C detection was achieved through the correlation of a sea surface temperature (SST) record based on the relative abundance (%) of *Neogloboquadrina pachyderma* sinistral within the planktonic assemblage, to the GISPII $\delta^{18}O_{ice}$ atmospheric temperature record. The relative abundance of the polar species *N. pachyderma* sin. is commonly used as a palaeo-indicator of polar waters (Bé, 1977; Pflaumann *et al.*, 1996; 2003), dominating the planktonic assemblage in waters of summer SST <8 °C (Pflaumann *et al.*, 1996). A minimum of 300 planktonic foraminiferal tests were counted from sample splits >150 μm to determine % *N. pachyderma* sin. with a reproducibility of ±5 %. The % *N. pachyderma* sin. maxima are tuned to stadials in the GISPII $\delta^{18}O$ climate record (Fig.

4.2a, b; Peck *et al.*, 2006) which provides a robust age model based on annual layer counting back to 50 kyr BP, with an estimated error of ±5 % (Meese *et al.* 1994).

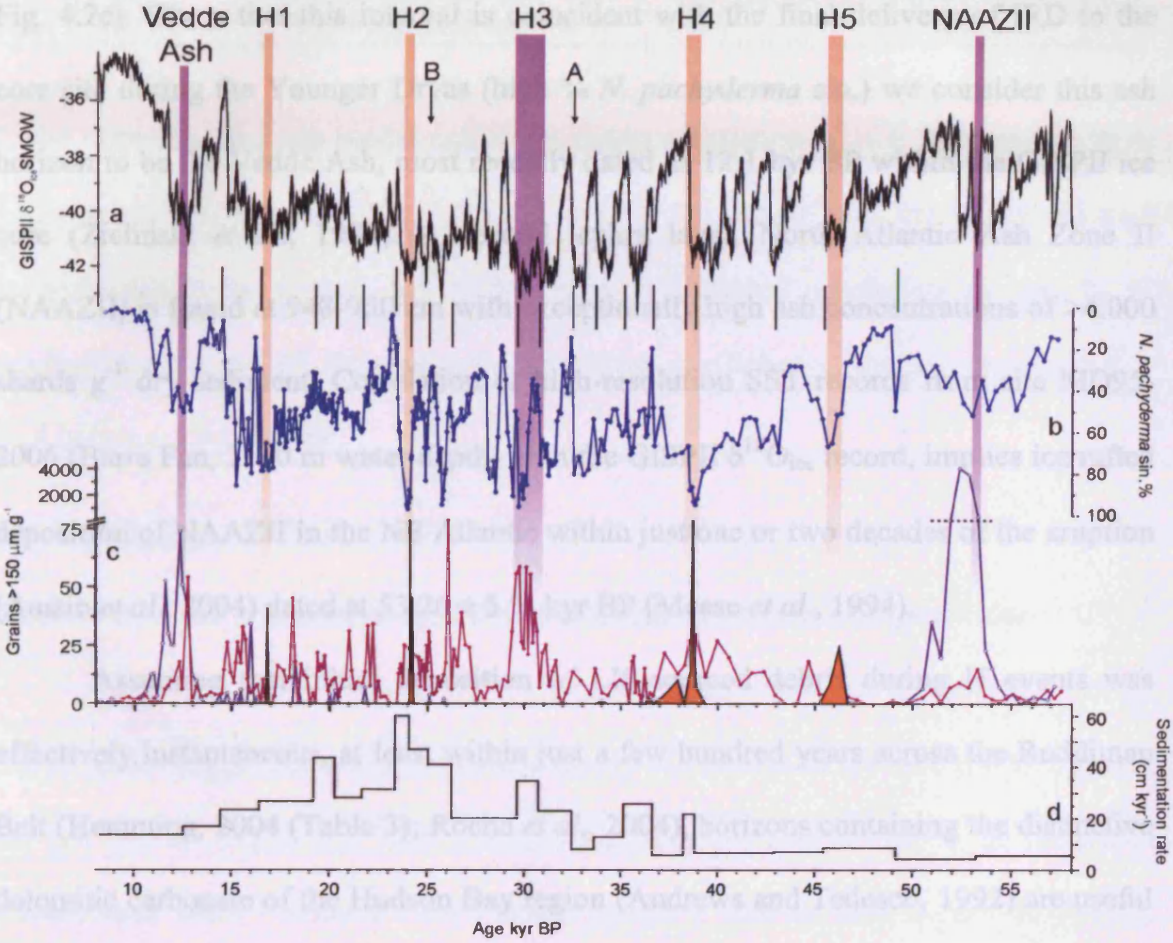

Fig. 4.2. Stratigraphic correlation of relative SST from MD01-2461 and atmospheric temperatures above Greenland from the GISPII $\delta^{18}O_{ice}$ record. The chronology of MD01-2461 is largely based on the visual correlation of SST and climatic temperature shifts. (a). High resolution $\delta^{18}O_{ice}$ record (5-point smoothed) from the Greenland summit GISPII ice core (http://depts.washington.edu/qil/datasets/gisp2_main.html; Grootes and Stuiver, 1997), (b). Relative abundance of *N. pachyderma* sin. (%, >150 µm planktonic assemblage), (c). Concentration of dolomitic carbonate (solid orange), volcanic debris (purple, filled circles) rhyolitic ash shards (lilac, open circles) >150 µm g^{-1} dry sediment, (d). Sedimentation rate, cm ky^{-1} at MD01-2461. Correlation coefficient of *N. pachyderma* sin. % and GISPII $\delta^{18}O_{ice}$ for entire section $r^2 = 0.70$; from A to the core top $r^2 = 0.82$; from B to the core top $r^2 = 0.84$.

Additionally, tephrochronology provides time-parallel marker-horizons allowing precise correlation of late Quaternary marine, terrestrial and ice-core records. Shards of rhyolitic ash are found within the sediment core between 160-210 cm, peaking at 192 cm (74 shards g^{-1} dry sediment), with a secondary peak at 182 cm (53 shards g^{-1} dry sed. Fig. 4.2c). Given that this interval is coincident with the final delivery of IRD to the core site during the Younger Dryas (high % *N. pachyderma* sin.) we consider this ash horizon to be the Vedde Ash, most recently dated as 12.1 kyr BP within the GISPII ice core (Zielinski *et al.*, 1997). A second tephra layer, North Atlantic Ash Zone II (NAAZII) is found at 948-950 cm with exceptionally high ash concentrations of >4,000 shards g^{-1} dry sediment. Correlation of high-resolution SST records from site MD95-2006 (Barra Fan, 2120 m water depth) with the GISPII $\delta^{18}O_{ice}$ record, implies ice rafted deposition of NAAZII in the NE Atlantic within just one or two decades of the eruption (Austin *et al.*, 2004) dated at 53.26 ± 5 % kyr BP (Meese *et al.*, 1994).

Assuming that initial deposition of LIS-sourced debris during H events was effectively instantaneous, at least within just a few hundred years across the Ruddiman Belt (Hemming, 2004 (Table 3); Roche *et al.*, 2004), horizons containing the distinctive dolomitic carbonate of the Hudson Bay region (Andrews and Tedesco, 1992) are useful stratigraphic marker horizons. Tuning of % *N. pachyderma* sin. with GISPII $\delta^{18}O_{ice}$ gives ages for dolomitic carbonate horizons in MD01-2461 (Fig. 4.2c) that are consistent with previously published ages of H events (Table 4.2), heightening confidence in the correlation of MD01-2461 % *N. pachyderma* sin. and atmospheric temperatures over Greenland.

Table 4.2. Published ages for North Atlantic H events

H event	*Age kyr BP*	*Basis*	*Source*
H1	16.8	Radiocarbon (400 yr reservoir correction)	Bond *et al.*, 1997
H2	24.1	Radiocarbon (400 yr reservoir correction)	Bond *et al.*, 1997
H3	30.1	Radiocarbon (400 yr reservoir correction)	Bond *et al.*, 1997
H4	38	GISPII correlation	Meese *et al.*, 1997
H5	45	GISPII correlation	Meese *et al.*, 1997

The finalised age model exhibits a strong correlation (r^2 = 0.70) between % *N. pachyderma* sin. and the GISPII $\delta^{18}O$ record for the period 58-8 kyr BP, while high accumulation rates around the LGM improve temporal resolution of the % *N. pachyderma* sin. record, increasing the correlation coefficient of the two records to r^2 = 0.84 between 25-8 kyr BP.

4.3 Results

4.3.1 Physical properties and IRD concentration and composition

Total IRD concentrations (Fig. 4.3c) rarely fall below 100 grains >150 μm g^{-1} dry sediment suggesting a near persistent supply of icebergs to the core site throughout the last glacial (60-10 kyr BP). Quartz constitutes on average 82 % of total IRD assemblages, while haematite coated grains generally account for a further 10 % (Fig. 4.3e). Constituents that make up the remainder include the distinctive Hudson Strait dolomitic carbonate (Fig. 4.3g), volcanic debris (Fig. 4.3f) and sedimentary lithics (most likely BIS-derived debris; Fig. 3d). Minor quantities of hornblende (see section 4.3.2), chalk, mica and a schist-like lithic are also found. Chalk clasts are frequently associated with peak BIS-IRD concentration between H2 and H1 (Peck *et al.*, 2006). Coccolithophore assemblages identify Late Cretaceous (Coniacian-Santonian; *pers. comm.* J. Young) age ranges similar to those from nearby core OMEX-2K, derived from

the glacial erosion of the Celtic Shelf by the Irish Sea ice stream (Scourse *et al.*, 2000). Occasional clasts of schist and mica flakes are noted in samples prior to H3.

Significant peaks in total IRD concentration are associated with the LIS-sourced dolomitic carbonate of H layers 4 and 2 (38.6 kyr and 24.1 kyr BP respectively). H5 and H1 (46.2 kyr and 16.8 kyr BP) are similarly identified by dolomitic carbonate-rich horizons and all four H events (H5, 4, 2 and 1) are associated with hightened magnetic susceptibility (Fig. 4.3b; Grousset *et al.*, 1993; Robinson *et al.*, 1995). Similar to Robinson *et al.* (1995), we find that variability of magnetic susceptibility does not represent a simple relationship between IRD-concentration/carbonate dilution. High susceptibility signals associated with LIS-sourced IRD horizons do not necessarily correspond to peak total IRD concentrations, particularly at H1 and H5, while high IRD concentrations at the LGM (between H2 and H1) leave no clear signal in the magnetic susceptibility record. It is the nature of the IRD, more than the abundance that influences the magnetic susceptibility signal. Ferrimagnetic-minerals (magnetite) associated with H events, doubtless derived from the plutonic rocks in the source region of Hudson Strait outlet (Grousset *et al.*, 1993) account for the discrete peaks in magnetic susceptibility associated with H events 5, 4, 2 and 1. H3 layers in the NE Atlantic are typically devoid of LIS-sourced debris and proposed to have a predominantly European origin (e.g. Grousset *et al.*, 1993; Gwiazda *et al.*, 1996; Snoeckx *et al.*, 1999). Within MD01-2461, H3 is recognised by a broad positive magnetic susceptibility signature associated with increased concentrations of volcanic material within the period 31.5-29.5 kyr BP. No dolomitic carbonate is observed within this interval.

From the XRF data we compare Ca/Fe with the magnetic susceptibility records (Fig. 4.3a; following Pälike *et al.*, 2001). Ca/Fe is predominantly controlled by Ca

variability (mainly calcium carbonate), decreasing towards the LGM as the ratio of lithogenic IRD to $CaCO_3$ increases. Similarly to the magnetic susceptibility record, correlation of Ca/Fe with the concentration of total IRD is inconsistent. However, consideration of lithological composition suggests that correlation of transient Ca/Fe excursions, superimposed onto the long-term climate signal, with anomalies in magnetic susceptibility may be a potentially useful provenance tool. High Ca/Fe 'detrital carbonate spikes' correspond to the high magnetic susceptibility anomalies and concentrated dolomitic carbonate horizons of H2 and H4. Smaller Ca/Fe 'spikes' are associated with lower dolomitic carbonate concentrations of H5 and H1. High Fe counts are found to accompany increased concentrations of volcanic debris (cf. Pälike *et al.*, 2001), with negative anomalies in Ca/Fe associated with NAAZII, H3 and the Vedde Ash. In-phase and anti-phase transient anomalies in Ca/Fe and magnetic susceptibility therefore locate Heinrich and volcanic-rich layers respectively. Further application may reveal the potential of coupled Ca/Fe-magnetic susceptibility records as preliminary indicators of Heinrich and ash layers in sediment cores.

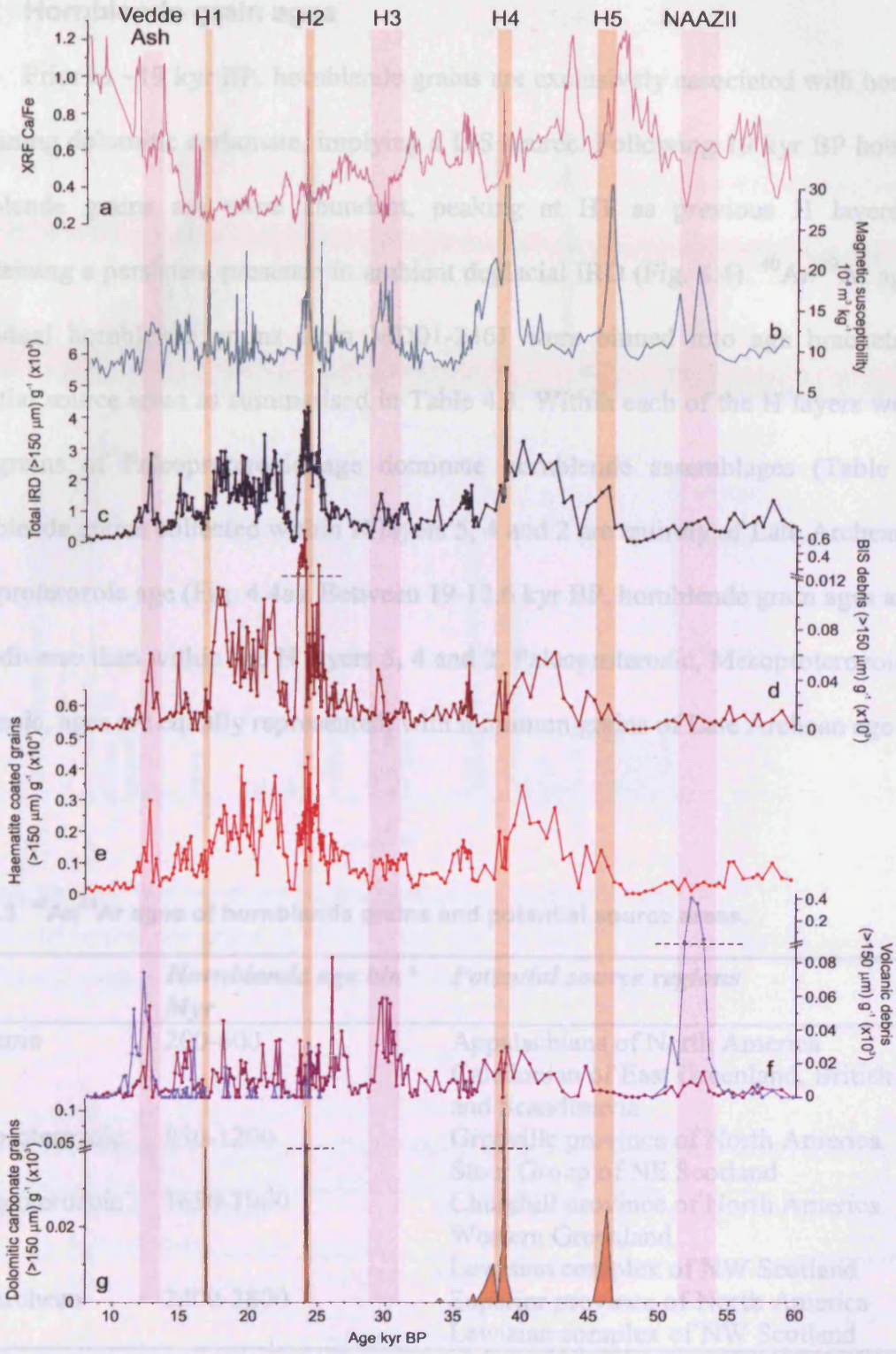

Fig. 4.3. Physical properties and IRD concentration plotted against age for MD01-2461. (a). XRF Ca/Fe, (b). magnetic susceptibility, concentration of IRD (>150 μm) g^{-1} dry sediment of (c). total IRD, (d). BIS debris, (e). haematite coated grains, (f). volcanic debris, rhyolitic tephra (lilac) all other (purple), (g). dolomitic carbonate. Ash layers and H3 located via purple bars. H layers (5, 4, 2 and 1) located via orange bars.

4.3.2 Hornblende grain ages

Prior to ~19 kyr BP, hornblende grains are exclusively associated with horizons containing dolomitic carbonate, implying a LIS source. Following 19 kyr BP however, hornblende grains are more abundant, peaking at H1 as previous H layers, but maintaining a persistent presence in ambient deglacial IRD (Fig. 4.4). $^{40}Ar/^{39}Ar$ ages of individual hornblende grains from MD01-2461 were binned into age brackets and potential source areas as summarised in Table 4.3. Within each of the H layers we find that grains of Paleoproterozic age dominate hornblende assemblages (Table 4.4). Hornblende grains collected within H layers 5, 4 and 2 are entirely of Late Archean and Paleoproterozoic age (Fig. 4.4a). Between 19-12.6 kyr BP, hornblende grain ages are far more diverse than within the H layers 5, 4 and 2. Paleoproterozic, Mesoproterozoic and Paleozoic, ages are equally represented, with minimum grains of Late Archean age (Fig. 4.4b).

Table 4.3. $^{40}Ar/^{39}Ar$ ages of hornblende grains and potential source areas.

Age	*Hornblende age bin** *Myr*	*Potential source regions*
Paleozoic	200-600	Appalachians of North America Caledonian of East Greenland, British Isles and Scandinavia
Mesoproterozoic	850-1200	Grenville province of North America Stoer Group of NE Scotland
Paleoproterozoic	1650-1900	Churchill province of North America Western Greenland Lewisian complex of NW Scotland
Late Archean	2400-2800	Superior province of North America Lewisian complex of NW Scotland

* following Hemming *et al.*, 1998.

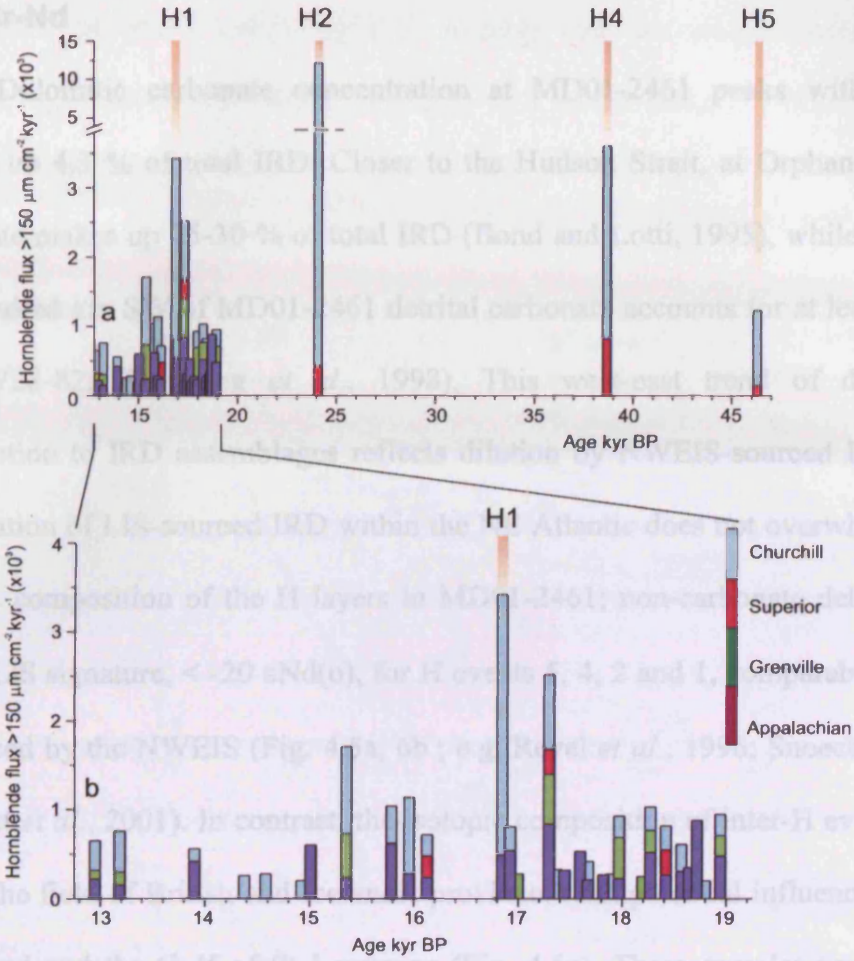

Fig. 4.4. Flux of $^{40}Ar/^{39}Ar$ dated hornblende grains to MD01-2461.
(a). Flux of hornblende grains (>150 µm) cm^{-2} kyr^{-1} to MD01-2461, with relative abundance of $^{40}Ar/^{39}Ar$ ages indicated. (b). Deglacial period (19.2-12.8 kyr BP) in detail.

Table 4.4. % of Paleoproterozoic age hornblende grains collected from MD01-2461 H layers

H event	*Number of dated hornblendes*	*% of Paleoproterozoic age (1650-1900 Myr)*
1	14	85.7
2	29	93.1
4	25	68
5	19	73.7

4.3.3 Sr-Nd

Dolomitic carbonate concentration at MD01-2461 peaks within H layer 2 making up 4.3 % of total IRD. Closer to the Hudson Strait, at Orphan Knoll, detrital carbonate makes up 25-30 % of total IRD (Bond and Lotti, 1995), while at a site just a few hundred km SW of MD01-2461 detrital carbonate accounts for at least 9 % of total IRD (V28-82; Hemming *et al.*, 1998). This west-east trend of decreasing LIS contribution to IRD assemblages reflects dilution by NWEIS-sourced IRD. However, this dilution of LIS-sourced IRD within the NE Atlantic does not overwhelm the Sr-Nd isotopic composition of the H layers in MD01-2461; non-carbonate debris maintain a strong LIS signature, < -20 εNd(o), for H events 5, 4, 2 and 1, comparable to sites little influenced by the NWEIS (Fig. 4.5a, 6b.; e.g. Revel *et al.*, 1996; Snoeckx *et al.*, 1999; Grousset *et al.*, 2001). In contrast, the isotopic composition of inter-H event debris falls within the field of British and Icelandic province, with potential influence from eastern Greenland and the Gulf of St Lawrence (Fig. 4.5a). Three samples representing IRD deposited between H5 and H4 cluster around the isotopic composition of modern day Irish Shelf deposits. Following H4, samples display significantly more radiogenic Sr-Nd isotopic compositions consistent with enhanced volcanic concentrations at H3.

Focusing on H2 an isotopic evolution may be observed across the event, with the Laurentide sourced layer effectively sandwiched between debris of NWEIS source (Fig. 4.5b; cf. Snoeckx *et al.*, 1999; Grousset *et al.*, 2000; 2001). εNd(o) values of -10 to -5 associated with pre-H2 IRD peak between 26.0-24.5 kyr BP suggest a predominantly Icelandic and BIS assemblage, supported by enhanced relative concentrations of both volcanic and BIS debris (Fig. 4.3d, f). Following deposition of H layer 2, with typical H layer εNd(o) of -29.7, a substantial influx of debris falls within the field of the British

Isles and Irish shelf, exhibiting little overlap with the isotopic composition of the volcanic-rich 'precursor' debris. Deglacial IRD Sr-Nd isotopic compositions again fall into the NWEIS field.

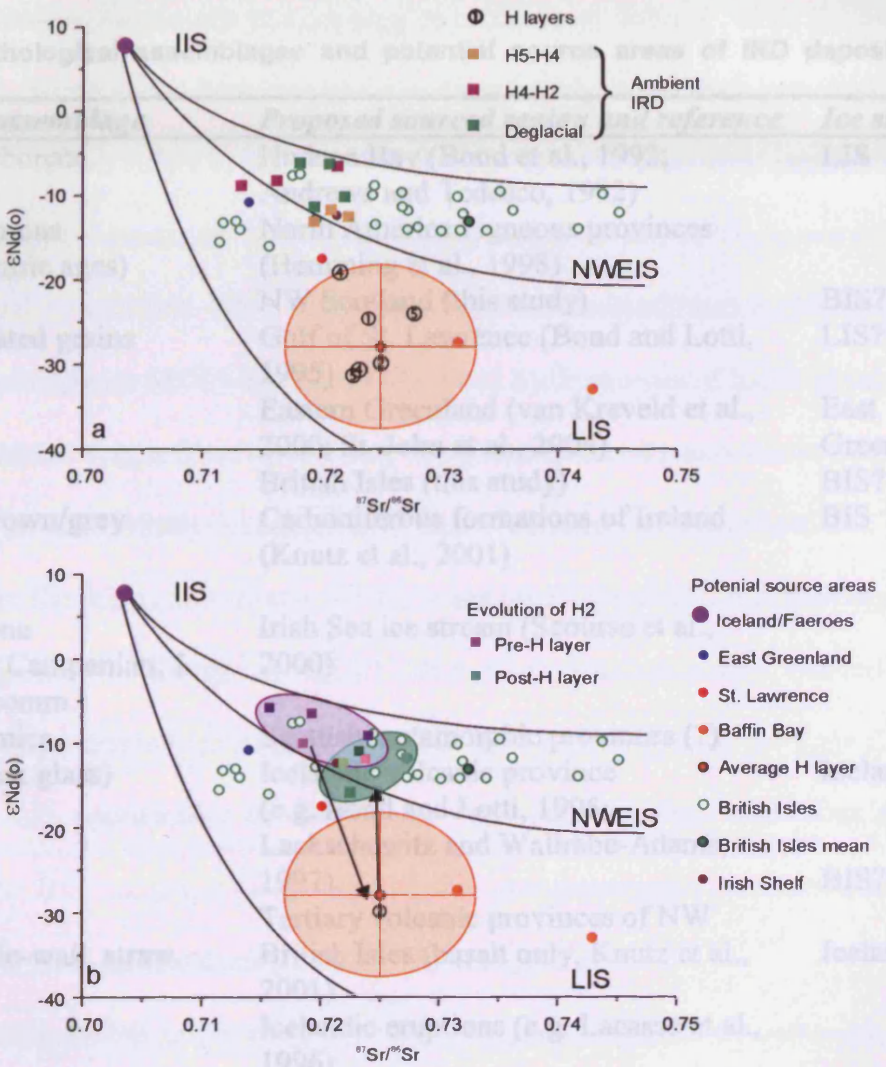

Fig. 4.5. Nd-Sr compositions of of IRD assemblages from MD01-2461.
Potential source areas (Grousset *et al.*, 2001) and British Isles samples (Davies, 1985). (a). H layer and ambient IRD compositions, (b). Nd-Sr composition of IRD across the H2 event.

4.4 Discussion

4.4.1 Provenance allocation

Potential source regions of the lithological components of IRD deposited at the site of MD01-2461 are listed in Table 4.5.

Table 4.5. Lithological assemblages and potential source areas of IRD deposited at MD01-2461.

Lithological assemblage	*Proposed sourced region and reference*	*Ice sheet*
Dolomitic carbonate	Hudson Bay (Bond et al., 1992; Andrews and Tedesco, 1992)	LIS
Hornblende grains (Paleoproterozoic ages)	North American igneous provinces (Hemming et al., 1998)	
	NW Scotland (this study)	BIS?
Haematite coated grains	Gulf of St. Lawrence (Bond and Lotti, 1995)	LIS?
	Eastern Greenland (van Kreveld et al., 2000; St. John et al., 2004)	East Greenland?
	British Isles (this study)	BIS?
Pale – dark brown/grey limestone Shale Black limestone Chalk (Upper Campanian; J Young pers. comm.)	Carboniferous formations of Ireland (Knutz et al., 2001) Irish Sea ice stream (Scourse et al., 2000)	BIS
Schist clasts/mica	Scottish metamorphic provinces (?)	
Obsidian (black glass) Basalt Pumice	Icelandic volcanic province (e.g. Bond and Lotti, 1995; Lackschewitz and Wallrabe-Adams, 1997).	Icelandic
	Tertiary volcanic provinces of NW British Isles (basalt only, Knutz et al., 2001)	BIS?
Tephra (bubble-wall, straw colour)	Icelandic eruptions (e.g. Lacasse et al., 1996)	Icelandic

Components are listed in descending order of relative abundance within each assemblage.

The Late Archaean and Paleoproterozoic hornlendes collected from H layers 5, 4 and 2 (Fig. 4.4a), fit the Hudson Strait source suggested by their exclusivity to dolomitic carbonate-rich layers. Although grains of this age may have been potentially sourced

from NW Scotland, consideration of all provenance proxies (the lithological assemblage, magnetic susceptibility, and Sr-Nd data) effectively eliminates this source region, favouring a LIS-source. Sedimentary grains comprising dark to light grey-brown limestones and shales characterise BIS deposits, considered to be derived predominantly from Carboniferous formations outcropping over much of Ireland. With the volcanic and haematite coated grains however, there is some ambiguity to their principal origin. Volcanic material ice rafted to the Barra Fan (site DAPC2, Fig. 4.1), primarily from Tertiary volcanic provinces of NW British Isles (Knutz *et al.*, 2001) is very distinct from that deposited at MD01-2461. Unlike the basalt-rich assemblages at the Barra Fan, volcanic assemblages at MD01-2461 are dominated by fragments of black glass, better fitting an Icelandic origin (Bond and Lotti, 1995; Lackschewitz and Wallrabe-Adams, 1997; Elliot *et al.*, 1998). Additionally, the distinctive crypto-crystalline basalt deposited at the Barra Fan site (Knutz, 2000), is not noted at our site. It is envisaged that volcanic fragments deposited at MD01-2461 were predominantly derived from Icelandic ice sheet-sourced icebergs entrained in the cyclonic gyre of the central North Atlantic (Fig. 4.1), approaching the European margin from the west, rather than drifting south along the BIS margin, a path which would have presumably been obstructed by icebergs calved from Ireland during much of the late glacial.

Haematite-coated grains are a persistent component of IRD assemblages across the Ruddiman Belt (e.g. Bond and Lotti, 1995). At MD01-2461 haematite-coated grains average 10 % (range 5-16 %) of the total IRD assemblage, fitting decreasing percentages west-to-east across the North Atlantic, that indicate the Gulf of St. Lawrence to be a principal source region (Bond and Lotti, 1995). A further north-to-south trend following the path of the East Greenland Current suggests red beds of

Eastern Greenland to be a secondary source region of haematite-coated grains (Bond *et al.*, 1997; van Kreveld *et al.*, 2000; St. John *et al.*, 2004). Principal component analysis of IRD assemblage concentrations at MD01-2461 determine one principle axis accounting for 84 % of variability, most likely reflecting total flux of IRD, which was derived predominantly from the local BIS as reflected by the high variability loading of the BIS assemblage (Table 4.6). High variability loading of haematite coated grains with respect to Icelandic ice sheet-sourced debris may indicate that the BIS was a important source of haematite coated grains to our core site rather than the East Greenland ice sheet or Gulf of St. Lawrence which, following Bond and Lotti (1995), we may expect to show distinct synchronicity with volcanic debris from the Icelandic ice sheet. Expansive outcrops of Old and New Red Sandstone are found in Wales, Scotland and border regions of England (Geological map of the British Islands, BGS, 1969), but not in Ireland where the Carboniferous formations source the limestones and shales of the BIS assemblage, perhaps accounting for the weaker correlation of these lithologies ($r^2 = 0.61$).

Table 4.6. Variability loadings of IRD components to total IRD flux to MD01-2461.

IRD assemblage component	*Variability loadings*
Volcanic debris	0.03
BIS	0.88
Haematite coated grains	0.47

4.4.2 IRD flux: Ice sheet growth, variability and decline

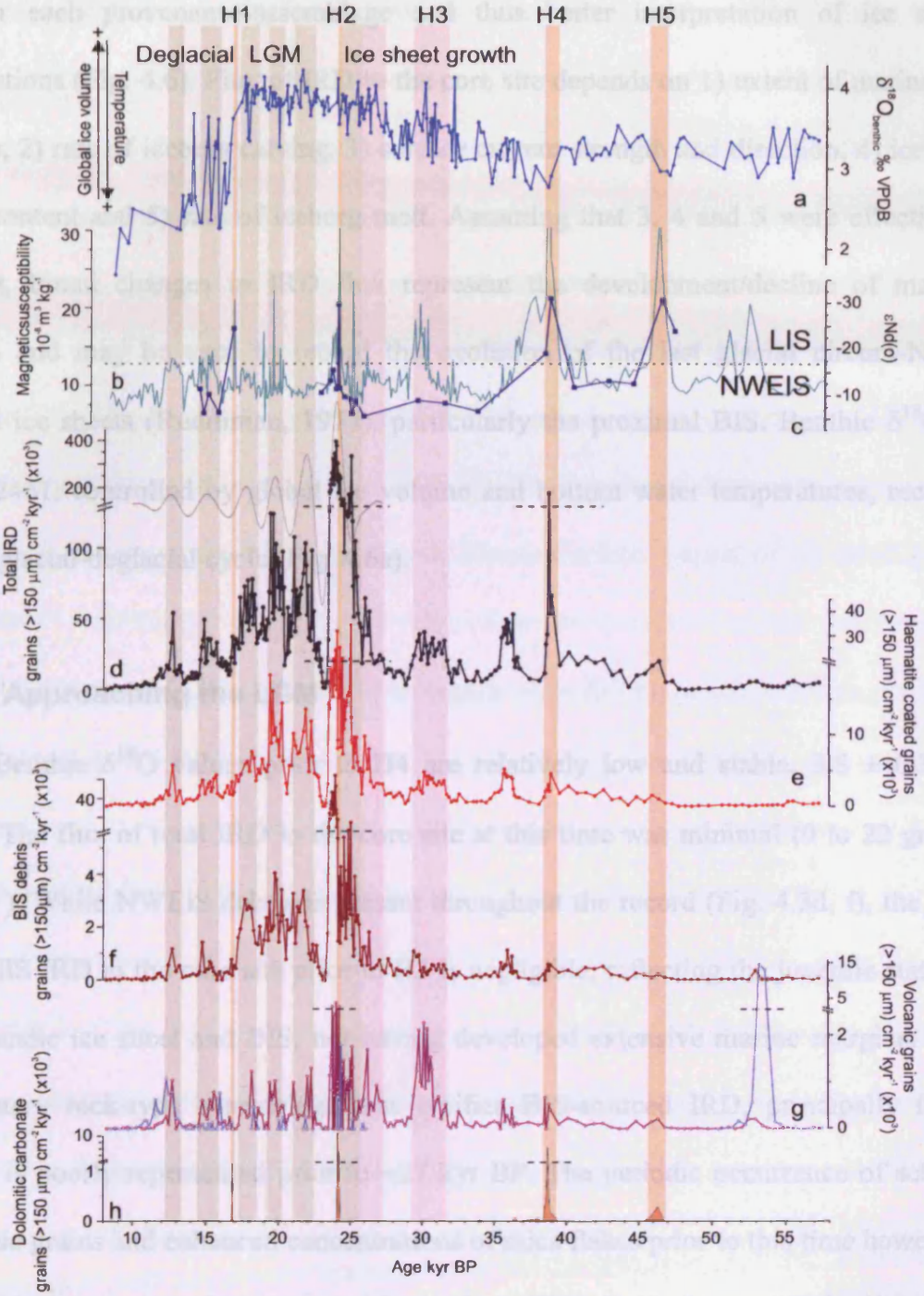

Fig. 4.6. Benthic $\delta^{18}O$ and IRD flux to MD01-2461 during the last glacial.
(a). $\delta^{18}O$ benthic (‰ VPDB) reflecting bottom water temperatures and global ice volume. (b). Magnetic susceptibility (c). εNd of non-carbonate fraction. εNd(o) < -20 indicative of an LIS-origin. Flux of IRD (>150 μm) cm^{-2} kyr^{-1} dry sediment of (d). total IRD with 2 kyr filter overlain in grey between 26.5-10 kyr BP, (e). haematite coated grains, (f). BIS debris, (g). volcanic debris, rhyolitic tephra (lilac), all other (purple), (h). dolomitic carbonate

Confidence in the age model permits conversion of IRD concentrations to IRD-flux for each provenance-assemblage and thus better interpretation of ice sheet contributions (Fig. 4.6). Flux of IRD to the core site depends on 1) extent of marine ice margins, 2) rate of iceberg calving, 3) surface current strength and direction, 4) iceberg debris content and 5) rate of iceberg melt. Assuming that 3, 4 and 5 were effectively constant, broad changes in IRD flux represent the development/decline of marine margins and may be used to record the evolution of the last glacial circum-North Atlantic ice sheets (Ruddiman, 1977), particularly the proximal BIS. Benthic $\delta^{18}O$ at MD01-2461, controlled by global ice volume and bottom water temperatures, records the last glacial-deglacial cycle (Fig. 4.6a).

4.4.2.1 Approaching the LGM

Benthic $\delta^{18}O$ values prior to H4 are relatively low and stable, 3.8 ± 0.3 ‰ VDPB. The flux of total IRD to the core site at this time was minimal (0 to 22 grains cm^{-2} yr^{-1}). While NWEIS debris is present throughout the record (Fig. 4.3d, f), the *flux* of NWEIS IRD to the core site prior to H3 is negligible, reflecting the juvenile state of the Icelandic ice sheet and BIS, not having developed extensive marine margins. The sedimentary rock-type assemblage that typifies BIS-sourced IRD, principally from Ireland, is poorly represented prior to ~27 kyr BP. The periodic occurrence of schist-type lithic grains and enhanced concentrations of mica flakes prior to this time however, suggest glacial erosion of a metamorphic province. We tentatively suggest that this IRD may have been sourced from glaciers overlying the Dalradian Supergroup of Scotland, reflecting glaciation of elevated landmasses in the north of the British Isles as early as H5. A predominantly local source of IRD at this time is supported by the high relative

abundance of BIS debris and haematite coated grains, minimal contribution of volcanic debris (just 0.5 % of total IRD, compared to a down core average of >1 %) and Sr-Nd isotopic compositions resembling modern Irish Shelf deposits. This finding is significant in that it demonstrates the presence of a BIS as early as 46 kyr BP, supporting previous speculations about the establishment of intermittent BIS marine margins prior to full glaciation at ~27 kyr BP (Knutz *et al.*, 2001; Bowen *et al.*, 2002).

Large-scale instability of the LIS is evidenced twice, at ~46.3 kyr BP (H5) and 38.6 kyr BP (H4), during this period of NWEIS growth. Small quantities of Icelandic and BIS debris may also be associated with H4. The brevity of these events suggests a short-lived advance of the BIS to sea level, allowing a brief period of ice calving into the ocean.

Following H4, benthic $\delta^{18}O$ increases with LGM values averaging 4.5 ‰ VDPB attained at ~27 kyr BP. Extensive ice sheet growth during this period is associated with cooling upper ocean conditions, as evidenced by increasing % *N. pachyderma* sin. (Fig. 4.2b), culminating with an abrupt increase in IRD flux at 26.5 kyr BP (Fig. 4.6d).

Icebergs derived from calving of Icelandic glaciers, evidenced by the enhanced flux of volcanic debis to the core site and more radiogenic εNd(o) values (Fig. 4.6c, g), increased in frequency from ~31.5 kyr BP associated with deposition of H3, and coinciding with the maximum northern extent of the Icelandic ice sheet (Gudmundsson *et al.*, 2003). The broad positive magnetic susceptibility signature, comparable in magnitude to H1, suggests elevated concentrations of ferromagnetic minerals similar to the other H events, however, the absence of both dolomitic carbonate and typical-H layer geochemical signatures eliminates a typical H event LIS-IRD provenance. Such

magnetite-bearing material may derive from the Gulf of St. Lawrence region (Thouveny *et al.*, 2000) or from plateau basalts from East Greenland and Iceland (Pirrung *et al.*, 2002). Farmer *et al.* (2003) highlight the inability of Sr and Nd isotopic data to clearly discriminate between European and southern Canadian Shield-derived IRD and call for re-assessment of assumed NWEIS-IRD events, specifically the origin of H3. Although the coupled lithological records presented here effectively 'ground truth' the isotopic data at MD01-2461 and determine a clear Icelandic ice sheet contribution to H3, an additional contribution from the Gulf of St. Lawrence cannot be ruled out.

A stepwise increase in flux of total IRD to the core site from 26.5 kyr BP is associated with the first significant appearance of debris that can be confidently attributed to the BIS, reflecting the development of extensive BIS marine margins, full glaciation of Ireland and establishment of the Irish Sea ice stream. This timing supports modelling of the Irish ice sheet, where calving of icebergs is predicted to have begun at 25 kyr BP (Siegert and Dowdeswell, 2002), and is consistent with the age of LIS advance suggested by Grenville- and Appalachian-province derived hornblendes in the western North Atlantic (Hemming and Hajdas, 2003). IRD records from both sides of the North Atlantic basin therefore suggest that LGM conditions (i.e. maximum ice sheet extent) began as early as ~27 kyr BP in the northern hemisphere.

4.4.2.2 Ice sheet variability

Maximum variability in the flux of IRD to the core site is identified between 26.5 kyr and the Younger Dryas, following the establishment of last glacial maximum NWEIS marine margins. There is little variation in benthic $\delta^{18}O$ around the LGM, suggesting that the fluxes of IRD derived from the NWEIS represented largely localised

events, apparently not associated with major ice volume change. A ~2 kyr periodicity of total IRD flux variability within this period exceeds the 99 % confidence limit and is clearly illustrated in the filtered record (Fig. 4.6d). Such millennial-scale variability of the NWEIS, thought to be linked to Dansgaard-Oeschger (D-O) climate variability of the Greenland ice core records has previously been documented by Bond *et al.* (1997), van Kreveld *et al.* (2000) and Knutz *et al.* (2001).

4.4.2.3 Deglaciation

Although the ~2 kyr periodicity of IRD flux clusters to MD01-2461 persists throughout the deglacial, the amplitude of these events falls significantly following the H1 'precursor' at 18.4-17.2 kyr BP when the last significant fluxes of BIS debris are recorded. Sr-Nd isotopic compositions characterize a principally BIS-sourced debris assemblage following H1. Conversely, the diverse range of ages derived from hornblende grains between 19-12.6 kyr BP suggest either the increased presence of LIS-sourced ice, derived from all four age provinces or the sourcing of hornblende grains from elsewhere. Hemming and Hajdas (2003) account for the appearance of Mesoproterozoic and Paleozoic aged ice-rafted hornblendes in the western North Atlantic as representing the south-eastward advance of the LIS across Appalachian and Grenville provinces between H3 and H1. Retreat of the LIS following H1 is inferred by the absence of grains younger than that of the Churchill Province (<1650 Myr) in the western North Atlantic after ~14 ^{14}C kyr. A European source for hornblende grains of <1650 Myr in NE Atlantic is therefore more feasible than a LIS source at this time. Caledonian bedrock of East Greenland, the British Isles and Scandinavia could have sourced Paleozoic aged hornblendes while metamorphic provinces of Northern Scotland

could have accounted for grains of Late Archean to Mesoproterozoic age, therefore requiring no input from the LIS and accounting for the absence of dolomitic carbonate associated with these grains. Free southwards drifting of icebergs calved from the ice streams draining the Scottish highlands, after 19 kyr BP and following retreat of the Irish ice sheet (Bowen *et al.*, 2002) may offer an explanation for the 'late' appearance of abundant, non-H event hornblende grains and associated grains of schist.

4.5. Summary and interpretation of 'European precursor' events

Identification of IRD of NWEIS origin preceding H events in the NE Atlantic prompted several authors to propose 'European precursor events', with the implication that they may play some mechanistic role in the initiation of LIS collapse (e.g. Grousset *et al.*, 2000). Records from MD01-2461 again demonstrate instability of the NWEIS preceding both H2 and H1, however, significant NWEIS activity around this time, potentially of D-O frequency, precludes the assignment of specific NWEIS instabilities as precursors to these H events. Furthermore, we find little evidence of ice rafting that can confidently be attributed to any significant variability of the NWEIS prior to H3, reflecting a juvenile state BIS lacking active marine margins. Although similarly to Snoeckx *et al.* (1999), Sr and Nd isotopic compositions of IRD prior to H4 display a clear NWEIS signature, IRD flux is at ambient glacial levels and therefore not representative of an 'event'. It may be argued that the >150 μm size fraction is insensitive to low level changes in background IRD (Moros *et al.*, 2004). However, we suggest that given the proximity of MD01-2461 to the last glacial BIS, any destabilisation of the SW extent of this former ice sheet is unlikely to go unrecorded in our coarse fraction record. Consistently, we are confident that no 'European precursor'

events, similar to those observed prior to H2 and H1, are associated with H4 or H5 in this core.

Whatever the trigger may have been for H event initiation, we find that instability of the NWEIS prior to the LIS was unlikely a necessary component. Indeed H events 5 and 4 occurred while the NWEIS was still in a juvenile state and apparently incapable of calving significant quantities of ice. On the other hand, H3 seems to be primarily of NWEIS origin. Steady pacing of H events (~7 kyr) and NWEIS instability following 26.5 kyr BP (~2 kyr) lead us to suggest that superimposition of independent LIS and NWEIS IRD events of differing frequencies may have lead to the sequencing of NWEIS-LIS sourced IRD at H2 and H1. Climatic sensitivity of the Greenland Ice Sheet is suggested by the pervasive ~1.5 kyr pulsing of ice rafted haematite coated grains from Eastern Greenland through the last glacial and into the Holocene (Bond *et al.*, 1997; 2001). Similar variability of the BIS (Knutz *et al.*, 2001; this study) lead us to suggest that millennial-scale fluctuation of circum-North Atlantic ice sheet marine margins was common place during the last glacial, perhaps in response to a similar driving force. In contrast, the ~7 kyr period of the iceberg armadas from Hudson Strait may reflect a very different controlling mechanism for the LIS, independent of other ice sheets. Such independent frequencies of ice sheet instabilities appear to oppose an ultimate underlying forcing mechanism that generated lagged responses in each of the ice sheets (cf. Scourse *et al.*, 2000). As debate over H event initiation mechanisms continues (e.g. Hemming, 2004; Hulbe *et al.*, 2004; 2005; Alley *et al.*, 2005) we add that whatever the trigger for H events may have been, it did not require the presence of an established NWEIS and nor did it appear to influence the steady ~2 kyr pacing of NWEIS instability.

Chapter 5

High Resolution Evidence for Linkages between NW European Ice Sheet Instability and Atlantic Meridional Overturning Circulation[1]

ABSTRACT

Published studies show that ice rafted debris (IRD) deposition preceding Heinrich (H) events H1 and H2 in the NE Atlantic was derived from the NW European ice sheets (NWEIS), possibly offering clues about ice sheet sensitivity and stability, and the mechanisms that caused periodic collapse of the Laurentide Ice Sheet (LIS). We present detailed lithological and geochemical records, including radiogenic isotope fingerprinting, of IRD deposits from core MD01-2461, proximal to the last glacial British Ice Sheet (BIS), demonstrating persistent instability of the BIS, with significant destabilisation occurring 1.5-1.9 kyr prior to both H1 and H2, dated at 16.9 kyr and 24.1 kyr BP respectively in the NE Atlantic. Paired Mg/Ca and $\delta^{18}O$ data from the surface dwelling *Globigerina bulloides* and subsurface dwelling *Neogloboquadrina pachyderma* sinistral are used to determine late-glacial variability of temperature, salinity and stratification of the upper water column. A picture emerges that the BIS was in a continuing state of readjustment and never fully reached steady state. Increased sea surface temperatures appear to have triggered the episode NWEIS instability preceding H1. It seems most probable that the so-called 'precursor' events were not linked to the H-events. However, if response to a common thermal forcing is considered, an increased response time of the LIS, up to ~2 kyr longer than the NWEIS, may be inferred. Negative salinity excursions of up to 2.6 indicate significant incursions of melt water associated with peaks in NWEIS instability. Decreased surface density led to a more stable stratification of the upper water column and is associated with reduced ventilation of intermediate waters, recorded in depleted epibenthic $\delta^{13}C$ (*Cibicidoides wuellerstorfi*). We suggest that instability and meltwater forcing of the NWEIS temporarily weakened Atlantic Meridional Overturning Circulation, allowing transient advance of southern-sourced waters to this site, prior to H events 1 and 2.

[1] Published in *Earth and Planetary Science Letters* as Peck, V.L., Hall, I.R., Zahn, R., Elderfield, H., Grousset, F.E., Hemming, S.R., Scourse, J.D. (2006). High Resolution Evidence for Linkages between NW European Ice Sheet Instability and Atlantic Meridional Overturning Circulation

5.1 Introduction

Numerical modelling suggests that increases in freshwater flux of just 0.01 Sv, if routed to the centres of active deep-water convection, have the capability to cause considerable reduction in the Atlantic Meridional Overturning Circulation (AMOC), accounting for mean annual temperature changes of between 5-10 °C in the circum-North Atlantic region over a matter of decades (Ganopolski and Rahmstorf, 2001). The last glacial NW European ice sheets (NWEIS; comprising the British, Icelandic and Fennoscandian ice sheets) likely achieved a maximum ice volume of ~10 x 10^6 km^3, approximately one third that of the North American, Laurentide ice sheet (LIS) (Charbit *et al.*, 2002), often considered to be the principal driver behind millennial scale variability in AMOC during the last glacial period (Vidal *et al.*, 1997; Zahn *et al.*, 1997; Elliot *et al.*, 2002). Rather than the volume of these freshwater reservoirs however, it is the location of the NW European ice sheets (NWEIS; comprising the British, Icelandic and Scandinavian ice sheets), close to the main North Atlantic convection centres, that enhances their potential to perturb AMOC and climate during episodes of accelerated ice sheet melting.

Despite intensive research into Heinrich (H) events (see recent review by Hemming, 2004) and Dansgaard-Oeschger (D-O) climatic oscillations that are associated with ~1.5 kyr ice rafted detritus (IRD) cycles in the NE Atlantic (e.g. Bond and Lotti, 1995; Lackschewitz *et al.*, 1998), there is no clear consensus on the underlying mechanism that caused these periodic phenomena. Hypotheses relating to H event initiation include external forcing, probably intimately linked to perturbations of AMOC dynamics (e.g. Bond *et al.*, 1997), and the internal dynamics of the LIS (MacAyeal, 1993; Marshall and Clarke, 1997). Modelling (MacAyeal,

1993; Marshall and Clarke, 1997) and lack of significant D-O frequency surging of the Hudson Strait ice stream (Andrews and Barber, 2002) suggest that the LIS was relatively stable and largely immune to high-frequency (climate) forcing, favouring internal instabilities as the trigger for periodic LIS collapse every 7-10 kyr (MacAyeal, 1993; Alley and MacAyeal, 1994). Conversely, the sensitivity of the smaller NWEIS of the last glacial is well documented (Fronval *et al.*, 1995; Elliot *et al.*, 1998; Knutz *et al.*, 2001). Recent studies have identified NWEIS instability prior to H-events 1 and 2 (Grousset *et al.*, 2000; Scourse *et al.*, 2000; Knutz *et al.*, 2002), possibly supporting a common external triggering mechanism of H events, assuming individual ice sheet response times were, in part, proportional to ice sheet size/extent of marine margin. Understanding the forcing and climatic feedbacks that propel these millennial scale cycles, including their interference with AMOC, is crucial for the development of predictive climate models (Ganopolski and Rahmstorf, 2001).

Here we present evidence from a marine sediment core for NWEIS variability preceding H1 and H2 (~16.8 kyr and ~24.0 kyr BP; Bond *et al.*, 1992; Bond *et al.*, 1993). Multi-proxy foraminiferal and lithologic geochemical analyses allow us to document the variability of the British (BIS), East Greenland/Icelandic (EGIIS) and Laurentide ice sheets in fine detail in a framework of AMOC variability.

5.2 Materials and methods

Sediment core MD01-2461 was recovered from the north-western flank of the Porcupine Seabight (51° 45' N, 12° 55' W) in a water depth of 1153 m (Fig. 5.1). The site is ideally located to monitor BIS variability as it is close to the last glacial Irish Sea ice stream, a principal outlet glacier draining the BIS (Scourse and Furze,

2001). As previous studies illustrate, a cyclonic surface gyre circulation in the subpolar North Atlantic routed iceberg drifts from the circum-North Atlantic ice sheets to this region (Ruddiman, 1997; Grousset *et al.*, 1993; Zaragosi *et al.*, 2001) so that the core records also monitor IRD derived from other North Atlantic margins.

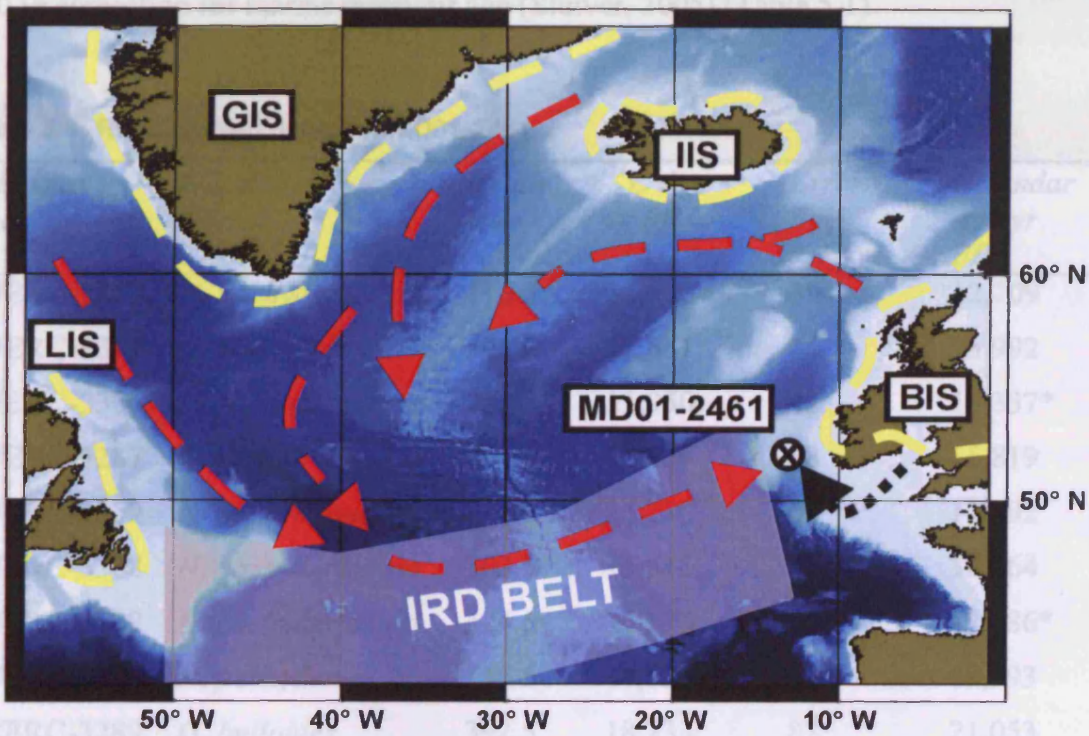

Fig. 5.1. Location of core MD01-2461 at the northeastern extent of the Ruddiman belt of preferential IRD accumulation. Dashed red lines indicate likely routes of icebergs derived from circum-North Atlantic ice sheets due to an anti-clockwise surface gyre during the last glacial (Ruddiman, 1977; Grousset *et al.*, 1993). Dashed yellow lines represent last glacial maximum ice sheet extent for the; BIS – British; IIS – Icelandic; GIS – Greenland; LIS – Laurentide ice sheets (IS). Dotted line indicates implied outflow from the Irish Sea ice stream.

The chronology of MD01-2461 is based on 15 monospecific foraminifera (*Globigerina bulloides*, or *Neogloboquadrina pachyderma* sinistral) AMS ^{14}C dates. Radiocarbon ages were calibrated to calendar years before present (yr BP) using the CALIB programme (version 5.0.1 with the MARINE04 data set), incorporating a 400 yr correction for marine reservoir age (Stuiver, 2005) (Table 5.1).

Table 5.1. Radiocarbon dates for MD01-2461

Laboratory Code	*Material*	*Depth cm*	*^{14}C Age yr BP*	*Error Age ± 1σ yr*	*Calendar Age yr BP*
SUERC-3302	*N. pachyderma* sin.	196.5	11,032	39	12,709
SUERC-3303	*G. bulloides*	208.5	12,551	46	13,992
SUERC-3306	*N. pachyderma* sin.	228.5	11,950	43	13,337*
SUERC-3287	*N. pachyderma* sin.	244.5	14,530	58	16,819
SUERC-3307	*N. pachyderma* sin.	276.5	15,118	64	17,692
SUERC-3308	*N. pachyderma* sin.	302.5	15,518	63	18,564
SUERC-3309	*N. pachyderma* sin.	324.5	15,174	60	17,586*
SUERC-3288	*N. pachyderma* sin.	356.5	17,130	77	19,993
SUERC-3289	*G. bulloides*	392.5	18,233	87	21,053
SUERC-3290	*N. pachyderma* sin.	412.5	18,665	89	21,688
SUERC-3292	*N. pachyderma* sin.	436.5	19,128	94	22,287
SUERC-2278	*G. bulloides*	478.0	20,193	118	23,702
SUERC-2279	*N. pachyderma* sin.	528.5	20,931	129	24,577
SUERC-2275	*N. pachyderma* sin.	570.5	21,565	128	25,647
SUERC-2274	*N. pachyderma* sin.	602.5	22,234	147	25,792

*Age reversals removed.

However, comparison of the relative abundance of *N. pachyderma* sin. (%; an apparent relative sea surface temperature (SST) proxy; Bé, 1977) with the GISPII $\delta^{18}O$ record (Grootes and Stuiver, 1997; Fig. 5.2b, c) suggests that the constant ^{14}C-reservoir assumption is likely incorrect. The climate-based correlation ($r^2 = 0.829$) suggests that the 400-year ^{14}C-reservoir correction is a considerable underestimate, with offset between the tuned and ^{14}C-based age model increasing following H2 and the last glacial maximum (LGM; Fig. 5.2a).

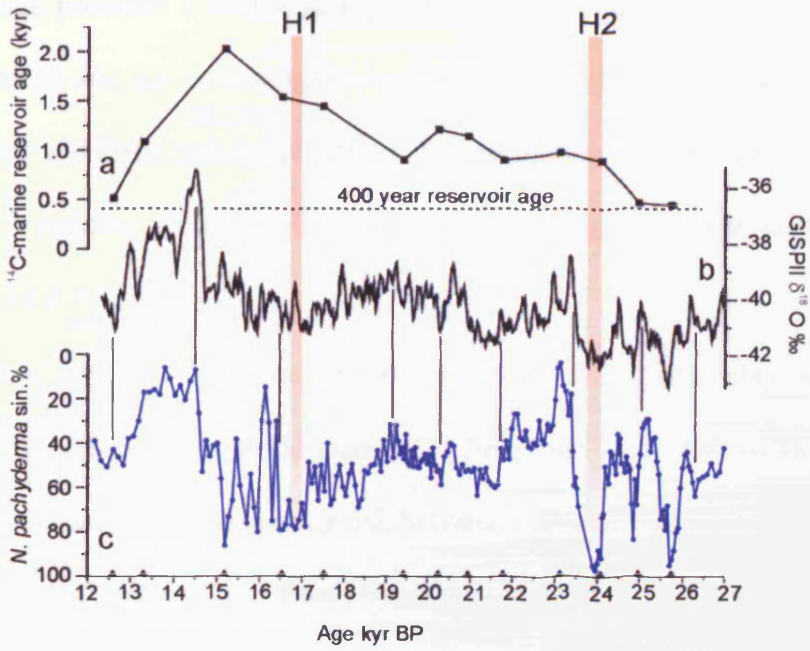

Fig. 5.2. Stratigraphic correlation between relative abundance of *N. pachyderma* sin. and GISPII ice core. (a) Suggested ^{14}C-marine reservoir ages determined from the age difference between calibrated ^{14}C ages and calendar years based on the correlation of *N. pachyderma* sin. % (c) with GISPII $\delta^{18}O$ (Grootes and Stuiver, 1997) (b). Dashed line indicates the present day North Atlantic ^{14}C-marine reservoir age of 400 years. Vertical lines indicate tie-points used for stratigraphic correlation. Black triangles in (c) indicate ^{14}C date. Orange bars locate H layers 1 and 2.

Elevated ^{14}C-marine reservoir ages have previously been interpreted from North Atlantic sediments, reflecting sea-ice or meltwater cover reducing air-sea gas exchange and isotope equilibration (Austin *et al.*, 1995; Voelker *et al.*, 1998; Waelbroeck *et al.*, 2001; Eiriksson *et al.*, 2004). Our correlation between *N. pachyderma* sin. % and the Greenland ice core palaeoclimatic record suggests ^{14}C-marine reservoir ages of up to ~2 kyr occurred at our site during periods of substantial meltwater release and ocean stratification. An additional consideration may be release of aged CO_2 during ice sheet melt (Domack *et al*, 1989). Here, we use the age model derived from tuning the *N. pachyderma* sin. % record to GISPII $\delta^{18}O$ profile which provides a robust stratigraphy that is comparable with the Greenland ice core record and palaeoceanographic profiles from other North Atlantic core sites (Veiga-Pires and Hillaire-Marcel, 1999). Sedimentation rates range between 12 and 60 cm kyr^{-1} yielding, at a sampling interval of 1-2 cm, a mean time step along the records of 60 ± 30 years.

Lithic grains >150 μm embedded within the silty clay sediment are considered to be ice rafted (Ruddiman 1977; Bond and Lotti, 1995). Through visual, lithological classification we distinguish between non-provenance specific quartz and haematite-coated grains, an East Greenland/Icelandic (EGIIS) assemblage of volcanic debris (pumice, black glass and basalt), LIS-sourced dolomitic carbonate (Andrews and Tedesco, 1992) and a BIS assemblage (shale, dark carbonates and black limestone) sourced in part from Carboniferous formations that outcrop across much of Ireland. Chalk clasts occasionally associated with this BIS assemblage support an Irish Sea ice stream source, with Coniacian-Santonian age coccoliths

(*pers. comm.* J. Young, Natural History Museum) suggesting erosion of the Celtic Shelf by the Irish Sea ice stream (cf. Scourse *et al.*, 2000).

As additional provenance fingerprints we use radiogenic isotopes ($^{143}Nd/^{144}Nd$) and $^{40}Ar/^{39}Ar$ ages of individual hornblende grains. The $^{143}Nd/^{144}Nd$ of the non-carbonate, >150 μm fraction was determined for 16 samples in the intervals associated with H2 and H1. Chemically separated Nd was analysed on a Finnigan MAT 261 mass spectrometer at Toulouse University, normalised and reported as ε_{Nd} following Grousset *et al.* (1998).

Hornblende grains were picked from the >150μm size fraction wherever present. Grains were co-irradiated with hornblende monitor standard Mmhb (age = 525 Myr; Samon and Alexander, 1987) and $^{39}Ar/^{40}Ar$ ratios of individual hornblende grains were determined at the Ar geochronology laboratory at Lamont-Doherty Earth Observatory. Resulting ages have been corrected for mass discrimination, interfering nuclear reactions, procedural blanks and atmospheric Ar contamination (Hemming *et al.*, 1998; Hemming *et al.*, 2000a; Hemming *et al.*, 2000b). The assignment of IRD assemblages to a specific ice sheet provenance is determined from the above suite of proxy-approaches and is discussed in detail in **Chapter 4**.

Upper water column temperature and vertical structure was determined through paired Mg/Ca and oxygen isotope analyses of surface-dwelling *G. bulloides* and subsurface dwelling *N. pachyderma* sin. Samples of 50 specimens where available (not less than 20) were crushed, homogenised and split. Samples for Mg/Ca analysis were cleaned following Barker *et al.* (2003) and analysed on an ICP-AES (Varian Vista) with a precision better than 0.4 % (2σ; liquid standard solution), and sample reproducibility of ≤4 %. Temperature calibration is discussed below (section

3.2). All stable isotope analyses were made using a ThermoFinnigan MAT 252 with an external reproducibility of ≤0.08 ‰ for $\delta^{18}O$ and 0.03 ‰ for $\delta^{13}C$. Benthic isotope measurements were made on 1-4 specimens of *Cibicidoides wuellerstorfi* where possible.

5.3 Results and discussion

5.3.1 Ice sheet instabilities

An almost constant flux of IRD to the core site throughout the period 26.5-17 kyr BP suggests constant readjustment of the BIS marine margins. Within this time, four distinct episodes of ice sheet instability may be inferred from enhanced IRD flux (Fig. 5.3d). The H1 and H2 layers, centred at 24.1 kyr BP and 16.9 kyr BP respectively, stand out in the records due to their high magnetic susceptibility (Fig. 5.3b; Grousset *et al.*, 1993; Wadsworth, 2005) and the presence of distinctive dolomitic carbonate sourced from the Hudson Strait region of the LIS (Fig. 5.3g; Andrews and Tedesco, 1992). Crustal debris derived from the Precambrian shield underlying the LIS is identified by ε_{Nd} values of <-24 (Fig. 5.3a; Snoeckx *et al.*, 1999; Grousset *et al.*, 2000; Grousset *et al.*, 2001). This is corroborated by the Paleoproterozoic age range (1650-1900 Ma) of the Churchill Province which dominates the assemblages of hornblende grains extracted from each of these IRD layers in our core (Fig. 5.3c; H1, 84 % n = 13; H2, 82 % n = 29; Hemming *et al.*, 2000). These are the type H layers *sensu strictu*. At this site they are each only 1-6 cm thick and represent 100-300 years within episodes of IRD deposition exceeding 2000 years (H2) in the NE Atlantic. Given the apparent synchronicity of H layer deposition across the IRD belt (cf. H layer ages compiled by Veiga-Pires and

Hillaire-Marcel, 1999, and Hemming, 2004) instability of the LIS and extensive iceberg discharge from the Hudson Strait lagged the regional increase in IRD deposition in the NE Atlantic by >1 kyr, consistent with the European 'precursor' events of Grousset *et al.* (2000) and Scourse *et al.* (2000). The high resolution records, robust age model and multi-proxy investigation of ice-ocean interaction presented in this study allow more detailed interpretation and accurate dating of these 'precursor' events than previous studies have allowed.

Prior to H2, the first phase of ice sheet activity is marked by enhanced fluxes of EGIIS and BIS sourced IRD (Fig. 5.3e, f) at 26.2 kyr BP, with associated radiogenic ε_{Nd} of -5.6 (just above 'd', Fig. 5.3a) reflecting the strong volcanic contribution. This initial episode of NWEIS instability and IRD deposition occurred 1.9 kyr prior to the first appearance of Hudson Strait sourced debris at 24.25 kyr BP and lasted 400 years. Enhanced deposition of BIS debris recommenced at 25.5 kyr BP and increased steadily for 300 years with little input from the EGIIS. IRD flux then rapidly increased, total IRD exceeding 350×10^3 grains cm^{-2} kyr^{-1} at 25.0 kyr BP. Increased fluxes of both volcanic and BIS debris, together with εNd values of -6.3, suggest bimodal sourcing of IRD from both the BIS and EGIIS in this phase of considerable NWEIS instability lasting 300 years. The timing of this peak in NWEIS instability recorded at MD01-2461 is, within the constraints of the age models, equivalent to that of the relatively radiogenic εNd 'precursor' IRD peak at MD95-2002 in the Bay of Biscay (Grousset *et al.*, 2000), and the Celtic Shelf chalk-rich IRD peak at the Goban Spur (Scourse *et al.*, 2000). Following this episode of substantial IRD deposition, the flux of volcanic debris decreased again while εNd values of -11 to -12, approaching the British Isles end member (Grousset *et al.*,

2001), became dominant for 900 years, until the arrival of LIS-sourced icebergs and H layer deposition. This entire episode of NWEIS instabilities is termed NWE2 (Fig. 5.3).

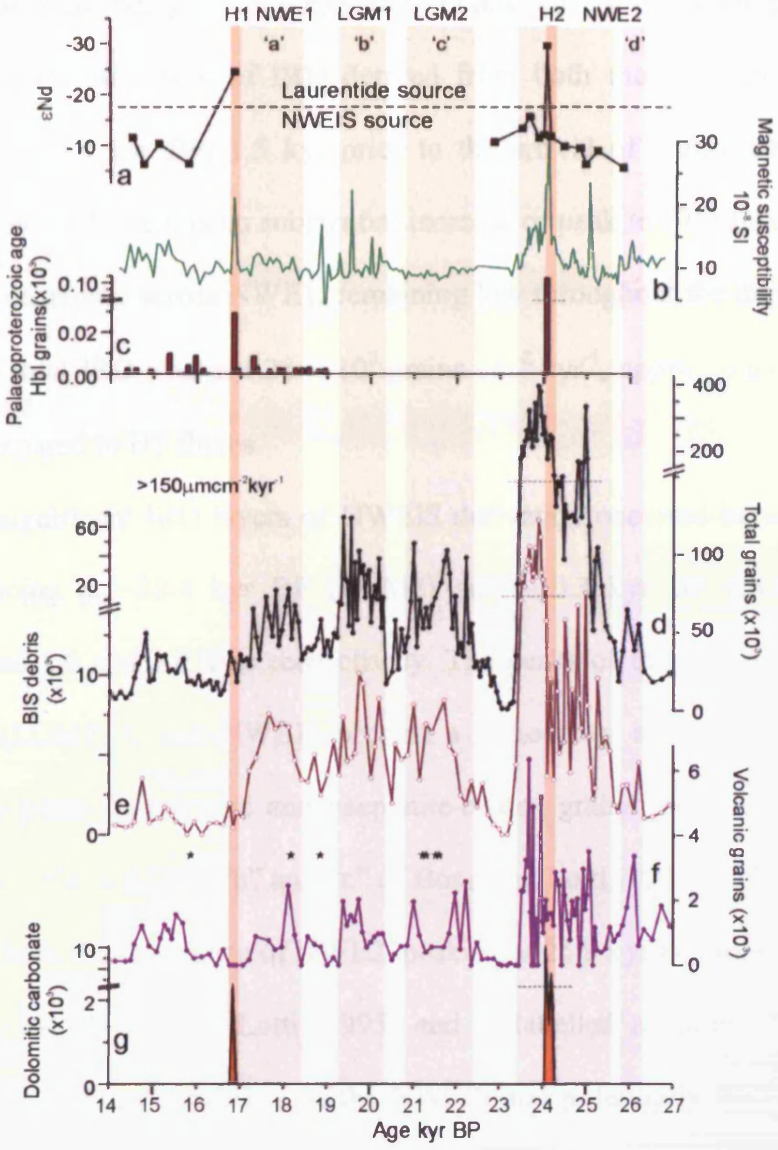

Fig. 5.3. Lithological and geochemical IRD records versus age from core MD01-2461. All measurements except magnetic susceptibility were made on the >150 μm fraction. All IRD counts are normalized to fluxes (grains g^{-1} × dry bulk density (g cm^{-3}) × sedimentation rate (cm kyr^{-1}) = grains cm^{-2} kyr^{-1}). (a) εNd of silicate fraction, (b) whole-core magnetic susceptibility (Wadsworth, 2005), flux of ice rafted (c) hornblende grains with Palaeoproterozoic (1650-1900Ma) $^{40}Ar/^{39}Ar$ ages, (d) total grains, (e) BIS grains, (f) volcanic grains and (g) dolomitic carbonate grains to MD01-2461 (>150 μm cm^{-2} kyr^{-1}). Note break in axes. Stars in (e) denote depths where Upper Cretaceous Chalk is found. Vertical bars highlight dominance of IRD provenance; Brown = BIS is main IRD source, purple = significant contribution from EGIIS, orange = LIS signature is recorded. Acronyms are as follows: H, Heinrich Layer; NWE, NW European ice sheet sourced events (numbers refer to respective H layers). LGM, last glacial maximum. Letters a, b, c and d refer to correlative events of Bond and Lotti (1995).

Similar sequencing of NWEIS IRD deposition is observed prior to H1, NWE1. A significant influx of IRD derived from both the BIS and the EGIIS, commenced at 18.4 kyr BP, 1.5 kyr prior to the arrival of Hudson Strait debris. Dissimilar to NWE2, there is no substantial increase or peak in IRD flux, rather total IRD steadily decreases across NWE1, remaining low throughout the deposition of H layer 1 when total IRD was just 28×10^3 grains cm^{-2} kyr^{-1}, approximately a 10-fold reduction compared to H2 fluxes.

Two significant IRD layers of NWEIS derivation occurred between H1 and H2, commencing at ~22.4 kyr BP (LGM2) and ~20.3 kyr BP (LGM1). These intervals lasted 1.6 and 1.0 kyrs respectively. The peaks of these three most recent IRD events (LGM2, 1 and NWE1) present a periodicity of 1.5-1.6 kyrs, likely correlating to peaks in volcanic and haematite-coated grains recognised within the North Atlantic IRD belt ("a", "b" and "c" of Bond and Lotti, 1995). IRD deposited at our core site from the first phase of NWE2, peaking at 25.9 kyr BP, may relate to "d" at ~23.0 ^{14}C kyr (Bond and Lotti, 1995) and is labelled accordingly (Fig. 5.3), supporting synchronous instability of the NWEIS and potentially the south-eastern extent of the LIS also.

5.3.2 Surface, subsurface and intermediate water conditions associated with ice rafting events

Except for intervals where the $\delta^{18}O$ of *G. bulloides* and *N. pachyderma* sin. are identical around the LGM, *N. pachyderma* sin. consistently displays heavier $\delta^{18}O$ than *G. bulloides* (Fig. 5.4a), reflecting the greater depth and lower temperature habitat of *N. pachyderma* sin. As Hillaire-Marcel and Bilodeau (2000) and Simstich *et al.* (2003) we interpret similar $\delta^{18}O$ values of surface and subsurface species to represent intensive mixing of the upper water column. However, this interpretation requires that each species calcifies in equilibrium with seawater $\delta^{18}O$ and ambient temperature, or that possible disequilibrium calcification is known and corrected for. The carbonate-water temperature equation of Shackleton (1974) is used to determine equilibrium calcite oxygen isotope composition from modern water column data (Fig. 5.5a; World Ocean Atlas, 1998). A factor of -0.27 ‰ is used to convert water on the SMOW scale to calcite on the VPDB (Fig. 5.5b). Assuming an average calcification depth of 30 m for *G. bulloides* (cf. Barker and Elderfield, 2002), $\delta^{18}O_{G.\ bulloides}$ from core top specimens predict a summer (~July) growth season, within water temperatures averaging ~12 °C. This growth season is later than that of April-June predicted by Ganssen and Kroon (2000), who assume *G. bulloides* isotopic temperatures reflect true SST, not the 0-60 m depth range within which the specimens calcified. Similar latitude core top $\delta^{18}O_{G.\ bulloides}$ from the Ganssen and Kroon (2000) data set (Fig. 5.5b) fit our core top values, reinforcing our interpretation of a summer bloom season at an average water depth of 30 m.

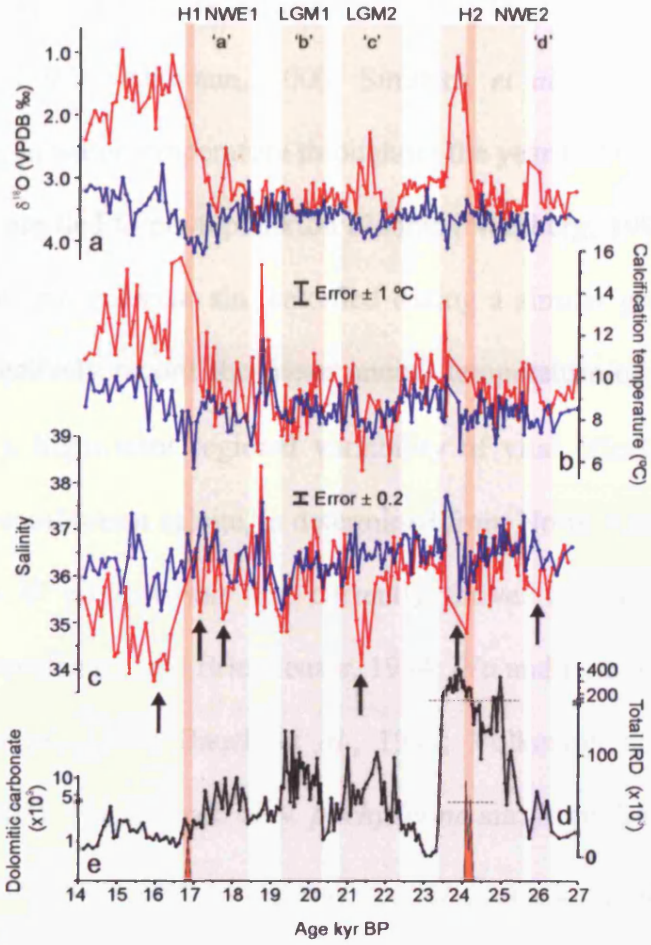

Fig. 5.4. Upper ocean climate records from core MD01-2461.

(a) $\delta^{18}O$ of *G. bulloides* (red, closed circles) and *N. pachyderma* sin. (blue, closed circles). (b) Calcification temperatures (°C) of *G. bulloides* (within upper 60 m of water column; red, closed circles) and *N. pachyderma* (100-200 m water depth; blue, closed circles). (c) SSS (red, closed circles) and subsurface salinity (blue, closed circles) based on *G. bulloides* and *N. pachyderma* sin. respectively. Flux of (d) Total IRD grains (> 150 μm), and (e) dolomitic carbonate grains (>150 μm) per cm^{-2} kyr^{-1} to core MD01-2461. Vertical bars and abbreviations as Fig. 5.3. Meltwater pulses indicated with vertical arrows on (c).

The lower limit of the present day summer thermocline, overlies the average depth of *N. pachyderma* sin. calcification, ~100-200 m (Kohfeld *et al.*, 1996; Carstens *et al.*, 1997; Volkmann, 2000; Simstich *et al.*, 2003), where there is negligible change in water temperature throughout the year (<0.6 °C). As fluxes in *N. pachyderma* sin. are tied to phytoplankton blooms (Nürnberg, 1995), it is likely that the majority of *N. pachyderma* sin. calcified during a similar growth season to *G. bulloides* yet effectively record the mean annual temperature of subsurface waters (Nürnberg, 1995). Significant regional variability of vital effect, offsetting $\delta^{18}O_{N.\ pachyderma\ \mathrm{sin.}}$ from equilibrium calcite, is determined from North Atlantic-Arctic Ocean core tops where *N. pachyderma* sin. currently thrive. Offsets range between 0 (Durazzi, 1981; Spielhagen and Erlenkeuser, 1994; Wu and Hillaire-Marcel, 1994) to -1‰ (Kohfeld *et al.*, 1996; Bauch *et al.*, 1997; Volkmann and Mensch, 2001; Simstich *et al*, 2003). The absence of *N. pachyderma* sin. from the top 1m of MD01-2461 precludes attempts to determine possible $\delta^{18}O_{N.\ pachyderma\ \mathrm{sin.}}$ disequilibria, yet it would appear that any offset at this site would certainly be <1 ‰, potentially zero (Durazzi, 1981). From these considerations we assume that both planktonic species calcified in, or close to, isotopic equilibrium (cf. Hillaire-Marcel and Bilodeau, 2000).

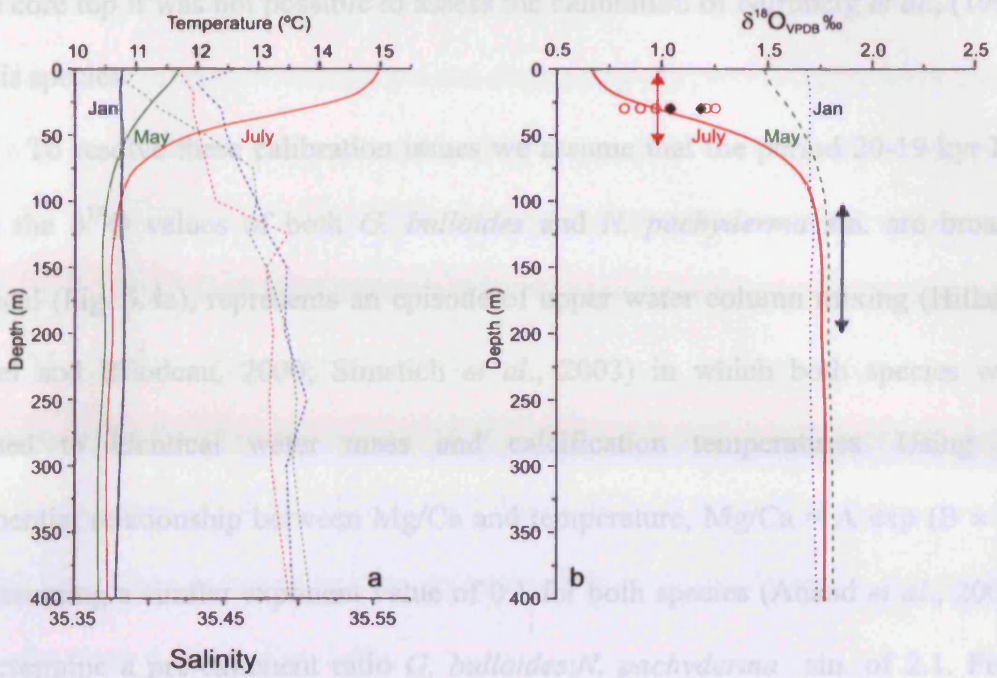

Fig. 5.5. Modern seawater temperature, salinity, and computed equilibrium $\delta^{18}O_{calcite}$ profiles from MD01-2461. (a) Hydrographic data (temperature – solid lines, salinity – dashed lines) for January, May and July (NODC (Levitus) World Atlas 1998). (b) computed equilibrium $\delta^{18}O_{calcite}$ following Shackleton (1974). Double-headed arrows locate average calcification depth of *G. bulloides* (red) and *N. pachyderma* sin. (blue). Core top $\delta^{18}O_{G.\ bulloides}$ (red, open circles from MD01-2461; black diamonds from box cores 88-06 and 88-07 at 51.4°N and 50.5°N; Ganssen and Kroon, 2000).

Mg/Ca of foraminifers is proven to be an effective palaeo-temperature proxy (Elderfield and Ganssen, 2000), but established calibrations for *G. bulloides* are not based on temperatures lower than ~10 °C. Applying the Mg/Ca-temperature calibration of Mashiotta *et al.* (1999) to core top *G. bulloides* Mg/Ca, we derive summer SSTs 2 °C in excess of modern SST (13.7 °C; World Ocean Atlas, 1998) and LGM SSTs of 10-11 °C, exceeding previous estimates for this region by up to 7 °C (e.g. Maslin *et al.*, 1995). These discrepancies suggest that the calibration of Mashiotta *et al.* (1999) is unsuitable at our core site. As *N. pachyderma* sin. is absent

in the core top it was not possible to assess the calibration of Nürnberg *et al.*, (1996) for this species.

To resolve these calibration issues we assume that the period 20-19 kyr BP, when the $\delta^{18}O$ values of both *G. bulloides* and *N. pachyderma* sin. are broadly identical (Fig. 5.4a), represents an episode of upper water column mixing (Hillaire-Marcel and Bilodeau, 2000; Simstich *et al.*, 2003) in which both species were exposed to identical water mass and calcification temperatures. Using the exponential relationship between Mg/Ca and temperature, Mg/Ca = A exp (B × T), and assuming a similar exponent value of 0.1 for both species (Anand *et al.*, 2003), we determine a pre-exponent ratio *G. bulloides*:*N. pachyderma* sin. of 2.1. From modern SST (30 m) and core top Mg/Ca values we derive a pre-exponent of 0.68 for *G. bulloides* and, by virtue of the pre-exponent ratio of 2.1, 0.32 for *N. pachyderma* sin., assuming a fixed pre-exponent ratio across the glacial-interglacial transition. This calibration compares well with that of Barker and Elderfield (2002; Mg/Ca = $0.72 \times e^{0.1T}$) for *G. bulloides* at 60° N in the North Atlantic. The *N. pachyderma* sin. Mg/Ca–temperature calibration effectively equates to the generic calibration of Anand *et al.* (2003; Mg/Ca = $0.38 \times e^{0.09T}$), with variability in estimated calcification temperature that may arise from these different calibrations being <1 °C at Mg/Ca = 0.78 mmol mol^{-1}, the average Mg/Ca composition of MD01-2461 *N. pachyderma* sin. Our calibration overestimates calcification temperatures by 2-3 °C compared to the T-Mg/Ca *N. pachyderma* sin. calibration of Nürnberg *et al.* (1996; Mg/Ca = $0.47 \times e^{0.08T}$) using laboratory cultures and Norwegian Sea core top samples. However, early-Holocene (9.6-8.6 kyr BP) *N. pachyderma* sin. calcification temperatures derived from our calibration average 10.3 °C (unpublished data) and compare well

with modern temperatures at a water depth of 150 m (10.6 °C; World Ocean Atlas, 1998)), substantiating our calibration and suggesting regional differences in the T-Mg/Ca *N. pachyderma* sin. relationship (Nürnberg, 1995). We consider combined analytical and calibration uncertainties of Mg/Ca-derived temperature estimates to amount to ± 1°C (Anand *et al.*, 2003).

The resulting temperature record derived from *G. bulloides* Mg/Ca suggests variability of SST within the range 6-16 °C (Fig. 5.4b), with a SST increase during the early deglacial of ~4 °C. Glacial SST trends derived from *G. bulloides* broadly parallel subsurface temperatures, as determined from *N. pachyderma* sin. Mg/Ca, within the range 6-12 °C (Fig. 5.4b).

Amplitudes of the temperature anomalies of the two species do not directly mirror the magnitude of coeval excursions in the paired $\delta^{18}O$ records of both species, that on occasion display an anti-phased trend between *G. bulloides* and *N. pachyderma* sin. $\delta^{18}O$ (Fig. 5.4a). This pattern alludes to changes not only in temperature, but seawater oxygen isotope (δ_w) composition and salinity, with implications for upper ocean water mass stratification. Calcification temperatures, based on Mg/Ca ratios, were used to subtract the temperature component from planktonic $\delta^{18}O$, allowing determination of δ_w following the oxygen isotope paleotemperature equation of Shackleton (1974). $\delta^{18}O$ values were corrected for global ice volume following Shackleton (2000). Assuming that the freshwater endmember $\delta^{18}O$ was similar to today, salinity was then determined following the modern North Atlantic δ_w-Salinity relationship, $\delta_w = S \times 0.61 - 21.3$ (Craig and Gordon, 1965), enabling estimates of density (σ_t) to be made using the International Equation of State of Seawater (UNESCO, 1980). Incorporating the errors associated

with the analytical precision for Mg/Ca and $\delta^{18}O$, temperature calibration uncertainties and assuming an error of estimate for salinity on δ_w of 0.08 that is derived from the North Atlantic surface δ_w-Salinity relation suggests an uncertainty envelope on density in the range 0.6-0.7 σ_t units. Total error on salinity estimates in the order of ± 0.2.

Overlapping density values at the two depth habitats (~30 m for *G. bulloides* and ~150 m for *N. pachyderma* sin.) suggest a well-mixed upper water column at this site for most of the late glacial (Fig. 5.6b). Elevated $\delta^{13}C_{benthic}$ (>1.5 ‰; Fig. 5.6c) during much of this time also suggest rapid ventilation of the mid-depth waters during the late glacial from a nearby source in the open North Atlantic (Oppo and Lehman, 1993; Zahn *et al.*, 1997). Following H1, SST averages ~4 °C warmer than average LGM temperatures, while a persistent offset of >1 ‰ is displayed between $\delta^{18}O_{G.\ bulloides}$ and $\delta^{18}O_{N.\ pachyderma\ sin.}$ and a ~0.7 ‰ reduction in $\delta^{13}C_{benthic}$. This data pattern indicates enhanced surface stratification and concomitant convection slowdown at this site in the course of enhanced meltwater shedding during deglaciation.

Periodic negative excursions in sea surface salinity (SSS) of up to 2.6 suggest recurrent melt water surges, with fluxes maximising following the major phases of NWEIS instability at NWE2, H2, LGM2 and 1, and NWE1 and finally at H1 (Fig. 5.4c). The LGM1 salinity reduction peaking at 19.2 kyr BP coincides with the 19-kyr meltwater pulse, supporting the contention (Clark *et al.*, 2004) that rapid sea level rise of 10-15m at this time in part originated within the North Atlantic.

These meltwater incursions frequently stratify the upper water column, inferred by divergent surface and subsurface water densities (Fig. 5.6b). $\delta^{13}C_{benthic}$

depletion by up to 1.2‰ during these episodes suggest reduced intermediate water ventilation, likely reflecting northwards penetration of Antarctic Intermediate Water (AAIW; Zahn *et al.*, 1997; Rickaby and Elderfield, 2005) (Fig. 5.6c). Several lowered $\delta^{13}C_{benthic}$ data points associated with each NWEIS melt water event reinforce the contention that reduced bottom water ventilation at our site, independent of LIS meltwater forcing, is a real feature of these events. Furthermore, each episode of melt water release, surface stratification and apparent AMOC reduction appears to have had a cumulative effect on the ^{14}C-marine reservoir age at MD01-2461 as each successive event is coincident with a further increase in marine reservoir age (Fig. 5.6). A temporary reversal in this trend is observed at 19.6 kyr BP, following a period of vigorous AMOC and upper water column mixing at the core site which went some way to 'resetting' the reservoir ages before meltwater associated with NWE1 and H1 caused reservoir ages to increase yet again.

While reduced $\delta^{13}C_{benthic}$ is a well documented feature of H events in the North Atlantic (e.g. Vidal *et al.*, 1997; Zahn *et al.*, 1997; Elliot *et al.*, 2002), reduced bottom water ventilation presented here, associated exclusively with NWEIS instability and melt water forcing highlights the significant effect that the smaller circum-North Atlantic ice sheets may have had on AMOC.

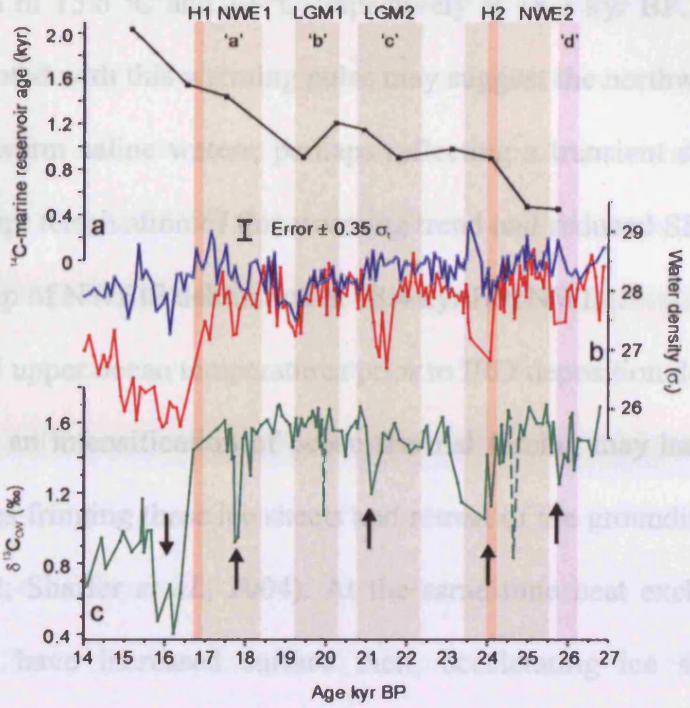

Fig. 5.6. Upper ocean density profile, intermediate water ventilation and ^{14}C-marine reservoir age proxy records from core MD01-2461. (a) ^{14}C-marine reservoir age (as Fig. 5.2a), (b) Density (sigma-t) for surface (*G. bulloides*; red) and subsurface (*N. pachyderma* sin.; blue) waters. Error bars indicate region of uncertainty in density calculation. (c) δ^{13}C of the benthic foraminifera *Cibicidoides wuellerstorfi*. Vertical bars and abbreviations the same as Fig. 5.3. Reduced surface density and upper water stratification (b) and associated reductions in δ^{13}C (c) indicated with vertical arrows. Dotted lines in (c) highlight one-point peaks that are potential 'outliers'.

5.3.3 Ice Sheet Processes in Response to Ocean-Climate Forcing

The records of surface and subsurface temperature display fine-scale variability, with salient anomalies that coincide with major IRD events. A notable warm pulse is recorded between 19.0-18.6 kyr BP in both surface and subsurface temperatures. A warming pulse at this time, possibly initiating NWEIS instability, has been noted at several core sites west of the British Isles (Knutz *et al.*, 2002; Lagerklint and Wright, 1999). At MD02-2461 this warming occurs over 400 years and amounts to an increase of ~8 °C for SST and ~5 °C for subsurface temperatures,

reaching maxima of 15.6 °C and 12 °C respectively at 18.7 kyr BP. An increase in SSS of ~3 associated with this warming pulse may suggest the northward penetration of low latitude, warm saline waters, perhaps reflecting a transient strengthening of the AMOC. Abrupt termination of this warming trend and reduced SSS is associated with initial step-up of NWEIS debris flux at 18.4 kyr BP, NWE1.

Increased upper ocean temperatures prior to IRD deposition derived from the NWEIS suggests an intensification of ocean thermal forcing may have led to basal melt of ice shelves fringing these ice sheets and retreat of the grounding line (Rignot and Jacobs, 2002; Shaffer *et al.*, 2004). At the same time heat exchange with the atmosphere may have increased surface melt, accelerating ice shelf break up (MacAyeal *et al.*, 2003) and ice stream flow (Zwally *et al.*, 2002). Increased ice accumulation on the BIS, caused by increased precipitation from a warmed atmosphere, possibly increased the interior ice sheet mass and thereby reduced stability further (Oppenheimer, 1998). Close coupling of ocean-climate and BIS stability is envisaged. It is suggested that BIS instability initiating NWE2, recorded by moderate BIS-IRD deposition, may have resulted from ice shelf break-up due to surface-subsurface warming above a critical threshold (cf. Vaughan and Doake, 1996; Rignot and Jacobs 2002; MacAyeal *et al.*, 2003). Within the 300 year duration of this phase, sufficient ice shelf was melted back to reduce any buttressing effect, triggering fast flow of tributary ice streams (De Angelis and Skvarca, 2003) producing the large and abrupt increase in IRD deposition during the peak of the NWE2 event at 25.0 kyr BP. Accelerated ice stream activity appears to have lasted for ~300 years, during which IRD deposition remained high and sufficient fresh water was released to stabilise the upper water column and reduce intermediate water

ventilation. After this unstable phase, the NWEIS, principally the BIS, appear to have restabilised, reducing IRD delivery and perhaps allowing ice volume to recover. Were collapse of the LIS interpreted to be in response to the same forcing as the NWEIS (cf. Scourse *et al.*, 2000), a response time of almost 2 kyrs in excess of the NWEIS may be implied from our records. As such it may be perceived that the so-called European 'precursor' events were not directly linked to the H events (cf. Grousset *et al.*, 2000), rather a manifestation of differing ice sheet response times to a common forcing, conceivably reflecting the greater mass of the LIS supporting a high thermal inertia and/or time taken for ocean warming to reach ice shelves buttressing the LIS. Limited marine-based BIS margins, and therefore greater ice sheet stability by the time of H1, following the retreat of the Irish Sea ice stream (McCabe and Clark, 1998), may account for the high rise in surface and subsurface temperatures apparently required to initiate BIS instability at NWE1 compared to NWE2.

The major influx of local BIS debris immediately following deposition of H layer 2 includes the shallow benthic foraminifera *Elphidium excavatum forma clavata* which suggests down-slope transportation from a proximal glaciomarine source (Osterman, 1984). Assuming marine margins remained, it seems plausible that increased SSTs, exceeding 10 °C, would have destabilised the BIS margin further, enhancing calving and initiating debris flow down the continental slope. A rise in sea level of 10 to 15 m associated with the collapse of the LIS (Yokoyama *et al.*, 2001; Chappell, 2002) may also have contributed to this destabilisation (Scourse *et al.*, 2000). The near absence of locally derived IRD coincident with or following H1 suggests that the BIS ice margin had retreated sufficiently to be unaffected by a

SST or sea level change associated with LIS collapse, or that exposed sea floor within the Irish Sea limited iceberg entry into the open ocean, glacial runoff freshening surface waters as opposed to ice rafting.

5.3.4 NW European ice sheet instability and AMOC variability

Decreased mid-depth water ventilation prior to the main LIS collapse events at H1 and H2 are noted in $\delta^{13}C_{benthic}$ records throughout the North Atlantic (Vidal *et al.*, 1997; Zahn *et al.*, 1997; Elliot *et al.*, 2002; Rickaby and Elderfield, 2005). Whereas the decline of intermediate-water ventilation is often progressive in these records, beginning up to 2.5 kyrs before full H conditions (H1; Zahn *et al.*, 1997), $\delta^{13}C_{benthic}$ at our site records temporary, 200-400 year, reduction in intermediate-water ventilation, associated with NWEIS instability/meltwater forcing, 1.2-1.8 kyr before full H-event conditions. $\delta^{13}C_{benthic}$ at MD01-2461 then decreases again associated with and following LIS-sourced IRD deposition and further meltwater release, in phase with records of complete AMOC collapse (Rickaby and Elderfield, 2005). Given that advance of AAIW to MD01-2461 was likely in compensation for reduced Glacial North Atlantic Intermediate Water (GNAIW) formation (Rickaby and Elderfield, 2005), far-reaching effects of the NWEIS-sourced meltwater pulses may be implied prior to both H1 and H2. It is envisaged that NWEIS-sourced meltwater extended to the area of GNAIW formation, weakening deep/intermediate water production and reducing AMOC. Had the meltwater pluses produced longer-term stratification of surface waters within this region than is observed at MD01-2461 they may account for the progressive, pre-H event spin-down of AMOC

recorded at more southerly sites (Zahn *et al.*, 1997). Regional comparison of benthic $\delta^{13}C$ records are discussed in detail in **Chapter 7**.

5.4 Summary

We demonstrate the apparent sensitivity and heightened response of the NWEIS to climatic warming with respect to the well grounded, stable LIS during the last glacial period. Despite the comparatively small ice volume of the NWEIS, their positioning with respect to the likely centre of last glacial North Atlantic deep or intermediate water formation appears to have made meltwater released from the NWEIS an effective means of causing basin wide AMOC variability, highlighting the important role of the NWEIS in millennial scale climatic events.

Chapter 6

Millennial-scale surface and subsurface palaeothermometry from the NE Atlantic, 55-8 kyr BP: A multi-proxy approach[1]

ABSTRACT

We present high-resolution records of climatic variability from planktonic foraminiferal Mg/Ca for the period 55-8 kyr BP from NE Atlantic core MD01-2461. The Mg/Ca of polar species *N. pachyderma* sin. (Mg/Ca_{Nps}) is inferred to record 'typical' mean annual subsurface conditions, and displays a strong relationship with the relative abundance of *N. pachyderma* sin. within the planktonic assemblage. Mg/Ca of *G. bulloides* (Mg/Ca_{Gb}) records summer sea surface temperature (SST) and predicts similar values to both the *N. pachyderma* sin. relative abundance and Mg/Ca proxies during episodes of year round mixing of the upper water column as suggested through paired $\delta^{18}O$ records. Enhanced seasonal thermocline during marine isotope stage 3 and meltwater events across the last glacial maximum is documented by divergent trends in surface and subsurface $\delta^{18}O$ and temperature estimates. Contrary to faunal records and Mg/Ca_{Nps}, H events are not the coldest events in summer-SST record, rather Mg/Ca_{Gb} based records presented suggest relatively mild summer surface ocean conditions associated with each of the last five Heinrich events in the NE Atlantic, with warming > 5 °C recorded at H1. This multi-proxy approach to upper ocean temperature reconstruction provides a more comprehensive picture of ocean-climate conditions during the last glacial and highlights area where further work is needed in understanding what it is that individual proxies are recording.

[1] Submitted to *Paleoceanography* as Peck, V.L., Hall, I.R., Zahn, R., Elderfield, H. Millenial-scale surface and subsurface palaeothermometry from the NE Atlantic: A multi-proxy approach

6.1. Introduction

To date, surface-ocean conditions for the glacial North Atlantic are largely based on planktonic foraminiferal diversity counts, with sea surface temperature (SST) calculated from the transfer function technique (TFT, Imbrie and Kipp, 1971), including the modern analogue technique (MAT, Prell, 1985), forming the most comprehensive reconstructions of last glacial maximum (LGM) conditions (CLIMAP project members, 1981; GLAMAP 2000, Pflaumann *et al.*, 2003). With the advent of temperature-sensitive organic biomarkers and trace metal ratios in foraminiferal shells as tools to infer palaeo-SST, a reassessment of the CLIMAP reconstruction of LGM conditions using a multi-proxy approach is now possible (Mix *et al.*, 2001; Kucera *et al.*, 2005). However, while validation of numerical climate models (e.g. Schäfer-Neth and Paul, 2003) relies on accurate palaeo-SST reconstructions, SST-estimates derived from multiple proxy approaches yield differing results (e.g. Nürnberg *et al.*, 2000; Bard, 2001; Kandiano *et al.*, 2004). This highlights the need for a fuller understanding of the parameters and processes that determine the linking of each palaeoproxy with temperature, e.g. habitat depth, growth season and preferred temperature range of the particular organism that serves as the signal carrier. Paired, multi-proxy SST records from the same core site have the potential to better characterise surface ocean conditions, for example seasonal variability of temperature and upper water column stratification (Barker *et al.*, 2005) provided the proxy-temperature relationship is well constrained.

Here we add to palaeoenvironmental reconstructions of the last glacial, presenting high-resolution multi-species foraminiferal Mg/Ca records as a means of determining absolute surface and subsurface temperature records from the NE

Atlantic between 55 and 25 kyr BP. These data extend the 25-8 kyr BP palaeothermometry records for site MD01-2461 reported by Peck *et al.* (2006) allowing upper ocean conditions to be assessed over the interval 55-8 ky BP. We compare these Mg/Ca-derived temperature records with the relative abundance of the polar species *Neogloboquadrina pachyderma* sinistral, representative of the faunal-diversity based technique upon which the majority of North Atlantic SST records are currently based (e.g. Maslin *et al.*, 1995, Madureira *et al.*, 1997, Kandiano and Bauch, 2003). Coupled with records of ice sheet instability, we investigate similarities or dissimilarities between these two proxy approaches during the last glacial.

6.2. Material and methods

Sediment core MD01-2461 was recovered from the north-western flank of the Porcupine Seabight (51° 45' N, 12° 55' W) in a water depth of 1153 m (Fig.6.1). Chronology of MD01-2461 is based on 25 ^{14}C AMS dates and the subsequent fine-tuning of the abundance record of *N. pachyderma* sin. to the GISPII $\delta^{18}O_{ice}$ record (Fig. 6.2a, b). Correlation between the two records is robust over their total length (55-8 kyr BP) to within r = 0.70, increasing to r = 0.84 between 25-8 kyr BP as temporal resolution in the marine record increases across the LGM and the last deglacial (Peck *et al.*, 2006; Peck *et al.* in press).

Fine-scale records of IRD provenance and flux (grains >150 μm cm^{-2} kyr^{-1}) from MD01-2462 (Peck *et al.*, 2006; Peck *et al.* in press) detail the history of growth and variability of the NW European ice sheets (NWEIS, comprising the British, Icelandic and Fennoscandian ice sheets), the east Greenland ice sheet and episodes of

Laurentide ice sheet (LIS) instability known as Heinrich (H) events (Heinrich, 1988; Broecker, 1994).

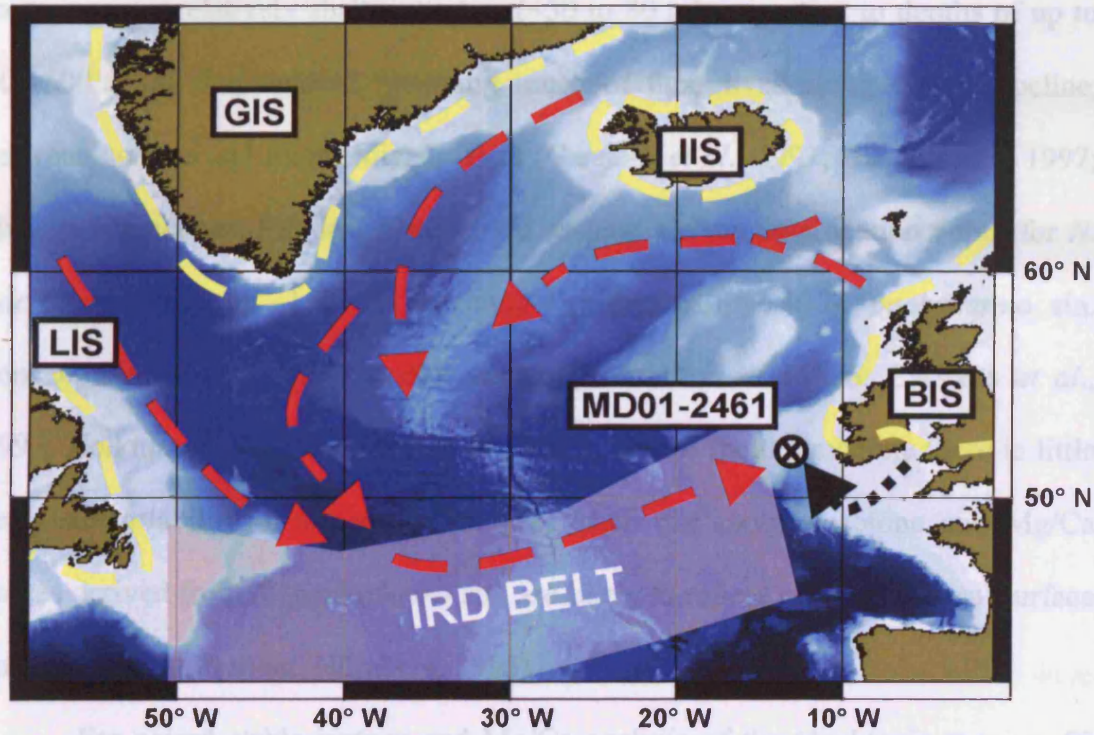

Figure 6.1. Location of core MD01-2461 at the north-eastern extent of the Ruddiman IRD belt. Dashed (red) lines indicate likely routes of icebergs derived from circum-North Atlantic ice sheets due to an anti-clockwise surface gyre during last glacial (following Ruddiman, 1977; Grousset *et al.*, 1993). Yellow dashed lines represent the limits of the last glacial ice sheets. B – British; I – Icelandic; G – Greenland; L – Laurentide. Black dotted line indicates implied outflow from the Irish Sea ice stream.

6.2.1. Trace element and stable isotope analysis

Upper water column temperature, thermocline and halocline structure are determined through paired Mg/Ca and oxygen isotope analysis of surface-dwelling *G. bulloides* and subsurface dwelling *N. pachyderma* sin.

Calcification of *G. bulloides* occurs in the upper 60 m of the water column (e.g. Schiebel *et al.*, 1997); within this paper we assume that Mg/Ca and stable isotope values are representative of a mean calcification depth of 30 m (cf. Barker

and Elderfield, 2002) and a preferred summer growth season centred on July (Hillaire-Marcel and Bilodeau, 2000; Peck *et al.*, 2006).

N. pachyderma sin. inhabit a broader and deeper depth domain. Juvenile forms occupy relatively shallow waters (~50 to 80 m), migrating to depths of up to 500-600 m as they mature, spending much of their lives along the pycnocline, between surface and intermediate waters (Carstens *et al.*, 1997; Bauch *et al.*, 1997; Hillaire-Marcel and Bilodeau, 2000). We assume a mean calcification depth for *N. pachyderma* sin. of ~150 m, reflecting the depth of peak *N. pachyderma* sin. concentrations in modern subpolar waters (Kohfeld *et al.*, 1996; Carstens *et al.*, 1997; Volkmann, 2000; Simstich *et al.*, 2003). Below the thermocline there is little seasonal variability of water temperatures, such that oxygen isotope and Mg/Ca values derived from *N. pachyderma* sin. are likely to reflect mean annual subsurface conditions at ~150 m (cf. Nürnberg, 1995).

For paired stable isotope and Mg/Ca analysis of the planktonic species, 50 individuals were selected wherever possible, with the minimum number of individuals used being 20. *G. bulloides* were selected from the 250-315 μm fraction and *N. pachyderma* sin. from 150-250 μm fraction. These narrow size fractions minimise variability in stable isotope and Mg/Ca measurements that may arise from varying chamber numbers/test size (Spero and Lea, 1996) and restricts the likely habitat depth interval within which the specimens calcified (Kroon and Darling, 1995). Considering that calcite dissolution may significantly alter Mg concentrations in foraminiferal tests (Rosenthal *et al.*, 2000; Rosenthal and Lohmann, 2002), average test weights were monitored along the core section using a high precision top pan balance. Specimens were then crushed between glass slides to break open the

chambers, mixed and then split, homogenising the sample for paired Mg/Ca and stable isotope analyses.

For stable isotope analysis, 50 % of the sample was immersed in 3 % hydrogen peroxide for 30 minutes and ultrasonicated in methanol for 15 seconds before excess liquid and residue was removed and tests dried out at 45°C. All stable isotope analyses were made using a ThermoFinnigan MAT 252 and carbonate preparation device with an external reproducibility of ≤0.08 ‰ for $\delta^{18}O$. All stable isotope values are reported on the VPDB scale, calibrated through the international NBS carbonate standard.

The remaining sample splits for Mg/Ca analysis were cleaned following *Barker et al.* (2003). Samples were diluted in 0.075 mol HNO_3 to a fixed Ca concentration of 100 ppm where possible, with no samples containing less than 40 ppm. Analyses were carried out on a Varian Vista ICP-AES. Intensity ratios were calibrated against elemental ratios following de Villiers *et al.* (2002) to eliminate any Ca matrix effect. Samples containing concentrations of Al above detection level 0.005 ppm (which at Ca concentrations of 80-100 ppm translates to Al/Ca < 0.1 mmol mol^{-1}), indicative of clay contamination, were discarded. Analytical precision determined from replicate runs of a standard solution of Mg/Ca = 5.130 (60 ppm Ca) and Mg/Ca = 1.289 (100 ppm Ca) was ≤0.4 % (2σ). Sample reproducibility is < 4 %.

6.2.2. Faunal counts

The relative abundance of the polar species *N. pachyderma* sin. is commonly used as a palaeo-indicator of polar waters (Bé, 1977; Reynolds and Thunell, 1986; Johannessen *et al*; 1994; Pflaumann *et al.*, 1996; 2003). In waters of summer SST <8 °C, this species dominates the planktonic foraminiferal assemblage (Pflaumann *et al.*, 1996) such that TFT SST estimates are significantly influenced by the relative abundance of *N. pachyderma* sin. within this region during glacial times (Kandiano and Bauch, 2003).

A minimum of 300 planktonic foraminiferal shells were counted from sample splits >150 μm (CLIMAP, 1976, 1984, standard size fraction) to determine *N. pachyderma* sin. %. Reproducibility error is found to be ± 5%.

6.3. Results and discussion

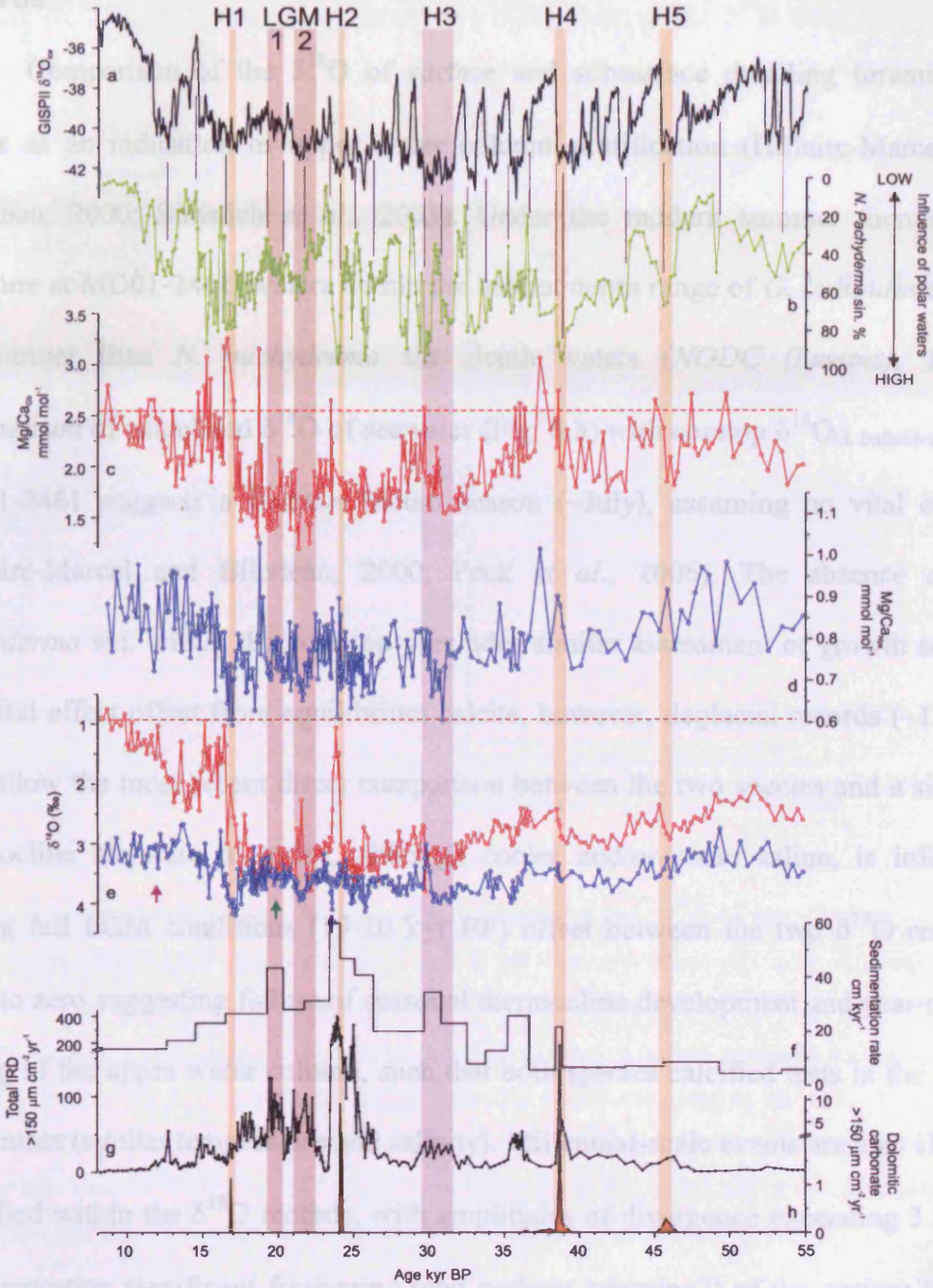

Figure 6.2. Climate, upper ocean temperatures and ice sheet activity as recorded at MD01-2461. (a). GISPII $\delta^{18}O$ ice core record (High-resolution $\delta^{18}O_{ice}$ record (5-point smoothed) from the Greenland summit GISPII ice core (http://depts.washington.edu /qil/datasets/gisp2_main.html; Grootes and Stuiver, 1997). (b). *N. pachyderma* sin. %, (c). Mg/Ca_{Gb}, Core top Mg/CaGb shown by red dashed line. (d). Mg/Ca_{Nps}, (e). Oxygen isotope records of *G. bulloides* (red) and *N. pachyderma* sin. (blue) (‰ VPDB), (f). sedimentation rate (g). flux of total IRD to the core site, (h). flux of LIS-sourced dolomitic carbonate to the core site (>150 µm cm^{-2} yr^{-1}). Orange bands locate H events H1, H2, H4 and H5. Purple bands locate Icelandic debris of H3. Brown band locates increased BIS debris flux at the LGM.

6.3.1. Coupling surface and subsurface Mg/Ca and oxygen isotope records

Comparison of the $\delta^{18}O$ of surface and subsurface dwelling foraminifera serves as an indication of upper water column stratification (Hillaire-Marcel and Bilodeau, 2000; Simstich *et al.*, 2003). Under the modern summer thermocline structure at MD01-2461, waters within the habitat depth range of *G. bulloides* are ~3 °C warmer than *N. pachyderma* sin. depth waters (*NODC (Levitus), 1998)*. Comparison of calculated $\delta^{18}O$ of seawater (Fig. 6.3) with coretop $\delta^{18}O_{G.\ bulloides}$ from MD01-2461 suggests a summer bloom season (~July), assuming no vital effects (Hillaire-Marcel and Bilodeau, 2000; Peck *et al.*, 2006). The absence of *N. pachyderma* sin. within the core top precludes similar assessment of growth season and vital effect offset from equilibrium calcite, however, deglacial records (~12 kyr BP), allow the most recent direct comparison between the two species and a similar thermocline structure to today, although cooler and/or more saline, is inferred. During full LGM conditions (19-20 kyr BP) offset between the two $\delta^{18}O$ records tends to zero suggesting failure of seasonal thermocline development and year-round mixing of the upper water column, such that both species calcified tests in the same water mass (similar temperature and salinity). Millennial-scale events are also clearly identified within the $\delta^{18}O$ records, with amplitudes of divergence exceeding 3 ‰ at H2, suggesting significant freshening (and perhaps warming?) of the surface layers while subsurface waters become cooler and/or more saline.

On a glacial-interglacial timescale, broad similarities between the paired $\delta^{18}O$ and Mg/Ca records are observed for both *G. bulloides* and *N. pachyderma* sin. However, at the millennial time scale, anomalies within either the $\delta^{18}O$ or Mg/Ca

records are frequently absent or even anti-phased within the paired record (e.g. 22-21 kyr and 16.8 kyr BP), reflecting the salinity component of the $\delta^{18}O$ record.

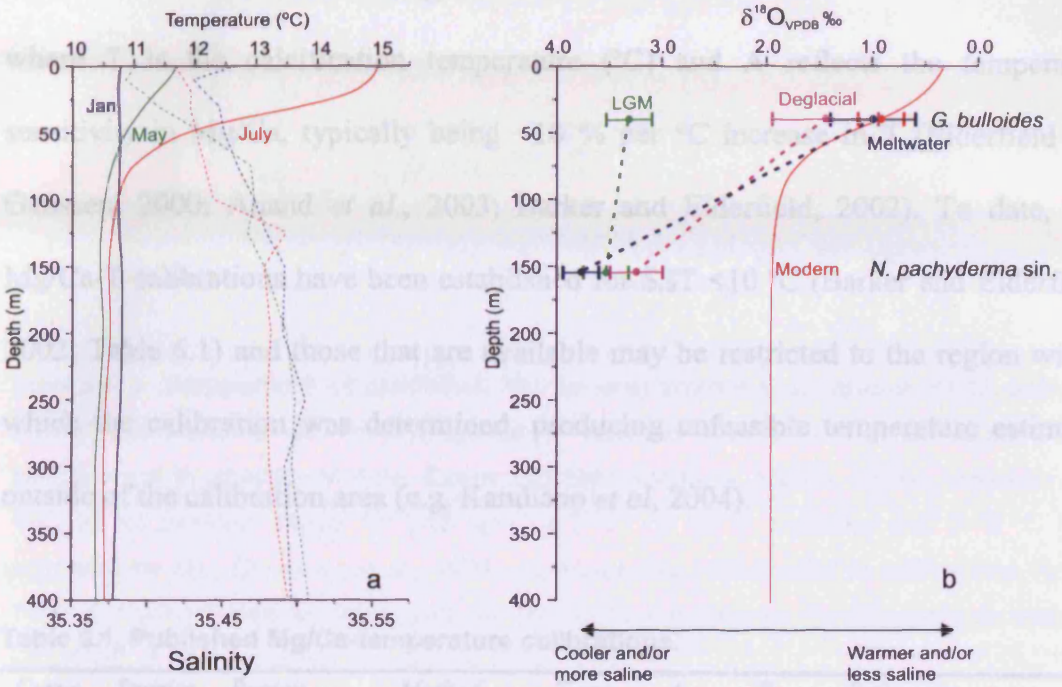

Figure 6.3. Upper water column temperature, salinity and $\delta^{18}O$ of equilibrium calcite at the site of MD01-2461. (a). modern T and S for January, May and July, (b). equilibrium calcite for modern (red); calculated from modern T and S using average conditions over the months of May, June, July. Average ore top $\delta^{18}O_{Gb}$ (red) supports average habitat depth of *G. bulloides* of ~30 m. *N. pachyderma* sin. haboitat depth assumed to be ~150 m. Deglacial conditions (purple) represented by average $\delta^{18}O$ of both *G. bulloides* and *N. pachyderma* sin. across the interval 13-10 kyr BP, LGM conditions from 20-19 kyr BP and meltwater event example from H2, 24 kyr BP. Selected time intervals are highlighted on Fig. 6.2e.

6.3.2. Mg/Ca-temperature calibration and shortfalls

Published Mg/Ca-temperature calibrations for both *G. bulloides* and *N. pachyderma* sin. are presented in Fig. 6.4 and Table 1, all taking the form

$$Mg/Ca = Be^{(AT)}$$

where T is the calcification temperature (°C) and A reflects the temperature sensitivity in Mg/Ca, typically being ~10 % per °C increase in T (Elderfield and Ganssen, 2000; Anand *et al.*, 2003; Barker and Elderfield, 2002). To date, few Mg/Ca-T calibrations have been established for SST <10 °C (Barker and Elderfield, 2002; Table 6.1) and those that are available may be restricted to the region within which the calibration was determined, producing unfeasible temperature estimates outside of the calibration area (e.g. Kandiano *et al*, 2004).

Table 6.1. Published Mg/Ca-temperature calibrations.

Curve	*Species*	*Region*	*Method*	*Temp range*	*A*	*B*	*Reference*
1	Gb	North Atlantic	Core top		0.1	0.72	Barker and Elderfield, 2002
2	Gb	North Atlantic	Core top		0.1	0.68	Peck et al., 2006
3	Gb	North Atlantic	Core top	8-22	0.081	0.81	Elderfield and Ganssen, 2000
4	Gb	Santa Barbara Basin	Core top	10-16	0.9	0.69	Pak et al., 2004
5	Gb		Culture	16-25	0.104	0.51	Lea et al., 1999
6	Gb	Southern Ocean	Core top and culture	10-25	0.108	0.47	Mashiotta et al., 1999
A	Nps	Norwegian Sea	Core top and culture	1-13	0.088	0.46	Nürnberg et al., 1996 (From Barker et al., 2005)
B	Nps	South Atlantic	Core top	-1-15	0.083	0.406	Nürnberg et al., 1996
C	Mixed	North Atlantic	Sediment trap	13-28	0.09	0.38	Anand et al., 2003
D	Nps	North Atlantic	See text		0.10	0.32	Peck et al., 2006

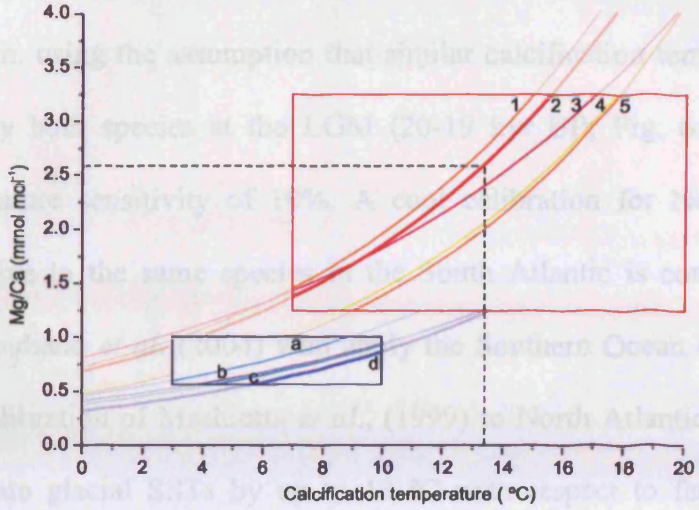

Figure 6.4. Comparison of published Mg/Ca-temperature calibrations for *G. bulloides* and *N. pachyderma* sin. Calibrations for *G. bulloides* in shades of yellow to pink; for *N. pachyderma* in shades of blue. Boxes highlight range of Mg/Ca values measured and 'optimal temperature range' for both species (7-22 °C for *G. bulloides* and 3-10 °C for *N. pachyderma* sin.; *Duplessy et al.*, 1991). Numbers and letters refer to calibrations listed in Table 1. Dashed lines represent core top Mg/CaGb and average modern water temperature at a depth of 30 m between May-July at MD01-2461.

For *G. bulloides* exponential values, A, vary within the range 0.081-0.104 such that the slope of the calibration curves, determining the amplitude of temperature anomalies, vary by up to 23 %. For *N. pachyderma* sin. variability of Mg/Ca-temperature sensitivity between calibrations is ~17 %. In turn the pre-exponent value, B, which largely determines the absolute temperature estimates accounts for the majority of variability between the calibrations, ~ 3 °C for *G. bulloides* (calibrations 1 and 5) and < 3 °C for *N. pachyderma* sin. (calibrations a and d; Fig. 6.4).

The calibrations selected in this study (Peck *et al.*, 2006) fall at the cooler and warmer extremes of the calibration spectra for *G. bulloides* and *N. pachyderma* sin. respectively (Fig. 6.5). They were determined via core top calibration of *G. bulloides*

assuming Mg/Ca-temperature sensitivity of 10 % (Peck *et al.*, 2006) and for *N. pachyderma* sin. using the assumption that similar calcification temperatures would be recorded by both species at the LGM (20-19 kyr BP; Fig. 6.3) and again, a Mg/Ca-temperature sensitivity of 10%. A cool calibration for North Atlantic *G. bulloides* relative to the same species in the South Atlantic is consistent with the findings of Kandiano *et al.* (2004) who apply the Southern Ocean core top-derived temperature calibration of Mashiotta *et al.*, (1999) to North Atlantic Mg/Ca records and overestimate glacial SSTs by up to 13 °C with respect to faunal based SST estimates (SST_{faunal}). Additionally, cooler temperature-calibrations likely reflect the fact that in this study core top samples are calibrated to temperatures at 30 m water depth, not SST *sensu stricto*. Support for the *G. bulloides* Mg/Ca-temperature calibration presented in *Peck et al.* (2006) is the marginally cooler calibration (-0.57 °C offset) of Barker and Elderfield (2002) derived from a North Atlantic core top at ~60° N, reinforcing the suggestion that significantly different Mg/Ca-temperature relationships exist between North and South Atlantic *G. bulloides*.

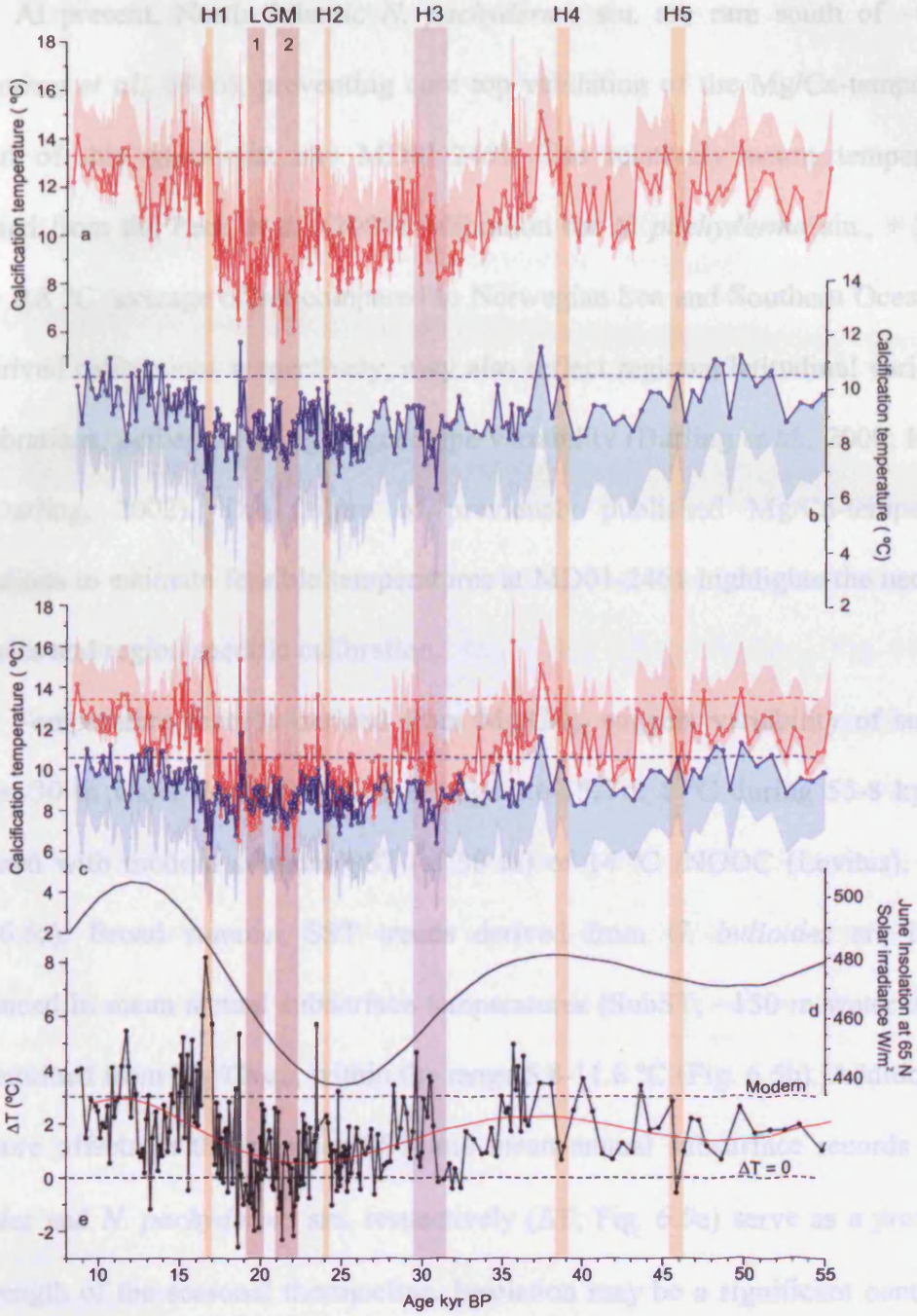

Figure 6.5. The range of calcification temperatures of *G. bulloides* and *N. pachyderma* sin. derived from published Mg/Ca-temperature calibrations. (a) Summer SST inferred from Mg/Ca_{Gb}. Red, open circles, Peck *et al.* (2006); High temperatre limit, Pak *et al.* (2004); Low temperature limit, Barker and Elderfield (2002). Modern summer SST shown by red dashed line, (b) Mean annual SubST inferred from Mg/Ca_{Nps}. Blue, open circles, Peck et *al.* (2006); Low temperature limit, Barker *et al.* (2005), (c) a and b on same temperature scale. Modern summer SST and mean annual SubST shown by red and blue dashed lines respectively, (d) June solar insolation at 65° N, (e). ΔT (SST-SubST; °C). A 6th order polynomial fit is shown in red. Modern ΔT and ΔT=0 shown with dash lines.

At present, North Atlantic *N. pachyderma* sin. are rare south of ~60° N (Pflaumann *et al.*, 1996), preventing core top validation of the Mg/Ca-temperature relation of this species at site MD01-2461. The relatively warm temperatures predicted from the Peck *et al.* (2006) calibration for *N. pachyderma* sin., + 2.9 °C and + 0.8 °C average offset compared to Norwegian Sea and Southern Ocean core top-derived calibrations respectively, may also reflect regional/latitudinal variability in calibrations, perhaps relating to genotype variability (Darling *et al.*, 2000; Kucera and Darling, 2002). The failure of previously published Mg/Ca-temperature calibrations to estimate feasible temperatures at MD01-2461 highlights the necessity of species and region specific calibration.

Temperature records derived from Mg/Ca_{Gb} suggest variability of summer SST (at 30 m water depth) within the range 5.6-15.7 ± 1 °C during 55-8 kyr BP, compared with modern summer SST (at 30 m) of 14 °C (NODC (Levitus), 1998) (Fig. 6.5a). Broad summer SST trends derived from *G. bulloides* are largely reproduced in mean annual subsurface temperatures (SubST; ~150 m water depth), as determined from Mg/Ca_{Nps}, within the range 5.8-11.8 °C (Fig. 6.5b). Additionally, downcore offsets in the summer SST and mean annual subsurface records of *G. bulloides* and *N. pachyderma* sin. respectively (ΔT; Fig. 6.5e) serve as a proxy for the strength of the seasonal thermocline. Insolation may be a significant control on the strength of the seasonal thermocline, as suggested by the broad-scale correlation between ΔT and insolation at 65° N (Fig. 6.2d). However, before detailed discussion of last glacial surface ocean conditions, surface and subsurface Mg/Ca records are compared with faunal records from MD01-2461.

6.3.3. Mg/Ca and faunal diversity records

N. pachyderma sin. % varies between 0 to 97 % through 55-8 kyr BP (Fig. 6.2b). Following Pflaumann *et al.* (1996) we would expect *N. pachyderma* sin. % to display a strong, negative correlation with summer SST derived from Mg/Ca_{Gb}. Using the *N. pachyderma* sin. %-summer SST calibration presented in Elliot *et al.* (1998), absolute values of last glacial to deglacial summer SSTs derived from the *N. pachyderma* sin. % record are comparable to those of TFT and MAT records from nearby core M23414 (Kandiano *et al.*, 2004) and the range of summer SST derived from Mg/Ca_{Gb} (5-14 °C); however, high amplitude, high frequency variability of the *N. pachyderma* sin. %-SST record often distinguishes it from Mg/Ca_{Gb} (Fig. 6.6a, b).

In general, closer correlation is in fact observed between the *N. pachyderma* sin. % and Mg/CaNps records. Rescaling of the *N. pachyderma* sin. %-temperature calibration (SubST = 11 - 0.048 × *N. pachyderma* sin. %) to subsurface temperatures illustrates co-variance of these two proxies, particularly during the period 29-8 kyr BP (Fig. 6.6c), suggesting that *N. pachyderma* sin. % is more representative of mean annual conditions (cf. Morey *et al.*, 2005), rather than summer SST (Pflaumann *et al.*, 1996) in this case.

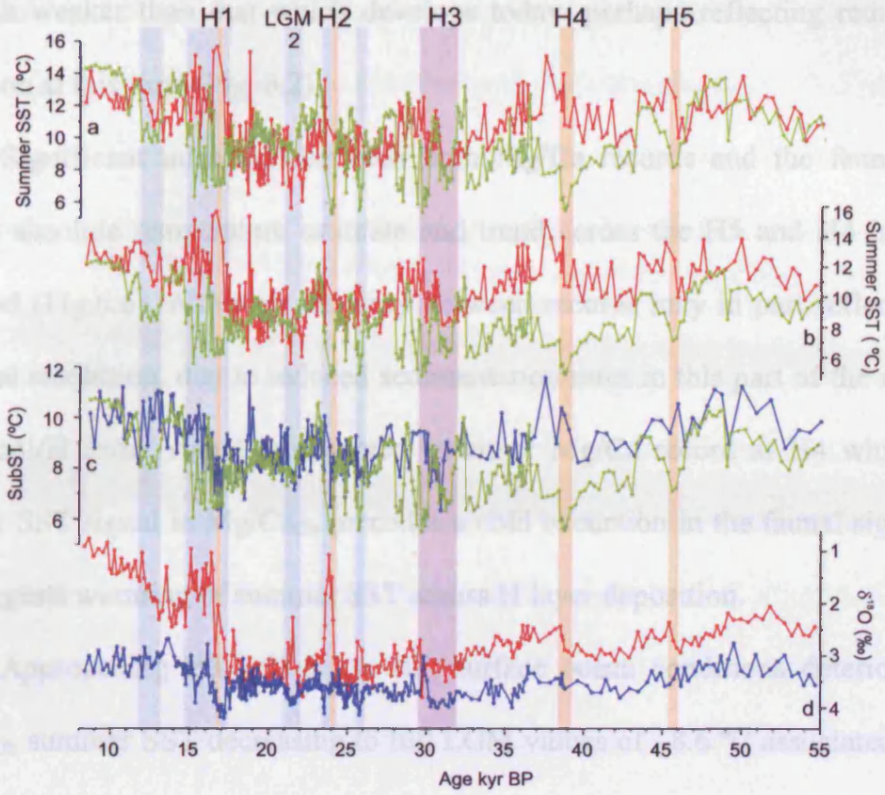

Figure 6.6. Comparison of surface and subsurface Mg/Ca-temperatures records with *N. pachyderma* sin. %-derived temperatures. (a). *N. pachyderma* sin. % - summer SST (calibrated following *Pflaumann et al.*, 1996; green) and Mg/Ca_{Gb} - derived Summer SST (red), (b). *N. pachyderma* sin. % temperature record rescaled to water temperatures at ~30 m water depth through linear interpolation of earliest Holocene and LGM (22-21 kyr BP; summer SST = 12.5-0.08 ×*N. pachyderma* sin. % with Mg/Ca_{Gb}-derived summer SST (red), (c). Rescaling of the *N. pachyderma* sin. %-temperature calibration (SubST = 11 - 0.048 × *N. pachyderma* sin. %) with Mg/Ca_{Nps} - derived subsurface temperature (blue). (d). Oxygen isotope records of *G. bulloides* (red) and *N. pachyderma* sin. (blue) (‰ VPDB). Orange bands locate H events H1, H2, H4 and H5.

6.3.4. Upper ocean conditions 55-26.5 kyr BP

Prior to ~35 kyr BP, summer SST inferred from the Mg/Ca_{Gb} record, average 11.7 ± 1.2 °C with a few intervals displaying summer SSTs comparable to today (~14 °C; NODC (Levitus), 1998). Within this period, Mg/Ca_{Gb}-derived temperatures are on average 1.7 °C warmer than Mg/Ca_{Nps}-temperatures, concurrent with an average $\delta^{18}O$ offset of 0.7 ‰, suggesting development of a seasonal thermocline at this site,

although weaker than that which develops today, perhaps reflecting reduced solar insolation at this time (Fig. 6.2).

Significant mismatch between both Mg/Ca records and the faunal record, both in absolute temperature estimate and trend across the H5 and H4 intervals is observed (Fig.6.6). Although disparity between records may in part reflect reduced temporal resolution, due to reduced sedimentation rates in this part of the record, no clear cool/H event signal is observed in either Mg/Ca record at H4 while a cold summer SST signal in Mg/Ca_{Gb} precedes a cold excursion in the faunal signal at H5 and suggests warming of summer SST across H layer deposition.

Approaching H3, ~31.5 kyr BP, surface ocean conditions deteriorate with Mg/Ca_{Gb} summer SST decreasing to full LGM values of ~8.6 °C associated with the apparent breakdown of the seasonal thermocline, noted by ΔT falling to 0 °C.

6.3.5. LGM-deglacial conditions and the British ice sheet

Expansion of the proximal BIS and establishment of extensive marine ice margins is likely to account for a stepwise increase in IRD flux to the core site at 26.5 kyr BP (Fig. 6.2h; Peck *et al.*, 2006) concurrent with extensive northern hemisphere glacial advance (Hemming and Hajdas, 2003). These enhanced glacial conditions are associated with minimal ΔT values, frequently 0 °C (consistent with similar $\delta^{18}O$ values of each species) suggesting mixing of the upper water column persisted into the summer months throughout much of the LGM, with surface and subsurface temperatures fluctuating within the range 6-11 °C for the majority of this period, up until ~17.5 kyr BP.

LGM summer SST estimates predicted by Mg/Ca_{Gb} analysis appear surprisingly high considering the proximity of our core site to the last glacial BIS, apparently at maximum extent at ~22 kyr BP (Bowen *et al.*, 2002). Mean annual atmospheric temperatures of -5 °C today define the climatic limit of ice sheet viability (Vaughan and Doake, 1996), such that the Mg/Ca_{Gb}-derived SSTs at MD01-2461 exceeded that expected for ice sheet growth or even to sustain stability suggesting that climatic conditions were not conducive to BIS stability, implying the possibility of a metastable state for much of the LGM. The almost constant high flux of IRD to the core site throughout the period 26.5-17 kyr BP (Fig. 6.2h) reflects constant readjustment of BIS marine margins, warm surface waters ensuring a constant moisture source and surface ice accumulation, counterbalancing ablation of the marine margin.

The apparent lack of seasonality at this time reflects minimal insolation and likely accounts for the generally good correlation between the three proxies, particularly Mg/Ca_{Nps} and *N. pachyderma* sin. % throughout the LGM.

Following the Younger Dryas (12 kyr BP) summer SST (Mg/Ca_{Gb}) is comparable to modern (core top) values. *N. pachyderma* sin. % tends to zero as temperatures exceed the optimal temperature range of this species (>10 °C; Duplessy *et al.*, 1991) and this proxy is saturated. Assuming that the youngest $\delta^{18}O$ and Mg/Ca_{Nps} values, ~8 kyr BP, are not affected by environmental stress, seasonal stratification comparable to today is suggested as insolation increases and ΔT approaches modern values (3 °C).

6.3.6. Millennial scale events; maybe H events were not so cold

Increased IRD fluxes and *N. pachyderma* sin. dominance (>75 %) of the planktonic assemblage documents the presence of polar waters at MD01-2461 during each of the H events (Fig. 6.2b). However, unlike the faunal record presented here and the majority of sub-polar North Atlantic SST records, predominantly based on faunal assemblages (e.g. Bond *et al.*, 1992, 1993; Maslin *et al.*, 1995; Madureira *et al.*, 1997; Kandiano and Bauch, 2003), H events are not the coldest events within the Mg/Ca_{Gb} summer SST record. Minima in Mg/Ca_{Nps} are clearly associated with H 3, 2 and 1, consistent with the faunal record (Fig. 6.6), yet Mg/Ca_{Gb} maintains ambient or even elevated values, particularly at H1. Anti-phasing of the Mg/Ca_{Gb} and *N. pachyderma* sin. % and Mg/Ca_{Nps} records is contradictory, the latter proxies suggesting reduced mean annual temperatures while Mg/Ca_{Gb} suggests ambient, even warmer summers. Furthermore, given that the apparent calcification temperature of *G. bulloides* is well within the optimal temperature range of this species during H1, the low abundance of *G. bulloides* coincident with the exceptionally warm summer SST derived from Mg/Ca_{Gb} is a paradox. Why are two SST proxies reconstructing very different conditions?

6.3.7. Robustness of Mg/Ca_{Gb} signal

Initially, we assess the potential of warm Mg/Ca_{Gb} H event signals being an artefact of sediment mixing. Discrete dolomitic carbonate horizons and high sedimentation rates (>25 cm kyr^{-1}) of H layers 1 and 2 are consistent with IRD-rich layers acting as a temporary barrier to bioturbation (Manighetti *et al.*, 1995). Moreover, Mg/Ca values of *G. bulloides* coincident with H layer 1 are substantially higher than those of specimens within the overlying sediment, and oppose

suggestions that 'warm' *G. bulloides* were mixed down from overlying post-H event sediments. Additionally, chronologically ordered ^{14}C-AMS dates across the last 40 kyrs suggest there was minimal mixing of foraminifera at these times.

Laboratory cultures have found that salinity changes of ambient seawater influences foraminiferal Mg concentrations, yet in comparison to temperature change this effect is negligible and meltwater overprinting would cause an underestimation of the Mg/Ca-derived temperature (Nürnberg *et al.*, 1996; Lea *et al.*, 1999), not the elevated temperatures we observe, particularly during H1. Similarly, dissolution of the tests could not have accounted for these anomalous temperatures (Rosenthal *et al.*, 2000). Firstly, all tests were intact, displaying no visual evidence of dissolution and shell weights remain stable throughout the record (variability of ~12 % between 45-10 kyr BP), increasing in the glacial suggesting preservation was good (*Barker and Elderfield*, 2002), and secondly, dissolution reduces Mg/Ca, underestimating calcification temperature. Discarding any samples with traceable Al (> 5 ppb in samples where Ca is > 80 ppm) eliminated the possibility of clay contamination elevating the Mg/Ca ratio (Barker *et al.*, 2003). Finally, a Mg/Ca_{Gb} from a nearby site (M23414), although at lower temporal resolution (multi-centennial time scale) also appears to record elevated summer SST coincident with H 4, 3 and 2, anti-phased with faunal records. We therefore conclude that our interpretation of warm summer SSTs is robust and reflect actual SSTs during H events.

6.3.8. Artificial seasonality and anomalous years

If mismatch of proxy-records prior to H3 may be accounted for by enhanced seasonality, could a similar scenario be applied to the meltwater events? Summer

SST <8 °C implied by *N. pachyderma* sin. dominance of the planktonic assemblage (>75 %) and increased fluxes of IRD reflecting increased iceberg density at the sea surface, suggest unfavourable conditions for surface-dwelling *G. bulloides* during the H events. While these surface ocean conditions were likely representative of the majority of years within a given sample interval, accounting for the dominance of polar species *N. pachyderma* sin. within the planktonic assemblage, summer SST >10 °C recorded by *G. bulloides* Mg/Ca, may represent a small percentage of mild summers, perhaps even exceptionally warm in the case of H1. Additionally, meltwater events have the potential to enhance seasonality of the upper water column through development of strong, shallow halocline, allowing thermocline development during the summer months. Furthermore, increasing insolation at H1 may account for the substantially warmer summer SST at this event. The high-resolution Mg/Ca_{Gb}-SST record provided by our core may have recorded brief 'snapshots' of reduced-ice or ice-free summers, when surface waters were able to warm during the summer months with no loss of latent heat.

Similar meltwater stratification of the upper water column is evident between 21.6-21.0 kyr BP, coincident with LGM2 (Fig. 6.4c, d). Unlike stratification at H1 however, there is not notable warming of the summer SSTs during this interval. Rather, *N. pachyderma* sin. % (<60 %) suggest ambient glacial SSTs, while Mg/Ca_{Gb} records some of the coldest summer SSTs of the entire record. Occasional negative ΔT values, of up to -2 °C (Fig. 6.2e), suggest inversion of the thermocline coincident with enhanced IRD flux and insolation minima, perhaps similar to the cold halocline layer of the Arctic Ocean (Björk *et al.*, 2002). Persistently cold SSTs associated with BIS ice calving at this time is consistent with glacier advance during extreme LGM

cooling (Bowen *et al.*, 2002). Comparison of Mg/Ca_{Gb} records during this LGM ice-rafting event with H2 and particularly H1, suggests that ocean-climate conditions may have been very different associated with collapse of the LIS, potentially somewhat improved, i.e. possibly milder during the summer months.

It may be possible that icebergs maintained low SSTs during ice rafting events out of equilibrium with episodes of climatic warming (cf. Lagerklint and Wright, 1999; Moros *et al.*, 2002). Had improved climatic conditions been associated with H events, the persistence of icebergs at the sea surface would have maintained cold SSTs at the site of MD01-2461, again accounting for the dominance of *N. pachyderma* sin. within the planktonic assemblage. Recent alkenone records from the western Mediterranean suggest abrupt warmings were concurrent with H events (H1, H3 and H5) in this region (Martrat *et al.*, 2004) and favour the possibility of climatic warming out of phase with iceberg-moderated SSTs in the central North Atlantic.

Alternatively, transient advections of subtropical surface waters coincident with H events, perhaps driven by the variable strength of a poleward flowing shelf edge current along the European margin (Kenyon, 1987) or zonality of low-latitude forcing winds (McIntyre and Molfino, 1996), may have carried warm surface waters to the site of MD01-2461, depositing *G. bulloides* carrying anomalously warm Mg/Ca signatures, yet not enough specimens to have influenced the planktonic assemblage record.

6.3.9. Implications of mild summers associated with Heinrich events

One mechanistic hypothesis for H event initiation involves climatically-forced catastrophic disintegration of ice shelves fringing the LIS (Hulbe *et al.*, 2004). Recent collapse of the Larsen ice shelves fringing the Antarctica Peninsula

demonstrate the vulnerability of ice shelves to climatic forcing and potential for rapid and wide-ranging distribution of icebergs (e.g. Doake *et al.*, 1998; MacAyeal *et al.*, 2003). Ice shelf expansion along the margin of the LIS is proposed to have occurred during the cold-culmination of a series of increasingly high-amplitude Dansgaard-Oeschger oscillations (Hulbe *et al.*, 2004). Subsequent climatic warming, at least during the summer months, is suggested to have initiated seasonal surface melt of the ice shelf. Repeated flooding and freezing cycles of surface meltwater would have propagated crevasses to the base of the ice shelf, eventually triggering rapid disintegration of the ice shelf and extensive dispersal of debris-laden icebergs (Hulbe *et al*, 1997; MacAyeal *et al.*, 2003; Hulbe *et al.*, 2004).

A principle criticism of the Hulbe model is that, to date, no palaeoclimate records indicate any such warming prior to or coincident with the H events (Alley *et al.*, 2005). The Mg/Ca_{Gb}-SST records presented here provide the first evidence of what may have been the previously 'unobservable short term warm periods' (Alley *et al.*, 2005) or at least evidence that summer conditions not as cold as previously considered.

While the data presented here may support one aspect of the ice shelf proposal hypothesis, further criticism of the Hulbe model focuses on the mismatch of predicted IRD-provenance and that observed with in Labrador Sea sediments (Hemming, 2004; Alley *et al.*, 2005). Like all H event initiation models, this proposal is far from ideal (Hemming, 2004), however, the potential role of a climatically responsive ice shelf is not ruled out. While Alley *et al.* (2005) favour a 'binge-purge'-type model (MacAyeal, 1993; Alley and MacAyeal, 1994), they concede that LIS-fringing ice shelves likely existed at certain times in the life cycle

of the LIS and certainly contributed to ice sheet behaviour. Combining aspects of both models, Hemming (2004) suggests that collapse of an ice shelf buttressing the Hudson Strait ice stream may have triggered massive purging of the LIS. Whatever the ultimate trigger, the occurrence of mild and perhaps even anomalously warm summers coincident with H events, appears to be evident and may be incorporated into future H event-initiation concepts.

6.4. Summary and conclusions

In this study, we suggest that Mg/Ca_{Nps} and *N. pachyderma* sin. % are reliable recorders of 'typical' mean annual conditions. Mg/Ca_{Nps} recording mean annual temperatures at ~150 m water depth, while *N. pachyderma* sin. % appears to record mean annual SST (cf. Morey *et al.*, 2005), rather than summer SST (Pflaumann *et al.*, 1996). Mg/Ca_{Gb} records summer SST. All three proxies predict similar palaeotemperatures during episodes of year-round mixing of the upper water column, yet quite different conditions when orbital parameters (prior to H3) or meltwater stratification promote seasonal variability. High resolution Mg/Ca_{Gb}-SST records appear to have captured evidence for mild summers, even warming, concurrent with H events, heavily documented in faunal assemblage SST records as representing the coldest intervals of the last glacial. Meltwater stratification and thermal isolation of the surface layer may have accommodated warming of surface waters during a few anomalously warm summers. During the majority of years, however, icebergs maintained the cool mean annual temperatures recorded in faunal diversity and subsurface temperatures records provided by Mg/Ca_{Nps}.

Mild summer SSTs during H events may not been recorded previously due to the inability of faunal diversity records to capture short-lived or even intra-annual conditions. The mild temperatures recorded, including exceptionally warm SSTs at H1, may represent just a small percentage of years within a given time interval, the resolution provided by faunal diversity reconstructions prohibiting identification of such anomalous years. Very few Mg/Ca-SST records have yet been produced within the mid-latitude North Atlantic. If confirmed elsewhere, then mild summers, perhaps even enhanced summer warming, as suggested from Mg/Ca_{Gb}-SST records of MD01-2461, may have played a key role in the initiation of H events during the last glacial.

Chapter 7

Progressive reduction in NE Atlantic intermediate water ventilation prior to Heinrich Events; a response to NW European ice sheet instabilities?[1]

ABSTRACT

We present high-resolution benthic $\delta^{13}C$ records from intermediate water depth core site MD01-2461 (1153 m water depth), from the Porcupine Seabight, NE Atlantic, spanning 43 to 8 kyr BP. At an average time-step of 160 ± 56 yr this core provides information on the linkage between records from the Portuguese Margin and high-latitude North Atlantic basin, allowing additional insights into North Atlantic thermohaline circulation (THC) variability during millennial-scale climatic events of the last glacial. Together, these records document both discrete and progressive reductions in Glacial North Atlantic Intermediate Water (GNAIW) formation preceding Heinrich (H) event 1, 2 and 4, recorded through the apparent interchange of glacial northern and southern-sourced intermediate water signatures along the European Margin. Close coupling of NW European ice sheet (NWEIS) instability and GNAIW formation is observed through transient advances of SCW along the European margin concurrent with pulses of ice rafted debris and meltwater release into the NE Atlantic between 27-16 kyr BP when the NWEIS was at maximum extent and proximal to Last Glacial Maximum convection zones in the open North Atlantic. It is such NWEIS instability and meltwater forcing that may have triggered reduced North Atlantic THC prior to collapse of the Laurentide ice sheet at H1 and H2. Precursory reduction in GNAIW formation prior to H4 may also be inferred. However, limited NWEIS ice volume prior to H4 and convection occurring in the Norwegian-Greenland Sea requires that if a meltwater trigger is invoked, as appears to be the case at H1 and H2, the source of meltwater prior to H4 is elsewhere, likely higher latitude ice sheets. Clarification of the sequencing and likely mechanisms of precursory decrease of the North Atlantic THC support theories of H event initiation relating to ice shelf growth during cold periods associated with reduced North Atlantic THC and subsequent ablation through subsurface warming and sea-level rise associated with further reductions in meridional overturning.

[1] Submitted to *Geochemistry, Geophysics, Geosystems* as Peck, V.L., Hall, I.R., Zahn, R., Scourse, J.D. Progressive reduction in NE Atlantic intermediate water ventilation prior to Heinrich Events; a response to NW European ice sheet instabilities?

7.1 Introduction

An increasing number of theories concerning the initiation of periodic collapse of the Laurentide ice sheet (LIS), so-called Heinrich (H) events call for improved understanding of phase relationships within the North Atlantic ice-ocean-climate system. A key unknown and critical component to several H event initiation theories (e.g. Moros *et al.*, 2002; Flückiger *et al.*, 2006) is the phasing of Atlantic Meridional Overturning Circulation (AMOC) perturbation with respect to LIS collapse.

Advance of Southern Component Water (SCW) into the North Atlantic during the last glacial is apparent from extensive mapping of benthic foraminiferal carbon isotopes from North Atlantic core sites, with high nutrient, low $\delta^{13}C$ Antarctic Bottom Water (AABW) bathing the North Atlantic basin at depths >3500 m as far north as the Rockall Trough (e.g. Oppo and Lehman, 1993; Sarnthein *et al.*, 1994, Curry and Oppo, 2005). The glacial mode of North Atlantic thermohaline circulation (THC) was highly sensitive to density contrasts between Glacial North Atlantic Intermediate Water (GNAIW) and SCW, most likely Antarctic Intermediate Water (AAIW) (e.g. Broecker *et al.*, 1990; Weaver *et al.* 2003; Rickaby and Elderfield, 2005). Significantly reduced ventilation of waters bathing intermediate depth North Atlantic sites during episodes of northern hemisphere ice sheet instability, particularly the H events, suggests reduced GNAIW formation, likely due to increased freshwater flux obstructing North Atlantic deep/intermediate water formation (e.g. Cortijo *et al.*, 1997; Vidal *et al.*, 1997; Ganopolski and Rahmstorf, 2001), and invasion of SCW to high northern latitudes (at depths < 2000 m) (Sarnthein *et al.*, 1994; Zahn *et al.*, 1997; Willamowski and Zahn, 2000; Elliot *et al.*,

2002; Rickaby and Elderfield, *2005*). However, this apparently straightforward cause-effect relationship between H event meltwater and intermediate water formation is questioned, with North Atlantic benthic $\delta^{13}C$ records suggesting that weakening of the North Atlantic THC may have begun up to 2.5 kyr prior to LIS instability (Zahn *et al.,* 1997; Willamowski and Zahn, 2000). Furthermore, recent investigation into AMOC variability using $^{231}Pa_{xs}/^{230}Th_{xs}$ suggest a substantial decrease in the rate of overturning prior to deposition of LIS-sourced ice rafted debris (IRD) (McManus *et al.*, 2004; Hall *et al.,* 2006), possibly driven by NW European ice sheet (NWEIS) sourced meltwater (Hall *et al.*, 2006). Flückiger *et al.* (2006) suggest that subsurface warming and relative sea level rise likely resulted from reduced AMOC prior to the H events, ablating and destabilising northern hemisphere ice sheet margins and initiating ice sheet collapse. Conversely, *Moros et al.* (2002) suggest that enhanced subsurface heat flux driven by a strengthened AMOC may have melted ice shelves and forced the retreat of grounding lines. These divergent theories require further investigation into the records of AMOC variability and phasing with ice sheet-surface ocean conditions.

We present benthic $\delta^{13}C$ records from sediment core MD01-2461 from the Porcupine Seabight, an intermediary for pre-existing NE Atlantic records, concentrated on the Iberian margin (Zahn *et al.*, 1997) and Rockall Trough-Irminger Sea (van Kreveld *et al.,* 2000; Elliot *et al.*, 2002; Knutz *et al*, 2002; Hall *et al.,* 2006; Rickaby and Elderfield, 2005). Combined with previously published records of ice sheet instability and surface ocean conditions from MD01-2461 (Peck *et al.,* 2006), we investigate at multi-centennial to millennial time steps the distribution of

intermediate waters along the European Margin to determine sequencing of North Atlantic ice sheet vs. THC events.

7.2 Materials and methods

Sediment core MD01-2461 was recovered from a seismically laminated sequence on the NW flank of the Porcupine Seabight (51° 45' N, 12° 55' W) at a water depth of 1153 m (Fig. 7.1b). The Porcupine Seabight represents N-S trending embayment in the continental shelf SW of Ireland, gradually deepening to the south, to ~3000 m water depth and opening onto the Porcupine Abyssal Plain. Thermohaline convection in the Labrador Sea and Norwegian-Greenland Sea drives present day circulation, through the formation of intermediate level Labrador Sea Water (LSW) and deeper North Atlantic Deep water (NADW). The latter water mass comprises three components that enter the North Atlantic Basin through the Wyville-Thomson, Iceland-Faeroe and Greenland-Iceland ridges (McCartney and Talley, 1984) to mix with the overlying LSW and re-circulate over the Porcupine Abyssal Plain (van Aken, 2000). This southward penetration of deepwater masses is compensated for by the northward flow of warm, saline surface waters to the Norwegian Sea via the North Atlantic Drift (NAD) and Eastern North Atlantic Waters (ENAW). Today, a pole-ward flow occurs at all depth levels along the eastern slope of the Porcupine Seabight (Rüggeberg *et al.,* 2005), however, the morphology of the Porcupine Seabight prevents direct throughflow of waters below ~ 500 m water depth where currents are topographically steered in a cyclonic direction (Frank *et al.,* 2004). ENAW overlies and mixes with Mediterranean Outflow Water (MOW), which currently bathes the site of MD01-2461 and is

characterised by a salinity maximum and oxygen minimum at a depth of 1000-1200 m (Frank *et al.*, 2004).

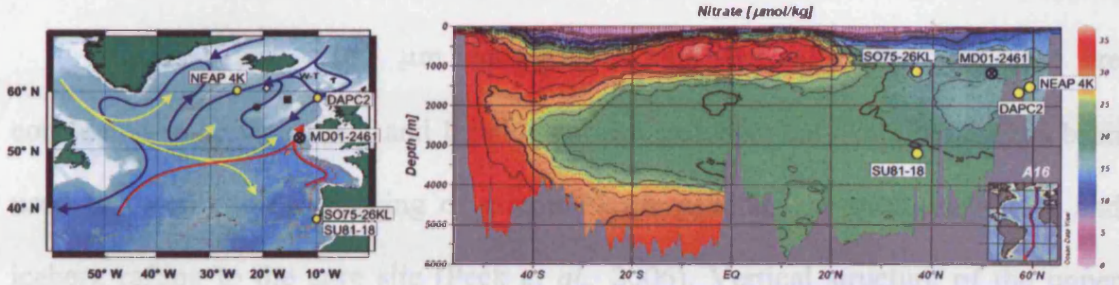

Fig. 7.1. Positioning of core sites discussed in this study and modern circulation scheme. (a). Locations of cores discussed in this study and the modern North Atlantic circulation scheme. Blue arrows illustrate the pathways of the NADW across the Wyville-Thomson Ridge (W-T) and recirculation in the eastern North Atlantic basin at ~ 2000-3000 m water depth. Yellow arrows represent LSW at 1500-2000 m. The dashed orange shows the path of MOW at ~ 1000 m depth, and red arrows show surface North Atlantic Current and ENAW (to depths of ~750 m). GEOSECS Station 23 (black, open diamond); V28-73 (black, filled circle) and VM29-198 (black, filled square) both from Oppo and Lehman (1993). Figure adapted from Frank *et al.* (2004). (b). eWOCE meridional section A16 showing modern day nitrate concentrations, with nutrient-rich AAIW clearly expressed at intermediate depth reaching as far north as ~20 °N. Nutrient depleted NADW fills the basin and flows south at depth. Cores discussed in this study are plotted on this meridional section to show their relation to modern day hydrography.

The 20.2 m core recovered olive-grey silty-clay sediments with frequent drop stones. Visual and x-radiograph evidence present no evidence of core disturbance or turbidite sequences within the interval studied. Geochronology of MD01-2461 is based on 25 monospecific foraminifera (*Globigerina bulloides* or *Neogloboquadrina pachyderma* sinistral) AMS ^{14}C dates and fine-tuning of the relative abundance of *Neogloboquadrina pachyderma* sinistral within the planktonic assemblage (*N.*

pachyderma sin. %) with the GISPII $\delta^{18}O$ record (*Peck et al.,* submitted). The GISPII-tuned age model (r^2 = 0.83, 27-8 kyr BP) suggests significantly enhanced ^{14}C-marine reservoir ages, exceeding 2 kyr during the deglacial (Peck *et al.,* 2006) (Fig. 7.2a). Sedimentation rates range between 12 and 60 cm kyr^{-1}.

Lithic grains >150 μm embedded within the silty clay sediment are considered to be ice rafted, and lithological and geochemical examination has been used to determine the phasing of circum-North Atlantic ice sheet instability and iceberg rafting to the core site (Peck *et al.,* 2006). Vertical structure of the upper water column is inferred from $\delta^{18}O$ records of surface and subsurface dwelling planktonic foraminifera *Globigerina bulloides* and *Neogloboquadrina pachyderma* sinistral, calcifying at an average depth of 30 m and 150 m respectively (see Peck *et al.,* 2006). Benthic, epifaunal species *Cidicidoides wuellerstorfi* accurately records the $\delta^{13}C$ of dissolved inorganic carbon in ambient bottom water at the core location as demonstrated by youngest $\delta^{13}C$ values from MD01-2461 of +1.1 ‰ VPDB that compares well with recent values derived from nearby core sites at similar water depths (1.07 ‰ VPDB at V29-198, 1139 m water depth; 1.17 ‰ VPDB at V28-73, 2063 m water depth) (Oppo and Lehman, 1993) and closely correlates with $\delta^{13}C$ of ambient water total CO_2 of +1.0 to +1.1 ‰ VPDB (between 1000-2000 m water depth, GEOSECS station 23; Fig. 7.1a). Between 1 and 4 specimens of *C. wuellerstorfi* were selected from the >250 μm size fraction wherever present, providing an average time-step of 160 ± 56 kyrs for benthic isotope records. Stable isotope analyses were made using a ThermoFinnigan MAT 252 with an external reproducibility of ≤0.08 ‰ for $\delta^{18}O$ and 0.03 ‰ for $\delta^{13}C$.

Whole ocean $\delta^{13}C$ changes (e.g. Curry *et al.*, 1988; Duplessy *et al.*, 1985; Duplessy *et al.*, 1988) will have affected the epibenthic $\delta^{13}C$ records from the different core sites used in this study equally and therefore are not considered an obstacle in our documentation of regional $\delta^{13}C$ gradients. Correction of our record for changes of the global ocean carbon reservoir demand robust constraints on mean ocean $\delta^{13}C$ variations that occurred during the last 40 kyr at high temporal resolution, which are currently unavailable.

7.3 Results and discussion

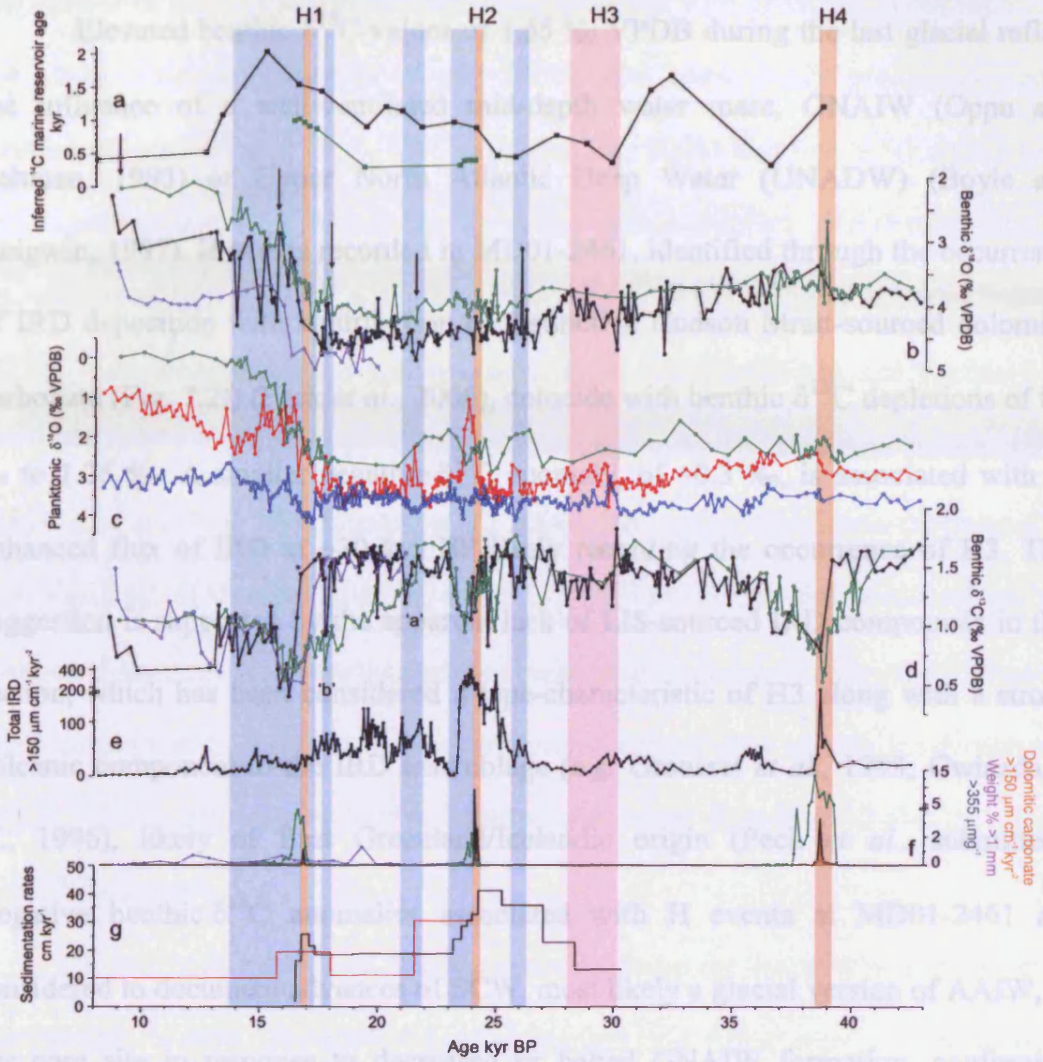

Fig. 7.2. Benthic stable isotope and IRD stacks from MD01-2461 and SO75-26KL and surface and subsurface oxygen isotopes from MD01-2461. Benthic and planktonic stable isotope and IRD stacks from MD01-2461, SO75-26KL and NEAP4K. Unless otherwise stated records from MD01-2461 are black, closed circles; SO75-26KL, green, open circles and NEAP4K purple, open circles. (a) Inferred ^{14}C marine reservoir ages for MD01-2461 (Peck et al., 2006) and SO75-26KL (see text). (b). $\delta^{18}O$ *C. wuellerstorfi*. Vertical arrows indicate tie-points synchronizing the record of SO75-26KL to MD01-2461 (SO75-26KL age model as published prior to 24 kyr BP). (c). $\delta^{18}O$ planktonic. Surface dwelling *G. bulloides* (MD01-2461, red; SO75-26KL, green) and subsurface dwelling *N. pachyderma* sin. from MD01-2461 (blue). (d). $\delta^{13}C$ *C. wuellerstorfi*, (e). Flux of total IRD at MD01-2461 (grains >150 µm cm^{-2} kyr^{-1}), (f). Flux of dolomtic carbonate at MD01-2461 (orange); concentration of total IRD at SO75-26KL (>355 µm g^{-1}); weight % >1 mm at NEAP4K, (g). Radiocarbon (black) and tuned (red) sedimentation rates. Blue vertical bars highlight episodes of surface ocean stratification. Orange vertical bars highlight H layers 4, 2 and 1, with H3 located by the purple bar.

7.3.1 Benthic $\delta^{13}C$ records from MD01-2461

Elevated benthic $\delta^{13}C$ values of 1.65 ‰ VPDB during the last glacial reflect the influence of a well-ventilated mid-depth water mass, GNAIW (Oppo and Lehman, 1993) or Upper North Atlantic Deep Water (UNADW) (Boyle and Keigwin, 1987). H events recorded in MD01-2461, identified through the occurrence of IRD deposition with contribution of distinctive Hudson Strait-sourced dolomitic carbonate (Fig. 7.2f) (Peck *et al.*, 2006), coincide with benthic $\delta^{13}C$ depletions of 0.6 ‰ to 1.25 ‰. A smaller negative $\delta^{13}C$ anomaly, of ~0.3 ‰, is associated with an enhanced flux of IRD at ~30 kyr BP likely recording the occurrence of H3. This suggestion is supported by the apparent lack of LIS-sourced IRD compounds in this section, which has been considered a type-characteristic of H3 along with a strong volcanic component to the IRD assemblage (e.g. Grousset *et al.*, 1993; Gwiazda *et al.*, 1996), likely of East Greenland/Icelandic origin (Peck *et al.*, submitted). Negative benthic $\delta^{13}C$ anomalies associated with H events at MD01-2461 are considered to document advances of SCW, most likely a glacial version of AAIW, to our core site in response to decreased or halted GNAIW formation, confirming restriction of deep-intermediate convection in the northern North Atlantic in the course of the events (e.g. Cortijo *et al.*, 1997; Vidal *et al.*, 1997; Zahn *et al.*, 1997, Rickaby and Elderfield, 2005).

An additional control on the ventilation of deep-intermediate waters in the North Atlantic during meltwater events might involve a change in the mode of North Atlantic deep water formation, from open-ocean convection under glacial conditions to buoyancy loss due to brine formation in the course of sea-ice formation in the Nordic Seas following meltwater surges (Dokken and Jansen, 1999). Recent studies

have suggested that brine formation proximal to ice margins persisted throughout the last glacial in the northern North Atlantic concurrent with open-ocean convection in the North Atlantic (Labeyrie *et al.,* 2005). The most likely preformed poorly ventilated signal (Vidal *et al.*, 1997; Elliot *et al.*, 2002) and low $\delta^{18}O$ signature of these intermediate brine waters being masked during ambient glacial conditions by the well-ventilated GNAIW and only becoming apparent during episodes of reduced MOC, when simultaneous negative anomalies in both planktonic and benthic $\delta^{18}O$ and benthic $\delta^{13}C$ are observed in North Atlantic records (Dokken and Jansen, 1999; Labeyrie *et al.,* 2005; Waelbroeck *et al.*, 2006). Such an interpretation challenges the interpretation of North Atlantic benthic $\delta^{13}C$ anomalies as documenting the northward penetration of southern sourced waters in response to reduced MOC as the rapid transmission of the North Atlantic-derived brine signal to both the Indian and Pacific Ocean necessitates active intermediate water formation (Labeyrie *et al.*, 2005; Waelbroeck *et al.*, 2006).

At site MD01-2461 we also see some evidence for the injection of low $\delta^{18}O$ intermediate waters, characteristic of formation via brine rejection, notably at meltwater event 'b' (18-17.7 kyr BP) with a well defined decrease of benthic $\delta^{18}O$ by 0.7 ‰ associated with a transient negative benthic $\delta^{13}C$ anomaly. Further benthic $\delta^{18}O$ (brine) anomalies are hinted at during H4, H3 and meltwater events at ~26 kyr BP and 'a' (21.8-20.9 kyr) although these anomalies are much less distinct and appear absent at H2. This lack of a clear brine signal together with the recently reported covariance of $^{231}Pa_{xs}/^{230}Th_{xs}$ and benthic $\delta^{13}C$ records from core DAPC2 (Hall *et al.,* 2006) provides convincing evidence that changes in bottom water ventilation along the northern European margin (inferred from $\delta^{13}C$) relate to

changes in the rate of MOC and the interchange of poorly ventilated southern and well ventilated northern sourced water masses (at least up to ~ 1700 m water depth) rather than the dominant injection of poorly ventilated brine waters from the Nordic Seas (Labeyrie *et al.*, 2005). This interpretation of benthic $\delta^{13}C$ data provides the basis for the following discussion.

While initial benthic $\delta^{13}C$ decreases in MD01-2461 directly coincide with the onset of H layer deposition, peak minima in benthic $\delta^{13}C$ coincide with maximum divergence in $\delta^{18}O$ from surface and sub-surface-dwelling planktonic foraminifers (Fig. 7.2b) that we interpret as indications of meltwater stratification of the upper water column (Peck *et al., 2006*). Benthic $\delta^{13}C$ values fall to their lowest values within the entire record, +0.4 ‰ VPDB, at 16.2 kyr BP, some 0.6-1.1 kyr after the incursion of the detrital carbonate peak indicative of H1 deposition at this site, coincident with offset between $\delta^{18}O$ *G. bulloides* and *N. pachyderma* sin. of > 2.5 ‰ indicating prominent meltwater stratification. Deglacial meltwater forcing is evident from persistent upper ocean stratification through 16.4-14.0 kyr BP, associated with significant sea level rise at this time (Bard *et al.*, 1990; Bard *et al.*, 1996). Benthic $\delta^{13}C$ values do not return to their elevated glacial levels but vary between 0.7-1.2 ‰ VPDB throughout the deglacial, plausibly reflecting a combination of changes involving the terrestrial biosphere and its influence on marine carbon reservoir $\delta^{13}C$ and establishment of the modern mode of North Atlantic THC. A decrease in benthic $\delta^{13}C$ of 0.5 ‰ at 13 kyr BP is captured by two data points only, but potentially reflects a convection slow-down in the North Atlantic during the Younger Dryas cold period (Boyle and Keigwin, 1987; Sarnthein *et al.*, 1994; Rickaby and Elderfield, 2005). In addition to the H events, short-lived negative $\delta^{13}C$ anomalies are observed

at 26-25.7 kyr, 21.8-20.9 kyr ('a') and 18-17.7 kyr ('b') BP, and directly coincide with intermittent meltwater stratification of the upper water column, and enhanced deposition of NWEIS-sourced IRD. Our timings of the two most recent events, 'a' and 'b' support dates of BIS ice sheet retreat determined from cosmogenic nuclide (^{36}Cl) surface-exposure dating of glacial erratic boulders and glacially smoothed bedrock sampled around the former ice margins in Ireland (Bowen *et al.*, 2002). IRD associated with meltwater event 'b' and an IRD peak with a similar NWEIS-signature prior to H2 (at 25.0 kyr BP) likely correspond to the well-documented 'European precursor' events (e.g. Grousset *et al.*, 2000; Scourse *et al.,* 2000). Freshwater surging associated with these episodes of NWEIS instability conceivably reached the area of GNAIW formation and caused transient, 200-500 year, reduction in northern sourced intermediate water flux, allowing brief northwards penetration of SCW to the MD01-2461 site (Peck *et al.,* 2006).

7.3.2 Intermediate water ventilation changes from NE Atlantic records

We compare the benthic $\delta^{13}C$ record of MD01-2461 with similar records of other North Atlantic sites to determine regional variability of intermediate water masses. In particular, we use the high-resolution record from core SO75-26KL from the Portuguese Margin at a water depth of 1099 m, similar to that of MD01-2461 (Zahn *et al.*, 1997). Data records from SO75-26KL have been published on a radiocarbon time scale applying a constant ^{14}C-marine reservoir age correction of 400 years (Zahn *et al.,* 1997; Willamowski and Zahn, 2000). Assessment of multiple ^{14}C data (e.g. Voelker *et al.*, 1998; Waelbroeck *et al.*, 2001), in agreement with age modelling of the MD01-2461 records (Peck *et al.,* 2006), suggest that NE Atlantic

marine ^{14}C reservoir ages were highly variable during the glacial period such that the radiocarbon time scale of SO75-26KL does not allow for a detailed comparison with MD01-2461. To attempt a synchronized time scale for SO75-26KL we graphically correlate the benthic $\delta^{18}O$ records of both cores by "tuning" the record of benthic $\delta^{18}O$ record from SO75-26KL to that of MD01-2461 across the delgaciation (24-8 kyr BP) (Fig. 7.2b). This procedure receives independent support from the observation that an IRD peak at SO75-26KL, on the synchronized timescale, is concurrent with the lithologically and geochemically distinct H layer 1 at MD01-2461, consistent with synchronous deposition of H layers 4 and 2 at the two sites (Fig. 7.2f). Additionally, the onset of deglacial warming/surface ocean freshening in the planktonic $\delta^{18}O$ records is simultaneous at the two sites (Fig. 7.2c). The synchronized timescale of SO75-26KL suggests marine ^{14}C-reservoir ages between 0.4 kyr to 0.9-1.0 kyr in the period 17.3-16.4 kyr BP at this site (Fig. 7.2a). A latitudinal gradient of reservoir ages during the deglaciation from ~1 kyr at 37° N (SO75-26KL) up to ~2 kyr at 52° N (MD01-2461) (Peck *et al.*, 2006) is comparable with the findings of Waelbroeck *et al.* (2001).

The lower resolution benthic $\delta^{13}C$ record from core NEAP 4K at Björn Drift (1627 m water depth; Fig. 7.1) (Rickaby and Elderfield, 2005) is used as reference for comparison with mid-depth ventilation changes in the high-latitude North Atlantic. The age model of NEAP 4K (> 13 kyr BP) is based on stratigraphical correlation (benthic and planktonic $\delta^{18}O$) with core BOFS 5K (*Barker et al.*, 2004), which has a radiocarbon-based age model incorporating the elevated marine reservoir ages of Waelbroeck *et al.* (2001; 1.9 kyr) for this time period. Temporal resolution at this site averages 500 years and does not allow for a detailed correlation

of the benthic $\delta^{18}O$ record with that of MD01-2461. A broad peak in weight % of the >1 mm size fraction, spanning ~20-9 kyr BP is of little use for correlation to the IRD events at the European Margin sites. Therefore, we have no firm control on the timing of isotope patterns along the benthic isotope records of NEAP 4K in relation to MD01-2461 and SO75-26KL and will use the record for a qualitative assessment of regional gradients only.

Table 7.1. Details of cores discussed in this study.

Core	Location	Water depth	Reference
NEAP-4K	Björn Drift 61° 29' N 24° 10' W	1627 m	Rickaby and Elderfield, (2005)
DAPC2	Rockall Trough 58° 58' N 09° 37' W	1709 m	Knutz et al., (2002)
SO75-26KL	Iberian Margin 37° 49' N 20° 30' W	1099 m	Zahn et al., (1997)
SU81-18	Iberian Margin 37° 46' N 10° 11' W	3135 m	Gherardi et al., (2005)

During the last glacial, an eastern branch of GNAIW was advected along the European Margin towards the Portuguese Margin, while northwards flowing SCW (likely AAIW) penetrated as far north as the Moroccan Margin as is indicated in paired benthic $\delta^{13}C$-Cd/Ca profiles (Fig. 7.1a) (Willamowski and Zahn, 2000). GNAIW therefore, maintained the well-ventilated ambient bottom water conditions ($\delta^{13}C$ >1.4 ‰ VPDB) recorded at both MD01-2461 and SO75-26KL during mean glacial conditions. Conversely, the offset, of up to 0.5 ‰, between the MD02-2461 and SO75-26KL benthic $\delta^{18}O$ records over the glacial interval suggests the additional influence of a warmer and / or low-$\delta^{18}O$ glacial mid-depth water mass at the upper Portuguese margin (Zahn *et al.,* 1997).

Similar absolute values of benthic $\delta^{13}C$ are recorded at both SO75-26KL and MD01-2461 associated with and following IRD deposition at H4, 2 and 1. However, decline into these benthic $\delta^{13}C$ anomalies starts considerably earlier at the Portuguese margin and appears more gradual, notably in the periods prior to H4 and H1. That is, mid-depth ventilation appears to deteriorate at the Portuguese margin up to 5 kyr prior to these two H events, and importantly, before the collapse of mid-depth ventilation at the site of MD01-2461. This contrast in mid-depth ventilation plausibly reflects the proximity of the northerly MD01-2461 to the site of mid-depth convection that provided the site with well-ventilated mid-depth waters even though the production of these waters was in decline. If so, the early decrease in benthic $\delta^{13}C$ at the Portuguese margin suggests that the production of mid-depth waters started to deteriorate well before H1 and H4 presumably because of a gradual built-up of meltwater surging before the LIS destabilised and large-scale iceberg calving occurred. The benthic $\delta^{13}C$ proxy close to the centres of convection would not resolve such an early decline in mid-depth convection.

7.3.3 Precursory meltwater forcing from the NWEIS

GNAIW convection in the open North Atlantic at the LGM (Sarnthein *et al.,* 1994; Vidal *et al.,* 1997), proximal to the fully advanced NWEIS, facilitated close coupling of NWEIS meltwater and overturning circulation. Within the H2 to H1 interval, benthic $\delta^{13}C$ at MD01-2461 suggests that bottom waters at this site remained well ventilated by GNAIW until ~16.6 kyr BP, the exception being the apparent transient advance of the GNAIW/SCW hydrographic front north of ~52° N at meltwater events 'a' and 'b'. At SO75-26KL, benthic $\delta^{13}C$ fell steadily over a ~5

kyr period approaching H1, following an abrupt shift by -0.5 ‰ at 21.4 kyr BP. Initiation of this trend of decreasing ventilation at SO75-26KL is coincident with event 'a' at site MD01-2461 when the apparent advance of SCW as displayed in a likewise brief episode of benthic $\delta^{13}C$ depletion centred on 21.2 kyr BP. Based on an IRD assemblage at MD01-2461 dominated by BIS-derived lithologies, this event has been suggested to constitute a reduction in GNAIW formation during an episode of NWEIS instability and associated meltwater surging into the NE Atlantic (Peck *et al.,* 2006). The end of this freshwater surge allowed intermediate water production to resume, reverting benthic $\delta^{13}C$ values at MD01-2461 back to elevated/GNAIW values at 20.9 kyr BP. However, continuing decrease of benthic $\delta^{13}C$ values recorded at SO75-26KL suggest GNAIW production did not fully recover and that North Atlantic THC was progressively weakening prior to the incursion of H1 icebergs and meltwater to the NE Atlantic. As no further meltwater forcing is evident in the planktonic $\delta^{18}O$ records of MD01-2461 until event 'b', at 17.8 kyr BP, convection was plausibly reduced by freshwater forcing at higher latitudes (e.g. Elliot *et al.,* 2002) or further to the west. $^{231}Pa_{xs}/^{230}Th_{xs}$ ratios at DAPC2 (1709 m water depth) in the Rockall Trough, increase towards production values at ~18.0 kyr BP, suggest substantially reduced rates of overturning (Hall *et al.,* 2006) concurrent with event 'b' which may represent either a second transitory advance of SCW or an episode of brine injection to MD01-2461 preceding H1 by ~0.9 kyr. However, Gherardi *et al.* (2005) use $^{231}Pa_{xs}/^{230}Th_{xs}$ records from the Iberian Margin to suggest that 'shallow' overturning in the NE Atlantic basin was vigorous until 16.5 kyr BP. Core SU81-18 used in their study is located at 3135 m water depth, some 2000 m deeper than both MD01-2461 and SO75-26KL. It may be possible that ^{231}Pa export at depths below

cores SO75-26KL, MD01-2461 and DAPC2 is recorded at SU81-18 accounting for these divergent signals, supporting a reduction in shallow overturn ($\leq$1700 m), while deeper convection was perhaps maintained, accounting for the lower $^{231}Pa_{xs}/^{230}Th_{xs}$ values recorded at SU81-18 at this time.

The low-resolution record of NEAP-4K closely follows the structure of the benthic $\delta^{13}C$ record of MD01-2461 and documents elevated $\delta^{13}C$ values around 1.4 ‰ throughout the interval between H2 and H1, suggesting persistent bathing of this site with GNAIW. This pattern confirms our contention of continued production of GNAIW, albeit at lower rates in response to NWEIS instabilities, at 'a' and 'b'.

Benthic $\delta^{13}C$ values of <0.7 ‰ VPDB at all three intermediate water depth sites reflect the prominence SCW between 16.2-15.4 kyr BP, implying large-scale collapse of GNAIW production following H1. Unlike the coupled H layer-benthic $\delta^{13}C$ collapse records of SO75-26KL, NEAP-4K and DAPC2 (Knutz *et al.*, 2002; Hall *et al.*, 2006) significantly reduced ventilation at MD01-2461 is not recorded until several hundred years after H1. Geochemical ($^{40}Ar/^{39}Ar$ dates of individual hornblende grains, Sr-Nd of carbonate-free IRD), magnetic susceptibility and lithological classification (dolomitic carbonate) each suggest that this is the only horizon within the deglacial interval (20-10 kyr BP) of MD01-2461 that contains a notable contribution of LIS-derived debris (Peck *et al.*, 2006). The H1 layer in MD01-2461 spans a few hundred years, whereas deposition at both DAPC2 and SO75-26KL is in the order of 1.0 kyr. While it appears plausible that MD01-12461 may have witnessed the earlier stages of H1 deposition in the NE Atlantic only, perhaps reflecting changing surface current patterns, it remains an issue to explain why benthic $\delta^{13}C$ at MD01-2461 does not decrease until after the H1 layer in this

core. One possible explanation is that the elevated $\delta^{13}C$ value recorded immediately following H1 layer deposition and measured from a single specimen of *C. wuellerstorfi* (asterisk on Fig. 7.2d) is not representative of ambient bottom water ventilation at this time and ventilation reduction at MD01-2461 was effectively simultaneous with H1. Alternatively, taking the benthic $\delta^{13}C$ record at MD01-2461 at face value across H1, the elevated benthic $\delta^{13}C$ levels may reflect a time-transgressive shoaling of reduced ventilation that reached the deeper sites in the north (NEAP-4K, DAPC2) first, before affecting MD01-2461.

At H2, a 'precursory' reduction in benthic $\delta^{13}C$ is observed at SO75-26KL at 25 kyr BP, ~1 kyr prior to H layer deposition, accompanied by a brief anomaly at MD01-2461 at 24.6 kyr BP. The abrupt decrease in benthic $\delta^{13}C$ at SO75-26KL is synchronous with the equally abrupt increase in IRD from the NWEIS at MD01-2461, representing instability of the BIS immediately preceding H2 (Peck *et al.*, submitted). Surface and subsurface planktonic $\delta^{18}O$ display an only minor divergence at this time (up to 0.5 ‰) indicating freshwater forcing at a smaller scale than during the 'a' and 'b' events, but its influence on GNAIW formation appears significant enough to produce the reduction in ventilation observed at SO75-26KL. Mid-depth ventilation recovers abruptly after this event before large-scale ventilation collapse occurs in the course of H2. Minimum ventilation of intermediate waters along the European Margin is seen in the benthic $\delta^{13}C$ record of both SO75-26KL and MD01-2461 that immediately follows the H2 IRD deposition in MD01-2461. Significant destabilisation of the BIS is suggested by a substantial increase in the flux of BIS-derived debris immediately following deposition of H2 at MD01-2461, perhaps triggered by sea level rise of up to 15 m associated with LIS-collapse

(Yokoyama *et al.,* 2001; Chappell, 2002). Consistently the maximum (>2.5 ‰) offset between $\delta^{18}O$ of the *G. bulloides* and *N. pachyderma* sin. which lags H layer deposition by ~300 yr is thought to be derived principally from NWEIS meltwater.

Similarly, to H1, a progressive decrease in benthic $\delta^{13}C$ preceding H4 by ~2 kyr is observed in SO75-26KL, while benthic $\delta^{13}C$ depletion at MD01-2461 occurred abruptly associated with H layer deposition. The short-lived increase in IRD flux associated with H4 plausibly reflects the juvenile state of the BIS at this time (Peck. *et al.*, submitted; **Chapter 4**), a contention that appears to be confirmed by the lack of a coeval freshwater signal in planktonic $\delta^{18}O$ (Fig. 7.2c). The limited extent of the NWEIS, coupled with North Atlantic deep-intermediate water convection likely occurring in a similar location to the contemporary ocean prior to the stage 3-2 boundary (Sarnthein *et al.,* 1994; Vidal *et al.,* 1997) suggest the NWEIS was an unlikely source of meltwater for triggering the reduction in mid-depth ventilation prior to H4. Rather, initial reduction in GNAIW production likely reflects other meltwater sources (van Kreveld *et al.*, 2000; Elliot *et al.*, 2002).

7.3.4 Ice sheet instability in response to North Atlantic THC changes

Several hypotheses attempting to explain the occurrence of H events, incorporating a range of internal and external forcing factors, have been proposed (e.g MacAyeal, 1993; Johnson and Lauritzen, 1995; Marshall and Clarke, 1997; Hunt and Maslin, 1998; Arbic *et al.,* 2004). Recent concepts have used the disintegration of ice shelves fringing the Antarctic Peninsula as a modern analogue for the sudden iceberg releases during H events (Hulbe, 1997; Hulbe *et al.,* 2004) and consider ocean subsurface temperatures, coupled with North Atlantic THC variability, as a

factor that may have destabilized the LIS through their effect on ice shelves and fringing ice margins (e.g. Moros *et al.*, 2002; Shaffer *et al.*, 2004; Flückiger *et al.*, 2006).

The concept of recurrent meltwater release from the NWEIS and surface ocean stratification, promoting transient weakening of the North Atlantic THC and regional cooling particularly appears to apply for the period preceding H1. Such cool conditions may also have promoted the growth of a LIS-fringing ice-shelf, perhaps priming the LIS for H event collapse (Hulbe, 1997; Hemming, 2004; Hulbe *et al.*, 2004). Subsequent subsurface warming and sea level rise (0.3–0.5 m), associated with the THC reduction, may then have played a role in undermining the ice shelf thus removing the buttressing support exerted on the feeder ice streams, leading to large-scale surging of the ice sheet (Flückiger *et al.*, 2006).

7.4 Conclusions

Benthic $\delta^{13}C$ records from NE Atlantic core MD01-2461 document interchange of well-ventilated northern-sourced and poorly-ventilated southern-sourced intermediate waters during the last glacial. Enhanced ventilation at MD01-2461 documented by $\delta^{13}C$ benthic values of >+1.6 ‰ VPDB, compared to early Holocene values of ≤1 ‰ VPDB suggests that well-ventilated GNAIW was bathing this core site, along with sites on the Björn Drift and Portuguese Margin at similar water depths during ambient LGM conditions. Frequent meltwater incursions, associated with instability of the NWEIS, appear coincident with weakened GNAIW formation leading to transient advances of SCW along the European margin. Such a scenario is likely to account for precursory reductions in North Atlantic THC prior to

both H 2 and 1 when NWEIS was at maximum extent and convection was more proximal. Progressive reduction in North Atlantic THC may also be inferred prior to H4, however the limited extent of the NWEIS coupled with the likely location of convection centres at higher latitudes precludes meltwater release from the NWEIS as the trigger.

LIS destabilisation therefore, appears to have consistently occurred following progressive (H1 and H4) or discrete (H2) reductions in the North Atlantic THC. The role that North Atlantic THC variability may have played in H event initiation is still debatable, yet a scenario where climatic cooling in response to surface ocean stratification and reduced North Atlantic THC promoted ice shelf growth, which were subsequently ablated through accompanying subsurface warming, triggering ice sheet collapse is consistent with the data reported here.

Chapter Eight

Summary and future work

8.1 Introduction

High-resolution, multi-proxy analyses from marine sediment core MD01-2461, have provided a detailed record of ice-ocean-climate interaction in the NE Atlantic during the last glacial period, with particular attention having been paid to the involvement of the NWEIS. An array of provenance proxies were applied to IRD records from a sediment core located on the NW European margin, off SW Ireland, providing insight into the activity of the NWEIS, and the Icelandic, Greenland and Laurentide ice sheets during the period 58-8 kyr BP. Sequencing of upper ocean conditions and wide-scale changes in North Atlantic THC with ice sheet instabilities at fine temporal resolution constrain our understanding of the circumstances under which H events occurred and we assess the consistency of the data presented here with recent H event trigger proposals. The principal findings are summarized and discussed below, followed by suggestions for further work.

8.2 Growth, instabilities and decline of the last glacial circum-North Atlantic ice sheets (Chapter 4)

Lithological assemblage, Sr-Nd isotopic compositions and $^{40}Ar/^{39}Ar$ ages of individual hornblende grains were used to identify individual ice sheet growth and

dynamics, and sequencing of instabilities of various circum-North Atlantic ice margins during the last glacial period.

Four episodes of LIS collapse are clearly recorded within this period 55-8 kyr BP, namely H1, H2, H4 and H5. In contrast, prior to ~31.8 kyr BP (~H3) very little IRD derived from the NWEIS can be traced, suggesting a juvenile state with no or very limited actively calving marine margins. Of the NWEIS, the IIS is the first to deliver IRD to MD01-2461, coincident with H3. Glacial advance over NW Europe in the subsequent 5 kyr is noted by the arrival of distinctive BIS-sourced debris from ~27.1 kyr BP. From this time on, through the LGM and the deglacial, constant readjustment of the IIS and BIS margins is documented in the pervasive delivery of NWEIS-sourced IRD, with peaks in NWEIS-IRD flux exhibiting a periodicity of ~2 kyrs. A significant step-down in total IRD flux across H1 reflects major retreat of the BIS, and northern hemisphere deglaciation.

The term 'European Precursor' first arose following discovery of European-sourced IRD deposits in the NE Atlantic prior to H1 and H2 (Grousset *et al.*, 2000; Scourse *et al.*, 2000) and speculation as to the significance of these events ensued; were these events an early climate signal such that the NWEIS was responding faster to the same driving force that destabilised the LIS? Or, did the precursor events some how trigger subsequent collapse of the LIS? Or, were the events merely coincidental? In addressing these questions it is noted firstly that two principal frequencies of North Atlantic ice sheet instabilities are evident in this study; high frequency instability of the BIS (also reported by Knutz *et al.*, 2001), similar to the 1-2 kyr instabilities of the East Greenland (Bond *et al.*, 1999), Icelandic (Elliot *et al.*, 1998) and Fennoscandian (Fronval *et al.*, 1995) ice sheets, in contrast to substantial surging

of the LIS which occurred with a ~7 kyr frequency. The steady pacing of NWEIS instability across the LGM appears unperturbed by collapse of the LIS at H1, suggesting independent oscillations of the smaller NWEIS and the larger LIS may have existed. Secondly, having identified the lack of actively calving NWEIS margins prior to H3, both H5 and H4 ensued without the possibility of a 'European precursor'. It is concluded therefore that 'European precursors' were not a generic part of H events and their expression in the IRD record of NE Atlantic sediment cores likely results from the coincidence of frequency of individual ice sheet instability.

8.3 Involvement of the NWEIS in episodes of abrupt climatic change; NWEIS meltwater stratification and AMOC variability (Chapter 5)

Ambient LGM (26-17.4 kyr BP) conditions at site MD01-2461 are characterised by year-round mixing of the upper water column (at least the upper 150 m) as inferred from the similar $\delta^{18}O$ values recorded in the tests of surface-dwelling *G. bulloides* and subsurface-dwelling *N. pachyderma* sin.. Mixed layer temperatures derived from Mg/Ca analyses average 8.6 °C over this period. Additionally, benthic $\delta^{13}C$ values >1.4 ‰ suggest that the site of MD01-2461 was in the path of a well-ventilated intermediate-depth water mass, most likely originating from the central North Atlantic convection centres of the LGM, i.e. Glacial North Atlantic Intermediate Water. Instability of the NWEIS, indicated by episodes of enhanced ice rafting, is often associated with meltwater release and stratification of the upper water column as indicated by divergent trends in the $\delta^{18}O$ records of the two planktonic species. Associated reductions in benthic $\delta^{13}C$ record decreased

ventilation of intermediate waters. Reduced GNAIW formation within the central north Atlantic at these times is proposed to have resulted from the fresh water forcing from the NWEIS at ~26 kyr, 24 kyr, 21.5 kyr, 17.6 kyr and 17.2 kyr BP.

8.4 Upper ocean climate reconstructions (Chapter 6)

High-resolution summer-SST records derived from $Mg/Ca_{G.\ bulloides}$ appear to have captured evidence for mild, even warm, summer conditions associated with the collapse of the LIS during the last glacial. H layer deposition at MD01-2461 does not coincide with the coldest episodes of the $Mg/Ca_{G.\ bulloides}$-SST record. Contrary to published faunal records and the relative abundance of *N. pachyderma* sin. within the same samples, H events coincide with mild, even elevated (H1), summer SSTs as predicted by $Mg/Ca_{G.\ bulloides}$ suggesting that climatic conditions during H events were perhaps not as extreme as previously evidenced. Mild summers, or even enhanced summer warming, as suggested from Mg/Ca-SST records of MD01-2461, may have played a key role in the initiation of H events during the last glacial, perhaps by climate-induced collapse of fringing ice shelves as proposed by Hulbe *et al.* (2004).

8.5 Mapping wide-scale THC variability along the European margin (Chapter 7)

The relationship between the episodes of NWEIS meltwater forcing recorded at MD01-2461 (and discussed in Chapter 5; Peck *et al.*, 2006) and basin wide North Atlantic thermohaline circulation variability is investigated through regional comparisons of benthic $\delta^{13}C$ records. It is concluded that NWEIS instability was the likely trigger of episodic reductions in GNAIW formation and transient advance of

southern component waters along the European Margin. The effect of NWEIS instability on thermohaline circulation appears to have been greatest at the LGM when the combined effects of maximum NWEIS ice volume and a more proximal site of intermediate water convection likely contributed to significant weakening in GNAIW production over several thousand years prior to H1.

8.6 Millennial scale climate variability

This thesis has focussed on millennial scale climate variability within the North Atlantic region and most observations have been fully accounted for by ice-ocean-climate variability within this region. However, there is increasing appreciation of low latitude and Southern Hemisphere involvement in episodes in abrupt climate change (e.g. McIntyre and Molfino, 1996; Broecker, 1998; Knorr and Lohman 2003; Pahnke and Zahn, 2005) and debate over the ultimate driver behind millennial scale climate variability (e.g. Little *et al*, 1997; Bond *et al.*, 2001; Rahmstorf and Alley, 2002). External, solar forcing would provide the best explanation for the global character of millennial-scale climate change, but changes in solar activity may be considered an ineffective means of climatic forcing with measured variability of solar output over the 11-year sun-spot cycle being just 0.1 % (Frohlich, 2000). However, larger amplitude changes may have been active on longer time-scales (Lean *et al.*, 1995; Beer *et al.*, 2000) and amplifying mechanisms, such as cloud cover (Svensmark and FriisChristensen, 1997) are invoked to account for observations of reduced solar activity (increased ^{10}Be concentrations) during cold episodes in both the Holocene and last glacial (Finkel and Nishiizumi, 1997; Bond *et al.*, 2001). During an unstable climatic period it is likely that small changes in solar

output had a stronger influence as a climatic driver, potentially triggering abrupt climatic changes. Additionally, non-linear response of the climate system to weak solar forcing may relate to stochastic resonance within the climate system (Rahmstorf and Alley, 2002).

Regarding H events however, it is increasingly apparent that internal dynamics of the LIS was the principal factor determining pacing. Direct climatic forcing of the LIS appears a less conceivable means of triggering an H event considering the time frame required for climatic forcing at the ice surface to penetrate to the base (Clarke *et al.*, 1999). Ice loss from the LIS during H events is predicted to be in the order of 5×10^5 km^3 or up to 14 % of the total ice sheet (Hemming, 2004). Recovery of this mass-deficit, particularly in the most active region of the LIS, the Hudson Strait ice stream, likely reflects the low frequency nature of H events relative to the smaller, more dynamic ice sheets in the NE Atlantic. Additionally, glaciological models suggest that attainment of a critical mass of the LIS was a pre-requisite to Hudson Strait surging (Marshall and Clarke, 1997). However, once this threshold mass was attained, the ice sheet became metastable and prone to substantial surging. Additionally, the development of ice shelves fringing the LIS may have enhanced susceptibility to climatic or oceanic forcing. In fact, many H event initiation proposals prescribe this preconditioning of the LIS to ensure susceptibility to trigger mechanisms such as seasonal warming (e.g. MacAyea*l et al.*, 2003; Hulbe *et al.*, 2004) or sea level or tidal forcing (e.g. Arbic *et al.*, 2004). In this scenario it is therefore conceivable that the ultimate trigger may not have been common to each event. That is, provided the LIS was in a ready state, any number of ice-ocean-climate perturbations might have triggered the initial response of the

Hudson Strait ice stream. This idea is consistent with the conclusion that 'European precursors' were not being a generic component to H events (**Chapter 4**) and the lack of evidence within MD01-2461 to suggest a common forcing was associated with the last four major instabilities of the LIS.

For H1, there is certainly some evidence presented in this study for increased seasonality and warm summers, coincident with rising insolation, which may support the scenario of Hulbe *et al.* (2004) where enhanced summer conditions shattered a LIS-fringing ice shelf and lead to ice stream surges. Correlation of MD01-2461 records to the Greenland ice core reveals an episode of apparently increasing solar activity associated with H1 and the warm summer temperatures, reinforcing the proposal of summer warming triggered a collapse of potential ice shelves fringing the LIS, at least the Hudson Strait ice stream during this event.

H2 was the first event to be associated with LGM conditions and sea level forcing related to instability from other circum-North Atlantic ice sheets should not be ruled out in this case, particularly given the low insolation and mild (but not warm) summers associated with this event. For H4 and H5 the temporal resolution provided by this study makes speculation on possible triggers difficult.

In conclusion, no ultimate forcing agent for H event initiation has been uncovered in this study. Rather, evidence presented here contributes to the growing knowledge of the climatic conditions under which H events occurred and it is considered that the final trigger that initiated LIS surges was not necessarily common to each H event.

8.7 Thoughts on further work

Below are issues raised in this study and implications for further studies and ideas of how some of these issues may be addressed in the future

8.7.1 Age models

Determining the true sequencing of ice-ocean-climate interactions from marine, terrestrial and ice-core records requires robust, high-resolution age models. Temporal and spatial variability of ^{14}C marine reservoir ages complicates correlation of radiocarbon-dated marine core records from different sites (e.g. Waelbroeck *et al.*, 2001; **Chapter 7**) and with terrestrial and ice core records (e.g. Voelker *et al.*, 2000). Tuning of SST records with a fixed reference, for example the GISPII or awaited North GRIP $\delta^{18}O_{ice}$ chronologies, allows core-to-core comparisons to be made with confidence, unaffected by localised ^{14}C reservoir effects. However, the underlying assumption that North Atlantic SSTs were in phase with air temperatures over Greenland, and that there were no latitudinal leads or lags in SST variability is unfounded. Additionally, SST to ice core record correlation is subjective, more so if attempts are made at inter-hemispheric comparisons.

8.7.2 IRD provenance

Further multi-proxy IRD provenance studies should be applied to better characterise debris derived from different ice sheets. Particular emphasis placed on distinguishing between Icelandic and East Greenland, East Greenland and Gulf of St. Lawrence sources, perhaps by tracing iceberg pathways back to source coupled with

extensive bedrock characterisation (lithological and geochemical) would be of great benefit to future studies of circum-North Atlantic ice margin dynamics.

8.7.3 Variability of the last glacial BIS.

Several records of IRD accumulation are available along the European Margin, positioned in the path of various NWEIS ice streams/glacial outlets (table 8.1). Accurate correlation of these records and terrestrial records may allow more detailed history of glaciation of the British Isles. Tuning of the *N. pachyderma* sin. %-SST record to the Greenland ice core records would determine a common age-model for each record (see section 8.7.1), independent of the temporally and perhaps spatially (e.g. Waelbroeck *et al.*, 2001) variable ^{14}C marine reservoir age and similar ages for horizons containing Hudson Bay sourced dolomitic carbonate would be expected, constraining these age models.

Table 8.1 Sites along the NW European Margin that may be compared in future studies

Core site	*Location*	*Nearest ice margin*	*Reference*
DAPC2	58° 58' N, 09° 36' W	NW Scotland	Knutz (2000)
MD95-2006	57° 02' N, 10° 03' W	NW Scotland	Knutz *et al.* (2001)
MD01-2461	51° 45' N, 12° 55' W	Ireland	This study
OMEX-2K	49° 05' N, 13° 25' W	Irish Sea Ice Stream	Scourse *et al.* (2000)

8.7.4 Palaeotemperature reconstructions

Accurate reconstructions of palaeo-sea surface temperature (SST) distribution is a prime means of assessing the ability of climate models to provide realistic representations of past and future climate states (e.g. Taylor *et al.*, 2004). The compilation of temperature reconstructions presented in this study underlines the necessity to develop our understanding of different palaeothermometry approaches, to determine which parameters are being recorded in each case, such that multi-proxy SST records may provide a comprehensive range of surface ocean conditions, for example, mean annual, seasonal extremes, surface and subsurface.

8.7.4.1 Species and region specific Mg/Ca-temperature calibrations for North Atlantic records

Extensive core-top, sediment trap and culturing of North Atlantic *G. bulloides* and *N. pachyderma* sin. are needed to assess the calibrations determined in this thesis and to investigate the nature of regional differences in same-species Mg/Ca-temperature relationship.

8.7.4.2 Further North Atlantic Mg/Ca records

Very few Mg/Ca-SST records have yet been produced within the mid latitude North Atlantic. More Mg/Ca records are required to access if the apparently mild summer conditions, even warming, observed within this region (Kandiano *et al.*, 2004; this study) is real and representative of a wider-reaching summer warming coincident with destabilisation of the LIS.

8.7.4.3 Additional proxy records applied to MD01-2461

Coupling of the $Mg/Ca_{G.\ bulloides}$ record with faunal diversity data has allowed informed interpretation of this record and better characterisation of upper water column structure and temporal variability, for example distribution of typical and atypical conditions within a given time slice. Application of additional approaches, such as, MAT and TFT, alkenones and dinocyst assemblages to the same core would improve our understanding of both palaeoenvironmental conditions at this site and of the climate signals that the individual proxies are carrying.

8.7.4.4 Individual specimen Mg/Ca analysis

Mg/Ca analysis of individual foraminifera specimens, particularly *G. bulloides*, could be used to determine distribution of summer-SST within a given time-slice, rather than the average of up to 50 years as is provided in this study.

8.7.5 AMOC

Contrary to conclusions drawn from the compilation of regional benthic $\delta^{13}C$ records presented in **Chapter 7**, Gherardi *et al.* (2005) interpret $^{231}Pa/^{230}Th$ records from the Portuguese Margin as representing active overturning circulation in the eastern North Atlantic basin up until 'a later phase of H1'. In addition, they claim that BIS instability following collapse of the LIS terminated intermediate water convection NW of the Rockall plateau, accounting for an apparent lag time of ~1 kyr in $^{231}Pa/^{230}Th$ records of AMOC reduction from the Portuguese Margin with respect to Bermuda Rise (McManus *et al.*, 2004). Perhaps these records are too deep (water depths >3000 m; McManus *et al.*, 2004; Gherardi *et al.*, 2005) to document the

intermediate water variability inferred in Chapter 7. Certainly, a recent $^{231}Pa/^{230}Th$ record from the Rockall Trough supports progressive spin-down of overturning at depths shallower than 2000 m (Hall *et al.*, submitted). To complement the comprehensive compilation of regional benthic $\delta^{13}C$ records from the European Margin presented in Chapter 7, production of $^{231}Pa/^{230}Th$ records from MD01-2461 and at shallower depth on the Iberian Margin (e.g. SO75-26KL) would be advised.

8.7.6 Interdisciplinary studies; data-model comparisons

1. Model reconstructions of North Atlantic $\delta^{18}O$ during H events (Paul and Mulitza, 2006) should consider the contribution of NWEIS-sourced meltwater in addition to the LIS.

2. Subsurface cooling of >3 °C followed by warming of 1-2 °C is predicted by models of AMOC (Shaffer *et al.* 2004; Flückiger *et al.* in press). The subsurface temperatures recorded in this study, ~150 m water depth, are likely too shallow to confidently compare with predicted in model outputs. Benthic Mg/Ca bottom water temperature records at this intermediate water depth site may provide a more realistic means of data-comparison comparison in this case.

3. The effect of icebergs at the sea surface, both meltwater stratification and the latent heat of ice melt, should be incorporated into climate models to better characterise the interaction of the upper ocean-climate (cf. Jongma *et al.*, 2004).

Appendix A

Age model

Core depth cm	Age kyr BP
134.5	8066
196.5	12590
228.5	14494
274.5	16472
348.5	19243
394.5	20300
434.5	21720
486.5	23380
528.5	24080
574.5	25060
624.5	26280
692.5	29660
730.5	30760
770.5	32500
780.5	33740
799.5	35220
836.5	36660
846.5	38400
856.5	38860
884.5	43060
902.5	45585
934.5	49280
952.5	53440
982.5	58680

Appendix B

IRD counts

Depth cm.	Quartz	Vol	tephra	DolC	Chalk	HCG	mica	various	carb	shale	black carb	g/b lst	TOTAL	Total IRD g^{-1}
120.5	253	3				38			3			2	299	54
124.5	181					34			1			3	219	132
128.5	256					43			3			2	304	71
132.5	208	2			1	32			2			2	247	78
136.5	245	2	2			48	1		4			3	305	112
140.5	150					22			3			2	177	83
144.5	254		3			36	2		3			4	302	193
148.5	186					34							220	136
152.5	171	2				19	1					5	198	161
156.5	165	3				28			2			4	202	172
160.5	288	3	3			30	9					3	336	149
164.5	266	2	3			42	1		3			4	321	274
168.5	149	3	5			20	3		1			2	183	185
172.5	372		15			40			1			10	438	365
174.5	264	2	13			19	3			2		1	304	300
176.5	295	1	4			24	1		1	3		8	337	262
180.5	270	1	28			25	1		2			4	331	304
182.5	263	3	26			35			4	2		4	337	679
184.5	248	3	12			30	3		3	2		7	308	768
186.5	290	3	8			32			4	3		6	346	1091
188.5	268	5	13			37			10			5	338	646
192.5	297	6	25			50	2		3	2	12		397	1175
194.5	263	2	17			35			3			13	333	997
198.5	349	8	6			44	2					9	418	2826
202.5	293		7			22			2			10	334	578
206.5	307	3	4			46	2		1			12	375	911
210.5	283	3	2			27	1		2			7	325	312
214.5	221	2				31						5	259	424
218.5	317	4				46			4			8	379	442
222.5	312	3				37			3	1		11	367	446
226.5	236	2	2			36			4			6	286	514
228.5	247	2				41	1		4			6	301	624
230.5	272	5				44			5			5	331	947
234.5	290	6	1			36			1			14	348	1519
238.5	277	5				29	3		2			5	321	847
242.5	308	2				25			11			4	350	1531
244.5	293	4	1			30	2		3	1		4	338	1478
246.5	437	9	1			49	1		5	1		10	513	1497
248.5	278	7				26	4		1	2	2	8	328	1031

Depth cm.	Quartz	Vol	tephra	DolC	Chalk	HCG	mica	various	carb	shale	black carb	g/b lst	TOTAL	Total IRD g^{-1}
250.5	331	6	2			38	3		1			7	388	1113
252.5	298	12				59	2					5	376	1034
256.5	258	6				40			1			2	307	1405
258.5	290	4				30			3				327	840
262.5	278	2	15			27	2		1			6	331	754
266.5	345	3				27							375	778
270.5	303	3	1			34	2		3	1		5	352	933
274.5	300		1			57	2		3			6	369	816
278.5	265	6	2			42	4		4			6	329	559
282.5	251		1			26	1		3			6	288	1533
284.5	317			13		18			3			2	353	1114
286.5	266					32			1			9	308	774
290.5	245					39	1		2	1	1	4	293	1267
294.5	289	1				43	1		6	1		20	361	1105
298.5	265	3				30	2		6			13	319	1723
306.5	261	2				31	1		7			16	318	2243
310.5	275	1				26	1		6			11	320	2909
314.5	305	2				35	6		4			20	372	2077
318.5	262	5				31	2		8			11	319	2893
322.5	364	3	3			43	3		5	1		12	434	2567
326.5	279		2			36	1		3			14	335	1286
330.5	296	4				47	1		7			12	367	1543
334.5	308	3				43	7		11			19	391	1581
338.5	353	2				46			3			7	411	2209
342.5	322					45	1		5	4		13	390	1685
346.5	356	1				41			4			20	422	1829
350.5	332					31	2					8	373	1605
354.5	305	3				56	2		4			9	379	2748
358.5	346	3				43	3		1			9	405	1889
362.5	271	2				42	1		2			5	323	2699
366.5	346	3				44	9		9			9	420	2110
370.5	332	4				43	1		9		1	16	406	2080
374.5	306	2				36	2		6		1	15	368	1915
378.5	265	1				34	3		6	2		9	320	1708
382.5	262	2	1			39	1		6			8	319	1260
386.5	296	2				52			1	1		10	362	1720
390.5	319	2				59	5			1		14	400	2046
394.5	255	2	1			26	1		1	2		10	298	1620
400.5	264	1				41	1		4			10	321	867
402.5	308	1				10			1			13	333	2023
406.5	301	2				39	3		3			13	361	1838
410.5	252	2				37			5			13	309	1561
414.5	278	3				31			7			10	329	3425
418.5	261	2				37			4	1		6	311	2190
422.5	269	1				37			11			14	332	2076
426.5	392	2				53	2		5		1	18	473	2124
434.5	284	1				37	2		1	4		12	341	2916

Depth cm.	Quartz	Vol	tephra	DolC	Chalk	HCG	mica	various	carb	shale	black carb	g/b lst	TOTAL	Total IRD g^{-1}
438.5	284	2	1			55	2		2		1	9	356	2424
442.5	277	5				36			1	1		9	329	2194
446.5	300	2				39			2			8	351	1338
450.5	321	5				46	3		1	2		3	381	2603
454.5	312					47	5		1			9	374	1573
458.5	296	4				53				4		8	365	872
462.5	284	1				47	3		1	1		14	351	913
466.5	281	1				41	1		6			5	335	967
470.5	385	2				28	10		2		3	5	435	644
474.5	253	1	1			29	1		2			8	295	170
482.5	242	2				28	4		2	3		19	300	157
486.5	389					41	2			5	3	23	463	1081
490.5	284					41			3	2	2	28	360	1688
494.5	278	2			1	24		6	8	8	4	43	374	2413
496.5	238	2				34	1	7	12	6	3	33	336	2179
498.5	244	2			3	28	2	2	16	6	3	44	350	2618
500.5	210	2			4	20	2	7	26	6	7	41	325	2758
502.5	193	2			1	23	3	2	28	8	6	49	315	2465
504.5	266	4				23	2	1	32	14	7	59	408	3418
506.5	214	1			1	23			21	9	6	44	319	2749
508.5	223				1	23	6		20	10	5	34	322	2230
510.5	218	3				25	11	1	10	14	3	34	319	2670
512.5	257					17	3		12	6	7	46	348	3588
514.5	245	1				27	2	1	9	7	2	36	330	2765
517.5	236					21	2	1	14	8	10	57	349	4173
520.5	220	4				21		5	27	3	4	46	330	4085
521.5	278	3				22	2	1	8	8	2	33	357	3338
523.5	289	1				24	2	2	7	7	5	35	372	3006
524.5	255	3			3	33	1		6	3		10	314	3831
526.5	277	3				25	2		18	8	2	25	360	3099
527.5	244	1		1		12		4	12	10	1	23	308	2724
528.5	281	12	1	14	2	12	3	1	4		1	8	339	2614
529.5	308	3		10	1	31	1		11			3	368	2295
532.5	276	4		1	1	20		2	9			5	318	4319
534.5	303	3		4		38	3		9	1		4	365	4176
536.5	270	4		2	1	40			8		1	3	329	2717
538.5	297	4	5			23	17		7	2		12	367	2341
540.5	377	4				48			9			11	449	2722
542.5	284	3				50	2		8			5	352	2691
545.5	357					19	3	1	5	1		6	392	2820
547.5	265	5				51	2		3			8	334	1794
548.5	308	3				30	3	1	5	1	1	15	367	2423
551.5	304	2				35	4		2			12	359	2303
554.5	263	1				36	6		8	2		4	320	2303
556.5	320	3				44	2					11	380	2360
559.5	264	2				40	3			1		6	316	2236
562.5	286	2			1	30	3			1		12	335	2800

Depth cm.	Quartz	Vol	tephra	DolC	Chalk	HCG	mica	various	carb	shale	black carb	g/b lst	TOTAL	Total IRD g^{-1}
564.5	335				2	37			8			8	390	2860
566.5	307	1			2	48	3		3	1		8	373	2194
568.5	286	3				41			7			5	342	2859
570.5	319	1				40	5		7			17	389	5489
572.5	276	2				23	11		12	1	1	6	332	2928
574.5	283	5			1	26	7	1	9			7	339	2093
576.5	311	7	1			47	5	1	8	2		9	391	1479
578.5	289					36	6		8			6	345	1052
580.5	282	2				33	3		3	2	1	4	330	1899
582.5	392	1				32	8		4			17	454	1986
586.5	334	1				48	4		2			11	400	1532
590.5	346	2				48	4		2			19	421	1053
594.5	331	5			1	42	3		2		1	18	403	916
598.5	301	3				43	2		4	2		6	361	863
602.5	338	10				36	2	2	1			12	401	383
606.5	303	6	1			47			2	2		12	373	777
610.5	288	5			3	55	1		5			7	364	1264
614.5	245	29			1	59	5		6	1		12	358	1020
618.5	275	15				46	1	2	1			5	345	801
622.5	297	2				53			2			12	366	1132
626.5	292	8				50	4		3	1		6	364	1060
630.5	262	7				47	3		2	1		8	330	760
634.5	241	15			1	52	3	1	7	1		9	330	861
638.5	258	8				42	1		5	3		10	327	1027
642.5	331	11				59	6	1	1			7	416	908
646.5	258	4				42	7	1		2		7	321	521
650.5	310	1			2	45	2	1	3			21	385	650
654.5	288	3				46	4		5	1		14	361	613
658.5	267	2			1	47	6			2		7	332	383
662.5	264	4			1	40	6	1	1	2		11	330	558
666.5	258	4			1	46	3		1		1	9	323	554
670.5	272	5				42	4	1		2		10	336	501
674.5	256	6				33	4			2	3	17	321	168
678.5	263	9				31	3	2		2	1	12	323	369
682.5	261	4				46	2	4	5	1		5	328	763
686.5	312	11				35	2	1	4			17	382	1074
690.5	330	14				28	2		3	2		10	389	1546
694.5	298	20				33	9	2	1	1		9	373	1094
698.5	293	17				37	6	3		1		6	363	567
702.5	343	14				28	6	2				2	395	664
706.5	276	19				40	3	1				4	343	1057
710.5	258	9				44	7	5	1	3		3	330	778
714.5	236	41			1	58	3	5	2			4	350	474
718.5	292	15				61		5	4	4		5	386	673
722.5	252	15			2	37	1	6	4			4	321	834
726.5	254	11			1	34	3	3	4	3		5	318	902
730.5	259	4			1	46	5	8	11	2		8	344	580

Depth cm.	Quartz	Vol	tephra	DolC	Chalk	HCG	mica	various	carb	shale	black carb	g/b lst	TOTAL	Total IRD g^{-1}
734.5	309	8			2	40	3	3	13	4		5	387	1057
738.5	323	8			1	40	2	2	3	1		7	387	1216
742.5	302	3				44	4	1	7	2		4	367	924
746.5	300	4			1	37	3	6	4	1		6	362	1251
750.5	304	9			2	29	3	2	6	2		7	364	753
754.5	288	2				37	5	6	4	1	1	3	347	448
758.5	277	1			1	40	1	3	2	2		5	332	186
762.5	333	3				20	2	3	4	2		6	373	557
766.5	282	1				21	3	3	4	2		5	321	443
770.5	278	6				28	7	8	2			5	334	755
774.5	296	5				31	4	6	4	1		4	351	696
778.5	289	2				33	4	3	5			6	342	679
780.5	326	4				18	2	2	5			5	362	1352
784.5	294	4		1		45	7	3	4	2		7	367	410
788.5	275	2				21	7		5	1		9	320	555
792.5	292	4				35	7	5		3		5	351	741
796.5	293	4			1	50	3	5	4	1		8	369	942
800.5	305	3			1	48	14	3	6	2		3	385	1108
804.5	292					21	8	2	2	5		6	336	1246
808.5	272	4			1	33	6	3	1			3	323	1462
810.5	254	5				42	2	7				4	314	1279
812.5	287	1			1	31	6	5	10			4	345	1642
814.5	285	3				43			13			6	350	1094
816.5	278	2				30	4		14	4		8	340	1581
818.5	249	1				31			8	1		3	293	1086
820.5	258					31	6	1	10	3		12	321	1430
822.5	289	1				40	2					3	335	1152
824.5	302	3			2	26	7	1	12	2		6	361	1823
826.5	280	4				38		3	1	2		4	332	724
828.5	288	1		1		32	5	5	7	3		7	349	513
832.5	317	2		1		19	3		5	1		5	353	803
836.5	267	2			2	25	3	3	7	2		2	313	526
840.5	278	6		1		25	13		4	1		2	330	1200
844.5	347	5		4	2	19	4	1	23			3	408	1038
846.5	281	3				36			2	3		7	332	1831
848.5	298	7		3		22		1	10				341	1324
850.5	296			3		19	1		3	2		3	327	1462
852.5	305	8		7		12	1	1	32	2		3	371	5560
854.5	281	3		4		12		1	2			2	305	2009
856.5	292	4		1	2	24	6	5	11	2		3	350	2590
860.5	310	2			1	38	2	1	9			6	369	2140
864.5	297	3				38	1	3	9	2		5	358	3238
868.5	280	3				34	5	1	7			4	334	2212
872.5	289	1				28	5	2	7	1		7	340	2796
876.5	294	2				27	13	3	10	1		8	358	2373
880.5	300	2			1	40	6	2	12	3		9	375	2579
884.5	297	1			1	31	5	2	8	1		7	353	1280

Depth cm.	Quartz	Vol	tephra	DolC	Chalk	HCG	mica	various	carb	shale	black carb	g/b lst	TOTAL	Total IRD g^{-1}
888.5	277				1	28		1	11	4		4	326	1499
892.5	277	1			1	26	7	1	3	1		5	322	256
896.5	300	6			1	50	3	1	13	2		10	386	1177
900.5	284	1				18	2	2	22	3		6	338	1346
904.5	303	3		2		31	5	1	10			2	357	1604
908.5	311	9		5	1	18	2	1	10	3		4	364	1788
912.5	293	2			2	27	2	1	6	1		6	340	489
916.5	302	1			1	20	17		6	2	1	3	353	560
920.5	306	1				9	26		8	3		1	354	52
924.5	320	2				28	3		3	3		8	367	30
928.5	288	1			1	15	4		2	5		6	322	40
932.5	311	4	1		2	32	5	2	2	5		3	367	116
936.5	323					23	2	2	4			3	357	213
940.5	275	2	5			28	3		5	2		6	326	421
942.5	284	4	23			26	8		4	2		5	356	545
944.5	291	1	23			17	3		4	4		6	349	301
946.5	232	4	69			28	2				1	7	343	594
948.5	38	4	341			1	5			1			390	4645
950.5	67	5	377			3						9	461	4372
952.5	195	8	196			21			1		1	4	426	793
954.5	320	3	19			23			5	1		4	375	453
956.5	307	2	15			28		1	8		3	7	371	374
958.5	309	1	7			36	3		4			4	364	366
960.5	288	2	3			20	2		4	2		8	329	361
962.5	293	2	2			49			6	1		9	362	756
964.5	305	1				40	7	1	3	2		3	362	934
968.5	293		2			33	1		3		1	8	341	508
972.5	293	3	1			27	1	1	5	3		2	336	674
974.5	275	1	3		1	25	2		5	2	2	5	321	811
976.5	321	4				36	6	1	5	2		3	378	520
980.5	283	1	1		1	24	3	1	7	3		2	326	1360
984.5	292	2				24	2	1	7	4		7	339	734
988.5	287					29	3	4	4	5		2	334	530
992.5	287	5			1	16	5		6	1		4	325	1138
996.5	299	1			1	39	5	1	12			2	360	768
1000.5	306	5				54	2	1	8	1		2	379	994

Appendix C

Sr and Nd isotopic composition of IRD

Depth	*Sr*	*εNd*
228.5	0.71946	-11.5
234.5	0.71827	-6.3
242.5	0.72201	-10.3
258.5	0.72075	-6.4
284.5	0.72414	-24.5
470.5	0.72325	-10.7
494.5	0.72396	-13.3
504.5	0.72251	-15.6
517.5	0.72724	-11.5
524.5	0.72195	-12.1
528.5	0.72504	-29.7
532.5	0.72382	-11.7
547.5	0.71854	-9.8
564.5	0.71932	-9.4
570.5	0.71928	-6.3
582.5	0.72405	-8.9
606.5	0.71571	-5.6
690.5	0.71335	-9
746.5	0.71633	-8.4
780.5	0.72145	-6.7
844.5	0.72171	-19.1
852.5	0.72787	-31
864.5	0.72079	-11.8
880.5	0.71935	-13.2
892.5	0.72225	-12.6
908.5	0.72305	-23.9
916.5	0.72322	-30.6

Appendix D

Hornblende grain $^{40}Ar/^{39}Ar$ ages

Depth cm.	*Ca/K*	*36/39*	*40*/39*	*Mol 40*	*Mol 39*	*%^{40}Ar**	*Age (yr)*	±
198.5	12.3217	0.14905	267.838	0.10168	0.00033	85.9	954.02	2.23
198.5	39.2275	0.08016	0.45	0.00733	0.00032	2	2.11	11.01
202.5	1.9855	0.12169	43.677	0.01214	0.00015	54.9	194.19	1.32
202.5	7.8753	0.04662	690.183	0.38902	0.00055	98.1	1854.84	1.16
202.5	7.8769	0.07875	604.754	0.39966	0.00064	96.3	1705.38	5.79
202.5	12.8227	0.11397	265.845	0.24766	0.00083	88.8	948.49	31.78
202.5	12.8836	0.0029	734.065	0.18884	0.00026	100	1927.05	3.1
202.5	15.7932	0.05097	100.336	0.02312	0.0002	87.3	418.48	5.37
202.5	23.5362	0.01225	7.229	0.00185	0.00019	72.6	33.62	1.92
202.5	27.6149	0.15379	46.247	0.12252	0.00136	50.7	204.99	2.51
206.5	5.5833	-0.0092	462.862	0.65707	0.00143	100.6	1426.02	2.27
206.5	6.3486	0.00468	619.684	2.29246	0.0037	99.8	1732.41	71.8
206.5	7.0646	0.01679	252.756	0.1784	0.0007	98.2	911.81	1.54
206.5	9.2612	0.02381	619.664	0.40184	0.00064	98.9	1732.38	5.78
206.5	11.6946	-0.01535	12.353	0.00116	0.00016	168.4	57.07	4.22
206.5	11.837	0.0358	102.57	0.07575	0.00068	91	426.78	5.49
206.5	12.574	0.00445	6.896	0.00376	0.00049	89.3	32.08	8.7
206.5	23.3126	0.05425	613.401	0.73716	0.00119	97.6	1721.09	2.28
206.5	37.8528	0.5356	11.947	0.07465	0.00044	7	55.23	21.14
218.5	1.9485	0.00567	507.574	3.42029	0.00672	99.7	1518.8	1.45
218.5	7.2359	0.03544	65.189	0.01592	0.00021	86.4	282.67	1.41
218.5	7.3322	0.26804	96.732	0.03042	0.00017	55	405.01	1
218.5	8.1962	0.01338	102.606	0.09061	0.00086	96.6	426.91	26.18
222.5	11.9969	0.0573	953.178	0.45711	0.00047	98.3	2249.83	3.12
226.5	8.8251	0.00941	643.557	0.54019	0.00084	99.6	1774.81	1.74
226.5	27.514	0.45018	452.818	0.26827	0.00046	77.2	1404.5	4.26
230.5	22.9061	-0.00128	5.149	0.00165	0.00043	133.3	24.01	29
230.5	33.4022	1.48542	17.297	0.46278	0.00102	3.7	79.42	1.17
230.5	36.07	0.66561	488.289	0.30598	0.00045	71.1	1479.37	
238.5	9.4332	0.03579	625.761	0.51972	0.00082	98.4	1743.3	12.51
240.5	6.9632	0.05188	103.81	0.65417	0.00552	87.3	431.37	14.75
240.5	9.8124	0.03515	75.573	0.07495	0.00088	88.3	323.87	14.98
240.5	41.4605	0.17834	12.33	0.03968	0.00063	19.1	56.97	12.71
242.5	10.0089	0.22352	114.117	1.61268	0.009	63.4	460	3
242.5	24.9251	0.11535	845.854	0.31856	0.00037	96.2	2060	17
242.5	9.1982	0.04513	658.591	0.7121	0.00106	98.1	1767	7
242.5	8.2599	0.0191	640.397	1.33385	0.00207	99.2	1736	6
248.5	7.1457	0.01129	636.491	0.38898	0.00061	99.5	1762.36	10.07
248.5	8.7105	0.02127	656.118	1.00382	0.00152	99.1	1796.72	5.5
248.5	9.2788	0.0106	647.146	0.80331	0.00124	99.6	1781.1	16.63
248.5	9.9714	0.00818	10.456	0.00355	0.00029	83.7	48.42	15.41
248.5	10.171	0.02823	659.954	0.51102	0.00077	98.8	1803.36	16.28
248.5	11.6014	0.04411	272.898	0.73146	0.00258	95.6	967.96	3.68
248.5	13.6276	0.0733	270.184	0.44375	0.00153	92.7	960.49	9.78

Depth cm.	Ca/K	36/39	40*/39	Mol 40	Mol 39	$\%^{40}Ar^*$	Age (yr)	±
248.5	25.8037	0.2647	14.294	0.01823	0.0002	15.5	65.88	6.14
248.5	28.8796	0.55314	82.911	0.12123	0.0005	33.5	352.42	6.43
258.5	5.3778	0.22429	54.302	0.02883	0.00024	45.1	238.43	7.53
258.5	6.8659	0.17062	16.813	0.11648	0.00174	25	77.25	7.29
258.5	8.7499	0.36969	105.233	0.08552	0.0004	49	436.62	4.47
258.5	8.7813	0.05215	669.654	0.57065	0.00084	97.8	1820.04	3.9
258.5	9.3021	0.0036	623.067	0.28757	0.00046	99.9	1738.48	7.15
258.5	12.0293	0.05171	106.949	0.06423	0.00053	87.8	442.93	15.21
262.5	7.0597	0.00552	632.71	3.67998	0.00582	99.8	1755.67	4.16
262.5	7.5619	0.02348	642.721	0.95464	0.00148	99	1773.34	11.89
262.5	10.7118	0.07314	635.569	0.27214	0.00042	96.8	1760.73	19.2
262.5	10.7783	0.01277	3.503	0.00844	0.00123	51	16.37	4.61
262.5	11.7259	0.00235	678.847	0.11078	0.00016	100	1835.71	12.74
262.5	15.9792	0.11517	98.444	0.15357	0.00117	74.5	411.42	7.05
262.5	18.2258	0.00664	9.622	0.00482	0.00045	88.4	44.61	17.23
266.5	4.1077	0.31708	60.863	0.01662	0.00011	39.4	265.22	5.21
266.5	6.1842	0.01018	636.205	0.83999	0.00132	99.6	1761.86	22.71
266.5	7.6452	0.11396	1262.38	0.73952	0.00057	97.4	2625.03	14.94
266.5	11.3965	0.00966	-0.124	0.00592	0.00258	-5.4	-0.58	7.22
266.5	18.3965	0.04767	0.87	0.08967	0.0063	6.1	4.08	1.85
284.5	4.5699	0.02726	111.307	0.20668	0.00174	93.4	458.86	4.79
284.5	5.1092	0.00891	670.198	1.25022	0.00186	99.6	1820.97	5.59
284.5	5.1253	0.12963	575.084	3.5837	0.00586	93.8	1650.44	8.66
284.5	5.1423	0.01078	629.185	0.97427	0.00154	99.5	1749.4	5.12
284.5	5.9215	0.00478	471.091	4.01976	0.00853	99.7	1443.46	6.51
284.5	6.2293	0.05958	651.695	0.30129	0.00045	97.4	1789.04	6.86
284.5	6.3861	0.01116	626.78	0.48152	0.00077	99.5	1745.12	7.69
284.5	7.8405	0.04441	597.918	0.17964	0.0003	97.9	1692.87	3.96
284.5	8.6254	0.01248	692.297	1.20064	0.00173	99.5	1858.39	5.12
284.5	9.1902	0.0382	663.309	0.61733	0.00092	98.4	1809.15	17.84
284.5	10.895	0.08494	109.841	0.17341	0.00129	81.6	453.52	13.18
284.5	12.2253	0.01574	610.905	0.70882	0.00116	99.3	1716.57	14.13
284.5	14.4025	-0.0065	682.059	0.18824	0.00028	100.4	1841.15	3.29
284.5	16.6025	0.0362	679.013	0.47839	0.0007	98.5	1835.99	12.5
286.5	7.5091	0.05494	72.416	0.75538	0.00857	81.9	311.44	7.19
286.5	8.1031	0.29756	15.555	0.15132	0.00147	15	71.58	9.6
286.5	9.1621	0.00642	669.193	0.65901	0.00099	99.8	1819.25	5.65
286.5	13.6202	0.08584	41.2	0.02945	0.00045	62.2	183.72	3.59
286.5	34.1571	1.51699	127.221	0.16596	0.00029	21.9	515.88	5.41
288.5	12.4645	0.21721	270.358	0.14208	0.00043	80.8	960.97	10.93
294.5	24.5447	2.42989	31.927	0.07552	0.0001	4.2	143.97	2.31
296.5	1.6054	0.28433	228.33	0.04464	0.00014	73.1	841.28	23.01
296.5	2.2214	0.01836	102.627	0.31617	0.00293	95	426.99	4.2
296.5	5.0979	0.01071	265.547	1.26635	0.00473	98.9	947.67	4.52
296.5	6.4093	0.00958	1289.611	1.34424	0.00104	99.8	2654.62	24.6
296.5	6.7428	0.01961	550.804	2.33389	0.00421	99	1604.19	5.35
296.5	10.9285	0.02063	601.754	0.42152	0.0007	99.1	1699.9	11.98
296.5	14.5529	0.02073	719.569	1.39303	0.00193	99.2	1903.52	0.96
296.5	20.4063	0.03258	133.924	0.01905	0.00013	93.8	539.37	0.92
296.5	23.0206	0.06241	116.362	0.0385	0.00029	86.8	477.17	3.37
298.5	12.9635	1.04418	692.546	1.6701	0.00168	69.1	1858.8	5.61

Depth cm.	Ca/K	36/39	40*/39	Mol 40	Mol 39	$\%^{40}Ar^*$	Age (yr)	±
300.5	21.9274	0.03129	0.212	0.00315	0.00037	2.4	1	4.7
300.5	40.512	0.01871	109.132	0.21591	0.00194	96.4	450.93	6.12
302.5	5.7288	0.02533	695.316	1.64646	0.00235	99	1863.44	3.41
302.5	6.5246	-0.00428	8.751	0.00948	0.00131	121.1	40.62	12.19
304.5	6.8578	0.19178	74.597	0.19653	0.0015	56.9	320.03	7.45
304.5	20.9044	0.04262	95.662	3.29604	0.03094	88.9	401	14.29
306.5	5.2505	0.02648	619.246	1.77783	0.00284	98.8	1731.62	6.52
306.5	25.5458	0.48328	56.475	0.06321	0.00032	28.2	247.35	8.97
310.5	5.1382	0.00896	203.479	0.88416	0.0043	98.8	766.57	5.85
310.5	13.2727	0.10466	27.451	0.02499	0.00043	47.3	124.47	6.33
312	1.592	0.01701	740.848	1.03995	0.0014	99.3	1937.96	17.93
314.5	7.5742	0.01594	263.119	0.20399	0.00076	98.3	940.92	12.11
314.5	11.004	0.09598	263.321	0.15495	0.00053	90.4	941.48	1.23
314.5	18.4871	0.09075	136.047	0.06344	0.00039	83.8	546.74	5.13
314.5	22.3005	0.02176	779.901	2.71977	0.0035	99.3	1999.52	7.4
314.5	25.7523	0.01655	4.424	0.00159	0.00019	52.9	20.65	9.94
314.5	26.9988	0.0066	4.348	0.00322	0.00062	82.7	20.3	46.56
316	9.445	0.00585	294.992	0.48237	0.00163	99.5	1027.61	8.69
320	8.0736	0.04127	630.072	0.38828	0.00061	98.1	1750.98	135.08
320	10.2473	0.00935	292.752	0.39533	0.00135	99.2	1021.65	35.88
320	18.9294	0.05169	98.609	0.02393	0.00021	87.1	412.04	1.9
320	19.7086	0.04522	17.268	0.01582	0.00053	57.6	79.29	2.76
320	20.6037	0.07067	78.445	0.09682	0.00099	79.5	335.1	9.8
322.5	10.6476	0.04032	114.072	0.12864	0.00103	90.8	468.9	7.3
322.5	12.3802	0.09204	1011.516	4.48696	0.00435	97.4	2326.85	8.89
322.5	16.2863	0.01052	610.191	0.25665	0.00042	99.6	1715.27	5.5
326.5	22.2045	0.06534	205.49	0.93318	0.00421	91.7	772.73	22.86
330.5	6.5966	0.02872	683.924	1.32325	0.00192	98.8	1844.3	8.48
330.5	25.6267	0.03474	74.184	0.02346	0.00028	88.8	318.41	8.7
332.5	19.6456	1.17287	44.106	0.10087	0.00026	11.2	196	6.13
332.5	24.4361	0.28961	10.929	0.07774	0.00081	11.3	50.59	2.14
334.5	6.045	0.05487	43.375	0.14018	0.00237	73	192.92	4.79
334.5	9.9872	0.02108	79.816	0.0626	0.00073	93.2	340.43	3.47
334.5	19.726	1.93038	59.058	0.08429	0.00013	9.3	257.89	3.99
336.5	9.6364	0.03448	667.342	0.44382	0.00066	98.5	1816.08	1.38
340.5	5.2191	0.00118	105.221	0.2573	0.00245	99.9	436.58	7.22
340.5	13.1071	0.03902	69.952	0.02963	0.00037	86.3	301.68	19.88
340.5	16.6929	0.05574	662.356	0.5497	0.00082	97.6	1807.5	2.16
340.5	16.9392	0.30265	25.316	0.02409	0.00021	22.1	115.09	8.44
344.5	3.9494	0.0254	5.467	0.02327	0.00182	42.6	25.48	7.05
344.5	13.7465	0.39728	24.149	0.02829	0.0002	17	109.94	5.32
344.5	15.8597	0.05804	1690.864	1.16365	0.00069	99	3042.27	10.12
350.5	10.2709	0.0235	1204.476	1.18803	0.00099	99.5	2560.45	7.76
392.5	11.7636	0.05189	261.397	0.16507	0.0006	94.6	936.11	4.89
392.5	24.2772	0.07052	65.782	0.02008	0.00024	76.6	285.04	8.16
528.5	23.9616	0.00528	632.074	0.734	0.00117	99.9	1722	8
528.5	6.6341	0.00232	627.351	3.03124	0.00484	99.9	1714	4
528.5	7.1779	0.03459	651.458	3.26506	0.00495	98.5	1755	4
528.5	20.9291	0.00936	624.039	0.68985	0.00111	99.7	1708	7
528.5	6.9732	0.00661	632.089	2.8812	0.00456	99.7	1722	5
528.5	7.9315	0.00292	664.073	1.30489	0.00197	99.9	1777	6

Depth cm.	Ca/K	36/39	40*/39	Mol 40	Mol 39	%^{40}Ar*	Age (yr)	±
528.5	9.865	-0.00025	671.713	0.43543	0.00065	100.1	1789	9
528.5	10.2027	0.00664	638.077	1.66879	0.00262	99.8	1732	6
528.5	7.778	0.03135	1317.058	0.68478	0.00052	99.3	2634	14
528.5	7.2894	-0.0038	672.426	0.39687	0.00059	100.2	1791	10
528.5	7.2935	0.01356	646.023	0.73672	0.00114	99.4	1746	9
528.5	9.2846	0.01734	958.679	0.75399	0.00079	99.5	2215	10
528.5	11.7167	0.01449	626.313	3.83827	0.00612	99.4	1712	4
528.5	22.3656	0.06694	662.852	1.20895	0.00179	97.2	1775	5
528.5	9.3201	0.01709	636.423	0.57179	0.0009	99.3	1729	10
528.5	13.002	0.01929	700.977	0.67778	0.00097	99.3	1838	9
528.5	7.3576	0.0064	700.946	2.70463	0.00386	99.8	1838	4
528.5	5.1404	0.00109	648.785	0.6459	0.001	100.0	1751	7
528.5	5.0617	0.04963	633.455	1.11089	0.00172	97.8	1724	6
528.5	10.7596	0.02571	717.996	0.41671	0.00058	99	1865	17
528.5	9.8444	0.0115	650.056	0.48802	0.00075	99.5	1753	13
528.5	8.1121	0.02494	654.691	0.54557	0.00083	98.9	1761	9
528.5	7.2894	0.07914	622.769	1.43914	0.00224	96.4	1705	5
528.5	9.7949	0.00325	628.448	3.92292	0.00626	99.9	1715	4
528.5	6.178	0.00636	612.305	0.92787	0.00152	99.7	1687	5
528.5	7.0366	0.01353	647.773	1.71026	0.00263	99.4	1749	5
528.5	14.5399	0.35153	640.397	0.40467	0.00055	86	1736	17
528.5	9.9966	0.6693	593.827	0.25494	0.00032	75	1654	22
528.5	18.6349	0.16842	606.574	0.13988	0.00022	92.5	1677	33
528.5	18.3974	0.03792	76.218	0.03192	0.00037	87.8	320	10
528.5	16.2449	0.28028	600.264	0.18462	0.00027	87.9	1665	19
852.5	30.8198	0.19073	1172.223	2.93543	0.00242	95.4	2476	8
852.5	23.3058	0.08778	1506.527	6.25239	0.00413	98.3	2821	5
852.5	11.619	0.15643	1311.429	3.83076	0.00284	96.6	2628	6
852.5	6.0337	0.02548	1179.526	3.61908	0.00306	99.4	2485	6
852.5	10.9845	0.0264	617.403	5.1195	0.00824	98.8	1696	3
852.5	13.0858	0.00601	652.15	1.50753	0.00232	99.8	1756	5
852.5	11.8229	0.02074	1313.721	2.26751	0.00173	99.6	2630	7
852.5	8.542	0.03641	617.774	1.80207	0.00288	98.3	1697	6
852.5	15.5648	0.05118	638.739	0.33286	0.00051	97.8	1733	12
852.5	18.6337	0.01662	624.524	0.25747	0.00041	99.3	1709	14
852.5	18.6022	0.03377	618.09	0.48288	0.00078	98.5	1697	10
852.5	13.8744	0.01921	603.784	0.34297	0.00057	99.2	1672	10
852.5	11.1755	0.02384	655.465	0.80903	0.00123	99	1762	6
852.5	9.3271	0.00177	647.443	0.87023	0.00135	100.00%	1748	6
852.5	6.4162	0.00155	632.596	1.51997	0.00241	100.00%	1723	6
852.5	15.5011	0.03051	1549.875	1.58799	0.00103	99.5	2861	9
852.5	7.7735	0.00177	686.482	1.37442	0.00201	100.0	1814	6
852.5	10.17	0.04306	665.57	0.56991	0.00084	98.2	1779	10
852.5	10.344	0.0747	773.185	1.628	0.00206	97.3	1952	6
852.5	8.2995	0.00527	683.48	1.72861	0.00253	99.8	1809	5
852.5	12.4177	0.01363	1305.38	2.6916	0.00207	99.7	2622	6
852.5	7.3504	0.08209	696.061	1.83862	0.00256	96.7	1830	6
852.5	9.9669	0.00055	652.433	0.56718	0.00087	100	1757	10
852.5	8.7611	0.01413	643.558	0.98134	0.00152	99.4	1742	5
852.5	13.9141	0.03246	644.44	0.38603	0.00059	98.6	1743	13
908.5	22.7059	0.02229	670.266	5.01771	0.0075	99.1	1787	4

Depth cm.	*Ca/K*	*36/39*	*40*/39*	*Mol 40*	*Mol 39*	*%^{40}Ar**	*Age (yr)*	±
908.5	10.0621	0.009	692.082	6.01032	0.0087	99.7	1823	5
908.5	15.774	0.03513	4466.54	36.04364	0.00811	99.8	4489	7
908.5	13.3157	0.0442	715.623	5.29119	0.00731	98.3	1862	4
908.5	6.6751	0.01469	653.289	6.63363	0.01012	99.4	1758	4
908.5	10.4519	0.09623	624.442	2.39102	0.00368	95.7	1708	5
908.5	8.5097	0.00797	669.465	2.80308	0.00419	99.7	1786	5
908.5	9.5878	0.07063	1299.241	3.16412	0.00241	98.4	2615	9
908.5	40.643	0.49572	610.804	0.4333	0.00058	80.5	1684	17
908.5	15.889	0.02576	698.966	1.02975	0.00147	99	1835	7
908.5	11.3732	0.0363	2767.066	1.43246	0.00052	99.6	3725	14
908.5	6.2443	0.01509	646.687	1.32324	0.00204	99.4	1747	6
908.5	9.9992	0.00819	627.582	0.64047	0.00102	99.7	1714	9
908.5	7.0302	0.00887	722.984	1.21886	0.00169	99.7	1873	6
908.5	10.9349	0.01431	660.407	0.74663	0.00113	99.4	1770	8
908.5	7.4965	0.00216	765.158	0.98025	0.00128	100.0	1940	9
908.5	7.8241	0.00328	668.864	1.38293	0.00207	99.9	1785	6
908.5	9.7944	0.08719	1200.302	0.5404	0.00044	97.9	2508	14

Appendix E

Faunal counts, stable isotopes and Mg/Ca

Depth cm.	Nps %	$\delta^{18}O_{Gb}$	$\delta^{13}C_{Gb}$	$\delta^{18}O_{Nps}$	$\delta^{13}C_{Nps}$	Mg/Ca_{Gb}	Mg/Ca_{Nps}	$\delta^{18}O_{Cw}$	$\delta^{13}C_{Cw}$
138.5	3	0.909	-0.830	3.300	0.414	2.298			
142.5	2	0.763	-0.634	3.005	0.377	2.794	0.885	1.645	1.076
146.5	1	1.100	-0.402	3.318	0.325	2.459	0.771	2.217	0.738
150.5	3	0.961	-0.556	2.898	0.306	2.371	0.963		
154.5	3	1.031	-0.437	3.277	0.139	2.484	0.876	2.038	0.817
158.5	2	0.835	-0.583	3.168	0.312	2.345	0.845	2.464	0.621
160.5	7	1.346	-0.446	3.326	0.318	2.325	0.853		
162.5	5	1.434	-0.899	3.362	0.301	2.216	0.899		
164.5	7	0.985	-0.360	3.021	0.359	2.414	0.929		
166.5	3	1.442	-0.859	2.831	0.238	2.221	0.868		
168.5	7	1.403	-0.653	3.205	0.212	2.368	0.854		
170.5	11	1.146	-0.797	3.079	0.268	2.199	0.980		
172.5		1.361	-0.455	2.871	0.482	2.553	0.798		
174.5	33	1.329	-0.689	3.323	0.355	2.192	0.824		
176.5	27.4	1.259	-0.567	3.395	0.499	2.494	0.881		
178.5	19	1.499	-0.825	3.196	0.246	2.505	0.876		
180.5	14.5	1.344	-0.695	3.062	0.354	2.652	0.824		
182.5	11.6	1.195	-0.576	3.057	0.383				
184.5	23.4	1.491	-0.685	3.087	0.494	2.653	0.724		
186.5	50	1.581	-0.181	3.024	0.384	2.476	0.770		
188.5	43	1.033	-0.472	3.411	0.347	2.465	0.927		
190.5	39	1.519	-0.909	2.841	0.520	2.427			
192.5	48	1.719	-0.726	3.048	0.340	2.256	0.778		
194.5	50.8	1.647	-0.841	3.035	0.306	2.183	0.935		
196.5	43	1.884	-0.582	3.233	0.288	1.988	0.865		
198.5	46.3	1.961	-0.380	3.180	0.463	2.052	0.868		
200.5	50	1.911	-0.286	3.138	0.326	2.066	0.954	2.220	0.643
202.5	38	1.963	-0.306	2.942	0.461	2.548	0.965		
204.5	37	2.310	-0.737	3.031	0.448	2.377	0.825	2.206	0.656
206.5	30	2.167	-0.464	2.990	0.399	1.809	0.959		
207.5								2.629	1.177
208.5	17	2.145	-0.269	2.943	0.120	2.091	0.848	2.367	0.837
210.5	17								
212.5	16	1.305	-0.736	2.689	0.430	2.092	0.771		
214.5	18	1.966	-0.560	2.675	0.358	1.877	0.861	2.637	1.075
215.5								2.552	0.901
216.5	6	2.284	-0.408			2.269	0.948		
217.5								2.512	0.794
218.5	11	2.451	-0.508			2.193	0.952		
219.5								3.657	1.100
220.5	18.5	2.025	-0.540	3.017	0.232	2.329	0.839		
221.5								2.615	0.671
222.5	14	2.393	-0.649	3.204	-0.102	2.014	0.756		

Depth cm.	Nps %	$\delta^{18}O_{Gb}$	$\delta^{13}C_{Gb}$	$\delta^{18}O_{Nps}$	$\delta^{13}C_{Nps}$	Mg/Ca_{Gb}	Mg/Ca_{Nps}	$\delta^{18}O_{Cw}$	$\delta^{13}C_{Cw}$
224.5	20.5	2.136	-0.523	3.120	-0.035	2.066	0.884		
226.5	12	1.927	-0.730	3.171	-0.054	2.059	0.817		
227.5								2.294	0.943
228.5	7	2.083	-0.731	3.167	-0.084	2.348	0.811		
229.5								2.293	0.772
230.5	26.5	1.973	-0.661	3.364	0.020	2.294	0.817		
232.5	53	1.988	-0.771	3.168	-0.119	2.726	0.858		
234.5	39	2.448	-0.320	3.550	0.004	2.445	0.778		
236.5	46	1.813	-0.724	3.206	-0.033				
237.5								3.241	0.924
238.5	41.2	1.780	-0.692	3.309	-0.104	2.055	0.872		
239.5								3.617	0.980
240.5	40	1.466	-0.419	3.335	0.158	2.384	0.818		
241.5						2.786			
242.5	56	0.955	-0.546	2.995	-0.192		0.832		
243.5						2.471			
244.5	86	1.715	-0.516	3.260	-0.109			2.320	0.867
245.5						3.078			
246.5	73	1.426	-0.564	3.371	0.018		0.859		
247.5						2.155			
248.5	65.5	1.755	-0.729	3.900	-0.063		0.874		
249.5						2.408		3.104	0.926
250.5	38	1.386	-0.430	3.555	-0.021		0.793	3.262	1.165
251.5						2.858		3.306	0.864
252.5	59	1.947	-0.707	3.507	-0.140	1.849	0.910		
253.5								3.227	0.986
255.5								3.587	0.988
256.5	76			3.423	-0.059		0.831		
257.5						2.504		2.224	0.636
258.5	54	1.717	-0.463	3.326	-0.092		0.677		
259.5								2.226	0.477
260.5	69	1.345	-0.537			2.342	0.878		
262.5	80	2.213	-0.555	3.153	0.188	2.178	0.834		
264.5	30	1.243	-0.599	3.361	0.111	2.468	0.780		
266.5	15	1.668	-0.508	2.784	0.380	2.099	0.815	3.036	0.681
268.5	31	1.515	-0.564	3.384	0.197	2.307	0.711	2.530	0.404
270.5	75	1.633	-0.366	3.707	0.110	2.025	0.729		
272.5	30	1.035	-0.419	3.580	-0.018	3.167	0.817	2.666	0.637
274.5	79	1.360	-0.591	3.513	0.100		0.723		
276.5	79			3.882	0.060		0.646	3.275	1.071
277.5		3.007	-0.601			3.253			
278.5	76.5			3.681	0.105		0.739		
280.5	65.7			3.942	0.101		0.606	3.594	1.444
282.5	76.8	2.035	0.109	4.040	-0.005		0.741		
284.5	78.5			3.952	0.134		0.701		
286.5	74.5			4.172	0.118		0.566		
288.5	67	2.563	-0.956	3.940	0.048	2.645	0.705		
290.5	77.4			4.042	-0.050		0.733		
291.5						1.774			
292.5	48.5	2.686	-0.942	4.199	0.080		0.771		

Depth cm.	Nps %	$\delta^{18}O_{Gb}$	$\delta^{13}C_{Gb}$	$\delta^{18}O_{Nps}$	$\delta^{13}C_{Nps}$	Mg/Ca_{Gb}	Mg/Ca_{Nps}	$\delta^{18}O_{Cw}$	$\delta^{13}C_{Cw}$
293.5						1.685			
294.5	58	3.051	-1.452	4.095	-0.208		0.752		
295.5						2.280			
296.5	50.7	2.993	-0.831	3.424	-0.040		0.813	3.798	1.562
297.5						1.676			
298.5	65.8	3.327	-0.815	3.691	-0.145		0.778		
299.5				3.744	-0.033				
300.5	50	3.430	-0.795	3.732	-0.293	2.125	0.795		
301.5						1.466		3.934	1.612
302.5	61.8	3.535	-0.963	4.016	-0.287	1.564	0.738		
303.5								4.114	1.435
304.5	40	3.220	-1.082	3.625	-0.158	1.802	0.734	3.691	1.556
305.5						1.748		3.920	1.565
306.5	67.7	3.002	-0.616	3.493	-0.101		0.766	4.000	1.393
307.5						1.569		4.023	1.406
308.5	65.2	2.523	-0.875	3.671	-0.188		0.752	3.345	0.923
309.5						1.700			
310.5	54.9	2.799	-1.048	3.617	-0.129		0.673	3.318	0.952
311.5						1.725			
312.5	50	3.345	-0.851	3.500	-0.285		0.676		
313.5								3.792	1.509
314.5	59.7	3.263	-1.143			1.544	0.766		
315.5								3.947	1.542
316.5	63.8	3.095	-1.181	3.404	-0.160	1.984	0.706		
318.5	53.8	3.103	-1.022	3.781	-0.051		0.705	3.890	1.301
319.5								3.782	1.567
320.5	49.4	3.121	-1.193	3.272	-0.347	1.692			
321.5						1.520			
322.5	58.9	3.237	-1.245	3.829	-0.139		0.730	4.006	1.536
323.5						1.498			
324.5	68.7	3.464	-0.990	3.057	-0.165				
325.5								3.897	1.587
326.5	65.2	3.321	-1.211	3.806	-0.162		0.630		
327.5						2.030			
328.5	52.3	3.826	-0.843	3.551	-0.185		0.688		
329.5						1.419		3.949	1.614
330.5	53.5	3.461	-0.995	3.853	-0.212		0.793		
331.5						1.302			
332.5	50	3.644	-0.676	3.460	-0.113	1.800	0.810		
333.5						3.150		3.963	1.540
334.5	49.6	3.195	-1.137	3.674	-0.400		1.039		
336.5	43.3	3.051	-0.839	3.312	-0.297	1.645	0.764	3.838	1.692
337.5								4.113	1.700
338.5	52.7	3.517	-0.841	3.761	-0.418	2.202			
339.5								3.938	1.640
340.5	38.5	3.266	-0.923	3.255	-0.308	1.733	0.901		
342.5	48.3	3.497	-1.155	3.715	-0.400	1.516		3.745	1.609
344.5	31.6	3.191	-0.999	3.404	-0.351	1.563	0.755	3.777	1.590
346.5	46.5			3.758	-0.439	1.526		3.706	1.460
348.5	32	3.142	-1.019	3.219	-0.291	1.402	0.719	3.983	1.624

Depth cm.	Nps %	$\delta^{18}O_{Gb}$	$\delta^{13}C_{Gb}$	$\delta^{18}O_{Nps}$	$\delta^{13}C_{Nps}$	Mg/Ca_{Gb}	Mg/Ca_{Nps}	$\delta^{18}O_{Cw}$	$\delta^{13}C_{Cw}$
350.5	39	3.227	-0.710	3.252	-0.214	1.448	0.725	3.910	1.525
352.5	44.9			3.540	-0.137	1.780	0.745		
354.5	42	3.171	-1.155	3.415	-0.284	1.371	0.710	3.911	1.622
356.5	47	3.413	-0.793	3.390	-0.428	1.564		3.751	1.588
358.5	36	3.354	-0.929	3.517	-0.272	1.656	0.703	3.914	1.581
360.5	48.5	3.535	-1.067			1.430	0.715		
362.5	50					1.494	0.789	3.849	1.625
364.5	43.2	3.529	-1.136	3.574	-0.348	1.385	0.794	3.908	1.628
366.5	50.5			3.524	-0.276	1.463	0.780	3.741	1.665
368.5	41.9	3.534	-0.987	3.681	-0.334	1.741	0.770	3.755	1.637
370.5	50.7			3.422	-0.290	1.661	0.794	3.786	1.578
372.5	51	3.508	-1.215	3.571	-0.303	1.570	0.732	3.762	1.682
374.5	48.1	3.191	-0.938	3.500	-0.328	1.651	0.765	3.845	1.462
376.5	47	3.483	-0.883	3.591	-0.369	1.416	0.804	3.756	1.617
378.5	44.8			3.517	0.012	1.686	0.755	3.240	1.073
380.5	49.2	3.526	-1.111	3.574	-0.360	1.788	0.726	3.827	1.563
382.5	45	3.081	-1.034	3.531	-0.119	1.579	0.748		
384.5	55.5	3.457	-0.976	3.569	-0.378	2.066	0.742	3.753	1.677
386.5	42.1					1.771	0.795		
387.5				3.514	-0.222				
388.5	50	3.390	-1.014	3.720	-0.242	1.939	0.741	3.777	1.554
390.5	52.6	3.179	-1.244	3.550	-0.169	1.907	0.700		
392.5	52	3.426	-1.123	3.508	-0.417	1.620	0.755		
394.5	58.7	3.096	-1.162	3.352	-0.295	1.574	0.719		
396.5	46	3.362	-1.212	3.701	-0.342	1.629	0.699	3.822	1.551
398.5	44	3.293	-1.034	3.471	-0.185		0.731		
399.5								4.005	1.408
400.5	40	3.171	-1.233	3.633	-0.268	1.819	0.719	3.677	1.530
402.5	41	3.431	-1.065	3.496	-0.366	1.883	0.765		
403.5								3.521	1.575
404.5	51	3.253	-1.156	3.575	-0.368		0.706		
406.5	54	3.418	-1.086	3.410	-0.546	1.733	0.841	3.855	1.610
407.5								3.729	1.567
408.5	49.5	3.366	-1.019	3.521	-0.425	1.382	0.678		
409.5								3.795	1.691
410.5	52.6	3.451	-1.176	3.541	-0.313	1.938	0.704		
412.5	51.8	3.122	-1.399	3.567	-0.340	1.709	0.804		
413.5								3.995	1.582
414.5	52.7	3.198	-1.520	3.723	-0.249	1.798	0.817		
416.5	51.1	3.224	-1.044	3.602	-0.158	1.965	0.725		
417.5						1.574		3.941	1.196
418.5	63.4	3.564	-0.920	3.798	-0.116		0.832		
419.5						1.363			
420.5	51.8	2.762	-0.766	3.636	0.008		0.692		
421.5						1.431		3.777	1.357
422.5	55.8	2.832	-0.826	3.843	-0.048		0.711		
423.5						1.190			
424.5	51.2	3.118	-0.773	3.944	-0.136		0.705	3.734	1.433
425.5						1.518		4.065	1.538
426.5	57.2	3.250	-0.859	3.845	-0.033		0.675		

Depth cm.	Nps %	$\delta^{18}O_{Gb}$	$\delta^{13}C_{Gb}$	$\delta^{18}O_{Nps}$	$\delta^{13}C_{Nps}$	Mg/Ca_{Gb}	Mg/Ca_{Nps}	$\delta^{18}O_{Cw}$	$\delta^{13}C_{Cw}$
428.5	58.8	2.274	-0.786	3.808	-0.160	1.694	0.701		
429.5								4.195	1.508
430.5	60			3.928	0.092		0.654		
432.5	58.6	3.235	-1.147	3.894	-0.045		0.670		
433.5						1.597		3.924	1.597
434.5	42.5			3.811	0.052		0.740		
435.5						1.652			
436.5	47.5	3.226	-1.190	3.768	-0.021		0.744		
437.5						1.563		3.978	1.501
438.5	39	3.527	-0.794	3.509	-0.055	1.460	0.728		
440.5	47.2	3.399	-0.752	3.759	0.022	1.517	0.689		
442.5	33.6	3.637	-0.663	3.671	-0.005	1.431	0.775		
443.5								3.807	1.472
444.5	26.9	3.609	-0.651	3.708	0.065	1.244	0.726		
445.5								3.631	1.431
446.5	26.9	3.577	-0.564	3.673	-0.035	1.433	0.750		
448.5	37.5	3.792	-0.591	3.624	-0.147	1.608	0.709		
449.5								3.762	1.464
450.5	38.5	3.486	-0.776	3.532	-0.164	1.510	0.771		
452.5	34.1	3.304	-0.877	3.572	-0.273	1.565	0.792		
454.5	41.5	3.275	-0.934	3.622	-0.189	1.946	0.775	3.912	1.458
456.5	42.1	3.098	-0.497	3.489	-0.079	1.780	0.861	3.800	1.550
458.5	39.8	3.248	-0.842	3.660	-0.021	1.704	0.801	3.955	1.581
460.5	40.6	3.043	-0.839	3.608	-0.130	1.691	0.801	3.860	1.418
462.5	29.4	3.156	-0.724	3.460	-0.242	1.891	0.704		
464.5	38.1	3.076	-0.700	3.633	-0.147	1.749	0.843		
466.5	40	3.206	-0.712	3.626	-0.109	2.058	0.794		
468.5	31.2	3.157	-0.879	3.611	-0.182	2.015	0.806		
470.5	34.1	3.134	-0.852	3.440	-0.105	1.761	0.749	3.759	1.631
472.5	32	3.120	-0.828	3.577	-0.015	1.859	0.794	3.805	1.488
474.5	20.6	3.285	-0.367	3.167	-0.196	1.634	0.830	3.637	1.574
476.5	6	2.986	-0.156	3.604	-0.191	1.891	0.740	3.735	1.423
478.5	4	3.017	-0.127	3.514	-0.467	2.055			
480.5	14.2	3.042	-0.521	3.337	-0.272	1.856	0.818		
482.5	16.7	3.055	-0.428	3.631	-0.226	1.841	0.834	3.858	1.256
484.5	27.7	3.026	-0.531	3.623	-0.101	1.809	0.747		
485.5								3.689	1.147
486.5	18	3.139	-0.223	3.567	-0.226	1.823	0.819		
488.5	43.8	2.906	-0.741	3.663	-0.449	1.765	0.718		
490.5	59.4	3.116	-0.545	3.816	-0.291	1.765	0.709		
492.5	55.5	2.920	-0.867	3.832	-0.103	2.647	0.706		
494.5	60.4	2.977	-0.436	3.985	-0.157	2.226	0.874		
495.5						1.538			
496.5	68.6	2.675	-0.312	4.102	-0.293		0.841		
498.5		2.439	-0.638			2.051			
500.5		1.831	-0.231	3.593	-0.303				
508.5		1.567	-0.300						
512.5		1.071	-0.251						
514.5				3.720	-0.199		0.776		
516.5	95			3.630	-0.392		0.613		

Depth cm.	Nps %	$\delta^{18}O_{Gb}$	$\delta^{13}C_{Gb}$	$\delta^{18}O_{Nps}$	$\delta^{13}C_{Nps}$	Mg/Ca_{Gb}	Mg/Ca_{Nps}	$\delta^{18}O_{Cw}$	$\delta^{13}C_{Cw}$
518.5	96			3.595	-0.177		0.724	3.797	1.055
520.5	97			3.536	-0.176		0.701		
521.5		1.900	-0.625						
522.5	94			3.666	-0.136		0.718	4.092	1.415
523.5		1.500	-0.503	3.664	-0.199				
524.5	88			3.500	-0.322		0.898		
526.5	91			3.339	-0.058		0.744		
528.5	91.7	2.324	-0.468	3.411	-0.240	1.819	0.681	3.521	1.126
529.5	73.2								
530.5	71.6			3.368	-0.153		0.859		
532.5	50.3	3.037	-0.849	3.541	-0.253	1.881	0.723		
534.5	55.3			3.525	-0.051		0.688	3.706	1.514
536.5	58.1	3.161	-1.192	3.586	-0.312		0.732		
538.5	43.7	3.453	-0.931	3.539	-0.382	1.707	0.741	3.891	1.368
540.5	45.2	3.048	-0.897			1.691	0.703	3.814	1.590
542.5	49.3	3.472	-0.982	3.719	-0.166	1.801	0.799	3.838	1.378
544.5	53.9	3.098	-0.804	3.365	-0.257	1.566	0.817		
545.5		3.360	-1.050	3.259	-0.262				
546.5	36	3.495	-0.752	3.439	-0.232	1.837	0.782	3.859	1.538
547.5	44.7								
548.5	41	3.583	-1.189	3.736	-0.171	1.834	0.782	3.668	1.669
549.5	38								
550.5	49.3	3.435	-0.837	3.652	-0.099		0.695	3.870	1.626
551.5	49.3	3.351	-0.767	3.532	-0.123	1.675			
552.5					-0.190				
554.5	53.4	3.415	-1.027	3.569	-0.122	1.767	0.753	3.399	0.834
556.5	46.4	2.974	-0.699	3.705	-0.267	1.563	0.720		
558.5	50	3.248	-0.990	3.740	0.002	1.547	0.765		
559.5	53	3.150	-0.871						
560.5	52	3.332	-0.746	3.819	-0.033	1.482	0.680	3.726	1.505
562.5	67.6	3.436	-0.845	4.001	-0.280	1.858	0.635	3.775	1.587
564.5	83.6	3.568	-0.986	3.983	-0.056	1.458	0.661		
566.5	56.4	3.311	-1.119	3.779	-0.192	1.640	0.795	3.768	1.527
568.5	67.7	3.450	-0.841	3.540	-0.057	1.597	0.754		
570.5	50.5	3.115	-0.683	3.971	-0.122	1.678	0.758		
572.5	45	3.646	-0.449	3.807	-0.064	1.595	0.692	3.800	1.687
574.5	33	3.536	-0.733	3.715	-0.428	1.812	0.781		
576.5	31	3.393	-0.817	3.707	-0.199	1.731	0.751		
578.5	29.2	3.729	-0.819	3.761	-0.421	1.732	0.727		
580.5	29	3.382	-0.730	3.546	-0.158	1.697	0.754	3.772	1.597
582.5	43.6	3.376	-0.684	3.674	-0.404	1.714	0.728		
584.5	37.8	3.421	-0.748	3.677	-0.248	1.757	0.763		
586.5	37.3	3.508	-0.638	3.584	-0.458	1.539	0.763	4.048	1.596
588.5	48	3.438	-0.732	3.882	-0.193	1.510	0.719		
590.5	53.8	3.490	-0.737	3.837	-0.361	1.908	0.743	3.513	1.702
591.5								3.550	1.601
592.5	74	3.430	-0.495	3.932	-0.317	1.924	0.809		
593.5						1.983		3.792	1.582
594.5	70	3.089	-0.745	3.735	-0.472	1.638	0.664		
595.5								3.654	1.430

Depth cm.	Nps %	$\delta^{18}O_{Gb}$	$\delta^{13}C_{Gb}$	$\delta^{18}O_{Nps}$	$\delta^{13}C_{Nps}$	Mg/Ca_{Gb}	Mg/Ca_{Nps}	$\delta^{18}O_{Cw}$	$\delta^{13}C_{Cw}$
596.5	78.9	3.438	-0.966	3.553	-0.489	1.544	0.758		
597.5								3.855	1.601
598.5	68.1	2.738	-0.663			1.965			
600.5	95			3.983	-0.110		0.687		
602.5	92.4			4.133	-0.370		0.703		
603.5								3.588	1.250
604.5	88.3			4.060	-0.122		0.692		
606.5	80.2								
608.5	78.2			3.880	-0.230		0.712	3.701	1.419
610.5	60.1	2.905	-1.002	3.695	-0.304				
611.5						1.748			
612.5	51.2	3.388	-0.948	3.820	-0.234	1.643	0.671	3.784	1.380
614.5	45.3	3.415	-1.100			1.642		2.466	1.629
616.5	44	3.457	-0.998	3.616	-0.235	1.613	0.748	3.958	1.653
618.5	50.4	3.213	-1.409	3.640	-0.109			3.871	1.331
620.5	52.6	3.195	-1.012	3.620	-0.172	1.556	0.763	3.693	1.412
622.5	57.6	3.394	-1.057	3.573	-0.286	1.564		3.416	1.507
624.5	64	3.453	-0.967	3.612	-0.293	1.630	0.673	3.779	1.499
626.5	56.3	3.213	-1.192	3.721	-0.376	1.729			
628.5	55	3.421	-0.903	3.601	-0.393	1.702	0.733	3.822	1.494
630.5	53.9	3.631	-0.848			1.662		4.004	1.411
632.5	49	3.234	-0.904	3.570	-0.069	1.768	0.745		
634.5	54.5					1.679		3.633	1.690
636.5	52.9	3.212	-0.530	3.671	-0.080	1.912	0.751		
638.5	42.2	3.332	-0.742	3.561	-0.479	1.458		3.500	1.570
640.5	51	3.207	-0.287	3.566	-0.059	1.602	0.802	3.497	1.555
642.5	41.4	2.980	-0.642	3.547	-0.373	1.646		3.430	1.638
644.5	34	3.097	-0.546	3.682	-0.158	1.962	0.788	3.781	1.644
646.5	32.1	3.266	-0.305	3.678	-0.169	1.630		3.532	1.516
648.5	33	3.258	-0.289	3.621	-0.127	1.775	0.834		
650.5	34.4			3.803	-0.237	1.736		3.381	1.307
652.5	30.2	3.145	-0.337	3.708	-0.236	1.877	0.843	3.433	1.439
654.5	31.5	3.390	0.072	3.765	-0.152	1.756		3.205	1.371
656.5	33	3.065	-0.237	3.854	-0.058	1.756	0.782	3.260	1.454
658.5	33.7	2.803	-0.652	3.561	-0.278	1.598		3.160	1.179
660.5	78	2.967	-0.566	3.855	-0.237	1.651	0.733		
662.5	82.2	3.216	-0.557			2.293		3.107	1.382
664.5	81.4	3.380	-0.470	3.716	-0.024	2.060	0.689		
666.5	74.1	3.326	-0.491	3.736	-0.379	2.235		3.497	1.396
668.5	89	3.116	-0.220	3.854	-0.154	1.894	0.798	3.271	1.242
670.5	62.3	3.016	-0.244	3.692	-0.293	1.747			
672.5	38.8	3.023	-0.252	3.511	-0.324	1.954	0.766	3.562	1.396
673.5	20.2								
674.5	18.8			3.582	-0.329	2.332		3.096	1.392
675.5	22.1								
676.5	26	2.874	-0.314	3.762	-0.281	2.038	0.712	3.525	1.240
678.5	34.8	2.739	-0.505	3.671	-0.280	2.030		3.332	1.492
680.5	60	2.903	-0.383	3.372	-0.145	2.211	0.820	3.307	1.400
682.5	66.8	3.017	-0.595			1.864			
684.5	77.3	3.257	-0.456	3.713	-0.211	1.869	0.816		

Depth cm.	Nps %	$\delta^{18}O_{Gb}$	$\delta^{13}C_{Gb}$	$\delta^{18}O_{Nps}$	$\delta^{13}C_{Nps}$	Mg/Ca_{Gb}	Mg/Ca_{Nps}	$\delta^{18}O_{Cw}$	$\delta^{13}C_{Cw}$
686.5	90.8	3.123	-0.282			2.310			
688.5	50	2.839	-0.408	3.686	-0.279	2.080	0.824	3.681	1.330
690.5	54.1	2.711	-0.416	3.746	-0.319	1.938			
692.5	96	2.767	-0.271	3.410	-0.152	2.576	0.761	3.518	1.400
694.5	88	3.799	-0.294	3.244	-0.315	2.368			
696.5	86	3.181	-0.285	3.012	-0.254	1.893	0.822		
698.5	80.4	3.286	-0.847			1.841		3.448	1.440
700.5	92	3.377	-0.526	3.366	-0.023	1.618	0.729	3.654	1.173
702.5	81.2	3.189	-0.412			1.572			
704.5	83			3.470	-0.150	1.905	0.815		
706.5	85.3	3.174	-0.618			1.818		4.033	1.826
708.5	60	3.166	-0.707	3.806	0.030	1.888	0.663	3.597	1.656
710.5	55.4					1.813			
712.5	49	3.198	-0.622	3.971	0.117		0.676	3.146	1.511
714.5	37.3	3.089	-0.766			1.721		3.403	1.457
716.5	34.5	3.153	-0.408	3.848	0.068	1.990	0.747	3.395	1.578
718.5	40.8	3.240	-0.581			1.749		3.548	1.464
720.5	50	3.327	-0.542	3.889	-0.145	2.180	0.705	3.592	1.641
722.5	47.5	3.081	-0.267			1.729		3.049	1.472
724.5	37.5	3.166	-0.597	3.979	0.002	2.067	0.681	3.592	1.606
726.5	44.1					1.982		3.491	1.512
728.5	50	3.181	-0.526	3.995	0.047	1.863	0.724	3.771	1.532
730.5	75.6	3.311	-0.500					3.167	1.484
732.5	64			3.898	-0.078		0.604		
734.5	66	3.227	-0.475			1.544		3.558	1.421
736.5	72	3.099	-0.160	3.849	0.025	1.535	0.733		
738.5	66	3.225	-0.409					3.483	1.496
740.5	81	3.498	-0.287	3.944	-0.008		0.789		
742.5	73.8	3.253	-0.472			1.573			
744.5	76	3.276	-0.200	3.978	-0.257	1.604	0.761		
746.5	75.5	3.221	-0.346	3.729	-0.242				
748.5	74	3.344	-0.052	3.828	-0.045		0.765		
750.5	54.6	3.309	-0.123	3.897	0.173	1.564		3.503	1.435
752.5	50	3.411	-0.269	3.843	-0.122	1.688	0.755	3.437	1.348
754.5	51	3.026	-0.261			1.710		3.419	1.460
756.5	28	3.252	-0.039	3.683	0.003	1.575	0.771	3.072	1.258
758.5	31.2	3.131	-0.302			1.790		3.456	1.636
760.5	38	3.266	0.063	3.695	0.085	1.715	0.780	4.106	1.501
762.5	41.3	2.977	-0.037			1.719		2.980	1.412
764.5	34	3.229	-0.094	3.776	0.020		0.851	3.397	1.355
766.5	14.7					1.637			
768.5	23.8	3.070	-0.230	3.726	0.147	1.666	0.814	3.111	1.460
770.5	80.3	2.874	-0.029			1.808		3.071	1.377
772.5	72	2.986	-0.181	3.824	0.149	1.911	0.757		
774.5	80.6	2.840	0.017			1.837			
776.5	78	2.967	-0.155	3.839	-0.003	1.831	0.747		
778.5	53.9	2.866	-0.345			2.258		3.089	1.549
780.5	75.2	3.002	-0.508	3.522	0.297	1.713	0.738	3.547	1.248
782.5	63.7	3.016	-0.609	3.734	-0.042			3.426	1.570
784.5	68.8			3.467	0.198	1.802	0.774	3.425	1.445

Depth cm.	Nps %	$\delta^{18}O_{Gb}$	$\delta^{13}C_{Gb}$	$\delta^{18}O_{Nps}$	$\delta^{13}C_{Nps}$	Mg/Ca_{Gb}	Mg/Ca_{Nps}	$\delta^{18}O_{Cw}$	$\delta^{13}C_{Cw}$
786.5	54.4	2.799	-0.436	3.906	0.126	1.950			
788.5	55.1	2.629	-0.185	3.594	0.125	1.905	0.747	3.157	1.307
790.5	49.1	2.650	-0.126	3.758	-0.213	2.050			
792.5	49.2	2.711	-0.244	3.566	-0.078	2.032	0.885	2.777	1.410
794.5	56.8	2.802	-0.392			1.930		2.940	1.184
796.5	61.7					2.176	0.758	3.147	1.584
798.5	59.5	2.712	-0.240			2.208			
799.5	35.8							3.090	1.291
800.5	54.8	2.746	-0.185			2.082	0.771	3.192	1.288
802.5	62.2	2.756	-0.315	3.887	-0.018				
804.5	70.7	2.917	-0.355	3.990	0.016	1.996	0.726	3.270	1.374
806.5	70	3.042	-0.502	3.744	-0.156	1.904			
808.5	67.3			3.634	0.041	2.081	0.825	3.299	1.324
810.5	56.9	2.995	-0.689	3.924	0.112	3.443		3.350	1.421
812.5	56.9			3.745	-0.085	2.571	0.737	3.075	1.151
814.5	56.7	2.759	-0.544	3.790	0.001	2.272		3.211	1.229
816.5	50	2.854	-0.283	3.569	0.035	2.144	0.728	3.311	1.237
818.5	54	2.794	-0.462			1.899			
820.5	63.7	2.660	-0.495			2.614	0.814	3.334	1.332
822.5	49	2.422	-0.284	3.684	-0.019	2.185		2.859	1.402
824.5	62.3			3.494	-0.056	2.054	0.813		
826.5	61	2.684	-0.206			2.046			
828.5	52.4			3.444	0.030	2.568	0.769	3.300	1.391
830.5	27.6	2.437	-0.775	3.206	-0.074	2.344			
832.5	19.8	2.706	-0.599	3.331	0.193	2.100	0.797		
834.5	48.2	2.642	-0.606			2.078			
836.5	66.7	2.481	-0.241	3.339	0.175	2.082	0.807	2.812	0.948
838.5	48.6	2.729	-0.733	3.510	-0.101	2.146		2.716	0.943
840.5	71.7					3.067	1.017	2.995	1.114
842.5	71	2.574	-0.409	3.514	-0.090	2.726			
844.5	70.1	2.485	-0.069	3.437	0.064	2.355	0.784		
846.5	66.8			3.433	-0.044	2.463			
848.5	88	2.437	-0.399	3.536	0.009	2.184	0.903	2.734	0.846
850.5	86.5	2.628	-0.264	3.347	-0.027	2.742			
852.5	93.5	2.709	-0.578	3.596	0.038	1.996	0.880	2.871	0.792
854.5	95	2.893	-0.624	3.631	0.074				
856.5	92	2.920	-0.656			1.978	0.829		
858.5	79	2.998	-1.105			2.355		3.239	1.563
860.5	76.9	2.787	-0.817	3.477	-0.063	1.988	0.729	3.233	1.529
862.5	68.3	2.903	-0.697			1.796		3.212	1.610
864.5	66.7	2.990	-0.580	3.570	0.073	2.264	0.736	3.024	1.381
866.5	61	2.999	-0.627	3.701	0.036	1.953		3.294	1.637
868.5	63.4	3.073	-0.606			2.234	0.822	3.359	1.642
870.5	66	2.885	-0.607	3.703	0.001	1.848		3.156	1.468
872.5	54	2.972	-0.761	3.455	0.175	1.896	0.817	3.086	1.477
874.5	53	2.963	-0.776	3.656	-0.055	2.331		3.150	1.532
876.5	54.1	3.092	-0.792	3.605	0.085	1.748	0.768	3.144	1.500
878.5	67	2.872	-0.731	3.806	0.102	1.863		3.226	1.565
880.5	63.5					1.902	0.788	3.154	1.618
882.5	57.2	3.040	-0.569	3.623	-0.182	1.934		3.296	1.695

Depth cm.	Nps %	$\delta^{18}O_{Gb}$	$\delta^{13}C_{Gb}$	$\delta^{18}O_{Nps}$	$\delta^{13}C_{Nps}$	Mg/Ca_{Gb}	Mg/Ca_{Nps}	$\delta^{18}O_{Cw}$	$\delta^{13}C_{Cw}$
884.5	69.8	2.858	-0.628			1.750	0.749	3.502	1.341
886.5	33.1	2.545	-0.663	3.685	0.032	2.465			
888.5	28.2	2.843	-0.156			2.420	0.808		
890.5	28.4	2.667	-0.395	3.504	-0.138	2.288		3.246	1.557
892.5	28.6	2.512	-0.239	3.291	0.064	2.190	0.863		
894.5	37	2.663	-0.514	3.454	-0.102	2.351		3.365	1.532
896.5	44.5	2.707	-0.505	3.330	-0.164	2.198	0.859	3.387	1.034
898.5	44	2.630	-0.571	3.579	-0.058	2.649			
900.5	53.6	2.366	-0.572	3.548	-0.025		0.818		
902.5	67	2.716	-0.499	3.439	-0.022	2.371			
904.5	65.3	2.855	-0.696	3.251	0.019	1.843	0.918		
906.5	51.7	2.943	-0.478	3.576	-0.184	2.086		2.932	0.830
908.5	50.9	2.694	-0.691	3.230	-0.179	1.813	0.775		
910.5	26.7			3.472	0.071	1.942		2.932	1.362
912.5	26.1	2.781	-0.492			2.297	0.868	2.883	0.907
914.5	19.1	2.650	-0.647	3.289	-0.170	2.205		3.014	1.141
916.5	26.9	2.809	-0.781	3.107	-0.175	2.204	0.837	3.239	1.051
918.5	18	2.665	-0.619	3.243	-0.103	2.705		3.348	1.203
920.5	15.2	2.571	-0.682	3.166	0.032	2.181	0.911	3.365	1.006
922.5	10	2.599	-0.460			2.104			
924.5	12.9	2.638	-0.511	3.164	-0.102		0.972		
926.5	13.4	2.427	-0.244	3.296	-0.244	2.243			
928.5	10	2.583	-0.246	2.996	-0.298	2.170	0.953	3.161	0.912
930.5	9	2.454	-0.386	3.385	-0.610	2.218			
932.5	49.6	2.190	-0.465	3.066	-0.133		0.783		
934.5	25.8	2.313	-0.264	2.757	-0.900	2.340			
936.5	23.8	2.298	-0.540	3.290	-0.437	2.710	0.984		
938.5	23	2.356	-0.378	3.383	-0.304	2.081		2.969	1.000
940.5	33	2.233	-0.304	2.971	-0.566	2.221	0.885	3.306	1.034
942.5	28	2.301	-0.705	3.380	-0.508	2.397			
944.5	38	2.056	-0.650	3.259	-0.331	2.371	0.933	3.115	1.100
946.5	31	2.262	-0.457	3.109	-0.390	2.110		3.149	1.451
948.5	46	2.372	-0.817	2.988	-0.359	1.952	0.771	2.859	1.231
950.5	52	2.617	-0.466	3.385	-0.493	2.238			
951.5								3.045	0.830
952.5	35	2.397	-0.664	3.328	-0.628	2.140	0.828		
953.5								3.488	0.822
954.5	49	2.598	-0.769	3.559	-0.443	1.812			
955.5								3.054	0.862
956.5	40	2.619	-0.672	3.358	-0.381		0.821		
958.5	37	2.444	-0.658	3.558	-0.735	1.997			
959.5								3.478	0.890
960.5	34	2.612	-0.447	3.483	-0.489	2.014	0.856		
961.5								2.855	0.990
962.5	49	2.709	-0.830	3.487	-0.661	2.424			
963.5								3.226	1.162
964.5	42	2.536	-1.048	3.332	-0.373	2.164	0.833		
965.5								3.461	1.228
966.5	26.8	2.531	-1.071	3.427	-0.838	2.183			
967.5								3.377	1.176

Depth cm.	Nps %	$\delta^{18}O_{Gb}$	$\delta^{13}C_{Gb}$	$\delta^{18}O_{Nps}$	$\delta^{13}C_{Nps}$	Mg/Ca_{Gb}	Mg/Ca_{Nps}	$\delta^{18}O_{Cw}$	$\delta^{13}C_{Cw}$
968.5	19.6	2.599	-1.202	3.189	-0.567	2.265	0.824		
969.5								3.366	1.151
970.5	25.4	2.271	-1.296	3.534	-0.268	2.127			
971.5								3.333	1.150
972.5	14	2.308	-0.924	3.206	-0.610	2.164	0.751		
973.5								3.081	1.024
974.5	15	2.446	-1.008	3.220	-0.539	2.511			
975.5								3.304	1.201
976.5	16.5	2.401	-0.886	3.148	-0.438	2.039	0.862		
977.5								2.967	1.174
978.5	24.3	2.545	-0.975	3.329	-0.610	2.228			
979.5								2.698	0.820
980.5	33.1	2.527	-0.787	2.913	-0.694	2.439	0.935		
981.5								3.445	1.224
982.5	65.3	2.449	-1.017	3.298	-0.384	2.197			

Nps %, relative abundance of *N. pachyderma* sin.; *Gb, G. bulloides*; *Cw, C. wuellerstorfi*

A

Alley RB, Andrews JT, Barber DC, Clark PU. 2005. Comment on "Catastrophic ice shelf breakup as the source of Heinrich event icebergs" by C. L. Hulbe et al. *Paleoceanography* **20**, PA1009, doi: 10.1029/2004PA001086

Alley RB, MacAyeal DR. 1994. Ice-rafted debris associated with binge/purge oscillations of the Laurentide Ice Sheet. *Palaeoceanography* **9**: 503-511

Anand PH, Elderfield H, Conte H. 2003. Calibration of Mg/Ca thermometry in Planktonic foraminifers from a sediment trap time series. *Palaeoceanography* **18**, 1050, doi: 10.1029/2002PA000846

Andrews JT. 1998. Abrupt changes (Heinrich events) in late Quaternary North Atlantic marine environments: a history and review of data and concepts. *Journal of Quaternary Science* **13** (1): 3-16

Andrews JT, Barber DC. 2001. Dansgaard-Oeschger events: Is there a signal off the Hudson Strait Ice Stream? *Quaternary Science Reviews* **21**: 443-454

Andrews JT, Tedesco K. 1992. Detrital carbonate-rich sediments, northwestern Labrador Sea: Implications for ice-sheet dynamics and iceberg rafting (Heinrich) events in the North Atlantic. *Geology* **20**: 1087-1090

Arbic BK, Macayeal DR, Mitrovica JX, Milne GA. 2004. Palaeoclimate - Ocean tides and Heinrich events. *Nature* **432** (7016): 460-460

Auffret GA, Boelaert A, Vergnaud-Grazzini C, Muller C, Kerbrat R. 1996. Identification of Heinrich Layers in core KS 01 North - Eastern Atlantic (46N, 17W), implications for their origin. *Marine Geology* **131**: 5-20

Auffret GA, Zaragosi S, Dennielou B, Cortijo E, Van Rooij D, Grousset F, Pujol C, Eynaud F, Siegert M. 2002. Terrigenous fluxes at the Celtic margin during the last glacial cycle. *Marine Geology* **188**: 79-108

Austin WEN, Bard E, Hunt JB, Kroon D, Peacock JD. 1995. The ^{14}C age of the Icelandic Vedde Ash: Implications for Younger Dryas marine reservoir age corrections. *Radiocarbon* **37**: 53-62

Austin WEN, Kroon D. 1996. Late glacial sedimentology, foraminifera and stable isotope stratigraphy of the Hebridean Continental Shelf, northwest Scotland. from Andrews JT, Austin WEN, Bergsten H, Jennings, AE (eds.). 1996. Late Quaternary Palaeoceanography of the North Atlantic Margins, *Geological Society Special Publication* No. 111, pp. 187-213

Austin WEN, Wilson LJ, Hunt JB. 2004. The age and chronostratigraphic significance of the North Atlantic Ash Zone II. *Journal of Quaternary Science* **19**: 137-146

B

Backstrom DL, Kuijpers A, Heinemeier J. 2001. Late Quaternary North Atlantic paleoceanographic records and stable isotopic variability in four planktonic foraminiferal species. *Journal of Foraminiferal Research* **31**: 25-32

Bard E. 2001. Comparison of alkenone estimates with other paleotemperature proxies. *Geochemistry, Geophysics, Geosystems* **2**(1), doi:10.1029/2000GC000050

Bard EM, Arnold B, Hamelin N, Tisnerat-Laborde N, Cabioch G. 1998. Radiocarbon calibration by means of mass spectrometic Th-230/U-234 and C-14 ages of corals: An updated database including samples from Barbados, Mururoa and Tahiti. *Radiocarbon* **40**: 1085-1092

Bard E, Arnold M, Mangerud J, Paterne M, Labeyrie L, Duprat J, Melieres MA, Sonstergaarde E, Duplessy JC. 1994. The North-Atlantic atmosphere-sea surface C-14 gradient during the Younger Dryas climatic event. *Earth and Planetary Science Letters* **126**(4): 275-287

Bard E, Hamelin B, Fairbanks RG, Zindler A, Mathieu G, Arnold M. 1990. U/th and C-14 ages of corals from Barbados and their use for calibrating the C-14 time scale beyond 9000years BP. *Nuclear Instruments & Methods in Physics Research Section B-Beam interactions with materials and atoms* **52**(3-4): 461-468

Barker S, Cacho I, Benway H, Tachikawa K. 2005. Planktonic foraminiferal Mg/Ca as a proxy for past oceanic temperatures: a methodological overview and data compilation for the Last Glacial Maximum. *Quaternary Science Reviews* **24**: 821-834

Barker S, Elderfield H. 2002. Foraminiferal calcification response to glacial-interglacial changes in atmospheric CO_2. *Science* **297**: 833-836

Barker S, Greaves M, Elderfield H. 2003. A study of cleaning procedures used for foraminiferal Mg/Ca paleothermometry. *Geochemistry, Geophysics, Geosystems* **4** (9), 8407, doi:10.1029/2003GC000559

Barker S, Kiefer T, Elderfield H. 2004. Temporal changes in North Atlantic circulation constrained by planktonic foraminiferal shell weights, *Paleoceanography* **19**: PA3008, doi: 10.1029/2004PA001004

Bauch D, Carstens J, Wefer G. 1997. Oxygen isotope composition of living Neogloboquadrina pachyderma (sin) in the Arctic Ocean. *Earth and Planetary Science Letters* **146**: 47-58

Bé AWH. 1977. An ecological, zoogeographic and taxonomic review of recent planktonic foraminifera, Oceanic Micropaleontology, Academic Press, New York, 1977, 1-100 pp.

Beck JW, Richards DA, Edwards RL, Silverman BW, Smart PL, Donahue DJ, Hererra-Osterheld S, Burr GS, Calsoyes L, Jull AJT, Biddulph D. 2001. Extremely large variations of atmospheric C-14 concentration during the last glacial period. *Science* **292** (5526): 2453-2458

Becker B, Kromer B. 1993. The continental tree-ring record - absolute chronology, C-14 calibration and climatic change at 11KA. *Palaeogeography Palaeoclimatology Palaeoecology* **103** (1-2): 67-71

Beer J, Mende W, Stellmacher R. 2000. The role of the sun in climate forcing. *Quaternary Science Reviews* **19**: 403-415

Bjork G, Soderkvist J, Winsor P, Nikolopoulos A, Steele M. 2002. Return of the cold halocline layer to the Amundsen Basin of the Arctic Ocean: Implications for the sea ice mass balance. *Geophysical Research Letters* **29** (11), doi:10.1029/2001GL014157

Bond G, Broecker W , Johnsen S, McManus J, Labeyrie L, Jouzel J, Bonani G. 1993. Correlations between climate records from North Atlantic sediments and Greenland ice. *Nature* **365:** 143-147

Bond G, Showers W, Cheseby M, Lotti R, Almasi P, deMenocal P, Priore P, Cullen H, Hajdas I, Bonani G. 1997. A pervasive millennial-scale cycle in North Atlantic Holocene and glacial climates. *Science* **278**: 1257-1266

Bond GC, Kromer B, Beer J, Muscheler R, Evans MN, Showers W, Hoffman S, Lotti-Bond R, Hajdas I, Bonani G. 2001. Persistent Solar Influence on North Atlantic Climate during the Holocene. *Science* **294**: 2130-2136

Bond GC, Lotti R. 1995. Iceberg discharges into the North Atlantic on millennial timescales during the last glaciation. *Science* **267**: 1005-1010

Bond GC, Showers W, Elliot M, Evans M, Lotti R, Hajdas I, Bonani G, Johnson S. 1999. The North Atlantic's 1–2 kyr climate rhythm: relation to Heinrich events, Dansgaard–Oeschger cycles and the Little Ice Age. *Geophys. Monogr.* **112**: 35-58

Bond GH, Heinrich H, Broecker WS, Labeyrie L, McManus J, Andrews J, Huon S, Jantschik R, Clasen S, Simet C, Tedesco K, Klas M, Bonani G, Ivy S. 1992. Evidence for massive discharges of icebergs into the North Atlantic Ocean during the Last Glacial period. *Nature* **360**: 245-249

Bond GWS, Cheseby M, Lotti R, Almasi P, deMenocal P, Priore P, Cullen H, Hajdas I, Bonani G. 1997. A Pervasive Millennial-Scale Cycle in North Atlantic Holocene and Glacial Climates. *Science* **278**: 1257-1266

Bowen DQ, Phillips FM, McCabe AM, Knutz PC, Sykes GA. 2002. New data for the Last Glacial Maximum in Great Britain and Ireland. *Quaternary Science Reviews* **21**: 89-101

Boyle EA, Keigwin LD. 1987. North Atlantic thermohaline circulation during the past 20,000 years linked to high-latitude surface temperature. *Nature* **330**: 35–40

Broecker WS. 1994. Massive iceberg discharges as triggers for global climate change. *Nature* **372**: 421-424

Broecker WS. 1998. Paleocean circulation during the last deglaciation: A bipolar seesaw? Paleoceanography **13**: 119-121

Broecker WS, Bond G, Klas MA. 1990. A Salt Oscillator in the Glacial Atlantic? 1. The Concept. *Paleoceanography* **5**: 469-477

C

Cacho I, Grimalt JO, Pelejero C, Canals M, Sirro FJ, Flores JA, Shackleton N. 1999. Dansgaard-Oeschger and Heinrich event imprints in Alboran Sea paleotemperatures. *Paleoceanography* **14**: 698-705

Cacho I, Grimalt JO, Sierro FJ, Shackleton N Canals M. 2000. Evidence for enhanced Mediterranean thermohaline circulation during rapid climate coolings. *Earth and Planetary Science Letters* **183**: 417-429

Carstens J, Hebbeln D, Wefer G. 1997. Distribution of planktic foraminifera at the ice margin in the Arctic (Fram Strait). *Marine Micropaleontology* **29**: 257-269

Chapman MR, Shackleton NJ, and Duplessy JC. 2000. Sea surface temperature variability during the last glacial-interglacial cycle: assessing the magnitude and pattern of climate change in the North Atlantic. *Palaeoceanogr. palaeocl.*, **157**: 1-25

Chappell J. 2002. Sea level changes forced ice breakouts in the Last Glacial cycle: new results from coral terraces. *Quaternary Science Review* **21**:1229-1240

Charbit S, Ritz C, Ramstein G. 2002. Simulations of Northern Hemisphere ice-sheet retreat: sensitivity to physical mechanisms involved during the Last Deglaciation. *Quaternary Science Reviews* **21**: 243-265.

Clark PU, McCabe AM, Mix AC, Weaver AJ. 2004. Rapid Rise of Sea level 19,000 Years Ago and Its Global Implications. *Science* **304**: 1141-1144

Clark PU, Pisias NG, Stocker TF, Weaver AJ. 2002. The role of the thermohaline circulation in abrupt climate change. *Nature* **415**: 863-869

CLIMAP project members.1984. The last interglacial ocean: *Quaternary Research* **21**: 123-224

CLIMAP project members. 1981. Seasonal reconstructions of the of the earth's surface at the Last Glacial Maximum. Geological Society of America Map and Chart Series MC-36, pp 18

CLIMAP project members. 1976. The surface of the ice-age earth. *Science* **191**: 1131–1137

Corliss BH, McCorkle DC,. Higdon DMA. 2002. Time series study of the carbon isotopic composition of deep-sea benthic foraminifera. *Paleoceanography* **17** (3): Art. No. 1036 2002

Craig H, Gordon LI. 1965. Deuterium and oxygen 18 variations in the ocean and the marine atmosphere, in *Stable Isotopes in Oceano-graphic Studies and Paleotemperatures*, E. Tongiorgi (Ed.) Lab. di Geol. Nucl., Cons. Naz. delle Ric., Pisa, Italy, pp. 9-130

Curry R, Dickson B, I. Yashayaev I. 2003. A change in the freshwater balance of the Atlantic Ocean over the past four decades. *Nature* **426**: 826-829

D

Dansgaard W et al. 1993. Evidence for general instability of past climate from a 250-kyr ice-core record. *Nature* **364**: 218–220

Darling KF, Wade CM, Stewart IA, Kroon D, Dingle R, Brown AJL. 2000. Molecular evidence for genetic mixing of Arctic and Antarctic subpolar populations of planktonic foraminifers. *Nature* **405**:43-47

Davies G, Glendhill A, Hawksworth C. 1985. Upper crustal recycling in southern Britain: evidence from Nd and Sr isotopes. *Earth and Planetary Science Letters* **75**: 1-12

de Angelis H, Skvarca P. 2003. Glacier Surge After Ice Shelf Collapse. *Science* **299**: 1560-1562

de Mol B, Van Rensbergen P, Pillen S, Van Herreweghe, K, Van Rooij D, McDonnell A, Huvenne V, Ivanov M, Swennen R, Henriet JP. 2002. Large deep-water coral banks in the Porcupine Basin, southwest of Ireland. *Marine Geology* **188** (1-2): 193-231

de Vernal A, Eynaud F, Henry M, Hillaire-Marcel C, Londeix L, Mangin S, Matthiessen J, Marret F, Radi T, Rochon A, Solignac S, Turon JL. 2005. Reconstruction of sea-surface conditions at middle to high latitudes of the Northern Hemisphere during the Last Glacial Maximum (LGM) based on dinoflagellate cyst assemblages, *Quaternary Science Reviews* **24**: 897-924

de Vernal A, Hillaire-Marcel C. 2000. Sea-ice cover, sea-surface salinity and halo-thermocline structure of the northwest North Atlantic: modern versus full glacial conditions. *Quaternary Science Reviews* **19**: 65-85

de Villiers S, Greaves M, Elderfield H. 2002. An intensity ratio calibration method for the accurate determination of Mg/Ca and Sr/Ca of marine carbonates by ICP-AES. *Geochemistry, Geophysics, Geosystems* **3**(1), doi:10.129/2001 GC000169

Doake CSM, Corr HFJ, Rott H, Skvarca P, Young NW. 1998. Breakup and conditions for stability of the northern Larsen Ice Shelf, Antarctica. *Nature* **391**: 778-780

Domack EW, Jull AJT, Anderson JB, Linick TW, Williams CR. 1989. Application of tandem accelerator mass-spectrometer dating to late Pleistocene-Holocene sediments of the East Antarctic continental shelf. *Quaternary Research* **31**: 277-287

Dowdeswell JA, Maslin MA, Andrews JT, McCave IN. 1995. Iceberg production, debris rafting, and the extent and thickness of Heinrich layers (H-1, H-2) in North Atlantic sediments. *Geology* **23**: 301-304

Duplessy JC, Labeyrie L, Juilletleclerc A, Maitre F, Duprat J, Sarnthein M. 1991. Surface salinity reconstruction of the North Atlantic during the Last Glacial Maximum. *Oceanol. Acta.* **4:** 311-324

Durazzi JT. 1981. Stable isotope studies of planktonic-foraminifera in North Atlantic core tops. Palaeogeography Palaeoclimatology Palaeoecology **33**: 157-172.

E

Edwards RL, Beck JW, Burr GS, Donahue DJ, Chappell JMA, Bloom AL, Druffel ERM, Taylor FW. 1993. A large drop in atmospheric 14C/12C and reduced melting in the Younger Dryas, documented with 230^{Th} ages of corals. *Science* **260**: 962-968

Eiriksson J, Larsen G, Krudsen KL, Heinemeier J, Simonarson LA. 2004. Marine reservoir age variability and water mass distribution in the Iceland Sea. *Quaternary Science Reviews* **23**(20-22): 2247-2268

Elderfield H, Ganssen G. 2000. Past temperature and d18O of surface ocean waters inferred from foraminiferak Mg/Ca ratios. *Nature* **405**: 442-445

Elliot ML. Labeyrie,. Duplessy JC. 2002. Changes in North Atlantic deep-water formation associated with the Dansgaard-Oeschger temperature oscillations (60-10 kyr). *Quaternary Science Reviews* **21**: 1153-1165

Elliot ML, Labeyrie L, Bond G, Cortijo E, Turon JL, Tisnerat N, Duplessey JC. 1998. Millennial-scale iceberg discharges in the Irminger Basin during the last glacial period: relationships with the Heinrich events and environmental settings. *Palaeoceanography* **13**: 433-446

F

Fairbanks RG, Mortlock RA, Chiu TC, Cao L, Kaplan A, Guilderson TP, Fairbanks TW, Bloom AL, Grootes PM, Nadeau MJ. 2005. Radiocarbon calibration curve spanning 0 to 50,000 years BP based on paired Th-230/U-234/U-238 and C-14 dates on pristine corals. *Quaternary Science Reviews* **24** (16-17): 1781-1796

Farmer GL, Barber DC, Andrews JT. 2003. Provenance of Late Quaternary ice-proximal sediments in the North Atlantic: Nd, Sr and Pb isotopic evidence. *Earth and Planetary Science Letters* **209**: 227-243

Fichefet T , Poncin C, Goosse H, Huybrechts P, Janssens I, Le Treut H. 2003. Implications of changes in freshwater flux from the Greenland ice sheet for the climate of the 21st century. *Geophysical Research Letters.* **30** (17) art. no. 1911

Finkel RC, Nishiizumi K. 1997. Beryllium 10 concentrations in the Greenland Ice Sheet Project 2 ice core from 3-40 ka. *Journal of geophysical research-oceans* **102** (C12): 26699-26706

Flower BP, Hastings DW, Hill HW, Quinn TM. 2004. Phasing of deglacial warming and laurentide ice sheet meltwater in the Gulf of Mexico. *Geology* **32**:597-600

Flückiger J, Knutti R, White JWC. (in press). Ocean-ice sheet interactions as potential trigger for Heinrich Events. *Paleoceanography.*

Frank N, Paterne M, Ayliffe L, van Weering T, Henriet JP, Blamart D. 2004. Eastern North Atlantic deep-sea corals: tracing upper intermediate water Delta C-14 during the Holocene. *Earth and Planetary Science Letters* **219** (3-4): 297-309

Friend CRL, Strachan RA, Kinny PD Watt GR. 2003. Provenance of the Moine Supergroup of NW Scotland: evidence from geochronology of detrital and inherited zircons from (meta)sedimentary rocks, granites and migmatites. *Journal of the Geological Society* **160**: 247-257

Frohlich C. 2000. Observations of irradiance variations. *Space Science Reviews* **94**: 15-24

Fronval T, Jansen E, Bloemendal J, Johnsen S. 1995. Oceanic evidence for coherent fluctuations in Fennoscandian and Laurentide ice sheets on millennium timescales. *Nature* **374:** 443–446

G

Ganopolski A, Rahmstorf S. 2001. Rapid changes of glacial climate simulated in a coupled climate model. *Nature* **409**: 153-157

Ganssen GM, Kroon D. 2000. The isotopic signature of planktonic foraminifera from the NE Atlantic surface sediments: implications for the reconstruction of past oceanic conditions. *Journal of the Geological Society, London* **157**: 693-699

Gronvold k, Oskarsson N, Johnsen SJ, Clausen HB, Hammer CU, Bond G, Bard E. 1995. Ash layers from Iceland in the Greenland GRIP ice core correlated with oceanic and land sediments. *Earth and Planetary Science Letters* **135**: 149-155

Grootes PM, Stuiver M. 1997. Oxygen 18/16 variability in Greenland snow and ice with 103 to 105-year resolution. *Journal of Geophysical Research* **102**: 26,455–26,470

Data set accessed from http://depts.washington.edu/qil/datasets/gisp2 _main. html.

Grousset FE, Cortijo E, Huon S, Hervé L, Richter T, Burdloff D, Duprat J, Weber O. 2001. Zooming in on Heinrich Layers. *Paleoceanography* **16** (3): 240-259

Grousset FE, Labeyrie JA, Sinko A, Cremer M, Bond G, Duprat G, Cortijo E, Huon S. 1993. Patterns of ice-rafted detritus in the glacial North Atlantic (40-55N). *Palaeoceanography* **8**: 175-192

Grousset FE, Parra M, Bory A, Martinez P, Bertrand P, Shimmield G, Ellam R. 1998. Saharan wind regimes traced by the Sr-Nd isotopic composition of the tropical Atlantic sediments: Last Glacial Maximum to today. *Quaternary Science Reviews* **17**: 395-409

Grousset FE, Pujol C, Labeyrie L, Auffret G, Boelaert A. 2000. Were the North Atlantic Heinrich events triggered by the behavior of the European ice sheets? *Geology* **28**: 123-126

Gudmondsson A, Van Vliet-Lanoë B,Bourgeois O, Dauteuil O, Embry JC, Guillou H, Schneider JL. 2003. The last glacial in Northern Iceland: Geothermal and permafrost controls. *Geophysical Research Abstracts, European Geophysical Society* **5**: 02868

Gwiazda RH, Hemming SR, Broecker WS. 1996. Provenance of icebergs during Heinrich event 3 and the contrast to their sources during other Heinrich episodes. *Paleoceanography* **11** (4): 371-378

Gwiazda RH, Hemming SR, Broecker WS. 1996. Tracking the sources of icebergs with lead isotopes: The provenance of ice-rafted debris in Heinrich layer 2. *Paleoceanography* **11** (1): 77–93

H

Hagen S, Hald M. 2002. Variation in surface and deep water circulation in the Denmark Strait, North Atlantic, during marine isotope stages 3 and 2. *Paleoceanography* **17** (4): Art. No. 1061

Hall IR, Moran SB, Zahn R, Knutz PC, Shen C-C, Edwards RL. (submitted). Accelerated draw-down of meridional overturning in the late-glacial Atlantic triggered by transient pre-H event freshwater perturbation. *Geophysical Research Letters.*

Hallock P. 1987. Fluctuations in the trophic resource continuum; a factor in global diversity cycles? *Paleoceanography* **2**: 457-471

Heinrich, H., 1988. Origin and consequences of cyclic ice-rafting in the Northeast Atlantic ocean during the past 130 000 years. *Quaternary Research* **29**: 142-152.

Hemming SR. 2004. Heinrich events: Massive late pleistocene detritus layers of the North Atlantic and their global climate imprint. *Reviews of Geophysics* **42**, RG1005,doi:10.1029/2003RG000128

Hemming, SR, Bond GC, Broecker WS, Sharp WD, Klas-Mendelson M. 2000. Evidence from 40Ar/39Ar ages of individual horneblende grains for varying Laurentide sources of iceberg discharges 22,000 to 10,500 14C yr B.P. *Quaternary Research* **54**: 372-383

Hemming SR, Broecker WS, Sharp WD, Bond GC, Gwiazda RH, McManus JF, Klas M, Hajdas I. 1998. Provenance of Heinrich layers in core V28-82, northeastern Atlantic: $^{40}Ar/^{39}Ar$ ages of ice-rafted hornblende, Pb isotopes in feldspar grains, and Nd-Sr-Pb isotopes in the fine sediment fraction. *Earth and Planetary Science Letters* **164**: 317-333

Hemming SR, Gwiazda RH, Andrews JT, Broecker WS, Jennings AE, Onstott TC. 2000. $^{40}Ar/^{39}Ar$ and Pb-Pb study of individual hornblende and feldspar grains from southeastern Baffin Island glacial sediments: Implications for the provenance of the Heinrich layers. *Canadian Journal of Earth Science* **37**: 879–890

Hemming SR, Hajdas I. 2003. Ice-rafted detritus evidence from Ar-40/Ar-39 ages of individual hornblende grains for evolution of the eastern margin of the Laurentide ice sheet since 43 C-14 ky. *Quaternary International* **99**: 29-43

Hemming SR, Hall CM, Biscaye PE, Higgins SM, Bond GC, McManus JF, Barber DC, Andrews JT, Broecker WS. 2002. $^{40}Ar/^{39}Ar$ ages and $^{40}Ar^*$ concentrations of fine-grained sediment fractions from North Atlantic Heinrich layers. *Chemical Geology* **182**: 583–603

Hill AE, Mitchelson-Jacob EG. 1993. Observations of a poleward-flowing saline core on the continental-slope west of Scotland. *Deep-sea research Part I - Oceanographic Research Papers* **40** (7): 1521-1527

Hillaire-Marcel C, Bilodeau G. 2000. Instabilities in the Labrador Sea water mass structure during the last climatic cycle. *Canadian Journal of Earth Science* **37**: 795-809

Hoffman PF. 1989. Precambrian geology and tectonic history of North America. In Bally AW, Palmer AR (Eds.), The geology of North America - An Overview, Geological Society America, Boulder CO. 47-512

Holliday NP, Pollard RT, Read JF, Leach H. 2000. Water mass properties and fluxes in the Rockall Trough. *Deep-sea research Part I – Oceanographic Research Papers* **47** (7): 1303-1332

Hughes TJ, Denton GH, Andersen BG, Schilling DH, Fastook JL, Lingle CS. 1981. The Last Great Ice Sheets: A Global View, in: G. H. Denton, T. J. Hughes (Eds.), The Last Great Ice Sheets, J. Wiley & Sons, NY, 1981, pp. 274

Hulbe CL. 1997. An ice shelf mechanism for Heinrich layer production. *Paleoceanography* **12**: 711-717

Hulbe CL. 2005. Reply to comment by Alley et al. on "Catastrophic ice shelf breakup as the source of Heinrich event icebergs". *Paleoceanography* **20**: PA1011, doi:10.1029/2004PA001118

Hulbe CL, MacAyeal DR, Denton GH, Kleman J, Lowell TV. 2004. Catastrophic ice shelf break up as the source of Heinrich event icebergs. *Paleoceanography* **19**, PA1004,doi:10.1029/2003PA000890

I

Imbrie J, Kipp NG. 1971. A new micropaleontological method for quantitative paleoclimatology: application to a late Pleistocene Caribbean core. In: Turekian KK (ed) The Late Cenozoic glacial ages. Yale University Press, New Haven pp 71-179

IPCC 2001 Synthesis Report, IPCC

J

Johannessen T, Jansen E, Flatøy A, Ravelo AC. 1994. The relationship between surface water masses, oceanographic fronts and paleoclimatic proxies in surface sediments of Greenland, Iceland, Norwegian Seas. *NATO ASI Ser. 1* **17**: 61-85

Johnson RG, Lauritzen SE. 1995. Hudson Bay-Hudson Strait jökulhlaups and Heinrich events: A hypothesis. *Palaeogeography Palaeoclimatology Palaeoecology* **117**: 123-137

Jongma JI, Dreisschaert, E, Fichefet T, Goosse H, Renssen H. 2004. Coupling an Iceberg Model to a 3d Climate Model: Simulation of Modern and Mid-HoloceneConditions. *Geophysical Research Abstracts* EGU 2004, Vol. 6

Jullien E, Grousset FE, Hemming SR, Peck VL, Hall IR, Jeantet C. (in press). Contrasting conditions preceding MIS3 and MIS2 Heinrich events. *Global and Planetary Change*

K

Kandiano ES, Bauch HA. 2003. Surface ocean temperatures in the north-east Atlantic during the last 500 000 years: evidence from foraminiferal census data. *Terra Nova* **15** (4): 265-271

Kandiano ES, Bauch HA, Müller A. 2004. Sea surface temperature variability in the North Atlantic during the last two glacial-interglacial cycles: comparison of faunal, oxygen isotopic, and Mg/Ca-derived records. *Palaeogeography, Palaeoclimatology, Palaeoecology* **204**: 145-164

Kenyon NH. 1987. Mass-wasting features on the continental slope of Northwest Europe. *Marine Geology* **74**: (1-2): 57-77

Knorr G, Lohmann G. 2003. Southern Ocean origin for the resumption of Atlantic thermohaline circulation during deglaciation. *Nature* **424**: 532-536

Knutz PC. 2000. Late Pleistocene glacial fluctuation and palaeoceanography on the continental margin of North West Britain. University of Wales, Cardiff (thesis)

Knutz PC, Austin WEN, Jones EJW. 2001. Millennial-scale depositional cycles related to British Ice Sheet variability and North Atlantic paleocirculation since 45 kyr B.P., Barra Fan, U. K. margin. *Paleoceanography* **16**: 53–64

Knutz PC, Hall IR, Zahn R, Rassmussen TL, Kuijpers A, Moros M, Shackleton NJ. 2002. Multiecadal ocean variability and NW European ice sheet surges during the last deglaciation. *Geochemistry, Geophysics, Geosystems* **3**(12): 1007

Kohfeld KE, Fairbanks RG, Smith SL, Walsh ID. 1996. Neogloboquadrina pachyderma (sinistral coiling) as paleoceanographic tracers in polar waters: Evidence from Northeast Water Polyna plankton tows, sediment traps, and surface sediments. *Paleoceanography* **11**: 679-699

Kroon D, Darling K. 1995. Size and upwelling control of the stable isotope composition *Neogloboquadrina dutertrei* (d'Orbigny), *Globigerinoides ruber* (d'Orbigny), *Globigerina bulloides* d'Orbigny: examples from the Panama Basin and Arabian Sea. *Journal of Foraminiferal Research* **25** (1): 39-52

Kucera M., Darling KF. 2002. Cryptic species of planktonic foraminifera: their effect on palaeoceanographic reconstructions. *Philosophical Transactions of the Royal Society, London* **360**: 695-718

Kucera M, Rosell-Melé A, Schneider R, Waelbroeck C, Weinelt M. 2005. Multiproxy approach for the reconstruction of the glacial ocean surface (MARGO). *Quaternary Science Reviews* **24**: 813-819

L

Lacasse C. 2001. Influence of climate variability on the atmospheric transport of Icelandic tephra in the subpolar North Atlantic. *Global and Planetary Change* **29** (1-2): 31-35

Lacasse C, Sigurdsson H, Carey S, Paterne M, Guichard F. 1996. North Atlantic deep-sea sedimentation of Late Quaternary tephra from the Iceland hotspot Source. *Marine Geology* **129** (3-4): 207-235

Lackschewitz KS, Baumann KH, Gehrke B, Wallrabe-Adams HJ, Thiede J, Bonani G, Endler R, Erlenkeuser H, Heinemeier J. 1998. North Atlantic ice sheet fluctuations 10,000-70,000 yr ago as inferred from deposits on the Reykjanes ridge, southeast of Greenland. *Quaternary Research* **49**:171-182

Lackschewitz KS, WallrabeAdams HJ. 1997. Composition and origin of volcanic ash zones in Late Quaternary sediments from the Reykjanes Ridge: Evidence for ash fallout and ice-rafting. *Marine Geology* **136** (3-4): 209-224

Lagerklint IK, Wright JD. 1999. Late glacial warming prior to Heinrich event 1: The influence of ice rafting and large ice sheets on the timing of initial warming. *Geology* **27**: 1099-1102

Lea DW, Mashiotta TA, Spero HJ. 1999. Controls on magnesium and strontium uptake in planktonic foraminifera determined by live culturing. *Geochimica et Cosmochimica Acta*. **63**: 2369-2379

Lean J, Beer J, Bradley R. 1995. Reconstruction of solar irradiance since 1610-implications for climate change. *Geophysical Research Letters* **22**: 3195-3198

Levitus S, Antonov JI, Boyer TP. 2005. Warming of the World Ocean, 1955-2003. *Geophysical Research Letters* **32**

Little MG, Schneider RR, Kroon D, Price B, Summerhayes CP, Segl M. 1997. Trade wind forcing of upwelling, seasonality, and Heinrich events as a response to sub-Milankovitch climate variability. *Paleoceanography* **12**: 568-576

M

MacAyeal DR. 1993. Binge/purge oscillations of the Laurentide Ice Sheet as a cause of the North Atlantic's Heinrich events. *Palaeoceanography* **8**: 775-784

MacAyeal DR, Scambos TA, Hulbe CL, Fahnestock MA. 2003. Catastrophic ice-shelf break-up by an ice-shelf-fragment-capsize mechanism. *Journal of Glaciology* **49**: 2-36

McCabe AM, Clark PU. 1998. Ice-sheet variability around the North Atlantic Ocean during the last deglaciation. *Nature* **392**: 373-377

McIntyre A, Molfino B. 1996. Forcing of Atlantic equatorial and subpolar millennial cycles by precession. *Science*, **5294**: 1867-1870.

McManus JF, Francois R, Gherardi JM, Keigwin LD, Brown-Leger S. 2004. Collapse and rapid resumption of Atlantic meridional circulation linked to deglacial climate changes. *Nature* **428**: 834-837

Mackensen A, Bickert T. 1999. Stable Carbon Isotopes in Benthic Foraminifera: Proxies for Deep and Bottom water Circulation and New Production. *In:* Fischer, G & Wefer, G (eds.), Use of Proxies in Paleoceanography - Examples from the South Atlantic, Springer, Berlin, Heidelberg, 229-254

Madureira LAS, van Kreveld SA, Eglinton G, Conte M, Ganssen G, van Hinte JE, Ottens JJ. 1997. Late Quaternary high-resolution biomarker and other sedimentary climate proxies in a northeast Atlantic core. *Paleoceanography* **12**: 255-269

Manighetti B, McCave IN, Maslin M, Shackleton NJ. 1995. Chronology for Climate-Change- developing age models for the biogeochemical ocean flux study cores. *Paleoceanography* **10** (3): 513-525

Marshall SJ, Clarke GKC. 1997. A continuum mixture model of ice stream thermomechanics in the Laurentide Ice Sheet .2. Application to the Hudson Strait Ice Stream. *Journal of Geophysical Research - Solid Earth* **102**: 20615-20637

Martrat B, Grimalt JO, Lopez-Martinez C, Cacho I, Sierro FJ, Flores JA, Zahn R, Canals M, Curtis JH, Hodell DA. 2004. Abrupt temperature changes in the Western Mediterranean over the past 250,000 years. *Science* **306** (5702): 1762-1765

Martinson DG, Pisias NG, Hays JD, Imbrie J, Moore TC, Shackleton NJ. 1987. Age dating and the orbital theory of the ice ages - development of a high-resolution-0 to 300,000-year chronostratigraphy. *Quaternary Research* **27** (1): 1-29

Mashiotta TA, Lea DW, Spero HJ. 1999. Glacial-interglacial changes in Subantarctic sea surface temperature and delta O-18-water using foraminiferal Mg. *Earth and Planetary Science Letters* **170**: 417-432

Maslin MA, Shackleton NJ, Pflaumann U. 1995. Surface water temperature, salinity, and density changes in the northeast Atlantic during the last 45,000 years: Heinrich events, deep water formation and climatic rebounds. *Paleoceanography* **10**: 527-544

Meese DA, Gow AJ, Alley RB, Zielinski GA, Grootes PM, Ram M, Taylor KC, Mayewski PA, Bolzan JF. 1997. The Greenland Ice Sheet Project 2 depth-age scale: Methods and results. *Journal of Geophysical Research-Oceans* **102**: 26411-26423

Meese DA, Gow AJ, Grootes P, Mayewski PA, Stuiver M, Taylor KC, Waddington ED, Zielinski GA. 1994. The accumulation record from the GISP2 core as an indicator of climate-change throughout the Holocene. *Science* **266**: 1680-1682

Mix AC, Bard E, Schneider R. 2001. Environmental processes of the ice age: land, oceans, glaciers (EPILOG). *Quarternary Science Review* **20**: 627-657

Morey AE, Mix AC, Pisias NG. 2005. Planktonic foraminiferal assemblages preserved in surface sediments correspond to multiple environment variables. *Quaternary Science Reviews* **24**: 925-950

Moros M, Kuijpers A, Snowball I, Lassen S, Backstrom D, Gingele F, McManus J. 2002. Were glacial iceberg surges in the North Atlantic triggered by climatic warming? *Marine Geology* **192** (4): 393-417

N

NODC (Levitus) World Ocean Atlas. 1998. Data provided by the NOAA-CIRES Climate Diagnostics Center, Boulder, Colorado, USA, from their web site at http://www.cdc.noaa.gov/

Nürnberg D. 1995. Magnesium in tests of *Neogloboquadrina pachyderma* sinistral from high northern and southern latitudes. *Journal of Foraminiferal Research* **25**: 350-368

Nürnberg D, Bijma J, Hemleben C. 1996. Assessing the reliability of magnesium in foraminiferal calcite as a proxy for water mass temperatures. *Geochim. Cosmochim. Acta.* **60**: 803-814

Nürnberg D, Müller A, Schneider RR. 2000. Paleo-sea surface temperature calculations in the equatorial east Atlantic from Mg/Ca ratios in planktic foraminifera: A comparison to sea surface temperature estimates from U-37(K'), oxygen isotopes, and foraminiferal transfer function. *Paleoceanography* **15**:124-134

O

Oppenheimer M. 1998. Global warming and the stability of the West Antarctic Ice Sheet. *Nature* **393:** 325-332

Oppo DW, Lehman SJ. 1993. Mid-depth circulation of the subpolar North-Atlantic during the last glacial maximum. *Science* **259** (5098): 1148-1152

Ortiz JD, A. C. Mix AC, Rugh W, Watkins JM, Collier RW. 1996. Deep-dwelling planktonic foraminifera of the northeastern Pacific Ocean reveal environmental control of oxygen and carbon isotopic disequilibria. *Geochim. Cosmochim. Acta* **60**: 4509-4523

P

Pak DK, Lea DW, Kennett JP. 2004. Seasonal and interannual variation in Santa Barbara Basin water temperatures observed in sediment trap foraminiferal Mg/Ca. *Geochemistry, Geophysics, Geosystems* **5**: Art. No. Q12008

Pälike H, Shackleton NJ, Rohl U. 2001. Astronomical forcing in Late Eocene marine sediments. *Earth and Planetary Science Letters* **193** (3-4): 589-602

Pahnke K, Zahn R. 2005. Southern hemisphere water mass conversion linked with North Atlantic climate variability. Science **307**: 1741-1746

Peck VL, Hall IR, Zahn R, Elderfield H, Grousset FE, and Scourse JD. (Submitted). High Resolution Evidence for Linkages between European Ice Sheet Instability and Atlantic Meridional Overturning Circulation. *Earth and Planetary Science Letters* **243**: 476-488

Pflaumann U, Duprat J, Pujol C, Labeyrie LD. 1996. SIMMAX: A modern analog technique to deduce Atlantic sea surface temperatures from planktonic foraminifera in deep-sea sediments. *Paleoceanography* **11**: 15-35

Pflaumann U, Sarnthein M, Chapman M, d'Abreu L, Funnell B, Huels M, Kiefer T, Maslin M, Schulz H, Swallow J, van Kreveld S, Vautravers M, Vogelsang E, Weinelt M. 2003. Glacial North Atlantic: Sea-surface conditions reconstructed by GLAMAP 2000. *Paleoceanography* **18** (3): 1065, doi:10.1029/2002PA000774

Pollard RT, Griffiths MJ, Cunningham SA, Read JF, Perez FF, Rios AF. 1996. Vivaldi 1991 - A study of the formation, circulation, and ventilation of Eastern North Atlantic Central Water. *Progress in Oceanography* **37**: 167-192

Prell WL. 1985. The stability of low-latitude sea surface temperatures: An evaluation of the CLIMAP reconstruction with emphasis on the positive SST anomalies, Technical report for the Department of Energy, TRO25, Brown Univ., Providence, RI.

R

Rahmstorf S, Alley RB. 2002. Stochastic resonance in glacial climate. *Eos* **83**: 129–135

Rashid H, Hesse R, Piper DJW. 2003. Origin of unusually thick Heinrich layers in ice-proximal regions of the northwest Labrador Sea. *Earth and Planetary Science Letters* **208**: 319-336

Rasmussen TL, Thomsen E. 2004. The role of the North Atlantic Drift in the millenial timescale glacial climate fluctuations. *Palaeogeography Palaeoclimatology Palaeoecology* **210** (1): 101-116

Rasmussen TL, Thomsen E, Labeyrie L, vanWeering TCE. 1996. Circulation changes in the Faeroe-Shetland Channel correlating with cold events during the last glacial period (58-10 ka). *Geology* **24** (10): 937-940

Rasmussen TL, Thomsen E, van Weering TCE, Labeyrie L. 1996. Rapid changes in surface and deep water conditions at the Faeroe margin during the last 58,000 years. *Paleoceanography* **11** (6): 757-771

Ravelo AC, Fairbanks RG. 1992. Oxygen isotopic composition of multiple species of planktonic foraminifera: recorders of the modern photic zone temperature gradient. *Paleoceanography* **7**: 815-831

Ravelo AC, Fairbanks RG, Philander SGH. 1990. Reconstructing tropical Atlantic hydrography using planktonic foraminifera and an ocean model. *Paleoceanography* **5**: 409- 431.

Revel M, Sinko JA, Grousset FE, Biscaye PE. 1996. Sr and Nd isotopes as tracers of North Atlantic lithic particles: Paleoclimatic implications. *Palaeoceanography* **11**(1): 95-113

Reynolds LA, Thunell RC. 1985. Seasonal succession of planktonic foraminifera in the subpolar North Pacific. *Journal of Foraminiferal Research* **15**: 282-301

Rickaby RE, Elderfield MH. 2005. Evidence from the high-latitude North Atlantic for variations in Antarctic Intermediate water flow during the last deglaciation. *Geochemistry, Geophysics, Geosystems* **6**: doi: 10.1029/2004GC000858

Rignot E, Jacobs SS. 2002. Rapid bottom melting widespread near Antarctic ice sheet grounding lines. *Science* **296**: 2020-2023

Rignot E, Thomas RH. 2002. Mass balance of polar ice sheets.. *Science* **297**: 1502-1506

Robinson SG, Maslin MA, McCave IN. 1995. Magnetic susceptibility variations in Upper Pleistocene deep-sea sediments of the NE Atlantic: Implications for ice rafting and paleocirculation at the last glacial maximum. *Palaeoceanography* **10**(2): 221-250

Roche D, Paillard D, Cortijo E. 2004. Constraints on the duration and freshwater release of Heinrich event 4 through isotope modelling. *Nature* **432**: 379-382

van Rooij, David; Blamart, Dominique; Unnithan, Vikram (2001): Porcupine Basin and Rockall Trough, off Western Ireland September 7 - 11, 2001: Cruise Report MD123-Géosciences Leg 2, part GEOMOUND, unpublished Cruise Report, Renard Centre for Marine Geology (RCMG). Gent University, Belgium, 67 pp

Rosenthal Y, Lohmann GP. 2002. Accurate estimation of sea surface temperatures using dissolution-corrected calibrations for Mg/Ca paleothermometry. *Paleoceanography* **17** (3): 1044, doi: 10.1029/2001PA000749

Rosenthal Y, Lohmann GP, Lohmann KC, Sherrell RM. 2000. Incorporation and preservation of Mg in Globigerinoides sacculifer: Implications for reconstructing the temperature and O-18/O-16 of seawater. *Paleoceanography* **15**:135-145

Ruddiman WF. 1977. Late Quaternary deposition of ice-rafted sand in the sub-polar north Atlantic (40 to 65N), *Geological Society of America Bulletin* **88**: 1831-1821

Ruddiman WF, Glover LK. 1972. Vertical mixing of ice-rafted volcanic ash in North-Atlantic sediments. *Geological Society of America Bulletin* **83**: 2817-2836

S

Samon SD, Alexander Jr. EC. 1987. Calibration of the interlaboratory ^{40}Ar-^{39}Ar dating standard, MMhb-1. Chemical Geology (Isotope Geoscience Section) **66**: 27-34

Sarnthein M, Gersonde R, Niebler S, Pflaumann U, Spielhagen R, Thiede J, Wefer G, Weinelt M. 2003. Overview of Glacial Atlantic Ocean Mapping (GLAMAP 2000). *Palaeoceanography* **18** (2), 1030,doi:10.1029/2002PA000769

Sarnthein M, Thiede J, Pflaumann U, Erlenkeuser H., Futterer D , Koopmann B, Lange H, Seibold E. 1982. Atmospheric and oceanic circulation patterns off Northwest Africa during the past 25 million years. In: Rad, U., K. Hinz, M. Sarnthein, and E. Seibold, (Eds.) Geology of the Northwest African Continental Margin. Springer, Berlin, pp. 545–604

Sarnthein M, Winn K, Jung SJA, Duplessy JC, Labeyrie L, Erlemkeuser H, Ganssen G. 1994. Changes in East Atlantic Deep Water Circulation Over the Last 30,000 years - 8 time-slice reconstructions. *Paleoceanography* **9**: 209-267

Sautter LR, Thunell RG. 1991. Seasonal variability in the $\delta^{18}O$ and $d^{13}C$ of planktonic foraminifera from an upwelling environment. *Paleoceanography* **3**: 307-334

Schäfer-Neath C, Paul A. 2003. The Atlantic Ocean at the Last Glacial Maximum: 1. Objective mapping of the GLAMAP Sea-Surface Conditions, Eds Wefer G., S. Mulitzer, V. Ratmeyer, Springer-Verlag Berlin pp 531-548

Schiebel R, Bijma J, Hemleben C. 1997. Population dynamics of the planktic foraminifer Globigerina bulloides from the eastern North Atlantic. *Deep-Sea Research Part I-Oceanographic Research Papers* **44**: 1701-1713

Schmidt MW, Spero HJ, Lea DW. 2004. Links between salinity variation in the Caribbean and North Atlantic thermohaline circulation. *Nature* **428**:160-163

SchmukerB, Schiebel R. 2002. Planktic foraminifers and hydrography of the eastern and northern Caribbean Sea. *Marine Micropaleontology* **46**: 387-403

Schulz M, Mudelsee M. 2002. REDFIT: Estimating red-noise spectra directly from unevenly spaced paleoclimatic time series. *Computational Geosciences* **8**: 421–426

Scourse JD, Furze MFA. 2001. A critical review of the glaciomarine model for Irish sea deglaciation: evidence from southern Britain, the Celtic shelf and adjacent continental slope. *Journal of Quaternary Science* **16**(5): 419-434

Scourse JD, Hall IR, McCave IN, Young JR, Sugdon C. 2000. The origin of Heinrich layers: evidence from H2 for European precursor events. *Earth and Planetary Science Letters* **182**: 187-195

Shackleton NJ. 1974. Attainment of isotopic equilibrium between ocean water and the benthonic foraminifer genus *Uvigerina*: isotopic changes in the ocean during the last glacial. Collogue CNRS Centre National de la Recherche Scientifique, Paris, 219 203-210

Shackleton NJ. 1969. The last interglacial in the marine and terrestrial records. *Philosophical Transactions of the Royal Society Series B* **174**:135-154

Shackleton NJ, 2000. The 100,000-year Ice Age Cycle Identified and Found to Lag Temperature, Carbon Dioxide and Orbital Eccentricity. *Science* **289:**1897-1902

Shackleton NJ, Fairbanks RG, Chiu TC. Parrenin F. 2004. Absolute calibration of the Greenland time scale: implications for Antarctic time scales and for Delta C-14. *Quaternary Science Reviews* **23** (14-15): 1513-1522

Shackleton NJ, Hall MA, Vincent E. 2000. Phase relationships between millennial-scale events 64,000-24,000 years ago. *Paleoceanography* **15** (6): 565-569

Shackleton NJ, Opdyke NJ. 1973. Oxygen isotope and palaeomagnetic stratigraphy of equatorial Pacific core V28– 238: Oxygen isotope temperatures and ice volumes on a 105 year and 106 year scale. *Quaternary Research* **3**: 39– 55

Shaffer G, Olsen SM, Bjerrum CJ. 2004. Ocean subsurface warming as a mechanism for coupling Dansgaard-Oeschger climate cycles and ice-rafting events. *Geophysical Research Letters* **31**: art. no. L24202

Shipboard Party 2001 (see van Rooij et al., 2001)

Siegert MJ, Dowdeswell JA. 2002. Late Weichselian iceberg, meltwater and sediment production from the Eurasian Ice Sheet: results from numerical ice-sheet modelling. *Marine Geology* **188**: 109-127

Simstich J, Sarnthein M, Erlenkeuser H. 2003. Paired delta O-18 signals of Neogloboquadrina pachyderma (s) and Turborotalita quinqueloba show thermal stratification structure in Nordic Seas. *Marine Micropalaeontology* **48**: 107-125

Snoeckx H, Grousset FE, Revel M, Boelaert A. 1999. European contribution of ice-rafted sand to Heinrich layers H3 and H4. *Marine Geology* **158**: 197-208

Spero HJ, Lea DW. 1996. Experimental determination of stable isotope variability in Globigerina bulloides: implications for paleoceanographic reconstructions. *Marine Micropalaeontolgy* **28**: 231-246

Spielhagen RF, Erlenkeuser H. 1994. Stable oxygen and carbon isotopes in planktonic foraminifera from Arctic Ocean surface sediments – reflection of the low-salinity surface water layer. *Geology* **119**: 227-250.

St John K, Flower BP, Krissek L. 2004. Evolution of iceberg melting, biological productivity, and the record of Icelandic volcanism in the Irminger basin since 630 ka. *Marine Geology* **212**: 133-152

Stuiver M, Braziunas TF, Becker B, Kromer B. 1991. Climatic, solar, oceanic, and geomagnetic influences on late-glacial and Holocene atmospheric C-14/C-12 change. *Quaternary Research* **35** (1): 1-24

Stuiver M. Reimer PJ, Reimer RW. 2005. CALIB 5.0 (www program and documentation) http://radiocarbon.pa.qub.ac.uk/calib/

Stuiver M, Reimer PJ, Bard E, Beck JW, Burr GS, Hughen K, Kromer B, McCormac G, VanderPlicht J, Spurk M. 1998. INTCAL98 radiocarbon age calibration, 24,000-0 cal BP. *Radiocarbon* **40:** 1041–1083

Svensmark H, FriisChristensen E. 1997. Variation of cosmic ray flux and global cloud coverage - A missing link in **solar**-climate relationships. Journal of atmospheric and solar-terrestrial physics **59**: 1225-1232

T

Tachikawa K, Elderfield H .2002. Microhabitat effects on Cd/Ca and delta C-13 of benthic foraminifera. *Earth and Planetary Science Letters* **202** (3-4): 607-624

Taylor, SP, Haywood AM, Valdes PJ, Sellwood BW. 2004. An evaluation of two spatial interpolation techniques in global sea-surface temperature reconstructions: Last Glacial Maximum and Pliocene case studies. *Quaternary Science Reviews* **23**: 1041-1051

U

UNESCO Background papers and supporting data on the International Equation of State of Seawater. 1980. *UNESCO Technical Papers in Marine Science* **38**: 192

V

Vance D, Archer C. 2002. Isotopic constraints on the origin of Heinrich event precursors. *Geochim. Cosmochim. Acta*, ***66***, Suppl. **1**: A798

van Kreveld SA, Ganssen GM, VanHinte JE, Melkert MM, Troelstra SR VanderBorg K, deJong A. 1995. A method for quantifying deep-sea carbonate dissolution using C-14 dating. *Radiocarbon* **37**: 585-592

van Kreveld S, Knappertsbusch M, Ottens J, Ganssen G, van Hinte JE. 1996. Biogenic carbonate and ice-rafted debris (Heinrich layers) accumulation in deep sea sediments from a Northeast Atlantic piston core. *Marine Geology* **131**: 21-46

van Kreveld S, Sarnthein M, Erlenkeuser H, Grootes P, Jung S, Nadeau MJ, Pflaumann U, Voelker A. 2000. Potential links between surging ice sheets, circulation changes, and the Dansgaard-Oeschger cycles in the Irminger Sea, 60-18 kyr. *Palaeoceanography* **15**(4): 425-442

Vaughan DG, Doake CSM. 1996. Recent atmospheric warming and retreat of ice shelves on the Antarctic Peninsula. *Nature* **379**: 328-331

Veiga-Pires CC, Hillaire-Marcel C. 1999. U and Th isotope constraints on the duration of Heinrich events H0-H4 in the southeastern Labrador Sea. *Paleoceanography* **14**: 187-199

Vidal L, Labeyrie L, Cortijo E, Arnold M, Duplessy JC, Michel E, Becqué S, van Weering TCE. 1997. Evidence for changes in the North Atlantic Deep Water linked to meltwater surges during the Heinrich events. *Earth and Planetary Science Letters* **146**: 13-27

Voelker AHL, Grootes PM, Nadeau MJ, Sarnthein M. 2000. Radiocarbon levels in the Iceland Sea from 25-53 kyr and their link to the Earth's magnetic field intensity. *Radiocarbon* **42**: 437-452

Voelker AHL, Sarnthein M, Grootes PM, Erlenkeuser H, Laj C, Mazaud A, Nadeau MJ, Schleicher M. 1998. Correlation of marine C-14 ages from the Nordic seas with the GISP2 isotope record: Implications for C-14 calibration beyond 25 kyr BP. *Radiocarbon* **40**: 517–534

Volkmann R. 2000. Planktic foraminifers in the outer Laptev Sea and the Fram Strait - Modern distribution and ecology. *Journal of Foraminifera Research* **30**: 157-176

Volkmann R, Mensch M. 2001. Stable isotope composition (delta O-18, delta C-13) of living planktic foraminifers in the outer Laptev Sea and the Fram Strait. *Marine Micropaleontology* **42**: 163-188

W

Wadsworth ER. 2005. The identification and characterisation of the North Atlantic Heinrich events using environmental magnetic techniques. Thesis St. Andrews

Waelbroeck C, Duplessy JC, Michel E, Labeyrie L, Paillard D, Duprat D. 2001. The timing of the last deglaciation in North Atlantic climate records, *Nature* **412**: 724–726

Weaver AJ, Hillaire-Marcel C. 2004. Global Warming and the Next Ice Age. *Science* **304**: 400-402

Williams RS Jr., Ferrigno JG. 1999. Estimated present-day area and volume of glaciers and maximum sea level rise potential, Satellite Image Atlas of Glaciers of the World, US Geological Survey (USGS).

Willamowski A, Zahn R. 2000. Upper ocean circulation in the glacial North Atlantic from benthic foraminiferal isotope and trace element fingerprinting. *Paleoceanography* **15**: 515–527

Wilson LJ, Austin WEN, Jansen E 2002 The last British Ice Sheet: growth, maximum extent and deglaciation. *Polar Research* **21** (2): 243-250

Wu GP, Hillaire Marcel C. 1994. Oxygen isotope compositions of sinistral Neogloboquadrina-pachyderma tests in surface sediments – North Atlantic Ocean. Geochim. Cosmochim. Acta **58**: 1303-1312

Y

Yokoyama Y, Esat TM, Lambeck K. 2001. Coupled climate and sea level changes deduced from Huon Peninsula coral terraces of the last ice age. *Earth and Planetary Science Letters* **193**: 579-587

Z

Zahn R, Schönfeld J, Kudrass H, Park M, Erlenkeuser H, Grootes P. 1997. Thermohaline instability in the North Atlantic during meltwater events: Stable isotope and icerafted detritus records from core SO75-26KL, Portuguese margin. *Paleoceanography* **12**(5): 696–710

Zaragosi S, Eynaud F, Pujol C, Auffret GA, Turon JL, Garlan T. 2001. Initiation of the European deglaciation as recorded in the northwestern Bay of Biscay slope environments (Meriadzek Terrace and Trevelyan Escarpment): a multi-proxy approach. *Earth and Planetary Science Letters* **188**: 493-507

Zielinski GA, Mayewski PA, Meeker LD, Gronvold K, Germani MS, Whitlow S, Twickler MS, Taylor K. 1997. Volcanic aerosol records and tephrochronology of the Summit, Greenland, ice cores. *Journal of Geophysical Research-Oceans* **102** (C12): 26625-26640

Zwally HJ, Abdalati W, Herring T, Larson K, Saba J, Steffen K. 2002. Surface melt-induced acceleration of Greenland ice-sheet flow. *Science* **297:** 218-222

Available online at www.sciencedirect.com
SCIENCE DIRECT
ELSEVIER
Earth and Planetary Science Letters 243 (2006) 476–488
EPSL
www.elsevier.com/locate/epsl

High resolution evidence for linkages between NW European ice sheet instability and Atlantic Meridional Overturning Circulation

V.L. Peck [a,*], I.R. Hall [a,*], R. Zahn [b,*,1], H. Elderfield [c], F. Grousset [d], S.R. Hemming [e], J.D. Scourse [f]

[a] *School of Earth, Ocean and Planetary Science, Main Building, Park Place, Cardiff University, Cardiff CF10 3YE, UK*
[b] *Institució Catalana de Recerca i Estudis Avançats (ICREA), and Universitat Autonoma de Barcelona, 08193, Bellaterra, Spain*
[c] *Department of Earth Sciences, Cambridge University, Downing Street, Cambridge CB2 3EQ, UK*
[d] *Departement de Geologie et Oceanographie, Université Bordeaux I, Avenue des Facultés, 33405 Talence cedex, France*
[e] *Department of Earth and Environmental Sciences, Lamont–Doherty Earth Observatory, 61 Route 9W Palisades, NY 10964, USA*
[f] *School of Ocean Sciences, University of Wales (Bangor), Menai Bridge, Angelsey, LL59 5AB, UK*

Received 12 June 2005; received in revised form 19 December 2005; accepted 20 December 2005
Available online 3 February 2006
Editor: E. Boyle

Abstract

Published studies show that ice rafted debris (IRD) deposition preceding Heinrich (H) events H1 and H2 in the NE Atlantic was derived from the NW European ice sheets (NWEIS), possibly offering clues about ice sheet sensitivity and stability, and the mechanisms that caused periodic collapse of the Laurentide Ice Sheet (LIS). We present detailed lithological and geochemical records, including radiogenic isotope fingerprinting, of IRD deposits from core MD01-2461, proximal to the last glacial British Ice Sheet (BIS), demonstrating persistent instability of the BIS, with significant destabilisation occurring 1.5–1.9 kyr prior to both H1 and H2, dated at 16.9 and 24.1 kyr BP, respectively, in the NE Atlantic. Paired Mg/Ca and $\delta^{18}O$ data from the surface dwelling *Globigerina bulloides* and subsurface dwelling *Neogloboquadrina pachyderma* sinistral are used to determine late-glacial variability of temperature, salinity and stratification of the upper water column. A picture emerges that the BIS was in a continuing state of readjustment and never fully reached steady state. Increased sea surface temperatures appear to have triggered the episode of NWEIS instability preceding H1. It seems most probable that the so-called 'precursor' events were not linked to the H events. However, if response to a common thermal forcing is considered, an increased response time of the LIS, up to ~2 kyr longer than the NWEIS, may be inferred. Negative salinity excursions of up to 2.6 indicate significant incursions of melt water associated with peaks in NWEIS instability. Decreased surface density led to a more stable stratification of the upper water column and is associated with reduced ventilation of intermediate waters, recorded in depleted epibenthic $\delta^{13}C$ (*Cibicidoides wuellerstorfi*). We suggest that instability and meltwater forcing of the NWEIS temporarily weakened Atlantic Meridional Overturning Circulation, allowing transient advance of southern-sourced waters to this site, prior to H events 1 and 2.
© 2006 Elsevier B.V. All rights reserved.

Keywords: NW European Ice Sheet; ocean–climate linkage; Atlantic Meridional Overturning Circulation; ice rafted debris; Heinrich events; ice sheet instability

* Corresponding authors.
E-mail addresses: peckvl@cf.ac.uk (V.L. Peck), hall@cf.ac.uk (I.R. Hall), rainer.zahn@uab.es (R. Zahn).
[1] Also at [a].

0012-821X/$ - see front matter © 2006 Elsevier B.V. All rights reserved.
doi:10.1016/j.epsl.2005.12.023

1. Introduction

Numerical modelling suggests that increases in freshwater flux of just 0.01 Sv, if routed to the centres of active deep-water convection, have the capability to cause considerable reduction in the Atlantic Meridional Overturning Circulation (AMOC), accounting for mean annual temperature changes of between 5–10 °C in the circum-North Atlantic region over a matter of decades [1]. The last glacial NW European ice sheets (NWEIS; comprising the British, Icelandic and Fennoscandian ice sheets) likely achieved a maximum ice volume of $\sim 10 \times 10^6$ km^3, approximately one third that of the North American, Laurentide ice sheet (LIS) [2], often considered to be the principal driver behind millennial scale variability in AMOC during the last glacial period [3–5]. Rather than the volume of these freshwater reservoirs however, it is the location of the NWEIS close to the main North Atlantic convection centres, that enhances their potential to perturb AMOC and climate during episodes of accelerated ice sheet melting.

Despite intensive research into Heinrich (H) events (see recent review [6]) and Dansgaard–Oeschger (D–O) climatic oscillations that are associated with ~1.5 kyr ice rafted detritus (IRD) cycles in the NE Atlantic (e.g. [7,8]), there is no clear consensus on the underlying mechanism that caused these periodic phenomena. Hypotheses relating to H event initiation include external forcing, probably intimately linked to perturbations of AMOC dynamics (e.g. [9]), and the internal dynamics of the LIS [10,11]. Modelling [10,11] and lack of significant D–O frequency surging of the Hudson Strait ice stream [12] suggest that the LIS was relatively stable and largely immune to high-frequency (climate) forcing, favouring internal instabilities as the trigger for periodic LIS collapse every 7–10 kyr [10,13]. Conversely, the sensitivity of the smaller NWEIS of the last glacial is well documented [14–16]. Recent studies have identified NWEIS instability prior to H events 1 and 2 [17–19], possibly supporting a common external triggering mechanism of H events, assuming individual ice sheet response times were, in part, proportional to ice sheet size/extent of marine margin. Understanding the forcing and climatic feedbacks that propel these millennial scale cycles, including their interference with AMOC, is crucial for the development of predictive climate models [1].

Here we present evidence from a marine sediment core for NWEIS variability preceding H1 and H2 (~16.8 and ~24.0 kyr BP; [20,21]). Multi-proxy foraminiferal and lithologic geochemical analyses allow us to document the variability of the British (BIS), East Greenland/Icelandic (EGIIS) and Laurentide ice sheets in fine detail in a framework of AMOC variability.

2. Materials and methods

Sediment core MD01-2461 was recovered from the north-western flank of the Porcupine Seabight (51° 45′ N, 12° 55′W) in a water depth of 1153 m (Fig. 1). The site is ideally located to monitor BIS variability as it is close to the last glacial Irish Sea ice stream, a principal outlet glacier draining the BIS [22]. As previous studies illustrate, a cyclonic surface gyre circulation in the subpolar North Atlantic routed iceberg drifts from the circum-North Atlantic ice sheets to this region [23–25] so that the core records also monitor IRD derived from other North Atlantic margins.

The chronology of MD01-2461 is based on 15 monospecific foraminifera (*Globigerina bulloides*, or *Neogloboquadrina pachyderma* sinistral) AMS ^{14}C dates. Radiocarbon ages were calibrated to calendar years before present (yr BP) using the CALIB programme (version 5.0.1 with the MARINE04 data set), incorporating a 400 yr correction for marine reservoir age [26] (Table 1). However, comparison of the relative abundance of *N. pachyderma* sin. (%; an apparent relative sea surface temperature (SST) proxy, [27]) with the GISPII δ^{18}O record [28] (Fig. 2b, c) suggests that the constant ^{14}C-reservoir assumption is likely incorrect. The climate-based correlation ($r^2 = 0.829$) suggests that the 400-yr ^{14}C-reservoir correction is a considerable

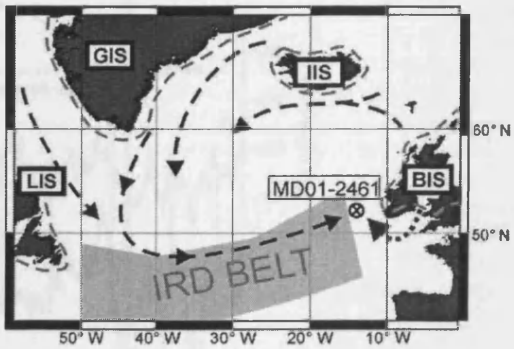

Fig. 1. Location of core MD01-2461 at the northeastern extent of the Ruddiman belt of preferential IRD accumulation [25]. Dashed black lines indicate likely routes of icebergs derived from circum-North Atlantic ice sheets due to an anti-clockwise surface gyre during the last glacial [23,25]. Dashed grey lines represent last glacial maximum ice sheet (IS) extent. B — British; I — Icelandic; G — Greenland; L — Laurentide. Dashed grey lines represent last glacial maximum ice sheet (IS) extent.

Table 1
Radiocarbon ages for MD02-2461

Laboratory code	Material	Depth (cm)	^{14}C age (yr BP)	Error age ($\pm 1\sigma$ yr)	Calendar age (a BP)
SUERC-3302	*N. pachyderma* sin.	196.5	11,032	39	12,709
SUERC-3303	*G. bulloides*	208.5	12,551	46	13,992
SUERC-3306	*N. pachyderma* sin.	228.5	11,950	43	13,337[a]
SUERC-3287	*N. pachyderma* sin.	244.5	14,530	58	16,819
SUERC-3307	*N. pachyderma* sin.	276.5	15,118	64	17,692
SUERC-3308	*N. pachyderma* sin.	302.5	15,518	63	18,564
SUERC-3309	*N. pachyderma* sin.	324.5	15,174	60	17,586[a]
SUERC-3288	*N. pachyderma* sin.	356.5	17,130	77	19,993
SUERC-3289	*G. bulloides*	392.5	18,233	87	21,053
SUERC-3290	*N. pachyderma* sin.	412.5	18,665	89	21,688
SUERC-3292	*N. pachyderma* sin.	436.5	19,128	94	22,287
SUERC-2278	*G. bulloides*	478.0	20,193	118	23,702
SUERC-2279	*N. pachyderma* sin.	528.5	20,931	129	24,577
SUERC-2275	*N. pachyderma* sin.	570.5	21,565	128	25,647
SUERC-2274	*N. pachyderma* sin.	602.5	22,234	147	25,792

[a] Age reversals removed.

underestimate, with offset between the tuned and ^{14}C-based age model increasing following H2 and the last glacial maximum (LGM; Fig. 2a). Elevated ^{14}C-marine reservoir ages have previously been interpreted from North Atlantic sediments, reflecting sea-ice or meltwater cover reducing air–sea gas exchange and isotope equilibration [29–32]. Our correlation between *N. pachyderma* sin. % and the Greenland ice core palaeoclimatic record suggests ^{14}C-marine reservoir ages of up to ~2 kyr occurred at our site during periods of substantial meltwater release and ocean stratification. An additional consideration may be release of aged CO_2 during ice sheet melt [33]. Here, we use the age model derived from tuning the *N. pachyderma* sin. % record to GISPII $\delta^{18}O$ profile which provides a robust stratigraphy that is

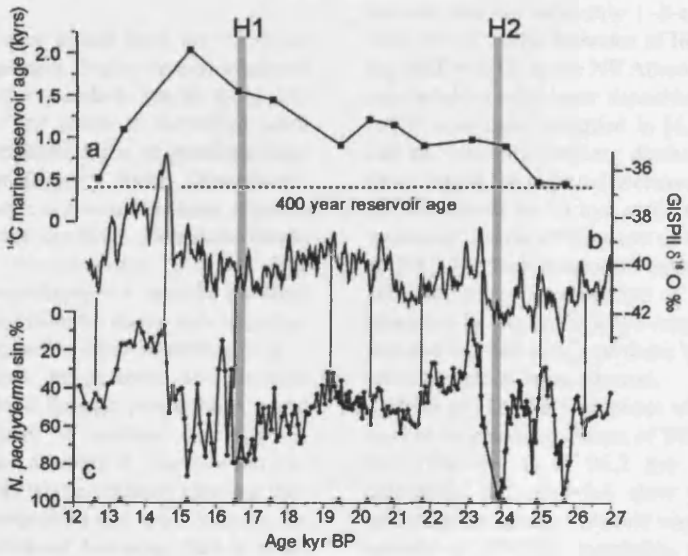

Fig. 2. Stratigraphic correlation between relative abundance of *N. pachyderma* sin. and GISPII ice core. (a) Suggested ^{14}C-marine reservoir ages determined from the age difference between calibrated ^{14}C ages and calendar years based on the correlation of *N. pachyderma* sin. % (c) with GISPII $\delta^{18}O$ [28] (b). Dashed line indicates the present day North Atlantic ^{14}C-marine reservoir age of 400 yr. Vertical lines indicate tie-points used for stratigraphic correlation. Black triangles in (c) indicate ^{14}C date. Grey bars locate H layers 1 and 2.

comparable with the Greenland ice core record and palaeoceanographic profiles from other North Atlantic core sites [34]. Sedimentation rates range between 12 and 60 cm kyr^{-1} yielding, at a sampling interval of 1–2 cm, a mean time step along the records of 60±30 yr.

Lithic grains >150 μm embedded within the silty clay sediment are considered to be ice rafted [7,25]. Through visual, lithological classification we distinguish between non-provenance specific quartz and haematite-coated grains, an East Greenland/Icelandic (EGIIS) assemblage of volcanic debris (pumice, black glass and basalt), LIS-sourced dolomitic carbonate [35], and a BIS assemblage (shale, dark carbonates and black limestone) sourced in part from Carboniferous formations that outcrop across much of Ireland. Chalk clasts occasionally associated with this BIS assemblage support an Irish Sea ice stream source, with Coniacian–Santonian age coccoliths (pers. comm. J. Young, Natural History Museum) suggesting erosion of the Celtic Shelf by the Irish Sea ice stream [cf. [18]].

As additional provenance fingerprints we use radiogenic isotopes ($^{143}Nd/^{144}Nd$) and $^{40}Ar/^{39}Ar$ ages of individual hornblende grains. The $^{143}Nd/^{144}Nd$ of the non-carbonate, >150 μm fraction was determined for 16 samples in the intervals associated with H2 and H1. Chemically separated Nd was analysed on a Finnigan MAT 261 mass spectrometer at Toulouse University, normalised and reported as ε_{Nd} following Grousset et al. [36].

Hornblende grains were picked from the >150 μm size fraction wherever present. Grains were co-irradiated with hornblende monitor standard Mmhb (age=525 Myr; [37]) and $^{39}Ar/^{40}Ar$ ratios of individual hornblende grains were determined at the Ar geochronology laboratory at Lamont–Doherty Earth Observatory. Resulting ages have been corrected for mass discrimination, interfering nuclear reactions, procedural blanks and atmospheric Ar contamination [38–40]. The assignment of IRD assemblages to a specific ice sheet provenance is determined from the above suite of proxy-approaches and is discussed in detail elsewhere [41].

Upper water column temperature and vertical structure were determined through paired Mg/Ca and oxygen isotope analyses of surface dwelling *G. bulloides* and subsurface dwelling *N. pachyderma* sin. Samples of 50 specimens where available (not less than 20) were crushed, homogenised and split. Samples for Mg/Ca analysis were cleaned following Barker et al. [42] and analysed on an ICP-AES (Varian Vista) with a precision better than 0.4% (1σ; liquid standard), and sample reproducibility of ≤4%. Temperature calibration is discussed below (Section 3.2). All stable isotope analyses were made using a ThermoFinnigan MAT 252 with an external reproducibility of ≤0.08‰ for $\delta^{18}O$ and 0.03‰ for $\delta^{13}C$. Benthic isotope measurements were made on 1–4 specimens of *Cidicidoides wuellerstorfi* where possible.

3. Results and discussion

3.1. Ice sheet instabilities

An almost constant flux of IRD to the core site throughout the period 26.5–17 kyr BP suggests constant readjustment of the BIS marine margins. Within this time, four distinct episodes of ice sheet instability may be inferred from enhanced IRD flux (Fig. 3d). The H1 and H2 layers, centred at 24.1 kyr BP and 16.9 kyr BP, respectively, stand out in the records due to their high magnetic susceptibility (Fig. 3b; [23,43]) and the presence of distinctive dolomitic carbonate sourced from the Hudson Strait region of the LIS (Fig. 3g; [35]). Crustal debris derived from the Precambrian shield underlying the LIS is identified by ε_{Nd} values of <−24 (Fig. 3a) [17,44,45]. This is corroborated by the Palaeoproterozoic age range (1650–1900 Ma) of the Churchill Province which dominates the assemblages of hornblende grains extracted from each of these IRD layers in our core (Fig. 3c: H1, 84% n=13; H2, 82% n=29) [40]. These are the type H layers sensu strictu. At this site they are each only 1–6 cm thick and represent 100–300 yr within episodes of IRD deposition exceeding 2000 yr (H2) in the NE Atlantic. Given the apparent synchronicity of H layer deposition across the IRD belt (cf. H layer ages compiled in [6,34]) instability of the LIS and extensive iceberg discharge from the Hudson Strait lagged the regional increase in IRD deposition in the NE Atlantic by >1 kyr, consistent with the European 'precursor' events of Grousset et al. [17] and Scourse et al. [18]. The high resolution records, robust age model and multi-proxy investigation of ice–ocean interaction presented in this study allow more detailed interpretation and accurate dating of these 'precursor' events than previous studies have allowed.

Prior to H2, the first phase of ice sheet activity is marked by enhanced fluxes of EGIIS- and BIS-sourced IRD (Fig. 3e, f) at 26.2 kyr BP, with associated radiogenic ε_{Nd} of −5.6 (just above 'd', Fig. 3a) reflecting the strong volcanic contribution. This initial episode of NWEIS instability and IRD deposition occurred 1.9 kyr prior to the first appearance of Hudson Strait sourced debris at 24.25 kyr BP and lasted 400 yr. Enhanced deposition of BIS debris recommenced at 25.5 kyr BP and increased steadily for 300 yr with little

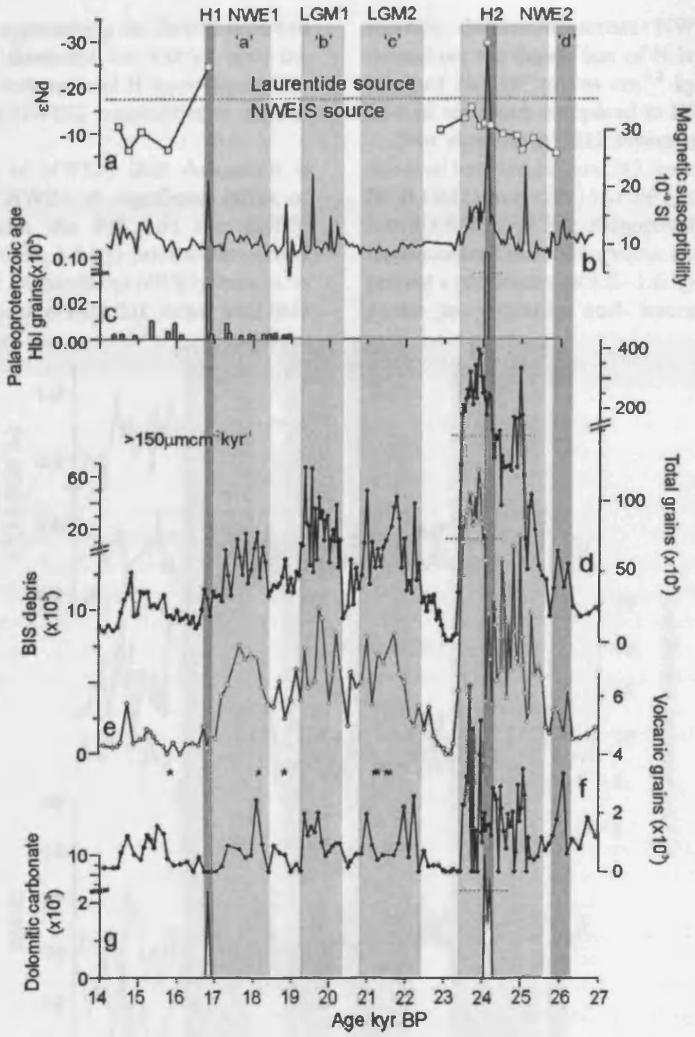

Fig. 3. Lithological and geochemical IRD records versus age from core MD01-2461. All measurements except magnetic susceptibility were made on the >150 μm fraction. All IRD counts are normalized to fluxes (grains g^{-1} × dry bulk density (g cm^{-3}) × sedimentation rate (cm kyr^{-1}) = grains cm^{-2} kyr^{-1}). (a) ε_{Nd} of silicate fraction, (b) whole-core magnetic susceptibility [43], flux of ice rafted (c) hornblende grains with Palaeoproterozoic (1650–1900 Ma) $^{40}Ar/^{39}Ar$ ages, (d) total grains, (e) BIS grains, (f) volcanic grains and (g) dolomitic carbonate grains to MD01-2461 (>150 μm cm^{-2} kyr^{-1}). Note break in axes. Stars in (e) denote depths where Upper Cretaceous Chalk is found. Vertical bars highlight dominance of IRD provenance; light grey = BIS is main IRD source; medium grey = significant contribution from EGIIS; dark grey = LIS signature is recorded. Acronyms are as follows: H, Heinrich Layer; NWE, NW European ice sheet sourced events (numbers refer to respective H layers). LGM, last glacial maximum. Letters a, b, c and d refer to correlative events of Bond and Lotti [7].

input from the EGIIS. IRD flux then rapidly increased, total IRD exceeding 350×10^3 grains cm^{-2} kyr^{-1} at 25.0 kyr BP. Increased fluxes of both volcanic and BIS debris, together with ε_{Nd} values of −6.3, suggest bimodal sourcing of IRD from both the BIS and EGIIS in this phase of considerable NWEIS instability lasting 300 yr. The timing of this peak in NWEIS instability recorded at MD01-2461 is, within the constraints of the age models, equivalent to that of the relatively radiogenic ε_{Nd} 'precursor' IRD peak at MD95-2002 in the Bay of Biscay [17], and the Celtic Shelf chalk-rich IRD peak at the Goban Spur [18]. Following this episode of substantial IRD deposition, the flux of volcanic debris decreased again while ε_{Nd}

values of −11 to −12, approaching the British Isles end member [45], became dominant for 900 yr, until the arrival of LIS-sourced icebergs and H layer deposition. This entire episode of NWEIS instabilities is termed NWE2 (Fig. 3).

Similar sequencing of NWEIS IRD deposition is observed prior to H1, NWE1. A significant influx of IRD derived from both the BIS and the EGIIS, commenced at 18.4 kyr BP, 1.5 kyr prior to the arrival of Hudson Strait debris. Dissimilar to NWE2, there is no substantial increase or peak in IRD flux, rather total IRD steadily decreases across NWE1, remaining low throughout the deposition of H layer 1 when total IRD was just 28×10^3 grains cm^{-2} kyr^{-1}, approximately a 10-fold reduction compared to H2 fluxes.

Two significant IRD layers of NWEIS derivation occurred between H1 and H2, commencing at ~22.4 kyr BP (LGM2) and ~20.3 kyr BP (LGM1). These intervals lasted 1.6 and 1.0 kyr, respectively. The peaks of these three most recent IRD events (LGM2, 1 and NWE1) present a periodicity of 1.5–1.6 kyr, likely correlating to peaks in volcanic and haematite-coated grains

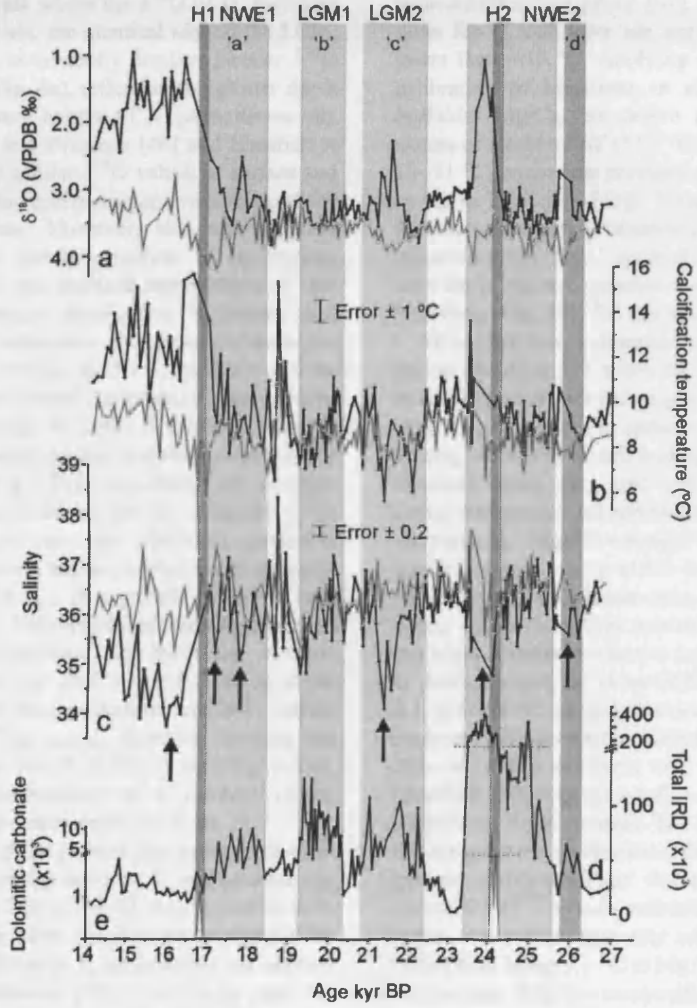

Fig. 4. Upper ocean climate records from core MD01-2461. (a) $\delta^{18}O$ of *G. bulloides* (black, closed circles) and *N. pachyderma* sin. (grey, open circles). (b) Calcification temperatures (°C) of *G. bulloides* (upper 60 m of water column; black, closed circles) and *N. pachyderma* sin. (100-200 m water depth; grey, open circles). (c) SSS (black, closed circles) and subsurface salinity (grey, open circles) based on *G. bulloides* and *N. pachyderma* sin., respectively. Flux of (d) total IRD, (e) dolomitic carbonate ($\times 10^3$; per $cm^{-2}kyr^{-1}$) to MD01-2461. Vertical bars and abbreviations as Fig. 3. Meltwater pulses indicated with vertical arrows on (c).

recognised within the North Atlantic IRD belt ("a", "b" and "c" of [7]). IRD deposited at our core site from the first phase of NWE2, peaking at 25.9 kyr BP, may relate to "d" at ~23.0 ^{14}C kyr [7] and is labelled accordingly (Fig. 3), supporting synchronous instability of the NWEIS and potentially the south-eastern extent of the LIS also.

3.2. Surface, subsurface and intermediate water conditions associated with ice rafting events

Except for intervals where the δ^{18}O of *G. bulloides* and *N. pachyderma* sin. are identical around the LGM, *N. pachyderma* sin. consistently displays heavier δ^{18}O than *G. bulloides* (Fig. 4a), reflecting the greater depth and lower temperature habitat of *N. pachyderma* sin. As Hillaire-Marcel and Bilodeau [46] and Simstich et al. [47] we interpret similar δ^{18}O values of surface and subsurface species to represent intensive mixing of the upper water column. However, this interpretation requires that each species calcifies in equilibrium with seawater δ^{18}O and ambient temperature, or that possible disequilibrium calcification is known and corrected for. The carbonate–water temperature equation of Shackleton [48] is used to determine equilibrium calcite oxygen isotope composition from modern water column data (Fig. 5a; [49]). A factor of −0.27‰ is used to convert water on the SMOW scale to calcite on the VPDB (Fig. 5b). Assuming an average calcification depth of 30 m for *G. bulloides* [50], $\delta^{18}O_{G.\ bulloides}$ from core top specimens predict a summer (~July) growth season, within water temperatures averaging ~12 °C. This growth season is later than that of April–June predicted by Ganssen and Kroon [51], who assume *G. bulloides* isotopic temperatures reflect true SST, not the 0–60 m depth range within which the specimens calcified. Similar latitude core top $\delta^{18}O_{G.\ bulloides}$ from the Ganssen and Kroon data set (Fig. 5b; [51]) fit our core top values, reinforcing our interpretation of a summer bloom season at an average water depth of 30 m.

The lower limit of the present day summer thermocline, overlies the average depth of *N. pachyderma* sin. calcification, ~100–200 m [47,52–54], where there is negligible change in water temperature throughout the year (<0.6 °C). As fluxes in *N. pachyderma* sin. are tied to phytoplankton blooms [53], it is likely that the majority of *N. pachyderma* sin. calcified during a similar growth season to *G. bulloides* yet effectively record the mean annual temperature of subsurface waters [55]. Significant regional variability of vital effect, offsetting $\delta^{18}O_{N.\ pachyderma\ sin.}$ from equilibrium calcite, is determined from North Atlantic–Arctic Ocean core tops where *N. pachyderma* sin. currently thrive. Offsets range between 0‰ [56–58] and −1‰ [47,53,59,60]. The absence of *N. pachyderma* sin. from the top 1 m of MD01-2461 precludes attempts to determine possible $\delta^{18}O_{N.\ pachyderma\ sin.}$ disequilibria, yet it would appear that any offset at this site would certainly be <1‰, potentially zero [56]. From these considerations we assume that both planktonic species calcified in, or close to, isotopic equilibrium (cf. [46]).

Mg/Ca of foraminifers is proven to be an effective palaeotemperature proxy [61], but established calibrations for *G. bulloides* are not based on temperatures lower than ~10 °C. Applying the Mg/Ca–temperature calibration of Mashiotta et al. [62] to core top *G. bulloides* Mg/Ca, we derive summer SSTs 2 °C in excess of modern SST (13.7 °C [49]) and LGM SSTs of 10–11 °C, exceeding previous estimates for this region by up to 7 °C (e.g. [63]). These discrepancies suggest that the calibration of Mashiotta et al. [62] is unsuitable at our core site. As *N. pachyderma* sin. is absent in the core top it was not possible to assess the calibration of Nürnberg et al. [64] for this species.

To resolve these calibration issues we assume that the period 20–19 ka BP, when the δ^{18}O values of both *G. bulloides* and *N. pachyderma* sin. are broadly identical (Fig. 4a), represents an episode of upper water column mixing [46,47] in which both species were exposed to identical water mass and calcification temperatures. Using the exponential relationship between Mg/Ca and temperature, $Mg/Ca = A\exp(B \times T)$, and assuming a similar exponent value of 0.1 for both species [65], we determine a pre-exponent ratio *G. bulloides*:*N. pachyderma* sin. of 2.1. From modern SST (30 m) and core top Mg/Ca values we derive a pre-exponent of 0.68 for *G. bulloides* and, by virtue of the pre-exponent ratio of 2.1, 0.32 for *N. pachyderma* sin., assuming a fixed pre-exponent ratio across the glacial–interglacial transition. This calibration compares well with that of Barker and Elderfield [50] ($Mg/Ca = 0.72 \times e^{0.1T}$) for *G. bulloides* at 60°N in the North Atlantic. The *N. pachyderma* sin. Mg/Ca–temperature calibration effectively equates to the generic calibration of Anand et al. [65] ($Mg/Ca = 0.38 \times e^{0.09T}$), with variability in estimated calcification temperature that may arise from these different calibrations being <1 °C at Mg/Ca = 0.78 mmol mol^{-1}, the average Mg/Ca composition of MD01-2461 *N. pachyderma* sin. Our calibration overestimates calcification temperatures by 2–3 °C compared to the T–Mg/Ca *N. pachyderma* sin. calibration of Nürnberg et al. [64] ($Mg/Ca = 0.47 \times e^{0.08T}$) using laboratory cultures and Norwegian Sea core top samples. However, early-

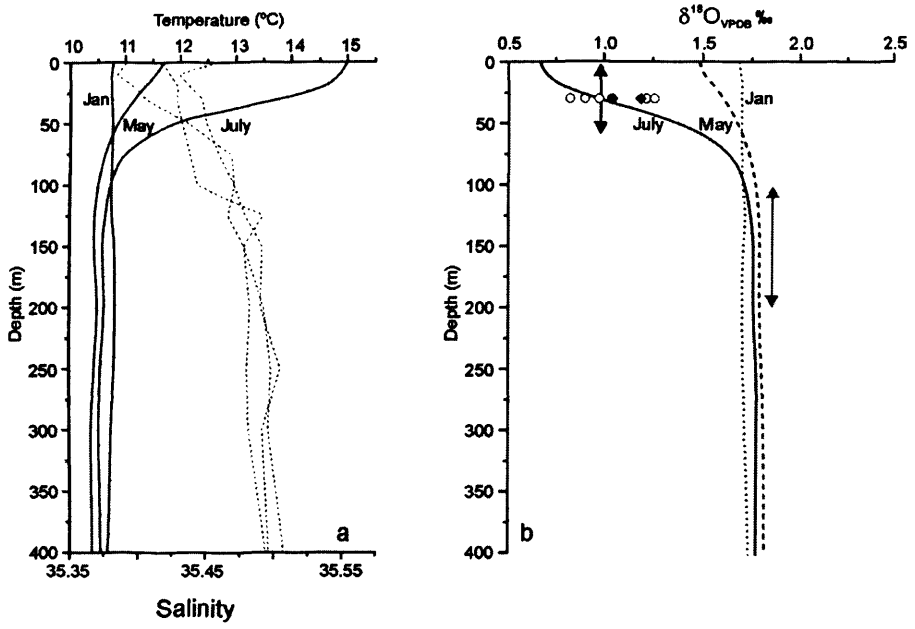

Fig. 5. Modern seawater temperature, salinity, and computed equilibrium $\delta^{18}O_{calcite}$ profiles from MD01-2461. (a) Hydrographic data (temperature - solid lines, salinity - dashed lines) for January, May and July [49]. (b) computed equilibrium $\delta^{18}O_{calcite}$ following [48]. Double-headed arrows locate average calcification depth of *G. bulloides* (black) and *N. pachyderma* sin. (grey). Core top $\delta^{18}O_{G.\ bulloides}$ (open circles from MD01-2461; Black diamonds from box cores 88-06 and 88-07 at 51.4°N and 50.5°N [51]).

Holocene (9.6–8.6 kyr BP) *N. pachyderma* sin. calcification temperatures derived from our calibration average 10.3 °C (unpublished data) and compare well with modern temperatures at a water depth of 150 m (10.6 °C; [49]), substantiating our calibration and suggesting regional differences in the T–Mg/Ca *N. pachyderma* sin. relationship [55]. We consider combined analytical and calibration uncertainties of Mg/Ca-derived temperature estimates to amount to ±1 °C [65].

The resulting temperature record derived from *G. bulloides* Mg/Ca suggests variability of SST within the range 6–16 °C (Fig. 4b), with a SST increase during the early deglacial of ~4 °C. Glacial SST trends derived from *G. bulloides* broadly parallel subsurface temperatures, as determined from *N. pachyderma* sin. Mg/Ca, within the range 6–12 °C (Fig. 4b).

Amplitudes of the temperature anomalies of the two species do not directly mirror the magnitude of coeval excursions in the paired $\delta^{18}O$ records of both species, that on occasion display an anti-phased trend between *G. bulloides* and *N. pachyderma* sin. $\delta^{18}O$ (Fig. 4c). This pattern alludes to changes not only in temperature, but seawater oxygen isotope (δ_w) composition and salinity, with implications for upper ocean water mass stratification. Calcification temperatures, based on Mg/Ca ratios, were used to subtract the temperature component from planktonic $\delta^{18}O$, allowing determination of δ_w following the oxygen isotope palaeotemperature equation of Shackleton [48]. $\delta^{18}O$ values were corrected for global ice volume following [66]. Assuming that the freshwater endmember $\delta^{18}O$ was similar to today, salinity was then determined following the modern North Atlantic δ_w–Salinity relationship, $\delta_w = S \times 0.61 - 21.3$ [67], enabling estimates of density (σ_t) to be made using the International Equation of State of Seawater [68]. Incorporating the errors associated with the analytical precision for Mg/Ca and $\delta^{18}O$, temperature calibration uncertainties and assuming an error of estimate for salinity on δ_w of 0.08 that is derived from the North Atlantic surface δ_w–Salinity relation suggests an uncertainty envelope on density in the range 0.6–0.7 σ_t units. Total error on salinity estimates in the order of ±0.2.

Overlapping density values at the two depth habitats (~30 m for *G. bulloides* and ~150 m for *N. pachyderma* sin.) suggest a well-mixed upper water column at this site for most of the late glacial (Fig. 6b). Elevated $\delta^{13}C_{benthic}$ (>1.5‰; Fig. 6c) during much of this time also suggest rapid ventilation of the mid-depth waters during the late glacial from a nearby source in the open

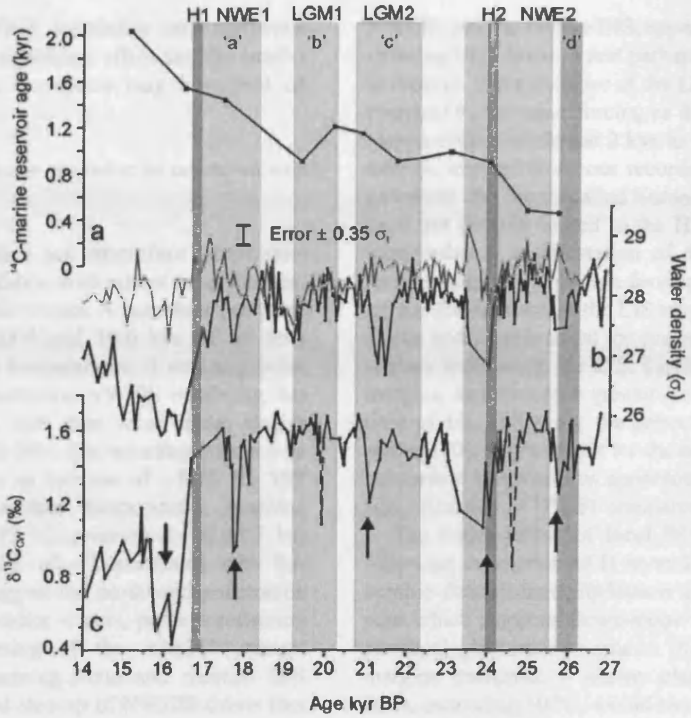

Fig. 6. Upper ocean density profile, intermediate water ventilation and ^{14}C-marine reservoir age proxy records from core MD01-2461. (a) ^{14}C-marine reservoir age (as Fig. 2a). (b) Density (σ_t) for surface (*G. bulloides*; black) and subsurface (*N. pachyderma* sin.; grey) waters. Error bars indicate region of uncertainty in density calculation. (c) δ^{13}C of the benthic foraminifera *Cibicidoides wuellerstorfi*. Vertical bars and abbreviations the same as Fig. 3. Reduced surface density and upper water stratification (b) and associated reductions in δ^{13}C (c) indicated with vertical arrows. Dotted lines in (c) highlight one-point peaks that are potential 'outliers'.

North Atlantic [4,69]. Following H1, SST averages ~4 °C warmer than average LGM temperatures, while a persistent offset of >1‰ is displayed between $\delta^{18}O_{G.\ bulloides}$ and $\delta^{18}O_{N.\ pachyderma\ sin.}$ and a ~0.7‰ reduction in $\delta^{13}C_{benthic}$. This data pattern indicates enhanced surface stratification and concomitant convection slowdown at this site in the course of enhanced meltwater shedding during deglaciation.

Periodic negative excursions in sea surface salinity (SSS) of up to 2.6 suggest recurrent meltwater surges, with fluxes maximising following the major phases of NWEIS instability at NWE2, H2, LGM2 and 1, and NWE1 and finally at H1 (Fig. 4c). The LGM1 salinity reduction peaking at 19.2 kyr BP coincides with the 19-kyr meltwater pulse, supporting the contention [70] that rapid sea level rise of 10–15 m at this time in part originated within the North Atlantic.

These meltwater incursions frequently stratify the upper water column, inferred by divergent surface and subsurface water densities (Fig. 6b). $\delta^{13}C_{benthic}$ depletion by up to 1.2‰ during these episodes suggests reduced intermediate water ventilation, likely reflecting northwards penetration of Antarctic Intermediate Water (AAIW; [4,71]) (Fig. 6c). Several lowered $\delta^{13}C_{benthic}$ data points associated with each NWE meltwater event reinforce the contention that reduced bottom water ventilation at our site, independent of LIS meltwater forcing, is a real feature of these events. Furthermore, each episode of meltwater release, surface stratification and apparent AMOC reduction appears to have had a cumulative effect on the ^{14}C-marine reservoir age at MD01-2461 as each successive event is coincident with a further increase in marine reservoir age (Fig. 6). A temporary reversal in this trend is observed at 19.6 kyr BP, following a period of vigorous AMOC and upper water column mixing at the core site which went some way to 'resetting' the reservoir ages before meltwater associated with NWE1 and H1 caused reservoir ages to increase yet again.

While reduced $\delta^{13}C_{benthic}$ is a well documented feature of H events in the North Atlantic [3–5], reduced bottom water ventilation presented here, associated

exclusively with NWEIS instability and meltwater forcing highlights the significant effect that the smaller circum-North Atlantic ice sheets may have had on AMOC.

3.3. Ice sheet processes in response to ocean–climate forcing

The records of surface and subsurface temperature display fine-scale variability, with salient anomalies that coincide with major IRD events. A notable warm pulse is recorded between 19.0 and 18.6 kyr BP in both surface and subsurface temperatures. A warming pulse at this time, possibly initiating NWEIS instability, has been noted at several core sites west of the British Isles [19,72]. At MD02-2461 this warming occurs over 400 yr and amounts to an increase of ~8 °C for SST and ~5 °C for subsurface temperatures, reaching maxima of 15.6 and 12 °C, respectively at 18.7 kyr BP. An increase in SSS of ~3 associated with this warming pulse may suggest the northward penetration of low latitude, warm saline waters, perhaps reflecting a transient strengthening of the AMOC. Abrupt termination of this warming trend and reduced SSS is associated with initial step-up of NWEIS debris flux at 18.4 kyr BP, NWE1.

Increased upper ocean temperatures prior to IRD deposition derived from the NWEIS suggests an intensification of ocean thermal forcing may have led to basal melt of ice shelves fringing these ice sheets and retreat of the grounding line [73,74]. At the same time heat exchange with the atmosphere may have increased surface melt, accelerating ice shelf break up [75] and ice stream flow [76]. Increased ice accumulation on the BIS, caused by increased precipitation from a warmed atmosphere, possibly increased the interior ice sheet mass and thereby reduced stability further [77]. Close coupling of ocean–climate and BIS stability is envisaged. It is suggested that BIS instability initiating NWE2, recorded by moderate BIS-IRD deposition, may have resulted from ice shelf break-up due to surface–subsurface warming above a critical threshold (cf. [73,75,78]). Within the 300 yr duration of this phase, sufficient ice shelf was melted back to reduce any buttressing effect, triggering fast flow of tributary ice streams [79] producing the large and abrupt increase in IRD deposition during the peak of the NWE2 event at 25.0 kyr BP. Accelerated ice stream activity appears to have lasted for ~300 yr, during which IRD deposition remained high and sufficient freshwater was released to stabilise the upper water column and reduce intermediate water ventilation. After this unstable phase, the NWEIS, principally the BIS, appear to have restabilised, reducing IRD delivery and perhaps allowing ice volume to recover. Were collapse of the LIS interpreted to be in response to the same forcing as the NWEIS (cf. [18]) a response time of almost 2 kyr in excess of the NWEIS may be implied from our records. As such, it may be perceived that the so-called European 'precursor' events were not directly linked to the H events (cf. [17]), but were rather a manifestation of differing ice sheet response times to a common forcing, conceivably reflecting the greater mass of the LIS supporting a high thermal inertia and/or time taken for ocean warming to reach ice shelves buttressing the LIS. Limited marine-based BIS margins, and therefore greater ice sheet stability by the time of H1, following the retreat of the Irish Sea ice stream [80], may account for the high rise in surface and subsurface temperatures apparently required to initiate BIS instability at NWE1 compared to NWE2.

The major influx of local BIS debris immediately following deposition of H layer 2 includes the shallow benthic foraminifera *Elphidium excavatum forma clavata* which suggests down-slope transportation from a proximal glaciomarine source [81]. Assuming marine margins remained, it seems plausible that increased SSTs, exceeding 10 °C, would have destabilised the BIS margin further, enhancing calving and initiating debris flow down the continental slope. A rise in sea level of 10 to 15 m associated with the collapse of the LIS [82,83] may also have contributed to this destabilisation [18]. The near absence of locally derived IRD coincident with or following H1 suggests that the BIS ice margin had retreated sufficiently to be unaffected by a SST or sea level change associated with LIS collapse, or that exposed sea floor within the Irish Sea limited iceberg entry into the open ocean, glacial runoff freshening surface waters as opposed to ice rafting.

3.4. NW European ice sheet instability and AMOC variability

Decreased mid-depth water ventilation prior to the main LIS collapse events at H1 and H2 are noted in $\delta^{13}C_{benthic}$ records throughout the North Atlantic [3–5,71]. Whereas the decline of intermediate water ventilation is often progressive in these records, beginning up to 2.5 kyr before full H conditions (H1; [4]), $\delta^{13}C_{benthic}$ at our site records temporary, 200–400 yr, reduction in intermediate-water ventilation, associated with NWEIS instability/meltwater forcing, 1.2–1.8 kyr before full H event conditions. $\delta^{13}C_{benthic}$ at MD01-2461 then decreases again associated with and following LIS-sourced IRD deposition and further meltwater

release, in phase with records of complete AMOC collapse [71]. Given that advance of AAIW to MD01-2461 was likely in compensation for reduced Glacial North Atlantic Intermediate Water (GNAIW) formation [71], far-reaching effects of the NWEIS-sourced meltwater pulses may be implied prior to both H1 and H2. It is envisaged that NWEIS-sourced meltwater extended to the area of GNAIW formation, weakening deep/intermediate water production and reducing AMOC. Had the meltwater pulses produced longer-term stratification of surface waters within this region than is observed at MD01-2461 they may account for the progressive, pre-H event spin-down of AMOC recorded at more southerly sites [4].

4. Summary

We demonstrate the apparent sensitivity and heightened response of the NWEIS to climatic warming with respect to the well grounded, stable LIS during the last glacial period. Despite the comparatively small ice volume of the NWEIS, their positioning with respect to the likely centre of last glacial North Atlantic deep or intermediate water formation appears to have made meltwater released from the NWEIS an effective means of causing basin wide AMOC variability, highlighting the important role of the NWEIS in millennial scale climatic events.

Acknowledgements

We thank H.J. Medley and B.T. Long for sample preparation, R.T. Chaudri for assistance with AMS sample preparation, M.J. Greaves for sharing his expertise in Mg/Ca analysis and G.G. Bianchi for stable isotope analysis. We are grateful to J.T. Andrews and H. Rashid for their constructive comments that greatly improved this manuscript. This work was funded by the Natural Environment Research Council.

References

[1] A. Ganopolski, S. Rahmstorf, Rapid changes of glacial climate simulated in a coupled climate model, Nature 409 (2001) 153–158.

[2] S. Charbit, C. Ritz, G. Ramstein, Simulations of Northern Hemisphere ice-sheet retreat: sensitivity to physical mechanisms involved during the last deglaciation, Quat. Sci. Rev. 21 (2002) 243–265.

[3] L. Vidal, L. Labeyrie, E. Cortijo, M. Arnold, J.C. Duplessy, E. Michel, S. Becqué, T.C.E. van Weering, Evidence for changes in the North Atlantic deep water linked to meltwater surges during the Heinrich events, Earth Planet. Sci. Lett. 146 (1997) 13–27.

[4] R. Zahn, J. Schonfeld, H.R. Kudrass, M.H. Park, H. Erlenkeuser, P. Grootes, Thermohaline instability in the North Atlantic during meltwater events: stable isotope and ice-rafted detritus records from core SO75-26KL, Portuguese margin, Paleoceanography 12 (1997) 696–710.

[5] M. Elliot, L. Labeyrie, J.C. Duplessy, Changes in North Atlantic deep-water formation associated with the Dansgaard–Oeschger temperature oscillations (60–10 kyr), Quat. Sci. Rev. 21 (2002) 1153–1165.

[6] S.R. Hemming, Heinrich events: massive Late Pleistocene detritus layers of the North Atlantic and their global climate imprint, Rev. Geophys. 42 (2004) RG 1005, doi:10.1029/2003RG000128.

[7] G.C. Bond, R. Lotti, Iceberg discharges into the North Atlantic on millennial time scales during the last glaciation, Science 267 (1995) 1005–1010.

[8] K.S. Lackschewitz, K.H. Baumann, B. Gehrke, H.J. Wallrabe-Adams, J. Thiede, G. Bonani, R. Endler, H. Erlenkeuser, J. Heinemeier, North Atlantic ice sheet fluctuations 10,000–70,000 yr ago as inferred from deposits on the Reykjanes ridge, southeast of Greenland, Quat. Res. 49 (1998) 171–182.

[9] G. Bond, W. Showers, M. Cheseby, R. Lotti, P. Almasi, P. deMenocal, P. Priore, H. Cullen, I. Hajdas, G. Bonani, A pervasive millennial-scale cycle in North Atlantic Holocene and glacial climates, Science 278 (1997) 1257–1266.

[10] D.R. MacAyeal, Binge/purge oscillations of the Laurentide ice sheet as a cause of the North Atlantic's Heinrich events, Paleoceanography 8 (1993) 775–784.

[11] S.J. Marshall, G.K.C. Clarke, A continuum mixture model of ice stream thermomechanics in the Laurentide Ice Sheet: 2. Application to the Hudson Strait Ice Stream, J. Geophys. Res., [Solid Earth] 102 (1997) 20615–20637.

[12] J.T. Andrews, D.C. Barber, Dansgaard–Oeschger events: is there a signal off the Hudson Strait ice stream? Quat. Sci. Rev. 21 (2002) 443–454.

[13] R.B. Alley, D.R. MacAyeal, Ice-rafted debris associated with binge–purge oscillations of the Laurentide Ice Sheet, Paleoceanography 9 (1994) 503–511.

[14] T. Fronval, E. Jansen, J. Bloemendal, S. Johnsen, Oceanic evidence for coherent fluctuations in Fennoscandian and Laurentide ice sheets on millennium timescales, Nature 374 (1995) 443–446.

[15] M. Elliot, L. Labeyrie, G. Bond, E. Cortijo, J.L. Turon, N. Tisnerat, J.C. Duplessy, Millennial-scale iceberg discharges in the Irminger Basin during the last glacial period, relationship with the Heinrich events and environmental settings, Paleoceanography 13 (1998) 433–446.

[16] P.C. Knutz, W.E.N. Austin, E.J.W. Jones, Millennial scale depositional cycles related to British Ice Sheet variability and North Atlantic palaeocirculation since 45 ka B.P. Barra Fan, U.K. margin, Paleoceanography 16 (2001) 53–64.

[17] F.E. Grousset, C. Pujol, L. Labeyrie, G. Auffret, A. Boelaert, Were the North Atlantic Heinrich events triggered by the behavior of the European ice sheets? Geology 28 (2000) 123–126.

[18] J.D. Scourse, I.R. Hall, I.N. McCave, J.R. Young, C. Sugdon, The origin of Heinrich layers: evidence from H2 for European precursor events, Earth Planet. Sci. Lett. 182 (2000) 187–195.

[19] P.C. Knutz, I.R. Hall, R. Zahn, T.L. Rassmussen, A. Kuijpers, M. Moros, N.J. Shackleton, Multidecadal ocean variability and NW European ice sheet surges during the last deglaciation, Geochem. Geophys. Geosyst. 3 (2002) 1077.

[20] G. Bond, H. Heinrich, W. Broecker, L. Labeyrie, J. McManus, J. Andrews, S. Huon, R. Jantschik, S. Clasen, C. Simet, K. Tedesco, M. Klas, G. Bonani, S. Ivy, Evidence for massive discharges of icebergs into the North Atlantic Ocean during the last glacial period, Nature 360 (1992) 245–249.

[21] G. Bond, W. Broecker, S. Johnsen, J. McManus, L. Labeyrie, J. Jouzel, G. Bonani, Correlations between climate records from North Atlantic sediments and Greenland ice, Nature 365 (1993) 143–147.

[22] J.D. Scourse, M.F.A. Furze, A critical review of the glaciomarine model for Irish sea deglaciation: evidence from southern Britain, the Celtic shelf and adjacent continental slope, J. Quat. Sci. 16 (2001) 419–434.

[23] F.E. Grousset, L. Labeyrie, J.A. Sinko, M. Cremer, G. Bond, J. Duprat, E. Cortijo, S. Huon, Patterns of ice-rafted detritus in the glacial North Atlantic (40–55°N), Paleoceanography 8 (1993) 175–192.

[24] S. Zaragosi, F. Eynaud, C. Pujol, G.A. Auffret, J.L. Turon, T. Garland, Initiation of the European deglaciation as recorded in the northwestern Bay of Biscay slope environments (Meriadzek Terrace and Trevelyan Escarpment), a multi-proxy approach, Earth Planet. Sci. Lett. 188 (2001) 493–507.

[25] W.F. Ruddiman, Late Quaternary deposition of ice-rafted sand in the sub-polar North Atlantic (lat 40° to 65°), Geol. Soc. Amer. Bull. 88 (1977) 1813–1821.

[26] M. Stuiver, P.J. Reimer, R.W. Reimer, CALIB 5.0, http://calib.qub.ac.uk/calib/2005.

[27] A.W.H. Bé, An ecological, zoogeographic and taxonomic review of recent planktonic foraminifera, Oceanic Micropaleontology, Academic Press, New York, 1977, pp. 1–100.

[28] P.M. Grootes, M. Stuiver, Oxygen 18/16 variability in Greenland snow and ice with 10(−3)- to 10(5)-year time resolution, J. Geophys. Res.,Oceans 102 (1997) 26455–26470 (http://depts.washington.edu/qil/datasets/gisp2_main.html).

[29] W.E.N. Austin, E. Bard, J.B. Hunt, D. Kroon, J.D. Peacock, The C-14 age of the Icelandic Vedde Ash — implications for younger Dryas marine reservoir age corrections, Radiocarbon 37 (1997) 53–62.

[30] A.H.L. Voelker, M. Sarnthein, P.M. Grootes, H. Erlenkeuser, C. Laj, A. Mazaud, M.J. Nadeau, M. Schleicher, Correlation of marine C-14 ages from the Nordic Seas with the GISP2 isotope record: implications for C-14 calibration beyond 25 ka BP, Radiocarbon 40 (1998) 517–534.

[31] C. Waelbroeck, J.C. Duplessy, E. Michel, L. Labeyrie, D. Paillard, J. Duprat, The timing of the last deglaciation in North Atlantic climate records, Nature 412 (2001) 724–727.

[32] J. Eiriksson, G. Larsen, K.L. Knudsen, J. Heinemeier, L.A. Simonarson, Marine reservoir age variability and water mass distribution in the Iceland Sea, Quat. Sci. Rev. 23 (2004) 2247–2268.

[33] E.W. Domack, A.J.T. Jull, J.B. Anderson, T.W. Linick, C.R. Williams, Application of tandem accelerator mass-spectrometer dating to late Pleistocene–Holocene sediments of the East Antarctic continental shelf, Quat. Res. 31 (1989) 277–287.

[34] C.C. Veiga-Pires, C. Hillaire-Marcel, U and Th isotope constraints on the duration of Heinrich events H0–H4 in the southeastern Labrador Sea, Paleoceanography 14 (1999) 187–199.

[35] J.T. Andrews, K. Tedesco, Detrital carbonate-rich sediments, north-western Labrador Sea: implications for ice-sheet dynamics and iceberg rafting (Heinrich) events in the North Atlantic, Geology 20 (1992) 1087–1090.

[36] F.E. Grousset, M. Parra, A. Bory, P. Martinez, P. Bertrand, G. Shimmield, R. Ellam, Saharan wind regimes traced by the Sr–Nd isotopic composition of the tropical Atlantic sediments: last glacial maximum vs today, Quat. Sci. Rev. 17 (1998) 395–409.

[37] S.D. Samon, E.C. Alexander Jr., Calibration of the interlaboratory ^{40}Ar–^{39}Ar dating standard, MMhb-1, Chem. Geol. (Isotope Geoscience Section) 66 (1987) 27–34.

[38] S.R. Hemming, W.S. Broecker, W.D. Sharp, G.C. Bond, R.H. Gwiazda, J.F. McManus, M. Klas, I. Hajdas, Provenance of Heinrich layers in core V28–82, northeastern Atlantic: $^{40}Ar/^{39}Ar$ ages of ice-rafted hornblende, Pb isotopes in feldspar grains, and Nd–Sr–Pb isotopes in the fine sediment fraction, Earth Planet. Sci. Lett. 164 (1998) 317–333.

[39] S.R. Hemming, G.C. Bond, W.S. Broecker, W.D. Sharp, M. Klas-Mendelson, Evidence from $^{40}Ar/^{39}Ar$ ages of individual hornblende grains for varying Laurentide sources of iceberg discharges 22,000 to 10,500 14C yr B.P. Quat. Res. 54 (2000) 372–383.

[40] S.R. Hemming, I. Hajdas, Ice-rafted detritus evidence from Ar-40/Ar-39 ages of individual hornblende grains for evolution of the eastern margin of the Laurentide ice sheet since 43 C-14 ky, Quat. Int. 99 (2000) 29–43.

[41] V.L. Peck, I.R. Hall, R. Zahn, F.E. Grousset, J.D. Scourse, The relationship of Heinrich events and their European precursors over the past 60 kyr BP: a multi-proxy ice rafted debris provenance study in the North East Atlantic Quat. Sci. Rev., submitted for publication.

[42] S. Barker, M. Greaves, H. Elderfield, A study of cleaning procedures used for foraminiferal Mg/Ca paleothermometry, Geochem. Geophys. Geosyst. 4 (2003) 8407, doi:10.1029/2003GC000559.

[43] E.R. Wadsworth, PhD Thesis, The identification and characterisation of the North Atlantic Heinrich events using environmental magnetic techniques, St. Andrews (2005).

[44] H. Snoeckx, F. Grousset, M. Revel, A. Boelaert, European contribution of ice-rafted sand to Heinrich layers H3 and H4, Mar. Geol. 158 (1999) 197–208.

[45] F.E. Grousset, E. Cortijo, S. Huon, L. Herve, T. Richter, D. Burdloff, J. Duprat, O. Weber, Zooming in on Heinrich layers, Paleoceanography 16 (2001) 240–259.

[46] C. Hillare-Marcel, G. Bilodeau, Instabilities in the Labrador Sea mass structure during the last climate cycle, Can. J. Earth Sci. 37 (2000) 795–809.

[47] J. Simstich, M. Sarnthein, H. Erlenkeuser, Paired delta O-18 signals of *Neogloboquadrina pachyderma* (s) and *Turborotalita quinqueloba* show thermal stratification structure in Nordic Seas, Mar. Micropaleontol. 48 (2003) 107–125.

[48] N.J. Shackleton, Attainment of isotopic equilibrium between ocean water and the benthonic foraminifer genus *Uvigerina*: isotopic changes in the ocean during the last glacial, vol. 219, Collogue CNRS Centre National de la Recherche Scientifique, Paris, 1974, pp. 203–210.

[49] NODC (Levitus) World Ocean Atlas, 1998, data provided by the NOAA-CIRES Climate Diagnostics Center, Boulder, Colorado, USA, from their Web site at http://www.cdc.noaa.gov/.

[50] S. Barker, H. Elderfield, Foraminiferal calcification response to glacial–interglacial changes in atmospheric CO_2, Science 297 (2002) 833–836.

[51] G.M. Ganssen, D. Kroon, The isotopic signature of planktonic foraminifera from the NE Atlantic surface sediments:

implications for the reconstruction of past oceanic conditions, J. Geol. Soc. (Lond.) 157 (2000) 693–699.

[52] J. Carstens, D. Hebbeln, G. Wefer, Distribution of planktic foraminifera at the ice margin in the Arctic (Fram Strait), Mar. Micropaleontol. 29 (1997) 257–269.

[53] K.E. Kohfeld, R.G. Fairbanks, S.L. Smith, I.D. Walsh, *Neogloboquadrina pachyderma* (sinistral coiling) as paleoceanographic tracers in polar waters: evidence from Northeast Water Polyna plankton tows, sediment traps, and surface sediments, Paleoceanography 11 (1996) 679–699.

[54] R. Volkmann, Planktic foraminifers in the outer Laptev Sea and the Fram Strait—modern distribution and ecology, J. Foraminiferal Res. 30 (2000) 157–176.

[55] D.N. Nürnberg, Magnesium in tests of *Neogloboquadrina pachyderma* sinistral from high northern and southern latitudes, J. Foraminiferal Res. 25 (1995) 350–368.

[56] J.T. Durazzi, Stable isotope studies of planktonic-foraminifera in North Atlantic core tops, Palaeogeogr. Palaeoclimatol. Palaeoecol. 33 (1981) 157–172.

[57] R.F. Spielhagen, H. Erlenkeuser, Stable oxygen and carbon isotopes in planktonic foraminifera from Arctic Ocean surface sediments — reflection of the low-salinity surface water layer, Geology 119 (1994) 227–250.

[58] G.P. Wu, C. Hillaire Marcel, Oxygen isotope compositions of sinistral *Neogloboquadrina-pachyderma* tests in surface sediments — North Atlantic Ocean, Geochim. Cosmochim. Acta 58 (1994) 1303–1312.

[59] D. Bauch, J. Carstens, G. Wefer, Oxygen isotope composition of living *Neogloboquadrina pachyderma* (sin) in the Arctic Ocean, Earth Planet. Sci. Lett. 146 (1997) 47–58.

[60] R. Volkmann, M. Mensch, Stable isotope composition (delta O-18, delta C-13) of living planktic foraminifers in the outer Laptev Sea and the Fram Strait, Mar. Micropaleontol. 42 (2001) 163–188.

[61] H. Elderfield, G. Ganssen, Past temperature and $\delta^{18}O$ of surface ocean waters inferred from foraminiferal Mg/Ca ratios, Nature 405 (2000) 442–445.

[62] T.A. Mashiotta, D.W. Lea, H.J. Spero, Glacial–interglacial changes in Subantarctic sea surface temperature and delta O-18-water using foraminiferal Mg, Earth Planet. Sci. Lett. 170 (1999) 417–432.

[63] M.A. Maslin, N.J. Shackleton, U. Pflaumann, Surface water temperature, salinity and density changes in the northeast Atlantic during the last 45,000 years: Heinrich events, deep water formation, and climatic rebounds, Paleoceanography 10 (1995) 527–544.

[64] D. Nürnberg, J. Bijma, C. Hemleben, Assessing the reliability of magnesium in foraminiferal calcite as a proxy for water mass temperatures, Geochim. Cosmochim. Acta 60 (1996) 803–814.

[65] P.H. Anand, H. Elderfield, H. Conte, Calibration of Mg/Ca thermometry in planktonic foraminifers from a sediment trap time series, Palaeoceanography 18 (2003) 1050, doi:10.1029/2002PA000846.

[66] N.J. Shackleton, The 100,000-year ice age cycle identified and found to lag temperature, carbon dioxide and orbital eccentricity, Science 289 (2000) 1897–1902.

[67] H. Craig, L.I. Gordon, Deuterium and oxygen 18 variations in the ocean and the marine atmosphere, in: E. Tongiorgi (Ed.), Stable Isotopes in Oceano-graphic Studies and Paleotemperatures, Lab. di Geol. Nucl.,Cons. Naz. delle Ric., Pisa, Italy, 1965, pp. 9–130.

[68] UNESCO background papers and supporting data on the International Equation of State of Seawater 1980, UNESCO Technical Papers in Marine Science, vol. 38, 1980, p. 192.

[69] D.W. Oppo, S.J. Lehman, Mid-depth circulation of the subpolar North Atlantic during the last glacial maximum, Science 259 (1993) 1148–1152.

[70] P.U. Clark, A.M. McCabe, A.C. Mix, A.J. Weaver, Rapid rise of sea level 19,000 years ago and its global implications, Science 304 (2004) 1141–1144.

[71] R. Rickaby, H. Elderfield, Evidence from the high-latitude North Atlantic for variations in Antarctic intermediate water flow during the last deglaciation, Geochem. Geophys. Geosyst. 6 (2005), doi:10.1029/2004GC000858.

[72] I.M. Lagerklint, J.D. Wright, Late glacial warming prior to Heinrich event: 1. The influence of ice rafting and large ice sheets on the timing of initial warming, Geology 27 (1999) 1099–1102.

[73] E. Rignot, S.S. Jacobs, Rapid bottom melting widespread near Antarctic ice sheet grounding lines, Science 296 (2002) 2020–2023.

[74] G. Shaffer, S.M. Olsen, C.J. Bjerrum, Ocean subsurface warming as a mechanism for coupling Dansgaard–Oeschger climate cycles and ice-rafting events, Geophys. Res. Lett. 31 (2004) L24202, doi:10.1029/2004GL020968.

[75] D.R. MacAyeal, T.A. Scambos, C.L. Hulbe, M.A. Fahnestock, Catastrophic ice-shelf break-up by an ice-shelf-fragment-capsize mechanism, J. Glaciol. 49 (2003) 2–36.

[76] H.J. Zwally, W. Abdalati, T. Herring, K. Larson, J. Saba, K. Steffen, Surface melt-induced acceleration of Greenland ice-sheet flow, Science 297 (2002) 218–222.

[77] M. Oppenheimer, Global warming and the stability of the West Antarctic ice sheet, Nature 393 (1998) 325–332.

[78] D.G. Vaughan, C.S.M. Doake, Recent atmospheric warming and retreat of ice shelves on the Antarctic Peninsula, Nature 379 (1996) 328–331.

[79] H. De Angelis, P. Skvarca, Glacier surge after ice shelf collapse, Science 299 (2003) 1560–1562.

[80] A.M. McCabe, P.U. Clark, Ice-sheet variability around the North Atlantic Ocean during the last deglaciation, Nature 392 (1998) 373–377.

[81] L.E. Osterman, Benthic foraminiferal zonation of a glacial–interglacial transition from Frobisher Bay, Baffin Island, N.W.T., Canada, in: H.J. Oertli (Ed.), Benthos '83, 1984, pp. 471–476.

[82] J. Chappell, Sea level changes forced ice breakouts in the last glacial cycle: new results from coral terraces, Quat. Sci. Rev. 21 (2002) 1229–1240.

[83] Y. Yokoyama, T.M. Esat, K. Lambeck, Coupled climate and sea-level changes deduced from Huon Peninsula coral terraces of the last ice age, Earth Planet. Sci. Lett. 193 (2001) 579–587.